

Holistic computational design within additive manufacturing through topology optimization combined with multiphysics multi-scale materials and process modelling

Bayat, Mohamad; Zinovieva, Olga; Ferrari, Federico; Ayas, Can; Langelaar, Matthijs; Spangenberg, Jon; Salajeghe, Roozbeh; Poullos, Konstantinos; Mohanty, Sankhya; Sigmund, Ole

DOI

[10.1016/j.pmatsci.2023.101129](https://doi.org/10.1016/j.pmatsci.2023.101129)

Publication date

2023

Document Version

Final published version

Published in

Progress in Materials Science

Citation (APA)

Bayat, M., Zinovieva, O., Ferrari, F., Ayas, C., Langelaar, M., Spangenberg, J., Salajeghe, R., Poullos, K., Mohanty, S., Sigmund, O., & Hattel, J. (2023). Holistic computational design within additive manufacturing through topology optimization combined with multiphysics multi-scale materials and process modelling. *Progress in Materials Science*, 138, Article 101129. <https://doi.org/10.1016/j.pmatsci.2023.101129>

Important note

To cite this publication, please use the final published version (if applicable).
Please check the document version above.

Copyright

Other than for strictly personal use, it is not permitted to download, forward or distribute the text or part of it, without the consent of the author(s) and/or copyright holder(s), unless the work is under an open content license such as Creative Commons.

Takedown policy

Please contact us and provide details if you believe this document breaches copyrights.
We will remove access to the work immediately and investigate your claim.



Snapshot Reviews in Emerging Fields



Holistic computational design within additive manufacturing through topology optimization combined with multiphysics multi-scale materials and process modelling

Mohamad Bayat ^{a,*}, Olga Zinovieva ^b, Federico Ferrari ^a, Can Ayas ^c,
Matthijs Langelaar ^c, Jon Spangenberg ^a, Roozbeh Salajeghe ^a, Konstantinos Poullos ^a,
Sankhya Mohanty ^a, Ole Sigmund ^a, Jesper Hattel ^a

^a Department of Civil and Mechanical Engineering, Technical University of Denmark, Lyngby, Denmark

^b School of Engineering & IT, University of New South Wales Canberra, Canberra, Australia

^c Department of Precision and Microsystems Engineering, Delft University of Technology, Delft, The Netherlands

ARTICLE INFO

Keywords:

Additive manufacturing
Topology optimization
Multiphysics simulation
Process-structure-property
Process multi-scaling

ABSTRACT

Additive manufacturing (AM) processes have proven to be a perfect match for topology optimization (TO), as they are able to realize sophisticated geometries in a unique layer-by-layer manner. From a manufacturing viewpoint, however, there is a significant likelihood of process-related defects within complex geometrical features designed by TO. This is because TO seldomly accounts for process constraints and conditions and is typically perceived as a purely geometrical design tool. On the other hand, advanced AM process simulations have shown their potential as reliable tools capable of predicting various process-related conditions and defects. Thus far, geometry design by topology optimization and multiphysics manufacturing simulations have been viewed as two mostly separate paradigms, whereas one should really conceive them as one holistic computational design tool. More specifically, AM process models provide input to physics-based TO, where consequently, not only the designed component will function optimally, but also will have near-to-minimum manufacturing defects. In this regard, we aim at giving a thorough overview of holistic computational design tool concepts applied within AM. First, literature on TO for performance optimization is reviewed and then the most recent developments within physics-based TO techniques related to AM are covered. Process simulations play a pivotal role in the latter type of TO and serve as additional constraints on top of the primary end-user optimization objectives. As a natural consequence of this, a comprehensive and detailed review of non-metallic and metallic additive manufacturing simulations is performed, where the latter is divided into micro-scale and deposition-scale simulations. Material multi-scaling techniques, which are central to the process-structure-property relationships, are reviewed next, followed by a subsection on process multi-scaling techniques, which are reduced-order versions of advanced process models and are incorporable into physics-based TO due to their lower computational requirements. Finally the paper is concluded and suggestions for further research paths discussed.

* Corresponding author.

E-mail address: mbayat@dtu.dk (M. Bayat).

1. Introduction

Additive manufacturing (AM) is conceived as one of the most decisive enabling elements of the fourth industrial revolution and this is to a large extent due to AM's nearly unlimited degree of geometrical freedom which would not be achievable via any other competing conventional manufacturing processes. This remarkable feature of AM has made this process a perfect match for the superior geometry design tool, topology optimization (TO). The very core salient feature of AM, its layer-by-layer way of building up a part [1], makes it possible to manufacture TO'ed components with sophisticated structures that function with optimal performance. After seminal works of Sigmund and the TopOpt group [2–6], there have been numerous attempts on designing parts with optimal performance and these problems cover a wide range spanning from basic solid mechanical or structural problems [7–9], to fluid dynamics [10], heat transfer [11–13] and photonics [14]. With the advent of AM it is possible to realize these complex geometries.

On top of this major advantage, there also exist several impeding challenges when implementing AM and these predominantly quality-related issues are currently the main obstacles preventing AM from being widely applied within relevant cutting-edge industrial sectors as a reliable manufacturing process. The paramount challenges above all are defects and anomalies in AM-manufactured parts [15]. Such defects could potentially form either due to our lack of knowledge about underlying physical phenomena taking place in AM processes or because of selecting inappropriate input process parameters that could lead to an unstable process.

At the same time and due to a crucial need for rapid certification for AM products, advanced numerical models have proven their capabilities as tools for predicting quality-related conditions of AM-made parts. Furthermore, these simulations have shown to be reliable tools for uncovering the mechanisms of defect formations which would have otherwise been very difficult or too expensive to detect via *in-situ* experimentations as done by [16–21]. These models cover a long list depending on the physics, the material and the process involved and there have been several review papers which have documented progress within each type of these numerical simulations. King et al. [22] and Markl and Körner [23] wrote two of the very first review papers on modelling metal AM and classified these models based on their length-scale and fidelity. Meier et al. [24] reviewed metal AM process models from a more theoretical viewpoint and then categorized these models based on their respective dimensions into three distinct scales of micro-, meso- and macro- or part-scale. Brenken et al. [25] wrote a review on fiber-reinforced fused filament fabrication (FFF). Rashid and Koç [26] wrote a thorough review about different modelling techniques for FFF and categorized them into four different groups. Ferro and Romanin [27], Wei et al. [28] and Bayat et al. [29] recently wrote comprehensive review papers on modelling of metal AM processes and they went in depth with all three scales of the existing models at micro-, meso- and part-scale (Fig. 1).

There has also been a number of thematic review papers of AM processes focusing on a specific process- or quality-related aspect with focus on residual stress formation in metal AM by Bartlett and Li [31], Fang et al. [32] and Bertini et al. [33]. Along the same lines, Luo and Zhao [34] and Paul [35] wrote review papers about finite element (FEM)-based modelling of LPBF and FFF processes, while Cook and Murphy [36] wrote a thematic review paper on fluid-based simulations of powder bed AM processes. Das et al. [37] reviewed progress in rheological characterizations of FFF and went through some related simulations for modelling the polymer fluid behavior inside FFF nozzles. Li et al. [38] and Zhang et al. [39] made review papers about microstructural simulations during metal AM while elaborating on different micro-scale simulations such as cellular automata, phase field, etc. for titanium alloys.

One may implement advanced process models, see Fig. 1, in designing the best process conditions for obtaining an AM part with acceptable quality. In this respect, TO and advanced process numerical simulations, could be viewed as reliable and robust geometrical design tools and multiphysics simulation tools for AM processes, respectively, see Fig. 1. Up until 2019, these two design tools were hardly linked together and there are fairly few works that demonstrate the implementation of TO and process simulations as an integrated unified holistic design tool. When it comes to processing complex geometrical features such as overhangs [40,41], channels [42–44], thin features, etc. that are all inseparable exponents of a TO'ed component, defect formation mechanisms become increasingly sophisticated and thus more difficult to resolve. Under such circumstances the TO'ed geometry might not be manufactured properly due to the formation of geometry-dependent process-related defects. Fig. 2 (b) is an example of a TO'ed component (Fig. 2 (a) is the TO'ed heat sink geometry) in which related process physics and constraints (here residual stresses) were not taken into account during the TO phase. The regions highlighted in red, show overhangs which are over the critical angle, hence support structures are needed to make the part processable, see Fig. 2 (c). Fig. 2 (d) is another failed example where the optimized geometry is disconnected from the base plate and this is because thermo-mechanical process constraints were not accounted for during the TO

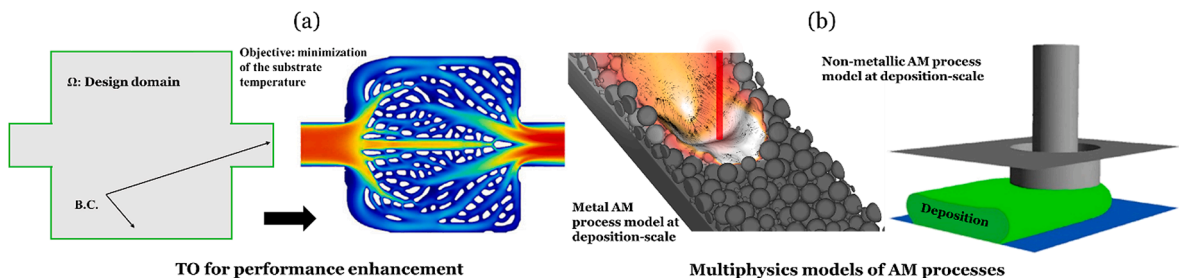


Fig. 1. (a) TO of a thermal management device [13] and (b) multi-physics deposition-scale models of metallic [29] and non-metallic AM processes [30]. (a) and (b) are denoted geometry design and multiphysics simulation tools in this paper, respectively.

phase.

In the AM community, these two tools, namely TO and process simulations have been traditionally viewed as two separate isolated disciplines, whereas in essence they ought to be considered subcomponents of the same holistic computational design approach. Moreover, to the author group's knowledge, there is no paper in the AM literature that covers the entire holistic computational design spectrum ranging from computational design using topology optimization (both performance and process optimization) to multi-physics simulation of both metal and non-metal AM, multi-scaling laws (process-structure-property) and finally reduced order modelling as a unified tool.

TO methods with physics-based AM constraints have nevertheless opened an entirely new paradigm where TO is linked to process models and these models act as an additional constraint to the main optimization objective. Therefore, such models are the cornerstone of the envisioned holistic computational design tool. The black box in Fig. 3 (right) shows the result of a physics-based TO method that accounts for process constraints. The main objective of the TO here is to maximize the stiffness while fulfilling two constraints of; (1) constraining the overall mass and (2) avoiding hotspots due to process heating loads. This relatively simple way of accounting for manufacturing constraints can further be augmented by the envisioned holistic computational design framework presented in the rest of Fig. 3 including all the process- and material multi-scalings is a quite novel concept within computational mechanics and thus has never been introduced before elsewhere.

Multiphysics simulations of AM processes at micro- and deposition-scale shown in the red box in Fig. 3 are ideal tools for predicting quality-related conditions of AM processes. Such models, depending on the type of process, could be employed for finding the *meso*-structure or the porosity pattern forming in the bulk of an AM component and in this way could aid to bypass laborious and lengthy experimentation [45]. Whereas microstructural models are implemented for finding grains' or dendrites' shape and size along with their evolution and nucleation in the course of metal AM processes. However, both these models, are only applicable to limited computational domains that can not easily be replicated in reality if an experimental sample of that tiny size needs to be manufactured. On the top of this, such advanced models, require very fine mesh resolutions to properly capture the physical phenomena occurring during AM. Therefore, it is not feasible to apply these models for predicting an entire real-size sample's conditions. The green box shows the solution to this major issue, the part-scale models which are used for modelling macro-scale phenomena during AM processes using shortcut calculation methods and within acceptable runtimes.

In this scenario as also outlined in Fig. 3, such part-scale simulations could be linked to TO and then they could serve as additional constraints to the primary TO constraints. This would allow for bypassing topologies which are prone to manufacturing defects as demonstrated in Fig. 2. One could furthermore, benefit from material multi-scaling laws and incorporate realistic material properties into the part-scale models via homogenization methods and integrated computational material engineering (ICME) which is also used for establishing process-structure-property relationships, see the purple box in Fig. 3. Therefore, the combination of AM process models and TO forms a holistic computational design tool where the geometry of the component is found by gradient-based TO methods, while respecting process constraints. These constraints are derived based on reduced-order part-scale simulations with averaged material properties found via material multi-scaling and homogenization methods which receive data from micro- and deposition-scale models.

Motivated by these observations, in this work we aim to give a thorough, descriptive and more importantly, a holistic overview of nearly all cross- and multi-disciplinary research outputs of AM with the focus on the application of computational design tools for geometrical and material design, respectively. Thus, we first focus on component performance improvement using topology optimization as a design tool that can determine the final geometry based on the predefined constraints and optimization objectives. Here we give an introduction to existing and mostly AM-related TO techniques while going through their respective literature. Then we move on to TO accounting for manufacturing constraints in the next section. This type of TO, which is a hallmark of the holistic

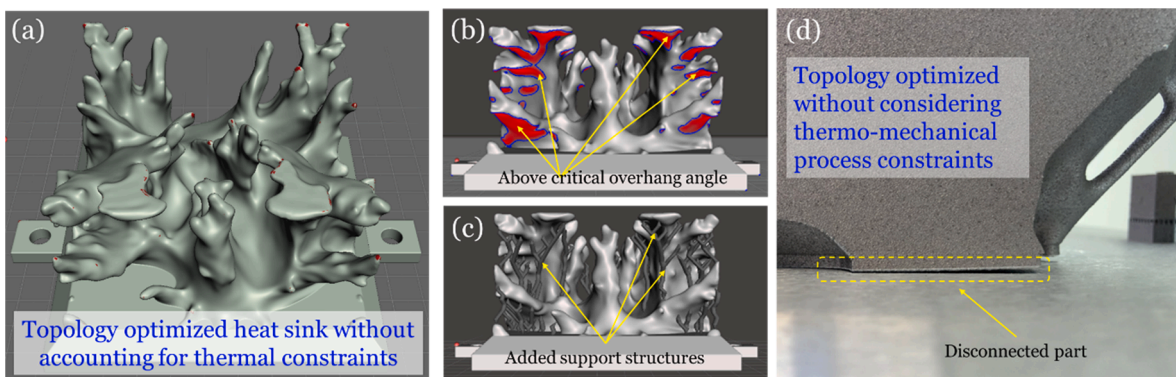


Fig. 2. (a) TO'ed heat sink to be manufactured with AM where the main optimization objective is to minimize the temperature of the bottom electronic chip while fulfilling the mass constraint. One can see that overheating could potentially form in red regions shown in (b) since the original TO does not involve any physics-based AM process constraints and therefore support materials are needed as shown in (c). (d) Another example of ordinary TO without accounting for thermo-mechanical process constraints and this has led to significant residual stresses that result in disconnection of the part.

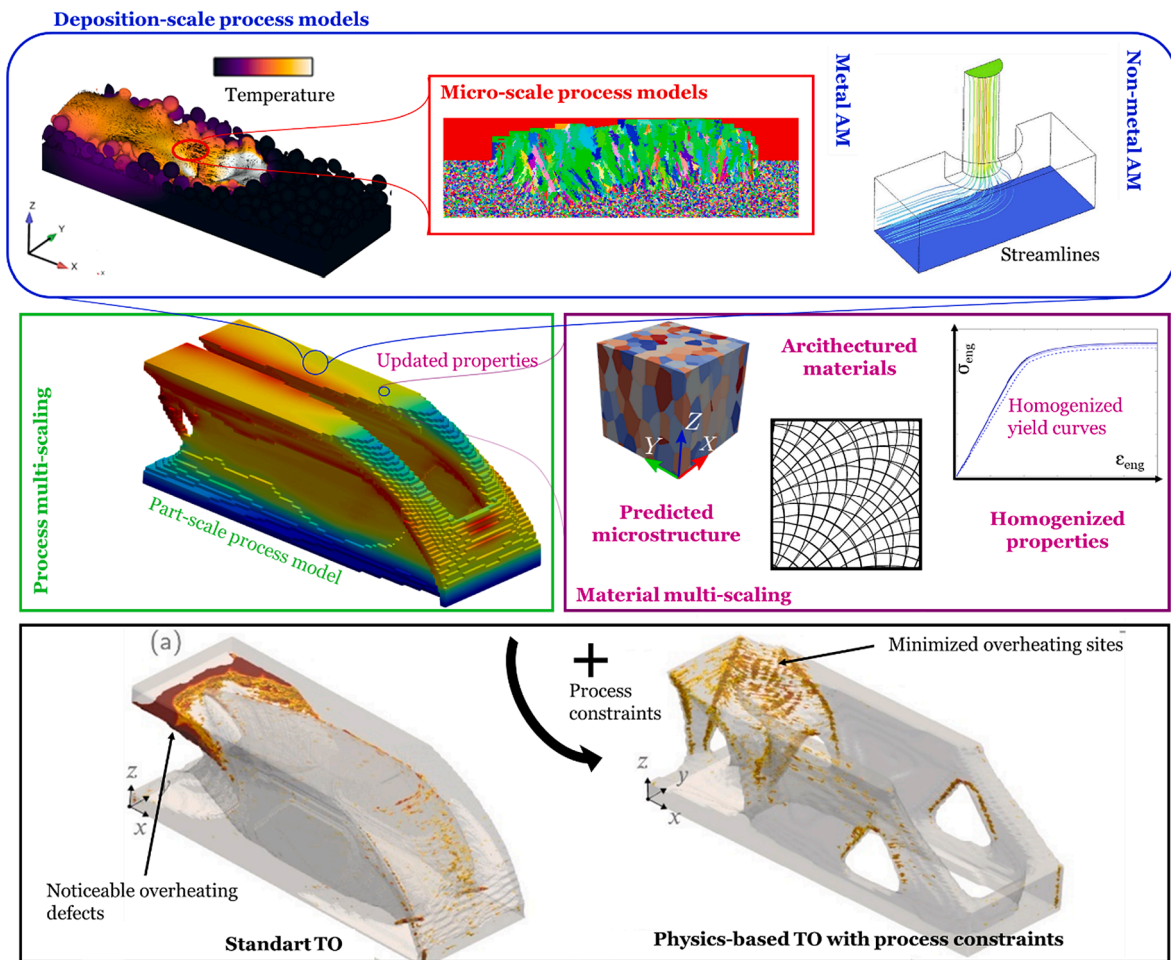


Fig. 3. An overview of the implementation of holistic computational design where AM process models and TO are fully linked. The blue box contains deposition-scale models for metallic and non-metallic AM processes in which the former is linked to a lower-scale model, namely the microstructural model at micro-scale. The light green box shows part-scale models that can predict process conditions of an entire part using process multi-scaling techniques. Purple shows homogenization methods and material multi-scaling techniques (process-structure-property) where the deposition-scale models provide inputs such as meso- and micro-structure of a print and homogenized engineering properties are outputs of these models. Finally, and in black, is the topology optimization with the inclusion of process constraints in which reduced order models are involved in topology optimization.

computational design tool, as opposed to the previously described conventional TO, seeks to determine the geometry of a component in a way that is optimized for least possible process-related defects. This is followed by Section 3, in which we elaborate on different modelling frameworks and methods for multiphysics simulation of both metal and non-metal AM processes at two different length-scales; micro-scale and deposition-scale. Here we also focus on the material models of metals and polymers while going through relevant governing equations and boundary conditions of AM process models. Finally, and as a natural continuation, we follow up with Section 4 and go through multi-scaling techniques where in 4.1. we cover structural and material multi-scaling for architected materials and ICME (process-structure-property relationships), respectively and in 4.2 we will show process multi-scaling for developing reduced-order, part-scale models that are an essential part of physics-based TO with AM process constraints. Here, we basically show how the different multiphysics models described earlier can be coupled to each other via proper cross length-scale linking techniques.

2. Computational design

2.1. Topology optimization – Component performance optimization

The definition of the best layout of a component is perhaps the most important step in a conceptual design phase, strongly affecting any further efficiency improvement. Topology optimization (TO) is a powerful tool for this purpose, giving non-trivial lightweight design solutions with extreme performances. In a nutshell, TO seeks the best distribution of one or more materials within a given design domain, extremizing a given performance criterion while fulfilling a set of constraints. The latter can be classified in three main

categories:

- Equilibrium constraints, usually expressed by a set of Partial Differential Equations (PDEs) based on the involved physic.
- Response constraints, expressing limitations on some of the response quantities.
- Manufacturing constraints, controlling the geometrical features of the design, or accounting for limitations, uncertainties, and cost of manufacturing processes.

Manufacturing constraints may drive the design away from the physics-based optimum. Nevertheless, they are pivotal to ensure the manufacturability of the design itself, and to provide robustness against production flaws and uncertainties. The rapid maturation of additive manufacturing (AM), backed up by advanced multiscale modeling and simulation [46], have opened exceptional possibilities for the interplay between design optimization and manufacturing [47]. To fully exploit such capabilities, especially for the design of extreme architected materials [48] and multi-physics components, a holistic integration of TO and AM should be pursued [49–51].

In the following, Section 2.1.1 overviews methods and tools commonly used in TO, emphasizing those playing a major role in AM integration, as will be discussed in Section 2.2. For exhaustive discussion of the broad field of TO, we refer to [52–54]. Then, sections 2.1.1 to 2.1.3 cover specific applications, such as the introduction of stress and buckling constraints, and heat and fluid transfer problems. These are relevant topics, when pursuing of a holistic integration of AM process modeling in the TO computational framework.

Before proceeding, we stress the role played by open-source software in the dissemination of TO. Several codes, written in popular programming languages, such as MATLAB, Python, etc.), and ranging from basic compliance minimization problems [55] to more advanced applications [9] are available. The recent survey [56] reviews and compares >120 available educational papers and software, giving a comprehensive outlook of their impact on education and industry.

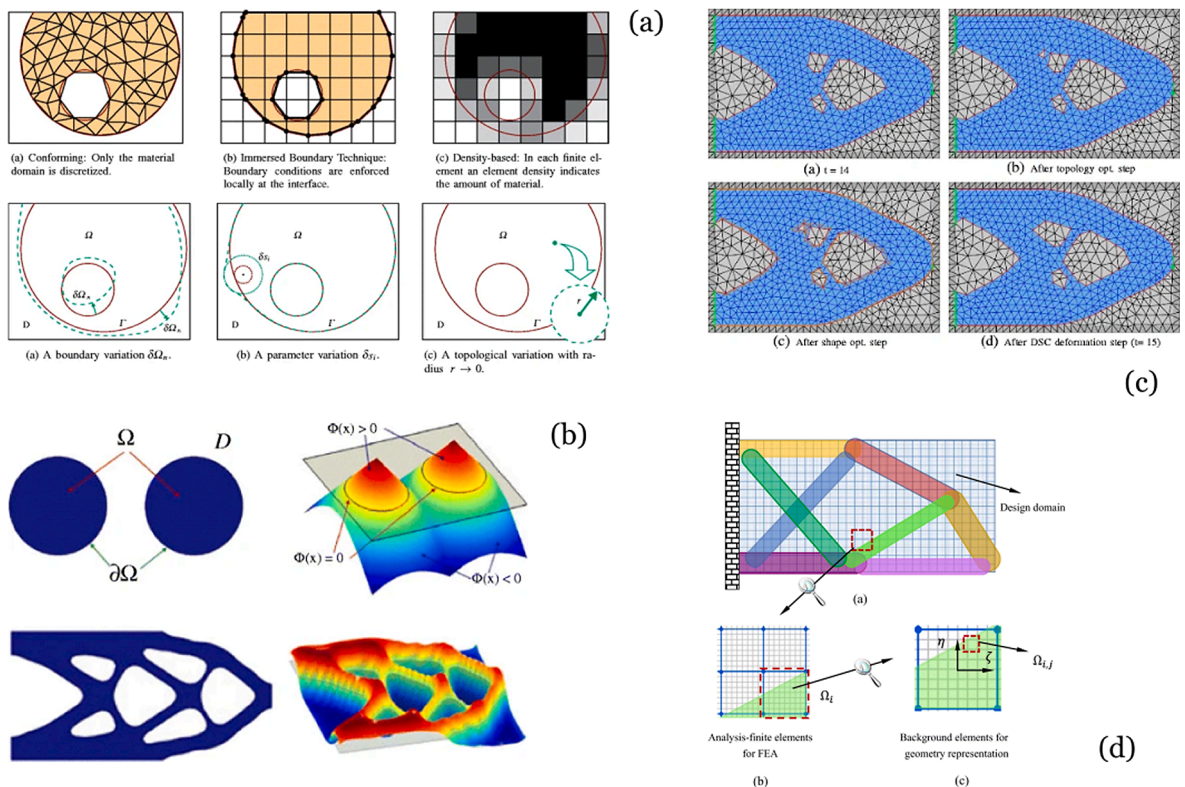


Fig. 4. (a) Illustration of three different shape representations: conforming (body-fitted) mesh, immersed boundary (either with local enforcement of boundary conditions, or with regularization of the solid/void interface), and density-based. The figures below show the modifications produced by three types of variations: boundary, size, and topological (reproduced from [73]). (b) Representation of a simple shape (top) and of a more complex, cantilever beam domain (bottom) by using the implicit description given by the level-set function (reproduced from [74]). (c) Combined topology and shape optimization by the DSC method. Top left: starting configuration; Top right: a hole is introduced by the TO step; Bottom left: the shape optimization step modifies the new boundary; Bottom right: the mesh is locally updated to fit the new configuration (reproduced from [107]). (d) MMC representation: geometrical primitives have high-level defined properties, and are mapped on the simulation grid (reproduced from [123]).

2.1.1.1. Concepts and methods of topology optimization

Topology Optimization (TO) seeks the best distribution of one or more materials, within a design domain Ω_D , while extremizing a given performance criterion and fulfilling a set of constraints. Namely, we want to identify the domain $\Omega_S \subseteq \Omega_D$, occupied by the solid (also called *material domain* in the following), and this can be cast as the following non-linear programming problem:

$$\begin{aligned}
 \min_{\rho(\mathbf{x}), u(\mathbf{x})} \quad & \mathbf{g}_0[\rho, u] \\
 \text{s.t.} \quad & \mathbf{R}[\rho, u] = 0 \\
 & \mathbf{g}_i^{(E)}[\rho, u] = 0 \quad i \in E \\
 & \mathbf{g}_j^{(I)}[\rho, u] \leq 0 \quad j \in I \\
 & \rho(\mathbf{x}) \in \{0, 1\} \\
 & u(\mathbf{x}) \in U
 \end{aligned} \tag{1}$$

where we have the two fields, for $\mathbf{x} \in \Omega_D$:

- $\rho = \rho(\mathbf{x})$, is the control field used to parametrize the geometry, (namely, to identify Ω_S). In structural applications, ρ assumes the meaning of a “relative density”, however, this is not necessarily proportional to the physical density of the solid.
- $u = u(\mathbf{x})$ is the field(s) of state variables, governing the response of the system. For example, this can represent the temperature, displacements, or the velocity field for a thermal, mechanical, or fluid system, respectively. For multi-physics applications we clearly have the state variables from each physics, satisfying the corresponding governing and coupling equations.

The two fields above are coupled by the, generally non-linear, relationship $\mathbf{R}(\rho, u) = 0$, stemming from the set of Partial Differential Equations (PDEs) governing the systems’ equilibrium. This set of equations is discretized, most often by the Finite Element Method (FEM) [57–60], or other suitable numerical methods [61–66].

The objective $\mathbf{g}_0[\rho, u]$ is the figure of merit measuring the performance of the current design, and the equality/inequality constraints $\mathbf{g}^{(E)}(\rho, u)$ and $\mathbf{g}^{(I)}(\rho, u)$ prescribe behavioural requirements on the design. Both can either represent global measures (i.e., thermal, or mechanical compliances, vibration frequencies, pressure losses, etc.), or the extremal values of local quantities (maximum/minimum of local displacements, temperature, stresses, etc.). In the latter case, a multi-objective optimization problem arises, which must be treated by dedicated optimization algorithms [67]. However, within TO practice it is common to reduce multiple objectives or constraints to one, by using a soft approximation to the maximum/minimum operators, such as the p -norm, Kreisselmeier-Steinhauser function [68,69], or more advanced aggregation strategies [70–72] (see sections 2.1.1-2.1.3).

2.1.1.1.1. Design parametrization approaches. The way in which $\rho(\mathbf{x})$ describes the material domain Ω_S depends on the parametrization chosen for the design geometry (cf. Fig. 4). Here we briefly review the most common approaches, addressing the interested reader to other review papers more focused on the subject for further details [53,54,73–75]. We may distinguish two main classes:

- (1) The micro-structural, or material approach, based on the distribution of a porous material whose effective properties may be artificially chosen or given by theoretical or numerical homogenization (see section 4.1.1).
- (2) The geometrical, sometimes referred to as “Lagrangian” approach [53,76], assuming a fixed isotropic or anisotropic material and making use of explicit or implicit boundary variations, and, possibly, occasional hole insertions.

Density-based TO is the most common representative from the first category, achieving the solid domain description by linking one or more material properties of the physical system to the field $\rho(\mathbf{x})$, by means of an indicator function [52]. For example, the strain energy of an elastic system with small strains and deformations may be expressed as

$$\begin{aligned}
 U[\mathbf{x}, \rho(\mathbf{x}), \mathbf{u}(\mathbf{x})] & := \frac{1}{2} \int_{\Omega_S \subseteq \Omega} C^{ijkl}(\mathbf{x}) \epsilon_{ij}[\mathbf{u}(\mathbf{x})] \epsilon_{kl}[\mathbf{u}(\mathbf{x})] d\mathbf{x} \\
 & = \frac{1}{2} \int_{\Omega} \chi_{\Omega_S} C_0^{ijkl} \epsilon_{ij}[\mathbf{u}(\mathbf{x})] \epsilon_{kl}[\mathbf{u}(\mathbf{x})] d\mathbf{x}
 \end{aligned} \tag{2}$$

where we have introduced $C^{ijkl}(\rho(\mathbf{x})) = \chi_{\Omega_S} C_0^{ijkl}$, with

$$\chi_{\Omega_S} = \begin{cases} 0 & \text{if } \mathbf{x} \in \Omega_D - \Omega_S \\ 1 & \text{if } \mathbf{x} \in \Omega_S \end{cases} \tag{3}$$

which is the characteristic function of the solid domain, and C_0^{ijkl} is the constitutive tensor of the solid material. In this way, the TO problem becomes a layout optimization problem, and all computations can be performed on the whole Ω_D , without the need to explicitly track the evolution of the material domain Ω_S .

In the second category, a main representative is perhaps the level-set approach [77–80], where the boundary of the solid domain is given by the zero level-set of an implicit function $\Phi(\mathbf{x})$, such that $\Phi(\mathbf{x}) > 0$, for $\mathbf{x} \in \Omega_S$, and $\Phi(\mathbf{x}) < 0$ otherwise (cf. Fig. 4 (b)). The level-set parametrization turns (1) into a shape optimization problem, where the designs’ topology cannot be changed, and is limited by the

connectivity of the initial guess. The possibility of hole nucleation and merging can be introduced in shape optimization methods by combining them with strategies making use of the topological gradient concept [81–84], such as bubble methods [85–87], and others. However, we point out that the distinction between density- and shape-based methods is often unclear, as discussed in [54]. Amstutz [82] proved the topological gradient equivalent to the density-based gradients computed with the SIMP method, making distinctions between density-based and “enriched” shape methods somewhat blurred [88–92]. Phase-field approaches, widely used for design problems involving damage or crack propagation [93–96], also fall in between the two main categories stated above.

When an accurate resolution of the design boundaries is pivotal for the accurate simulation of the physics, as it is often the case for fluid and multi-physics problems, topology and shape optimization are usually combined [75,97–100]. To this end, body-fitted meshes can be used [101–103], coupled with physics-informed anisotropic mesh adaptation [104,105], to avoid expensive global re-meshing operations. A body-fitted strategy that has gained popularity is the Deformable Simplicial Complex (DSC) method [106,107], which allows the combination of topology changes (i.e., hole nucleation) and boundary changes, preserving the accurate interface representation by fast local remeshing. Among many other applications, DSC has been successfully used for stress-based TO [108], and for fluid applications by Zhou et al. [109]. Immersed boundary methods, such as eXtended-FEM [110–112] or CutFEM [113–115] offer an interesting alternative to body-fitted discretization, finding wide application in both density-based and level-set methods, and seem very promising for solving advanced multi-physics problems. Andreassen, Aage et al. [116,117], have shown a close connection between density-based and level-set methods, when interfaces are treated by the CutFEM methods.

Finally, we recall the feature-based parametrizations [118], the most popular being the Moving Morphable Component (MMC) method [119–123]. These are based on geometrical primitives (bars with tunable dimensions, or other similar geometries) with high-level defined properties, which then are mapped onto a uniform, computational grid (cf. Fig. 4 (d)). These methods, which still make use of the main ingredients of density-based methods, may sometimes provide easier integration of the geometrical and manufacturing constraints within the TO process.

2.1.1.2. Relaxation of the optimization problem and numerical treatment. The parametrization of Eqs. (2) and (3) makes (1) an integer programming problem, where at every point of the design domain Ω_D we may have material ($\rho(\mathbf{x}) = 1$), or no material ($\rho(\mathbf{x}) = 0$). Early works by Beckers et al. [124,125], and recent contributions [126–128], have solved elementary instances of (1) by integer programming; however, this soon becomes prohibitive as the number of design variables increases, and non-linear constraints are considered.

Therefore, we turn (1) into a continuous optimization problem by allowing the relative density to take any value $\rho(\mathbf{x}) \in [0, 1]$, for $\mathbf{x} \in \Omega$, and by using it to interpolate the material properties governing the physical response. For example, the Solid Isotropic Material with Penalization (SIMP) [129,130] interpolates the Young’s modulus as:

$$E(\mathbf{x}) = E^{(\min)} + (E^{(0)} - E^{(\min)})\rho(\mathbf{x})^p \tag{4}$$

where $E^{(0)}$ is the value on the solid ($\rho(\mathbf{x}) = 1$), and $E^{(\min)} \ll E^{(0)}$ that of the material mimicking void ($\rho(\mathbf{x}) = 0$). The penalization factor $p > 1$ promotes discrete solutions to the optimization problem, as intermediate values $\rho \in (0, 1)$ become uneconomical when p is raised, due to the linear increase of the mass, and the sublinear increase of the stiffness.

The SIMP-interpolated elasticity tensor can be physically realized as the effective tensor of an isotropic, porous material. Indeed, Bendsoe and Sigmund [131] proved that, for a Poisson ratio $\nu = 1/3$, the bulk and shear moduli corresponding to a SIMP interpolation with $p \geq 3$ are within the Hashin-Strickman bounds [132] (both in 2D and in 3D). The SIMP method is by far the most popular interpolation for compliance minimization. SIMP-like stress interpolations, physically grounded from the homogenization point of view, have been formulated by Duysinx and Bendsoe [133], and by Lipton [134] (see section 2.1.1 for a discussion of stress problems). However, alternative schemes may perform better for specific applications [135,136]. Among these, we recall the Rational Approximation of Material Properties (RAMP) [137], which was introduced to preserve the concave nature of the complementary energy and provides non-zero derivative at $\rho(\mathbf{x}) = 0$, thus facilitating material reintroduction. Interpolations based on other available bounds for effective properties of mixtures, such as the Reuss-Voigt bounds, have been proposed by Swan and Arora [138], and Swan and Kosaka [139], whereas ad hoc interpolation models are sometimes developed for advanced multi-physics applications [140]. Finally, many of these classical material interpolation models have been extended to allow multi-material design [141,142].

With the SIMP relaxation, problem (1) becomes a continuous optimization problem and can be treated by gradient-based optimization methods [143]. Specifically, (1) takes the form of a bi-level optimization problem [144–146], where the “upper” level involves optimization with respect to the relative density $\rho(\mathbf{x})$, and at the “lower” level, the residual equation $R[\rho, u] = 0$ can also be turned into an optimization problems. For instance, in the linearized elasticity setup the residual is associated with the following system of equations

$$\begin{aligned} \sigma_{ij}^j + b^i &= 0 && \text{in } \Omega \\ \sigma^{ij} &= C^{ijkl} \epsilon_{kl} && \text{in } \Omega \\ \epsilon_{kl} &= \frac{1}{2} (u_{ij} + u_{ji}) && \text{in } \Omega \\ \sigma^{ij} \hat{n}_j &= \bar{t} && \text{in } \partial\Omega_t \\ u_i \hat{n}_i &= \bar{u} && \text{in } \partial\Omega_u \end{aligned} \tag{5}$$

where \bar{u} and \bar{t} are the prescribed displacements and tractions on the respective portions of the boundary $\partial\Omega_u$ and $\partial\Omega_t$, respectively, \hat{n} is the outward normal unit vector, and b_i are the components of the body force. The system (5) can be equivalently written as the following minimization problem [147,148]

$$\min_u \Pi[u] := \frac{1}{2} \int_{\Omega} \sigma^{ij} \epsilon_{ij} - b^i u_i \, d\Omega - \int_{\partial\Omega} \bar{t}^i u_i + \sigma^{ij} \hat{n}_i \bar{u}_j \, d\Omega \quad (6)$$

where $\Pi[u]$ is the total potential energy.

We can identify two strategies for tackling the optimization problem:

- Simultaneous ANalysis and Design approach (SAND). In this case, state and design variables are kept separate, and the “lower” optimization level is solved simultaneously with the upper one [149]. This approach has been quite popular in the early days of structural optimization [150–152], and some recent works have applied it to TO [153–156], often using interior point Newton methods for the solution of the whole non-linear system. A general discussion about merits and limitations of the SAND approach can be found in the benchmark paper by Rojas-Labada et al. [157].
- Nested ANalysis and Design approach (NAND). In this case the lower optimization level is explicitly resolved at each re-design step, and the objective and all constraints depending on the state variables implicitly depend on the design ones, via the relationship $u = u(\rho)$. This approach, is nowadays the most used in TO applications.

In either case, a central step in the optimization process is the sensitivity analysis, computing the objective and constraint gradients with respect to the control field $\rho(x)$. The adjoint method is the standard for performing sensitivity analysis in the context of the NAND approach. Requiring only one additional state solution for each objective and constraint function, irrespective of the number of design variables, the adjoint method is computationally much more efficient than the so-called *forward* sensitivity analysis, for all the problems of interest (i.e., when we have less constraints than design variables).

The works by Haug and Rousselet [158–160] are classical for linear and eigenvalue-based objectives in structural mechanics, comprising either size, shape, or topology variations. A thorough discussion about sensitivity analysis in non-linear mechanics can be found in the work by Cardoso and Arora [161], and, on a more mathematical stance, by Kohn and Strang [162,163] and in the monographs by Lions [164] and Lurie [165]. Recent surveys on analysis methods, applied to a wide range of non-linear and transient problems are [166–169].

Although the most common approach is the so-called “*discretize-then-optimize*”, based on computing the sensitivities of the discretized system, some recent works have shown the advantage of using continuous adjoints, i.e., the “*optimize-then-discretize*” philosophy [170–172]. The two approaches lead to very similar results in most easy, single-physics applications. Continuous adjoints have proven effective for fluid [173,174] and contact [175] problems, and other advanced applications, whereas they are seldomly used for simpler applications. We also mention the recent increase in the use of automatic differentiation (AD) [176,177] for sensitivity analysis. The spreading of AD, which is likely linked to that of Neural Network-based approaches, may spare cumbersome derivations and implementations for complex problems. However, its efficiency is still debated, and its use as a black-box computational tool should be critically questioned.

Based on the sensitivity information, the update of the design field $\rho(x)$ is then performed by a non-linear programming algorithm. So-called Optimality Criteria (OC) algorithms, introduced by Prager and Taylor [178] for basic compliance problems, still find application in simple problems, mostly limited to a single constraint, and educational codes [55,179,180]. The OC concept has then been extended by the CONvex LINearization (CONLIN) method by Fleury and Braibant [181–183], allowing treatment of more advanced structural design and TO problems, also considering multiple constraints [184–191]. Then, as a generalization of the CONLIN, the Method of Moving Asymptotes (MMA) [192], and its globally convergent variant (GCMMA) [193,194], both developed by Svanberg, have proven very effective in solving a broad class of TO problems, and are today the most used optimization methods.

Overall, first order, dual methods have become the standard for solving TO problems in the NAND form, due to the high CPU and memory cost of computing second-order information. However, Sequential Quadratic Programming (SQP) packages, making use of approximate second-order information, are sometimes used. Among these, we recall IPOpt [195,196], the popular implementation of the Interior Point Newton method by Wächter and Biegler, and SNOPT [197], using a limited memory quasi-Newton method. These two have been reviewed and compared to the MMA-type methods in [157,198,199]. Kocvara and Stingl have also developed a package for semidefinite programming, [200], which finds increasing application in eigenvalue-based TO [201], and free material optimization [202–204].

We recall that there are also countless works proposing heuristic and *meta*-heuristic methods for TO problems. These methods may be viable alternative only for small-scale, purely academic examples; however, they are not suitable for solving large-scale problems, especially considering complex process modelling and manufacturing constraints. A critical review of non-gradient based methods applied to TO can be found in Sigmund [5], showing that these are not competitive with the gradient-based ones, neither for the computational cost, nor in terms of quality of the results. Another approach, commonly going under the name of “*evolutionary*” methods, combines a gradient-based optimization framework, but still considering discrete design updates (i.e., $\rho = \{0, 1\}$). Among these we have the Evolutionary Structural Optimization (ESO) [205], only allowing the removal of elements with low strain energy from the design domain, and the Bidirectional-ESO (BESO), giving the possibility to reintroduce elements in the design domain [206,207]. These methods end up being algorithmically very similar to classical density-based (and level-set) TO, basically mapping

continuous variables to discrete updates [208]. Nevertheless, their efficiency and generality when faced with harder problems such as compliant mechanisms or stress constraints is questionable, and they also lack a mathematically sound definition of convergence [209,210].

Finally, in the last few years there has been a huge increase of Artificial Intelligence (AI) related techniques within TO. A recent work by Woldseth et al. [211] gives a critical review about the role and efficiency of AI methods, applied to the most diverse tasks in TO. As by now, it is hard to envision AI directly replacing the simulation, or optimization tasks within large-scale TO. On the other hand, their use for post-processing operations, or for the coupling with AM design rules, may be directions for future explorations.

2.1.1.3. Homogenization and de-homogenization approaches to topology optimization. Following this approach, the design is built from a meso-scale, architected material, and the goal is to find the local volume fraction and orientations of such porous material, to realize the locally optimal, homogenized properties.

The approach, dating back to Bendsøe and Kikuchi [215], and Suzuki and Kikuchi [216], was originally based on selecting a unit cell (see Fig. 5 (a) for the most elementary example of a square unit cell), and by using 1st order, asymptotic homogenization theory to compute its effective material properties (see sections 4.1.1, and 4.1.3). Alternatively, optimal rank- n laminates are obtained by combining layers of material in a recursive process, by keeping the hypothesis of separation of scales [129,217] (see Fig. 5 (a)).

Following the “rank” approach, Gibiansky and Cherkov [218] have proved that rank-2 laminates are optimal for designing 2D

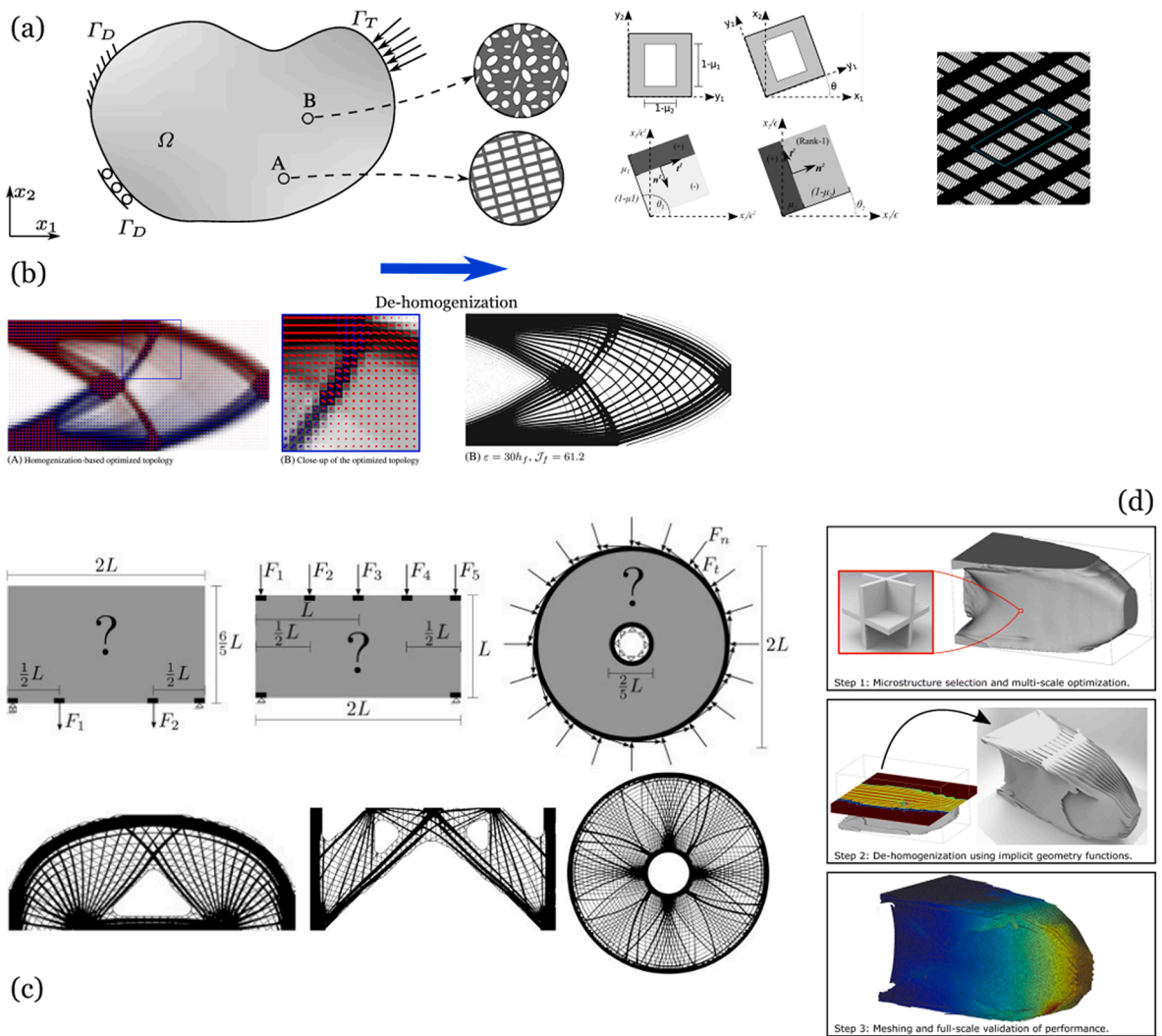


Fig. 5. (a) Homogenization-based TO aims at the best distribution within the design domain of a given porous material, defined by unit cells (here, a square-with-hole cell is shown), or by rank- n laminates, ensuring separation of scales (reproduced from [46]). (b) The de-homogenization step can be used for extracting a single scale design, with a prescribed periodicity, from the optimized locally homogenized material properties (reproduced from [212]). (c) Examples of de-homogenized structures obtained from anisotropic porous materials, subjected to multiple load cases, (reproduced from [213]). (d) Large-scale 3D cantilever beam, de-homogenized considering an open-face truss lattice (reproduced from [214]).

structures with maximum stiffness, under a single load case [219,220]. For multiple load cases, the optimal stiffness can be realized by rank-3 and rank-6 laminates with non-orthogonal layers in 2D and 3D, respectively, as discussed by Avellaneda and Milton [221], and Lipton [222,223].

The optimal parameters of the porous material can then be used to extract a single-scale design with a tunable level of *meso*-scale features (see Fig. 5 (b)). This is the basis of the *de-homogenization* method, recently developed by Groen and Sigmund [212] revisiting the works of Bendsøe and Kikuchi [215], and Pantz and Trabelsi [224,225].

When dealing with ambiguous, locally singular orientation fields [226], the de-homogenization step still poses some challenges, which require special treatment [214,227]. However, very promising, fine-scale designs, with a near optimal performance have been obtained at a low fraction of the computational cost required by conventional, single-scale TO [214,228]. De-homogenization is currently extended to the infill design for coated structures [229], problems with multiple load cases [213], and buckling design [230].

2.1.1.4. Regularization strategies, length scale imposition and robust design. Without any regularization, the original TO problem lacks a solution even in the continuous setup, as shown by Lurie [165], and Kohn and Strang [231]. This results in mesh dependency of the discretized solutions: the optimized design *qualitatively* changes when refining the mesh, a phenomenon first acknowledged by Kenon-Tung, Olhoff and Cheng [232,233].

A survey on numerical instabilities appearing in TO can be found in Sigmund and Peterson [234], whereas Diaz and Sigmund [235] explained another spurious effect: the formation of checkerboard patterns in the optimized design. This originates from the use of low order finite elements and can be cured by choosing higher orders for the discretization of the state and control fields (u and ρ), as discussed by Jog and Haber [236]. Alternative approaches, using node-based discretization of the ρ field also fall in the framework of Jog and Haber, as they cure the phenomenon only for some choices of the discretization orders [237,238].

To avoid mesh-dependency of solutions first methods were based on explicitly constraining the oscillations of the density field [239,240], thus avoiding designs with infinitely many, infinitely small holes [239]. The existence of solutions to the TO problem with total variation regularization was proven by Ambrosio et al. [241] and Petersson [242], and their mesh-independency by Sigmund and Petersson [243].

Nowadays, the most used regularization approach, not requiring additional constraints or penalization terms, is based on domain filters. First introduced by Sigmund in the context of compliance minimization problems [6,244], sensitivity filtering of the objective function,

$$\widetilde{\nabla_{\rho} g_0}(\mathbf{x}) = \frac{\int_{\Omega_D} \omega(\mathbf{x} - \boldsymbol{\xi}) \rho(\boldsymbol{\xi}) \nabla_{\rho} g_0(\boldsymbol{\xi}) d\Omega}{\int_{\Omega_D} \omega(\mathbf{x} - \boldsymbol{\xi}) \rho(\boldsymbol{\xi}) d\Omega} \quad (7)$$

where $\omega(\mathbf{x} - \boldsymbol{\xi}) = \max(0, r_{\min} - |\mathbf{x} - \boldsymbol{\xi}|)$ is a linearly decaying kernel, is used to average the original density-weighted sensitivity, $\nabla_{\rho} g_0(\mathbf{x})$, over a region of radius r_{\min} . This has proven to avoid checkerboards and mesh-dependency in several applications, and Sigmund and Maute [245] have interpreted the sensitivity filtered minimum compliance problem, as the minimization of a non-local elasticity problem.

When using the sensitivity filter (7), the same field $\rho(\mathbf{x})$ is used both for the parametrization of the optimization problem, and control of the material properties. Another method, commonly named “*density filter*” [244,246] relies on introducing an additional field, obtained as

$$\tilde{\rho}(\mathbf{x}) = \frac{\int_{\Omega_D} \omega(\mathbf{x} - \boldsymbol{\xi}) \rho(\boldsymbol{\xi}) d\Omega}{\int_{\Omega_D} \omega(\mathbf{x} - \boldsymbol{\xi}) d\Omega} \quad (8)$$

such that $\tilde{\rho}(\mathbf{x}) \in [0, 1]$ becomes the field interpolating the material properties, whereas $\rho(\mathbf{x})$ is just the auxiliary variable updated by the optimizer. However, Jansen et al. [247] have shown that a physical interpretation of can be given to $\rho(\mathbf{x})$, as the electron beam used for micro- and nanolithography, whereas $\tilde{\rho}(\mathbf{x})$ acts as the scattered field, and a subsequent thresholding of this field (see below) mimics the etching process. The existence of solutions to the compliance minimization problem, regularized by the density filtering was proven by Bourdin [248].

A similar regularization effect given by (8) can be obtained by applying a PDE-based smoothing [249,250] such that the regularized field $\tilde{\rho}(\mathbf{x})$ is the solution to the Helmholtz problem, equipped with Neumann-like boundary conditions

$$\begin{aligned} \nabla \cdot (\mathcal{L}_0^2 \nabla \tilde{\rho}(\mathbf{x})) + \tilde{\rho}(\mathbf{x}) &= \rho(\mathbf{x}) & \mathbf{x} \in \Omega \\ \nabla \tilde{\rho}(\mathbf{x}) \cdot \hat{\mathbf{n}} &= 0 & \mathbf{x} \in \partial\Omega \end{aligned} \quad (9)$$

where parameter \mathcal{L}_0^2 in (9) is related to the filtering radius used for building the kernel $\omega(\mathbf{x} - \boldsymbol{\xi})$, such that $\mathcal{L}_0^2 = \frac{r_{\min}}{n\sqrt{3}}$ (and n is the number of space dimensions) [251]. Träff and Høghøj have recently extended the diffusion PDE filter described above, introducing an advection term, capable of representing milling constraints [252].

When using (8) and (9) artificial phenomena are likely to appear near the boundaries of the design domain, because of the attraction effect of the Neumann boundary conditions [253]. This may trigger artifacts in the optimization, especially if stress or other

boundary effects are involved [254]. Clausen and Andreassen [255] have proposed a simple strategy to resolve this issue, which is based on applying zero-Dirichlet boundary on an extended void domain of width r_{min} outside the design domain. Alternatively, Wallin et al. [250] proposed to modify the second equation of (9), making it a mixed boundary condition

$$(\nabla \cdot \tilde{\rho}) \cdot \hat{\mathbf{n}} = -\ell_s / \ell_s^2 \tilde{\rho} \quad \mathbf{x} \in \partial\Omega \tag{10}$$

where ℓ_s is the material length scale allowed at the boundaries. Equation (10) clearly includes the two extreme cases of Neuman or Dirichlet for $\ell_s \rightarrow 0$ and $\ell_s \rightarrow \infty$, respectively.

Linear filtering methods naturally promote grayscales (i.e., transition regions between solid and voids), which is a drawback from the manufacturing point of view. Such grayscales can be eliminated in a post processing phase, by projecting the design to a discrete 0/1 material distribution. However, for sensitive applications, such as photonics and phononics [256,257], this can dramatically alter the component’s response. To reduce the development of grayscales in the optimized design, several nonlinear filters have been based on morphological operators [258], harmonic and geometric means [259], and more general non-linear paradigms [260,261], or explicit introduction of geometric constraints [262].

Another non-linear filter operation is density projection. This consist of applying a smooth approximation of the Heaviside function to the filtered field $\tilde{\rho}(\mathbf{x})$, to obtain a more discrete density field $\hat{\rho}(\mathbf{x})$. Projection was first applied to TO by Guest et al. [263], referring to an idea first introduced in [264], obtaining the relative density as

$$\hat{\rho}(\mathbf{x}) = 1 - e^{-\beta\tilde{\rho}(\mathbf{x})} + \tilde{\rho}(\mathbf{x})e^{-\beta} \tag{11}$$

where β is a parameter governing the curvature of the approximation at $\tilde{\rho} = 0$. When (11) is applied on top of density filtering, and β is large enough, the minimum length scale r_{min} is implicitly imposed on the solid regions. Combining (11) with local constraints, also a maximum solid length scale can be achieved [265], whereas Wu et al. [266] achieved maximum length scale control of porous structures by constraining the local volume fraction. Imposing a length scale on the void region can be achieved by the complementary of (11) [258]

$$\hat{\rho}(\mathbf{x}) = e^{-\beta(1-\tilde{\rho}(\mathbf{x}))} - (1 - \tilde{\rho}(\mathbf{x}))e^{-\beta} \tag{12}$$

and a simultaneous control of the solid and void length scales was achieved by Carstensen and Guest through multiple phase projection [267].

Both (11) and (12) are limit cases of a more general expression, called η -projection [268]

$$\hat{\rho}(\mathbf{x}) = \frac{\tanh(\beta\eta) + \tanh(\beta(\tilde{\rho}(\mathbf{x}) - \eta))}{\tanh(\beta\eta) + \tanh(\beta(1 - \eta))} \tag{13}$$

where a threshold $\eta \in [0, 1]$ defines the saddle point of the Heaviside approximation.

A benefit of equation (13) is that it can be used for encoding geometrical uncertainties, distributed along the design boundaries, in the TO formulation. This allows accounting for manufacturing errors which are common to Laser Powder Bed Fusion (LPBF) methods: the over- or under-deposition of material, resulting in a dilation/erosion of the design. These variations may be represented by considering the projection threshold as a random variable $\eta(\theta) \in [\eta_D, \eta_E]$, having uniform Probability Density Function within two extreme values (see Fig. 6).

In this way, the relative density and all response quantities become random variables, turning the TO problem into a stochastic one, where a robust design concept is pursued. For problems involving compliance minimization and a volume constraint (and vice-versa), the robust approach can be simplified by considering only two values η_D (giving a dilated design) and η_E (giving an eroded design) such

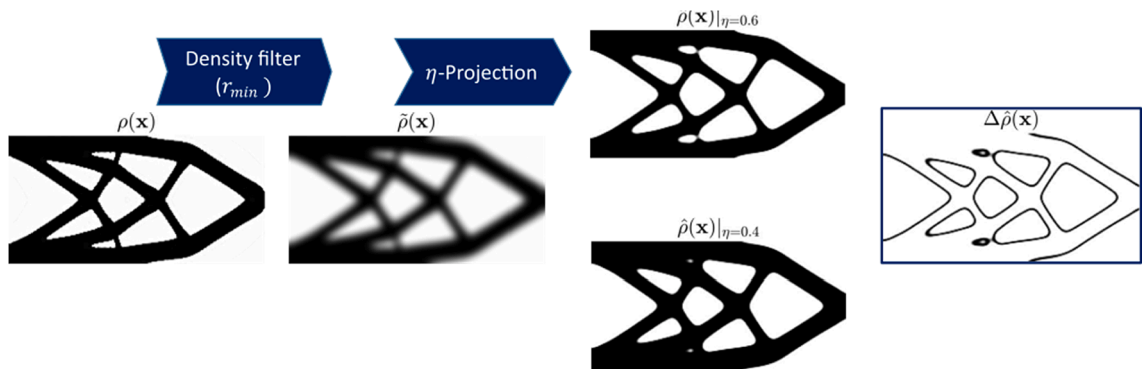


Fig. 6. Representation of geometrical uncertainties by the η threshold projection of (13). Starting from the design variables field $\rho(\mathbf{x})$, the application of linear filtering smears out the material distribution, giving the intermediate field $\tilde{\rho}(\mathbf{x})$. A layer of material with width r_{min} is then given as the difference between the projected densities $\hat{\rho}(\mathbf{x})$, associated with two threshold values $\eta_D < \eta_E$, such that η_D is the dilated design (over-deposition of material) and η_E the eroded design (under-deposition).

that $\eta_D < \eta_E$ and $\eta_E = 1 - \eta_D$. Minimizing the compliance of the eroded design, while enforcing the volume constraint on the dilated one, will automatically ensure robustness of the blueprint design, corresponding to the intermediate threshold $\eta_B = \hat{A}^{1/2}(\eta_E + \eta_D)$. Moreover, Wang et al. [269] proved that the three-field, robust approach implicitly imposes both solid and void length scales on the blueprint design (see also the survey paper by Lazarov et al. [251]).

For more advanced problems, as those covered in sections 2.1.1 to 2.1.3, the selection of arbitrary threshold values may not guarantee robustness, and fully stochastic methods must be used, in turn increasing the computational cost. Lazarov et al. [270,271] used first order perturbation methods for the robust design of compliant mechanisms, and Schevenels et al. [272] accounted for spatially varying manufacturing errors by defining the threshold η as a random field.

Examples of robust TO design in the context of stress and buckling problems can be found in the works by da Silva et al. [273], and Jansen et al. [274], respectively.

2.1.2. Mechanisms design, stress constraints and non-linear response

The discussion on concepts and methods of TO was mostly based on the compliance problems and linearized elasticity. Here we shortly overview some topics involving more advanced physics, stressing points that are relevant from the AM perspective.

Design of compliant mechanisms and displacement constraints. Compliant mechanisms are devices converting forces and displacements between input and output, exploiting large deformations of the mechanisms' components. They find applications in several engineering fields (c.f., soft robotic, MEMS/NEMS, etc.), and have always received attention within TO [244,278–280]. We refer to [281], for an up-to-date review of the topic.

Compared to the linear elastic, minimum compliance design problem, the design of compliant mechanisms introduces several complications. First, there is a tendency to create hinge-like connections, as a natural way to maximize the mechanism's flexibility (cf. Fig. 7 (a)). Such connections must be avoided, as they are sensitive to both stress concentrations and manufacturing uncertainties. Hinged connections may be partly inhibited by introducing a stress constraint, as shown by de Leon et al. [282], and others [276,283,284] (cf. Fig. 7 (b)). A more effective strategy is to use the robust formulation [269,285], imposing a length scale on the blueprint design. This however comes at the price of a higher computational cost, since the objective of the design problem (a local displacement) is not self-adjoint, and two to three FE simulations are needed at each re-design step [286,287].

The large deformations capability of compliant mechanisms inherently calls for geometric non-linear FE modelling, giving completely different optimization outcomes compared to those from linear modelling [246,270,288].

Other important applications may require the control of local deflections, and examples can often be found in design for multi-physics (c.f. [289,290]).

Self-weight and design-dependent loads. For most mechanical structures, the carried payload dominates self-weight. However, self-weight may become relevant during the manufacturing process, e.g., considering supporting structures, or printing setups and orientations different than the operating ones. Moreover, for structural and civil engineering components, the self-weight becomes a dominant contribution [291]. The removal or introduction of material simultaneously modifies the systems' response, and the load itself [292–294]. Moreover, the point (or surface, or volume) of application of the load depends on the design itself [295]. These complications require a careful choice of the design parametrization and material interpolation to avoid convergence issues [296,297].

Stress-constrained problems. Geometric constraints, such as corners and holes, introduce stress concentrations and singularities in the design [298]. Moreover, stresses are the fundamental ingredient of elastic–plastic behaviour, and other failure theories. Giraldo-Londoño and Paulino [299] have addressed TO under several failure surfaces, encoded in a unified formulation.

Two main difficulties arise in stress-constrained problems: (1) the efficient treatment of the many local constraints, and (2) the

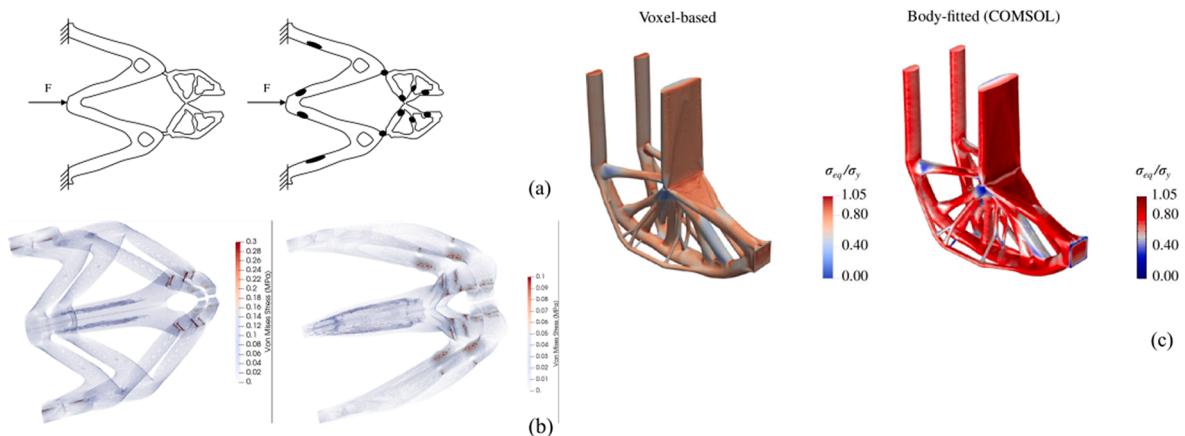


Fig. 7. (a) Schematic of a gripper design, with black dots marking the locations where stress concentrations happen (figure reproduced from [275]). (b) 3D design for the gripper, consisting of ~ 10 million voxels, without (left) and with (right) stress constraints (reproduced from [276]). (c) Large-scale, minimum weight design of the L-beam, discretized by 16.4 million elements, and imposing a maximum local stress constraint with the Augmented Lagrangian method (reproduced from [277]).

singular character of each of them.

For the first point, by imposing a stress limit locally the constraint's number becomes proportional to that of mesh elements. As discussed earlier in [section 2.1.1](#), the high number of local constraints may be reduced to one by using aggregation methods (such as the p -norm or KS functions) [300–302]. However, the aggregation often performs poorly as the number of constraints scales to hundreds of thousands, or even millions. To remedy this, the use of an Augmented Lagrangian (AL) function has been proposed, almost simultaneously by [303] and da Silva et al. [277,304], achieving large scale designs with hundreds of millions of local constraints. The comparison between AL and aggregation functions in [277,304], clearly shows the superior performance of the former, for large numbers of constraints. A Matlab implementation of the AL approach to stress constrained TO can be found in [305].

Concerning (2), a way for fulfilling the stress constraint at a point, would be to eliminate the material at that point, thus removing the stress constraint itself. This, which is a feature of so-called optimization problems with vanishing constraints [306], introduces convergence issues and enhances the tendency to converge to suboptimal solutions. To alleviate this problem, several constraint relaxation techniques have been proposed [307]. The most popular are the ϵ -relaxation by Cheng and Guo [308], and the qp -relaxation proposed by Bruggi [309]. Other recent works proposed polynomial scaling of stress constraints as a form of relaxation [303,305].

Large deformations and non-linear material models. Designs obtained by considering large deformations can be quite different from those obtained for linear elasticity, as shown by Buhl et al. [310]. Large deformations modelling should be backed by proper hyperelastic material models, to avoid spurious phenomena occurring at high compression levels, as discussed by Klarbring and Strömberg [311]. Another classical issue, shared also by buckling problems (see [section 2.1.2](#)), is the instability of low-density elements, undergoing large distortions and causing computational problems. This was avoided by Wang et al. [312], by using an interpolation scheme weighting the strain energy density between non-linear strains (on high density regions) and linear strains (on low density regions). A similar approach was followed also by [313]. Alternatively, other works proposed to remove the low-density regions from the computational domain [314–316].

A few works, such as Wu and Arora [317], Kemmler and Lipka [318], and Ramanthalla and Swan [319] have also included non-linear stability analysis in TO, whereas Russ and Waisman [320] also included damage and local yielding, achieving designs that balance the stability and plastic failure. These considerations are important for imperfection sensitive structures or when the post-buckling response is of interest, such as for shell structures [321] and composites [322]. However, completely non-linear stability analysis is still computationally very expensive to be integrated in large-scale TO, and therefore most applications rely on linearized buckling analysis, discussed in the next section.

2.1.3. Introduction of buckling criteria

Designs optimized for compliance, or stress criteria, often consist of thin bars subjected to tension and compression, with little bending and shear forces. Such configurations are optimal for achieving high stiffness with the least material; however, may show poor stability [326,327]. Therefore, accounting for buckling strength in TO is crucial for ensuring the functioning of the designed parts.

Early attempts to include buckling into homogenization-based TO can be found in Neves et al. [328,329], Rodrigues et al. [330], and Folgado and Rodrigues [331]. These works already highlighted the main challenges of buckling TO, still encountered nowadays, such as the occurrence of simultaneous buckling modes for a nearly identical load factor, and the onset of non-physical buckling modes. Both these issues are common to other optimization problems involving eigenvalues, for example vibration frequencies, and a discussion of their adverse effect on the convergence towards a well-defined, buckling resistant design, can be found in Bruyneel et al. [332,333] and Ferrari Sigmund [333].

The coalescence of several buckling modes is a natural trend for optimized designs [327,334,335]. In this case, the eigenvalues become non-differentiable [336]. Therefore, specialized techniques must be used for solving the optimization problem, often requiring the addition of many constraints [334,337] and a more involved sensitivity analysis. Aggregation strategies based on the p -norm or the KS functions are often used also in this context [68], reducing the many constraints to a single, differentiable one.

Spurious, non-physical buckling modes are prone to appear in regions with low relative density, as numerical artifacts triggered by the bad bounding of the Rayleigh quotient over such regions [338]. However, highly localized, unphysical buckling modes may also occur in the solid material, as pointed out by Ferrari and Sigmund [339] and by Russ and Waisman [320].

Large-scale, buckling TO still retains some complexity; however, recent works making use of highly efficient numerical methods, such as Bian and Feng [340], Dunning et al. [341], and Ferrari and Sigmund [339] who have shown interesting 3D buckling TO, with up to a million design variables.

Such promising developments have sparked a revived interest in buckling TO, and for its application to architected materials, which can greatly enhance the yielding and stability performance of components. Clausen et al. [342] have shown a huge gain in the buckling strength of a compliance optimized design, by replacing the massive material with a regular triangular lattice infill, at the same volume fraction. The infill optimization was then addressed by Thomsen et al. [343], with the goal of getting closer to the theoretical limits of compressive strength (cfr. [Fig. 8](#) (a)). Thomsen et al. based the investigation on linear homogenization theory, perfectly periodic lattices, and used the Floquet-Bloch decomposition and linearized buckling analysis for identifying the most critical instability modes. Designs achieved for square, triangular, and hexagonal honeycomb infills, for either uni-axial, biaxial and shear stresses (cfr. [Fig. 8](#)) show improvements of the buckling strength in the range of 240–480%, at the price of a slight stiffness reduction of 15–50%. Post-evaluation of these lattices by large deformation, non-linear modeling [344], and testing on printed samples [324], confirmed their superior performance compared to classical, single-scale lattices (cfr. [Fig. 8](#) (b)).

Stability of 3D hierarchical lattices was investigated by Andersen et al. [7], showing that at low volume fractions, open face (OF) truss lattices outperform the buckling resistance of stiffness-optimized closed-face (CF) ones (cfr. [Fig. 8](#) (c)). However, for complex lattices with multiple scales, subjected to general load cases, the best buckling strength between OF or CF configurations is still

debated. Wang and Sigmund [345] recently proposed a set of parametrized 3D lattices, transitioning between pure plate-based (thus CF) to hybrid plate/truss structures, improving the buckling resistance by 4.2 to 8.6 times, at the cost of reducing the stiffness by 20–40%. These lattices were restricted to be isotropic, and to have a single length scale, which makes them easier to manufacture (cfr. Fig. 8 (d)). Finally, we recall that a relevant problem is linked to the assumption of separation of scales, and the distinction between microscopic and infill instabilities [346,347]. On this line, the work by Christensen et al. [230] is the first contribution to de-homogenization for buckling design, considering an isotropic multi-scale lattice, and both global (macroscopic) and local (infill) buckling constraints.

2.1.4. Application to thermal and fluid problems

Heat and fluid transfer are also classical TO applications (see review papers from Alexandersen and Andreassen [348] and Dbouk [349], and Zhou et al. [350] for recent industrial applications. Table 1 lists governing equations for thermal TO.

The earliest heat transfer optimization task is perhaps the so-called volume-to-point problem [351]: find the best strand of highly conductive material, within a low conductive domain, to convey the heat generated pointwise to a heat sink. Here, the control field $\hat{\rho}(\mathbf{x})$ describes the relative density of high conductive material, and product between the thermal input $Q(\mathbf{x})$ and the temperature field $T(\mathbf{x})$, usually called “thermal compliance”, is minimized [352]. Another common requirement is to bound, or to minimize, the maximum temperature across the design domain [353]. When conduction is the only heat transfer mechanism modeled, and the heat generation is uniform across the domain, optimized designs often show paths with tree-like branches, for both temperature and thermal compliance objectives. However, Yan et al. [354] have proven the sub-optimal nature of tree-like branches, compared to designs composed of infinitely many, infinitely thin lamellae or needles (cf. Fig. 9). This configuration, resembling a rank-1 conductive composite has a performance very close to theoretical bounds. Avoiding tree-like local minima was achieved also by Guest and Carstensen, by introducing geometrical constraints on the design [355].

Convective effects are completely disregarded in a pure conduction model, i.e., when considering only temperature boundary conditions in the set of equations (14). This may be a reasonable assumption if the design domain is sufficiently thin, or if it has a small surface in contact with the convective fluid. On the other hand, convective effects play an important role in many design tasks. The correct modeling of natural or forced convection within a topology optimization procedure is not an easy task [356,357]. Since convection is a boundary-dominated phenomenon, the first approach is to explicitly track the evolution of the design boundaries, and level-set, or body fitted approaches can become handy for this task [358,359]. Density-based methods achieve the same modeling by introducing a heat transfer coefficient $h(\rho(\mathbf{x}))$ depending on the density gradient, as outlined by Bruns [360], and then further elaborated by Iga et al. [361]. The density-based representation of convection finds several applications, including air cooled heat sinks

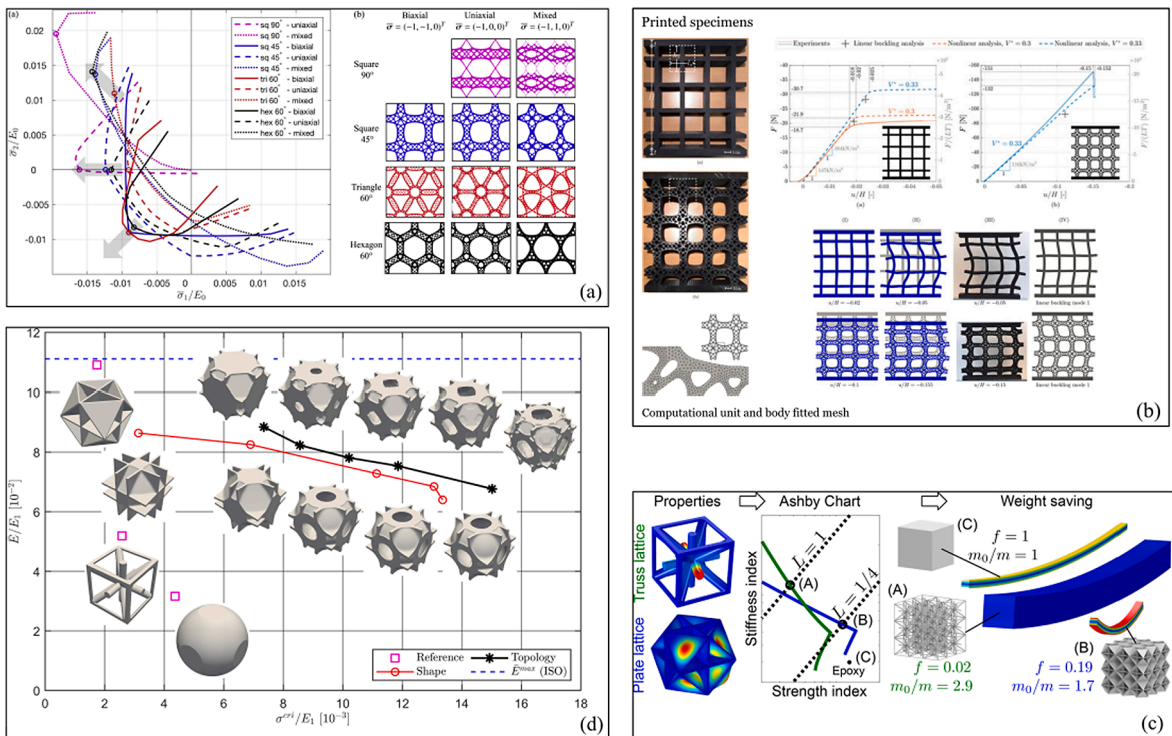


Fig. 8. (a, b) Examples of multiscale hierarchical lattices achieving extreme buckling resistance (reproduced from [323;324]). (c, d) Comparison between stiffness and buckling strength properties of open face (OC), truss-like lattices and closed-face (CF), plate-like lattices (reproduced from [7;325]).

Table 1

Governing equations for the heat transfer models commonly used in TO. For the steady state case, Ω_D is the design domain, $\kappa(\mathbf{x}) = \kappa(\rho(\mathbf{x}))$ and $h(\mathbf{x}) = h(\rho(\mathbf{x}))$ are the (design-dependent) thermal conductivity and heat transfer coefficient, respectively. $Q(\mathbf{x})$ is the heat generation rate and $T(\mathbf{x})$ the temperature distribution, with its far field value T_∞ , and prescribed value on the Dirichlet boundary \bar{T} . Compared to steady-state, in the transient model we have two extra parameters: the fluid density, $\rho(\mathbf{x}) = \rho(\rho(\mathbf{x}))$ and heat capacity, $c_p(\mathbf{x}) = c_p(\rho(\mathbf{x}))$. For the conjugate heat transfer model, Ω_S is the solid domain, Ω_F the fluid domain, $\sigma = -p\delta_{ij} + \mu(\nabla\mathbf{v} + \nabla\mathbf{v}^T)$ is the simplified stress tensor, depending on the fluid pressure (p) and dynamic viscosity (μ), \mathbf{v} is the fluid velocity and β is the coefficient of thermal volume expansion. \mathbf{s} is the momentum term and \mathbf{g} the gravity acceleration vector.

	System of equations	
Steady-state heat transfer	$-\nabla \cdot (\kappa(\mathbf{x})\nabla T(\mathbf{x})) = Q(\mathbf{x}) \quad \mathbf{x} \in \Omega_D$ $\kappa(\mathbf{x})\nabla T(\mathbf{x}) \cdot \hat{\mathbf{n}} = h(\mathbf{x})(T - T_\infty) \quad \mathbf{x} \in \Gamma_q$ $T(\mathbf{x}) = \bar{T} \quad \mathbf{x} \in \Gamma_T$	(14)
Transient heat transfer	$\rho(\mathbf{x})c_p(\mathbf{x})\partial_t T(\mathbf{x}) - \nabla \cdot (\kappa(\mathbf{x})\nabla T(\mathbf{x})) = Q(\mathbf{x}, t) \quad \mathbf{x} \in \Omega_D$ $\kappa(\mathbf{x})\nabla T(\mathbf{x}) \cdot \hat{\mathbf{n}} = h(\mathbf{x})(T - T_\infty) \quad \mathbf{x} \in \Gamma_q$ $T(\mathbf{x}) = \bar{T} \quad \mathbf{x} \in \Gamma_T$ $T(\mathbf{x}, t_0) = T_0$	(15 a)
Conjugate heat transfer	$\rho(\mathbf{x})\mathbf{v} \cdot \nabla\mathbf{v} - \nabla \cdot \sigma = \mathbf{s} - \rho_0\mathbf{g}(1 - \beta(T - T_0)) \quad \mathbf{x} \in \Omega_F$ $\nabla \cdot \sigma = 0 \quad \mathbf{x} \in \Omega_F$ $\rho(\mathbf{x})\mathbf{v} \cdot \nabla T(\mathbf{x}) - \nabla \cdot (\kappa(\mathbf{x})\nabla T(\mathbf{x})) = Q(\mathbf{x}) \quad \mathbf{x} \in \Omega$	(15 b)

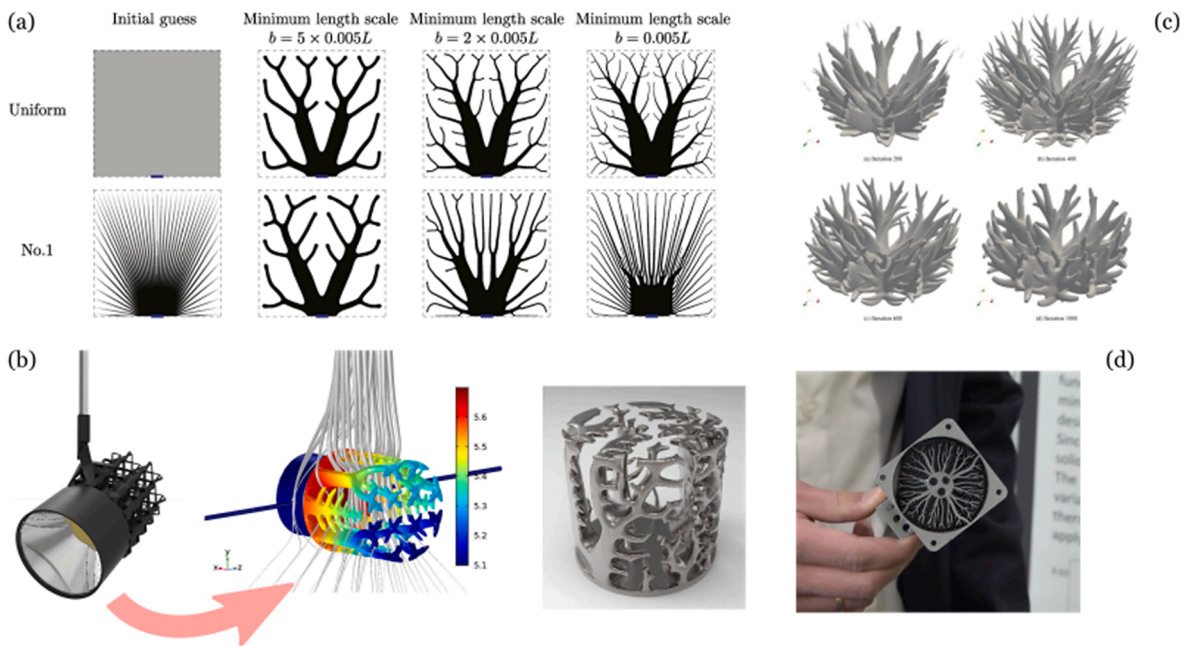


Fig. 9. (a) shows the optimized tree-like structures obtained for the volume-to-point problem in the 2D setup, as opposed to the needle like configuration (reproduced from [354]). (b) shows topology optimized heat sinks designs, obtained by using a CjHT model (reproduced from [365]). (c) displays some heat sink designs obtained by CjHT modeling and for different length scales (reproduced from [365]).

[362,363], or the design of thermal-electric activated MEMS [364].

The methods discussed in the previous paragraph still entail a constant heat transfer coefficient for the convective fluid, thus hindering the correct modeling of the dynamics of the cooling process. The realistic simulation of convection-dominated problems requires a *conjugate heat transfer* model (CjHT), where both the solid and fluid media are represented, and coupled by a diffusion equation (see equations (16)). In the CjHT framework, Poissons' equation still governs the heat transfer in the solid, whereas the Navier-Stokes equation governs the heat and mass transfer in the fluid. Such modeling becomes computationally more expensive and prone to convergence issues, due to the non-linearity of the Navier-Stokes equation as well as its velocity pressure coupling, and the strong coupling between convection and diffusion. Alexandersen et al. applied CjHT for designing 2D devices under natural convection and laminar flow [356], assuming incompressibility, and using the Boussinesq equation for the convection–diffusion coupling. The same authors then extended the model to 3D problems in a later work [365]. Among others, Marck and Privat addressed the design of thermo-fluid devices [366], whereas Kontoleon et al. addressed TO problems involving both laminar and turbulent fluid convection, coupled with thermal losses [173]. To reduce the computational cost of the CjHT simulations, simplified models have been developed, based on the following assumptions: (i) the fluids' inertia contribution is negligible, and (ii) the dynamic viscosity linearly depends on the average velocity. These assumptions turn the Navier-Stokes equation into a linear, Poisson-like one, with variable coefficients.

These simplified models, commonly going under the name of “*poor man’s approaches*” allow for a cut of almost 80% of the CPU time, still providing simulation results close to those of a full modeling [367,368].

Concerning transient problems, considerably fewer research works exist in the literature, compared to the steady state model. This is due to the increase in the computational cost, especially for the sensitivity analysis, which, depending on the chosen objective, may become substantially higher than that for the steady state case [370,371]. A general reference for structural optimization under the effect of transient loads is [372]. The optimal design, according to minimum average or maximum temperature may substantially change depending on the duration of the heat load, as shown by Wu et al. [373], and also others [374,375]. For short-time pulses, the optimization mostly exploits the heat capacity of the material, distributing it near the sources in flower-like shapes [376–378]. Other recent works have proposed some alternative objective functions, better aimed at the transient setting [379], or alternative formulations for the transient analysis [380].

Transient effects play an important role for devices subjected to short time heat pulses, or when the heat time profile influences the final performance. This is the case when designing effective coolers for electronic components [381], or other devices for which an instantaneous thermal response is fundamental, such as thermo-optical silicon modulators [382]. Also, transient behavior substantially affects CJHT, by correctly modeling the turbulent flow in cooling channels, and thus enhancing the optimization capabilities. This has been shown both for heat exchangers by Dilgen et al. [100], and for the design of fluid diodes (a device similar to a Tesla valve), by Lin et al. [369] (cf. Fig. 10).

The coupling of thermal and mechanical responses has also received much attention in TO, due to possibilities offered by design for multi-physics applications, and also due to the need for protection against thermally induced stresses. Early works, by Rodrigues and Fernandes [383], and by Jog [384], considered homogenization-based compliance minimization under thermal and mechanical loads simultaneously. The thermo-mechanical coupling was then leveraged by Sigmund and Torquato [385] for designing materials with non-conventional properties, such as negative thermal expansion, using a bi-material and void TO formulation. Building on the same concept, Sigmund then systematically discussed the optimal design of single [290] and bi-material [289], thermo- and electro-thermally actuated MEMS.

In many aerospace applications, and whenever high local temperatures are achieved during manufacturing processes, thermal stresses may trigger unexpected failure mechanisms. In this case, design for minimum compliance does not adequately guarantee structural integrity, and thus stresses, or other failure-related quantities, must be controlled. Wang et al. [386] indirectly achieved this by backin compliance minimization with an additional requirement of having a low directional thermal expansion, whereas several other works [387–389] deal with minimization of thermally induced stresses. This is still a very active research field in TO, as many challenges are involved, such as stress singularity, dealing with many constraints, modeling of design-dependent thermal effects, etc. More references on thermo-elastic TO for stress minimization can be found in the recent work by Deaton and Gandhi [390]. Wu et al. also introduced buckling constraints on the minimum mass design of bi-material structures [391], since buckling can be triggered by the differential deformation of the regions in contact, with different expansion coefficients. The interplay between mechanical and

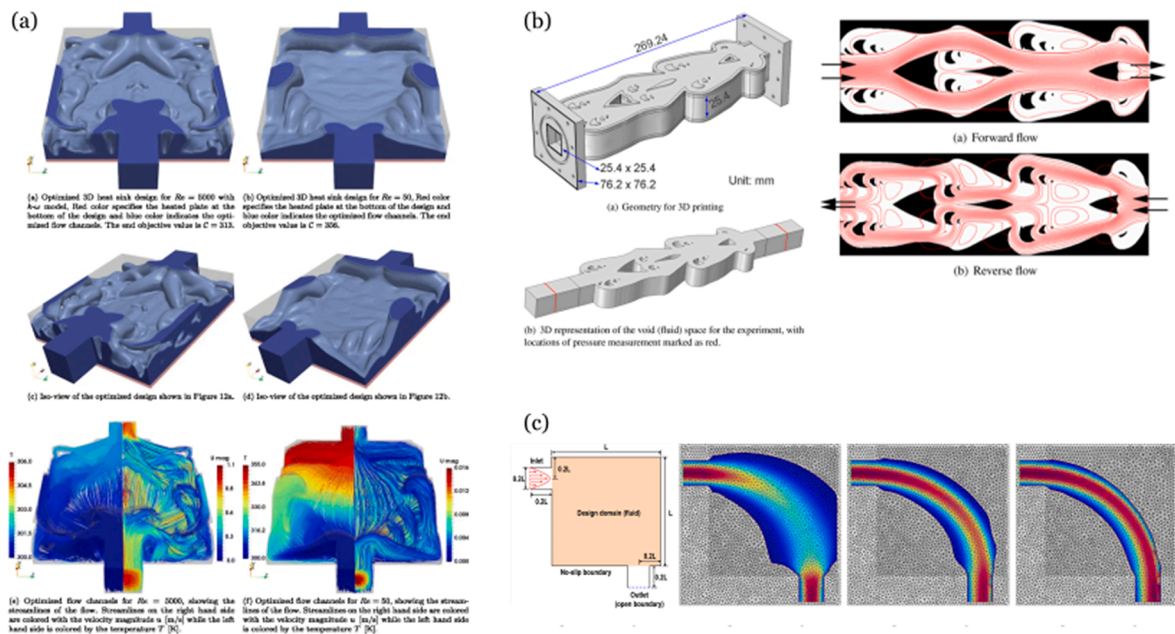


Fig. 10. (a) optimized design of a 3D heat sink, for simultaneous pressure drop minimization and heat exchange maximization, considering turbulent flow (reproduced from [100]), (b) design of a fluid diod, minimizing pressure drop for flows in the forward direction, while inhibiting the flow in the reverse direction (reproduced from [369]) (c) Fluid control device, designed for Navier-Stokes flow and increasing values of the maximum velocity constraint (reproduced from [109]).

thermal response is also considered in design tasks where the devices have to dissipate heat, and withstand an external load. This is explored in several works, often including the thermoelastic modeling of the material properties [67,392–395].

2.2. Topology optimization – Process influence

Design for manufacturing

As earlier discussed, TO enables the generation of highly efficient and performant structural designs, however in its base form, it easily results in geometries that are extremely complex to realize. Consideration of the restrictions posed by specific manufacturing processes next to structural performance is therefore essential. This relates to the concept of ‘Design for Manufacturing’ (DfM), a term that dates back to the eighties [396]. DfM encompasses an overarching philosophy to consider manufacturing-related aspects at an early design stage, to prevent costly and complex modifications later on. Also within the field of TO, DfM has been studied extensively since a long time [397] and for a variety of common manufacturing processes, including milling (e.g. [398]) and more recently in particular multi-axis machining ([399–401]), casting (e.g. [402,403]), turning, rolling and forging [404]. For a more extensive overview, the reader is referred to [405].

2.2.1. Design for additive manufacturing: Design rules

Also AM processes come with specific restrictions that will necessitate design adaptations and/or addition of support structures when not considered as an integral part of the TO process. This has been recognized and demonstrated in [406,407,408] among others. Given the rapid rise in importance of AM, a new and actively developing branch of DfM known as Design for Additive Manufacturing (DfAM) has emerged. Here we first review the three most pertinent restrictions that can be captured directly by geometric AM design rules and their consideration in TO. These rules are typically established empirically by extensive experimental characterization of processes [409]. Benchmark geometries used for such characterization studies are reviewed by [410]. As processes are continuously refined and designers aspire to fully utilize AM process capabilities, design rule sets are growing more intricate and complex. A potential way to handle this may be the use of data-driven approaches, such as the machine learning approach introduced by [411]. Main geometric AM design aspects that have been addressed in various TO studies in recent years are illustrated in Fig. 11: restrictions on feature size, overhang angle and enclosed voids, generation of support structures, choice of build direction and aspects pertaining to hybrid manufacturing processes.

2.2.1.1. Feature size restriction. A common class of restrictions relevant to all AM processes concerns limitations on the size of a particular feature. This includes the minimum thickness of walls, minimum diameter of holes and cylinders, etc. Such restrictions are, at least on a global level, easily imposed in TO formulations through the use of minimum feature size constraints. In density-based methods the filtering techniques or robust formulation described in section 2.1. and e.g. [412] can be readily applied for this. For instance, in [413] the minimum and maximum member sizes are made to be equal to the deposition nozzle size, to obtain design features of uniform width. For TO methods utilizing a level-set design description, also minimum feature size constraints have been developed [414].

Two remarks are in order here. Firstly, the mentioned approaches globally impose a minimum feature size in TO regardless of the specific feature type. Therefore, these approaches cannot make a distinction for design rules that include size restrictions on, e.g. cylindrical pillar diameter vs. thicknesses of vertical walls. For such cases, a geometry-dependent minimum feature size constraint is

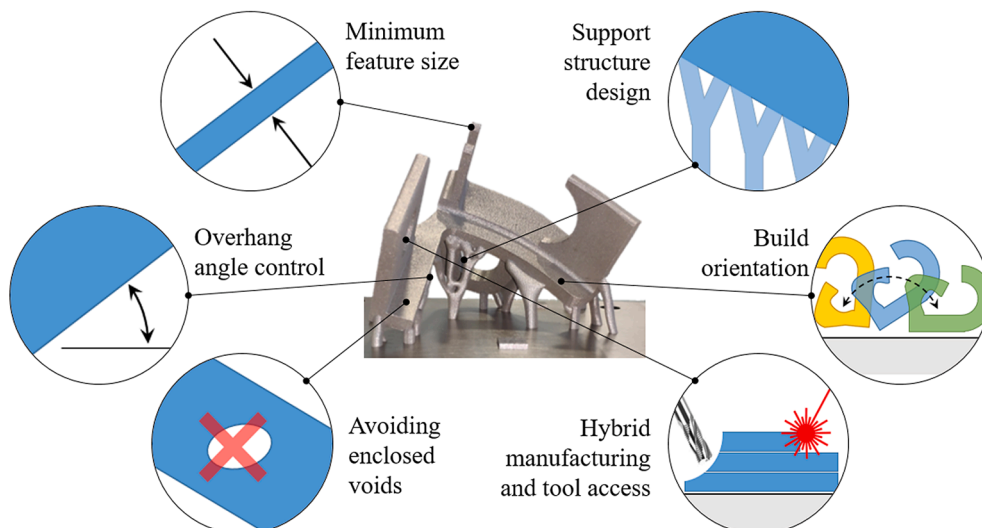


Fig. 11. Overview of geometric AM design aspects that have been considered in TO.

required. Secondly, at present, the resolution and minimum feature sizes achievable with e.g. LPBF technologies has reached a level that is challenging to achieve with TO. For example, to attain a 1 mm resolution for a 100 mm cube, a finite element mesh of 1 million elements is required. Features below the mesh resolution cannot be generated or analyzed in the TO. Hence the use of feature size constraints might be unnecessary in such cases. The situation is very different for AM processes with relatively low resolution with respect to the typical part size, such as WAAM. Next to local feature size constraints, the need to define toolpaths to form an integer number of adjacent beads leads to additional size restrictions in this process. TO methods focused on this aspect have recently been proposed by [415].

2.2.1.2. Overhang angle restriction. A second geometric design rule applicable to most AM processes is limiting the inclination of downfacing (overhanging) surfaces with respect to the base plate. Typically characterized by a critical *overhang angle*, this geometric restriction could not be imposed by previously proposed methods and has received a lot of attention in the TO community. To structure this review, we divide the proposed approaches into two main groups:

- (1) Direct surface inclination control.
- (2) Geometric process modeling.

Below each of these categories is discussed in more detail, together with the most pertinent references. Note that a typical design rule for metal LPBF processes is a minimum overhang angle of 45° [416,417]. However, as AM technologies are advancing, better process control allows for smaller overhang angles by careful adjustment of the process parameters (e.g. [418,419]). Furthermore, for other processes (e.g. FDM, SLA), different overhang criteria apply. Therefore, TO overhang angle measures that can easily accommodate various overhang angle limits, independent of the analysis mesh offer a clear advantage.

The first category includes all methods that in one way or another measure the inclination of the part surface during the TO process, evaluate its deviation from the base plate or the build direction, and use this together with a given critical overhang angle to construct a global overhang measure. Early attempts to formulate an effective overhang constraint based on this concept however produced unprintable geometries (e.g. [420]), as shown in Fig. 12 (a). Matching the overhang angle requirement on all downfacing surfaces is insufficient to render a printable structure, as patterns with upside-down cones (or triangles, in 2D) would still be allowed. Various measures to close this loophole have meanwhile been proposed and demonstrated ([420–422,423]), see also Fig. 12 (b). These rely on enforcement of a minimum length scale or the part or the edge detection algorithm, in addition to the surface inclination constraint, which renders the sharp downwards pointing tips seen in Fig. 12 (a) infeasible.

In density-based TO approaches, the surface inclination is obtained through locally evaluated density gradients (e.g. [424]) or through a plane fitting procedure [422]. When using a level set description, the boundary normal is readily available through the gradient of the level set function. In both cases, the local constraints must be aggregated to a single global constraint, which can introduce a degree of constraint relaxation. Furthermore, in feature-based TO variants, such as MMC [121], the inclination of features such as beams and plates is typically explicitly and directly controlled by a design variable (e.g. [425]). A more elaborate feature-driven approach based on cone-shaped primitives is proposed in [426], which includes an additional requirement related to the overlap between the features.

In the second category of methods to provide overhang control, a highly simplified, geometrically defined process model is introduced. Processing a ‘blueprint’ design field with this process model results in a layout where all unprintable features have been removed. This can then be considered as the virtually printed design and its structural performance can be evaluated (i.e. using the process model as a filter), or alternatively the difference between obtained and blueprint design can be used as a measure of printability and control through e.g. a constraint.

Early examples of this approach are given by [427] and [428]. The simplified geometric process model in both works involves a small region in which, based on the desired overhang angle, a condition is enforced that printed material should be sufficiently supported by material printed in a previous layer. The printability of the entire output field is ensured by evaluating this condition in a

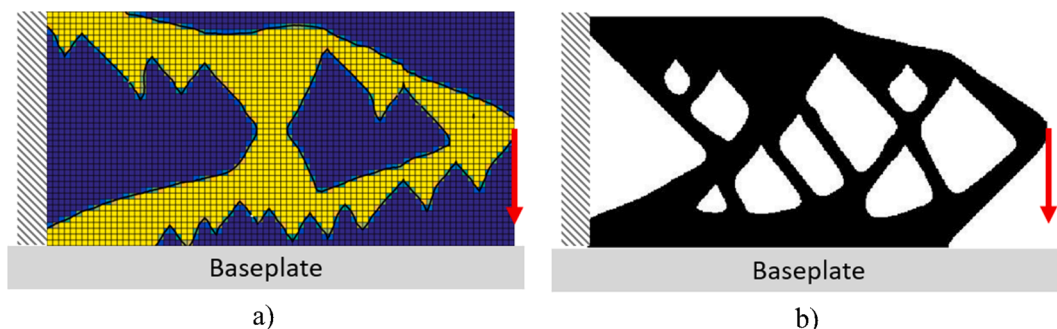


Fig. 12. (a) TO compliance minimization design obtained with a 45° overhang constraint on downfacing boundaries (Van de Ven, 2015). Although the constraint is met everywhere, the design is not printable since the downward pointing tips require support. (b) TO design obtained using a local overhang angle constraint in combination with a minimum feature size restriction. This effectively eliminates the option to form sharp tips [422].

layer-by-layer manner similar to the actual process order. A benefit of the filter approach is that full agreement with the overhang angle requirement is enforced in every optimization iteration. The existing methods rely on density-based TO, and different formulations differ in how intermediate density values are handled, which defines their convergence characteristics.

Various improvements have been proposed to generalize these methods further: [429] adapted the approach by Langelaar to unstructured meshes and arbitrary overhang angles, [430] proposed a version with similar capabilities based on front propagation, with a comparative study presented in [431]. Delissen et al. [432] further improved the spatial accuracy and demonstrated the feasibility of applying this filter to a large-scale problem consisting of 9 million elements. The obtained geometry proved printable without requiring additional support structures aside from those generated by the TO process, as seen in Fig. 13. A disadvantage of the filter approach is that any minimum length scale restrictions previously imposed on the design may be lost, as unprintable regions are removed. In the study by [433], an approach is proposed to combine the overhang filter by Langelaar with the robust formulation ([269]) to preserve length scale control. Furthermore, the filter tends to produce sharp corners that might result in stress concentrations when no smoothing is applied. In [434] a remedy for this potential problem has been proposed.

Besides these two main categories that encompass the majority of approaches, various other directions have been explored. One direction of particular interest is using physical models to enhance the printability of designs instead of exact geometric relations. An example is the approach by [435], where it is attempted to eliminate undesired overhangs by introducing a constraint on the stiffness of the structure at intermediate stages of the printing process against a downward vertical load. To limit the increase in computational effort, not every layer of the printed part is considered but only selected intermediate stages. These methods have not become popular for overhang control due to their imprecise enforcement of the overhang design rule combined with their high computational cost. However, while not successful for constraining overhang angles, these approaches can be seen as the first attempts at including a physics-based as opposed to geometry-based AM process simulation in the TO process. In order to address DfAM restrictions that are not easily captured by geometrical design rules, consideration of more detailed process physics is a necessity, as discussed further in 2.2.2.

2.2.1.3. Enclosed void restriction. A third geometrical aspect that has been investigated to integrate into TO is the elimination of enclosed voids. In powder bed processes, but also in e.g. wire-feed processes that require inspection or post-processing of all printed surfaces, fully enclosed voids are to be avoided as they prevent powder evacuation, inspection etc. A pragmatic solution is to add small powder evacuation holes after optimization ([432], Fig. 13), however this may result in loss of performance. Therefore, DfAM approaches to entirely prevent enclosed voids are desired. Following the first approach by [436], several other methods have been proposed. For density-based TO, methods to suppress enclosed voids are based on the solution of an auxiliary problem ([437,438,439]). Any enclosed voids can subsequently be distinguished from accessible voids from the solution of this auxiliary problem. In particular, steady state heat transfer or equivalent is often applied, and although solving an additional PDE adds computational cost to each iteration, this still is modest compared to the mechanical analysis. For feature-based TO methods, enclosed voids are prevented through control of the feature centroids [440], although this can result in a substantial reduction of the design freedom.

The studies by Gaynor et al. [441] and Xiong et al. [442] follow a different philosophy. Instead of suppressing enclosed voids, here the emphasis is on creating connections to the outside such that powder can be evacuated. Another variation on this topic is found in papers where the focus is not on eliminating enclosed voids but on ensuring that these are overhang-free and fully self-supporting. Examples are [443] and [444], and this approach applies primarily to non-powder-based processes.

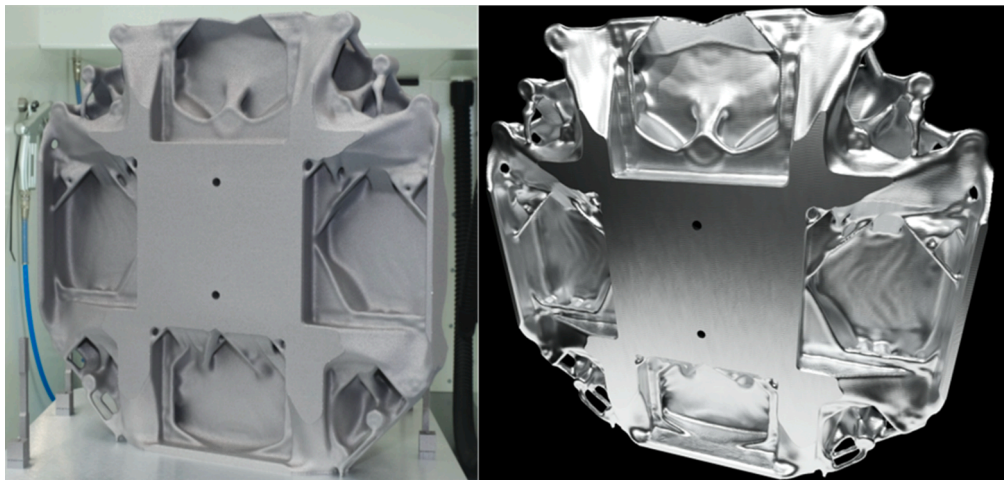


Fig. 13. Optimized motion system chuck produced in aluminum through LPBF (height 400 mm). Eigenfrequency maximization through TO was performed in combination with an overhang constraint. The obtained geometry proved printable without additional support structures [432]. The two central holes were added manually to facilitate powder evacuation.

2.2.1.4. Process aspects: Support structures. Thus far, the discussion has focused on generating parts by TO that fully comply with typical AM design rules (feature size, overhang angle, enclosed voids). However, this requirement considerably limits the design freedom and can result in an undesired performance reduction. The alternative is to use so-called support structures, sacrificial structures added to the part to be printed, to satisfy printability requirements. These supports must be removed in a post-processing step, adding time and costs. Nevertheless, when part performance is prioritized, the addition of support structures can provide a welcome increase in the design space.

The location and shape of the support structures can be viewed as part of the process settings since the final part geometry does not define these aspects. Designing these support structures is nontrivial because a trade-off must be found between the positive impact on part performance and the disadvantages of supporting structures (increased printing time and material usage, increased post-processing cost). Motivated by this, TO methods have been proposed that instead of generating self-supporting structures allow for the addition and even optimization of supports. We distinguish three cases: firstly, those where part and support are optimized simultaneously, e.g. [445]. Secondly, studies are dedicated to only the optimization of support structures while considering the part geometry as fixed, e.g. [446,447]. While the support layout is explicitly designed in both these categories, in the third category, only the possibility of supporting certain downfacing surfaces is considered without designing the actual supports. An example is given by Mirzendehtel et al. [448].

A final geometrical aspect related to this is the consideration of the support removal process. Minimizing the contact area between part and support to reduce post-processing time was already considered in [445] and further detailed in e.g. [449]. Access to the supports is required to facilitate removal by e.g. machining or other means. This is considered in: [443,450]. Moreover, in [451] next to support generation to meet the overhang requirements, the forces due to post-processing operations such as drilling exerting on the printed part are considered part of the TO process. Since post-processing can be responsible for a significant percentage of the overall production cost of a printed part, it deserves more detailed consideration in DfAM approaches. Combinations with previously developed machining DfM methods for TO seem promising (e.g. [452;399–401]), and complex questions of process order in support removal and where to clamp parts during post-processing need to be addressed in future studies.

2.2.1.5. Process aspects: Orientation. A final geometric process parameter that strongly affects AM costs and/or DfAM design freedom is the orientation of a part with respect to the base plate. While some processes allow for part reorientation during the additive process (e.g. certain extrusion-based setups [453]), in most prevalent AM processes, the orientation of a part is fixed. For a given part, this orientation directly affects which surfaces are overhanging as well as their inclination, and as a consequence, the amount of support material needed to print the part. Also, the local surface roughness depends on the angle between the part surface and the base plate, which can be a consideration when minimizing post-processing effort. When the part is being designed through TO, the orientation choice similarly affects which geometries are self-supporting.

Outside the TO domain, approaches to find optimal part orientations to minimize support or ensure surface quality exist e.g. [454]. An early attempt to integrate part orientation choice in a TO process was presented in [455], however, this study was limited to 2D. It relied on considering a multitude of candidate orientations in the optimization, and gradually focusing the design evolution on the one that resulted in the least support material. This may have merit when only a few candidate orientations are to be considered, which can be the case when certain predefined parts are included in the TO problem. However, for free 3D orientation optimization, more recent studies [444,456,457] take a different approach and include the orientation through angular design variables directly into the optimization problem. While this proves effective, it is easy for the TO process to get trapped in an inferior local optimum due to the multimodal behavior of the response functions in terms of the orientation variables [455,457]. Using different starting points is advised to avoid this.

Part orientation not only affects the required amount of support material (or performance reduction for a self-supporting design), but also the way anisotropy in material properties manifests itself in the produced part. Depending on the process, the typically layer-wise deposition results in anisotropy of e.g. the elasticity tensor, strength and/or fatigue behavior [458,459]. Full consideration of these important aspects is still a challenge [460]. [461] demonstrate simultaneous optimization of part orientation and topology in the context of WAAM, considering orthotropic material properties. In [440], anisotropy in the elasticity tensor is considered using a transversely isotropic material model, and the build orientation of multiple components was optimized such that the performance of a final part obtained after a predefined assembly process was maximized. The additional consideration of an assembly step allows the application of this method to parts that are too large to fit in a build chamber.

Next to the build orientation, also the orientation of scanning/deposition trajectories can have a strong influence on local material properties and part performance. This was taken into account in a TO setting in [462], in combination with an overhang restriction. Here trajectories were directly coupled to part shape by generating them using an offset method. This is not a necessity, and many other trajectories are technically feasible. A generalization could therefore be to introduce separate design variables for trajectory control. This was recently demonstrated in [463] where the significant elastic anisotropy observed in stainless steel plates produced with WAAM, described by a cubic material model, was exploited. To maximize the stiffness of a part, its topology was optimized simultaneously with the deposition path of the intended WAAM. This is achieved by introducing an additional design variable field controlling the local deposition direction. The geometric layout and the deposition path optimized for two load-cases are depicted in Fig. 14. The results show that the deposition directions align approximately at 45° with respect to the load path, which corresponds to the stiffest direction determined experimentally. The structural stiffness was increased by more than 53% compared to conventional deposition directions along the load path. While this study shows the promising potential of deposition direction optimization, using these optimized directions to obtain a possible deposition path (shown in Fig. 14 (c) and (d) for the two load cases considered) resulted

in non-equidistant deposition trajectories. The concurrent optimization of deposition path and design using the offset method [464] can achieve overlap/gap-deposition which is extended to 3D in [465].

Furthermore, in [464], the mechanical properties of parts printed along contour offsets [465] are simulated. However, the material properties may be affected by the altered deposition patterns and may differ from the experimentally obtained ones on different geometries. This aspect requires further study and potentially a full consideration of the thermo-mechanical process history is necessary. Furthermore, it is relevant to point out the similarity of this trajectory optimization problem with the body of literature on TO of fiber reinforced structures. As manufacturing of fiber reinforced composites can also be considered an additive process, and in fact AM technologies exist that combine material extrusion with fiber reinforcement, interesting synergies can be expected in this area.

2.2.1.6. Hybrid manufacturing. The combination of AM and another manufacturing process, as present in [440], is also found in so-called hybrid manufacturing processes. Typically this refers to an integration of additive and subtractive steps (e.g. [466]), but also other combinations exist, e.g. AM and forging [467]. Machines offer this capability in a single integrated setup, which allows for e.g. in-situ post-processing [468]. These novel capabilities also lead to new DfAM challenges. For example, integrated AM and milling lead to different access possibilities for surface post-processing than when considering separate AM and milling processes in sequence, through alternating additive and subtractive steps. In [469], a TO approach for hybrid manufacturing combines AM overhang constraints and a constraint on the milled volume. In [470], design rules for hybrid manufacturing are presented, which may form the inspiration for future hybrid DfAM TO approaches. For intermittent additive and subtractive operations, process planning must also be considered in the TO formulation to ensure toll access for the subtractive steps. Hybrid manufacturing, and in general, the consideration of different manufacturing steps and their process order significantly increase the design envelope and the development of TO methods capable of exploiting this additional freedom presents a direction for future research.

Finally, two general remarks regarding the discussed geometric aspects are in order to conclude this part. Firstly, it is noticed that while a large number of, sometimes slight, variations of methods have been proposed, hardly any study makes a direct comparison between different methods to determine their relative advantages and disadvantages. Notable exceptions are [431] and [471]. More comparative studies on aspects such as effectiveness, convergence behavior, computational cost, compatibility with other geometry control measures, etc., would help advance the field. To facilitate this, providing source code with publications is strongly encouraged. Secondly, AM technologies are advancing at a steady pace. Where a few years ago, a 45° overhang angle was considered the limit for powder-bed metal printing, new process control strategies allow significantly shallower angles. We may reach a point where certain design rules can be abandoned altogether, as they are rendered obsolete by superior AM technologies. The concept of contact-free supports, for example, strongly reduces the required post-processing effort [472]. At least design rules, and the associated questions regarding their implementation in TO, should be updated with the present state of the art in AM.

2.2.2. Beyond design rules: Process physics induced restrictions

Empirically established, geometrical design rules for various AM processes have been used extensively in TO with the aim to ensure the manufacturability of the optimized designs. Such geometrical design rules and their TO implementations for feature size, overhanging surfaces, and enclosed voids have been reviewed above. However, not all relevant effects can be captured in simple geometric rules, and hence a more detailed analysis of the AM process becomes imperative. The thermal and mechanical state of the part during AM must be considered to assess potential defects and manufacturability concerns. Especially in metal AM processes, heating and cooling cycles experienced during the manufacturing might cause overheating [473], part distortions, and residual stresses [474] and [31]. While a thermal model can predict overheating, distortions and residual stresses require mechanical modeling. Therefore, TO

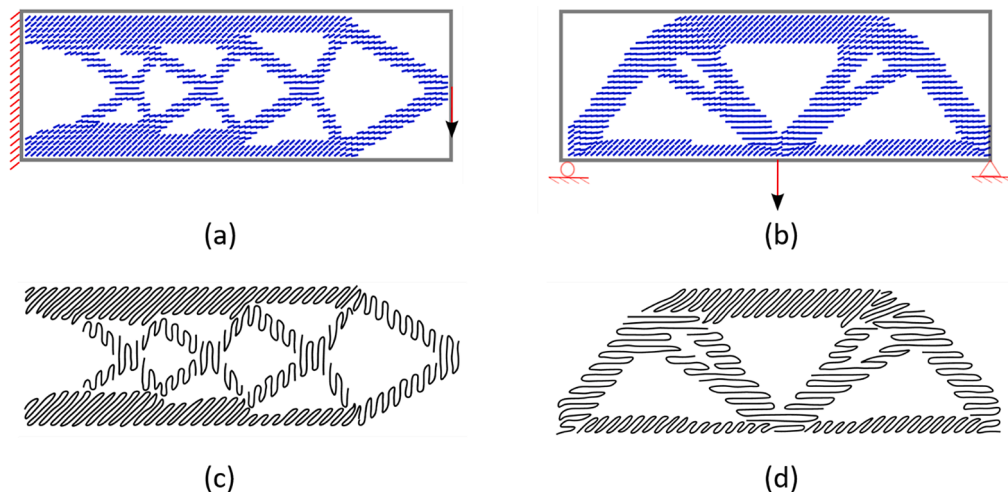


Fig. 14. Optimized deposition directions corresponding to (a) cantilever and (b) bridge problems with the indicated loading and boundary conditions. Possible deposition paths along the optimized deposition directions for (c) cantilever and (d) bridge problems [463].

schemes that account for the process physics can be grouped as TO methods with restrictions based on *i*) thermal models and *ii*) (thermo-)mechanical models, i.e. in the latter, the thermo-mechanical coupling can be included.

In contrast to the geometry-based restrictions described above, simulating the complex process physics in every TO iteration and computing the associated sensitivities required for gradient-based optimization algorithms is computationally challenging. The transient nature of temperature evolution demands time integration. Also, at high temperatures presence of inelastic deformations necessitates the due account for material nonlinearities. In short, the physics-based restrictions in TO are extraordinarily computationally expensive and thus have only recently been flourishing. Although fewer studies exist that integrate physics-based process models into TO, we discuss them in more detail as we anticipate that most future developments will be in this direction. Moreover, all existing studies in the literature entail various simplifications for computational tractability.

2.2.2.1. Thermal restrictions. Especially in precision metal parts, overheating during LPBF adversely affects the part quality leading to defects such as balling and dross formation [475] compromising the surface quality. Moreover, local overheating can affect the local microstructural evolution and hence the resulting physical properties of the part [408].

The geometric layout of the part is one of the factors that can cause overheating besides process parameters and material properties. For instance, it is well-known that overhanging surfaces are prone to overheating during metal and polymer AM, but overhangs are not the unique cause of the overheating. Any geometric feature that hinders heat evacuation towards the base plate (which acts as a heat sink) is a potential cause for overheating, as exemplified in Fig. 15.

One of the first attempts to incorporate restrictions in TO based on a thermal model was [476]. In this study, the heat conduction behavior of the support structure was incorporated for a fixed part design with a simplified transient AM process simulation to ensure manufacturability. In their finite element framework, layers of elements are activated sequentially to mimic the layer-by-layer building of the part and sacrificial supports. The laser motion is then represented by modeling a particular element as a heat source at the time of interest. The objective function for TO is the difference between the ambient and predicted temperature at a few observation points integrated over the time domain, and sensitivities of the design response are calculated by the adjoint method. Because the geometric layout of the part is fixed, the optimized performance is not compromised upon ensuring manufacturability by adding supports. Numerical examples showed that the topology optimized support structure exhibits a good thermal conduction capability and dissipates heat efficiently during the AM process. However, the algorithm's high computational cost was deemed unsuitable for large-scale 3D applications.

Ranjan et al. [477] recently presented a TO scheme where a thermal constraint is formulated using a computationally inexpensive simplified thermal model exploiting local steady-state thermal analysis to detect geometric features of the AM part leading to overheating [478]. This study also demonstrated that existing TO methods that rely purely on geometric overhang restrictions do not ensure avoiding overheating. However, the physics-based constraint upon identifying a process-associated critical threshold can suppress geometric design features, including but not limited to overhangs, thus eliminating local overheating in a computationally efficient manner.

The simplified thermal model is based on novel simplifications besides those commonly employed in AM process simulation, such as layer-by-layer deposition (discarding the laser scanning patterns), lumping several material layers into a single simulation layer, and omission of radiation and convection. These process multi-scaling techniques are described in depth in section 4.2. With only these frequently employed simplifications, the computational times for thermal AM models are still prohibitive, especially for integration with TO. However, novel simplifications of temporal and spatial decoupling and localized steady-state responses provide extraordinary computational gains of over 2 orders of magnitude. At the same time, the correct locations prone to overheating, even though overheating is a transient phenomenon, can be accurately identified with steady-state thermal analysis performed on successive small portions of the entire part. This simplified model depicted in Fig. 16 considers subsets of the part geometry termed *slabs* where subsequent slabs mostly overlap. For each slab, at the top boundary, heat flux is applied, while the bottom of the slab is assumed to be a heat sink. Temperatures are obtained from a steady-state thermal finite element analysis. Note that most finite element nodes are

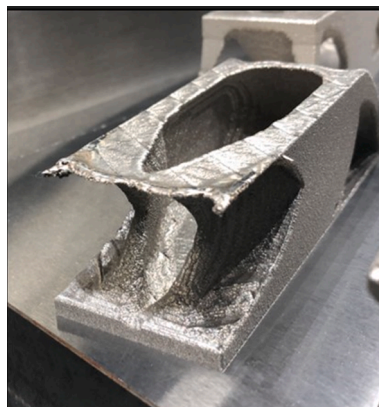


Fig. 15. LPBF build failure before the completion of the part due excessive overheating.

typically considered in multiple slabs. Therefore, the maximum temperature for each node indicates the local conductivity and thus the predisposition to overheating [479].

Note that the extensively-simplified thermal models are neither intended to capture quantitative temperature values nor have experimentally verified. However, they can capture correct locations prone to overheating and with an error in maximum temperature prediction of less than 10% compared with the fully transient layer by layer thermal models including convection and radiation heat loss [478]. Moreover, advantages of combining physics-based AM restrictions with TO have been recently validated by experiments [480]. Designs optimized for minimum compliance by conventional TO, TO with geometric overhang restrictions [428], and TO with physics-based overheating restrictions [481] have been built by LPBF using Inconel 718 powder and monitored by an optical tomography system for detecting overheating. It was found that standard TO, as anticipated, leads to severe overheating and even build failure. TO with physics-based restrictions resulted in a significant reduction in overheating compared to the part layout generated by TO with geometry-based overhang restriction, as illustrated in Fig. 17. This observation again reveals that avoiding acute overhangs with geometric design restrictions is insufficient to prevent overheating.

Optical tomography measurements performed by Ranjan et al. [480] also revealed that the nature of laser scanning patterns significantly influences overheating behavior. Therefore, TO methods integrated with physics-based models accounting for specific scan patterns are needed. This forms a significant challenge for future research, as the level of detail required to capture the effects of specific scan patterns is considerably higher than what is offered by the models used in the presented studies. Such reduced-order part-scale simulations are discussed in section 4.4 under process multi-scaling methods.

2.2.2.2. Mechanical restrictions. Mechanical field quantities such as distortions and residual stresses are usually predicted by either purely mechanical models with an ad-hoc treatment of the thermal effects (e.g. [482]) or with one-way coupled thermomechanical simulations (e.g. [483]). An estimated thermal strain (a.k.a. *inherent strain* [484]) is typically used as an input in the former. In contrast, in the latter, the temperatures obtained from a thermal model are used to generate loads in a mechanical simulation.

To provide some background, we start with several studies exploring the scanning path optimization for a fixed part geometry to reduce residual stress and distortion inherent in the metal melting and solidification process. It is desirable to tailor the scanning path for a given geometry to avoid build failures. In this context, [485] investigated the scan pattern design of islands to reduce part deformation after cutting off apart from the build platform. Part deformation is simulated by layer-by-layer (de)activation of finite elements to mimic material addition and part cut-off steps, by means of solving multiple static equilibrium problems. Optimized scanning patterns of a simple block and a connecting path with a more complex geometry have been validated experimentally with LPBF. The amount of post cut-off bending has been reduced by 23% for the simple block, while the deformation of the near tip region of the connecting road has been approximately halved. Xu et al. [486] optimized the island-type scanning patterns of a fan blade with a more complex geometry in a very similar manner. This study demonstrated that the optimized scanning path exhibits smaller maximum distortion numerically. Chen et al. [487] presents a level set-based scanning path optimization enabling layer-wise continuous scanning again using the inherent strain method. However, the anisotropy of the residual stress is accounted for by scanning orientation-dependent inherent strain vectors. This study also reported a concurrent optimization of laser scanning path and topology, and has shown that the maximum von-Mises strain in an L-bracket with an optimized scanning pattern can be further reduced with the concurrent optimization of the structure. In [488] the scanning strategy is optimized simultaneously with the geometry of an inner lattice to minimize the cut-off warpage. There is synergy between the asymmetry of the residual stresses due to the scanning strategy and the enhanced overall stiffness due to the inner lattices is exploited. Design optimizations on quasi 2D and 3D problems and there's experimental verification using a metal LPBF reduced the cutoff warpage up to 39.4%.

Early examples of mechanical models used to ensure additive manufacturability during TO considered how the self-weight of the structure evolves during the fabrication steps in a layer-by-layer manner. A density-based TO formulation, accounting for minimizing compliance against gravity loads during each fabrication stage, indirectly reduces overhang patterns because they experience a disproportionate deformation [489]. However, in contrast to geometric approaches where overhangs are directly constrained, unsupported overhanging regions may still exist depending on the penalty associated with the additional compliance due to the fabrication stages. A similar TO methodology using a constraint on the compliance of the intermediate build stages of a topology in the level

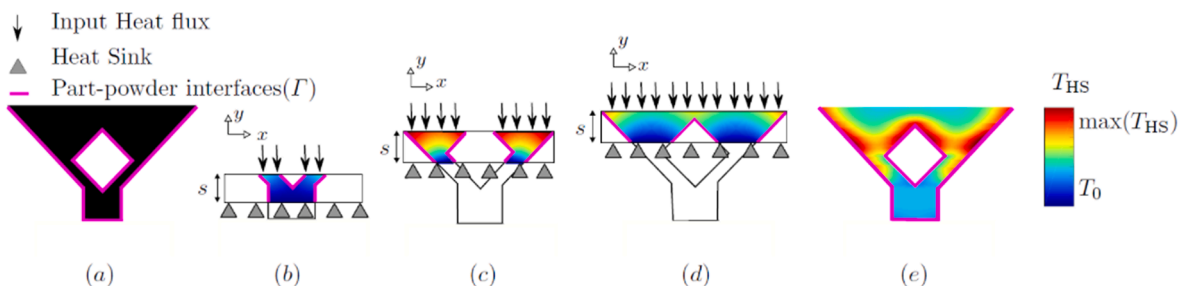


Fig. 16. Detection of overheating using the slab analysis for (a) the geometry depicted. The contour levels of temperature are obtained with a steady state thermal analysis on (b-e) subsections of the geometry as it is being built in time. For each slab with thickness s , heat flux is applied at the top, and its bottom acts as a heat sink while the part-powder interfaces Γ denoted by magenta are insulated. (f) The maximum temperature from all slab calculations for the entire part is given [477].

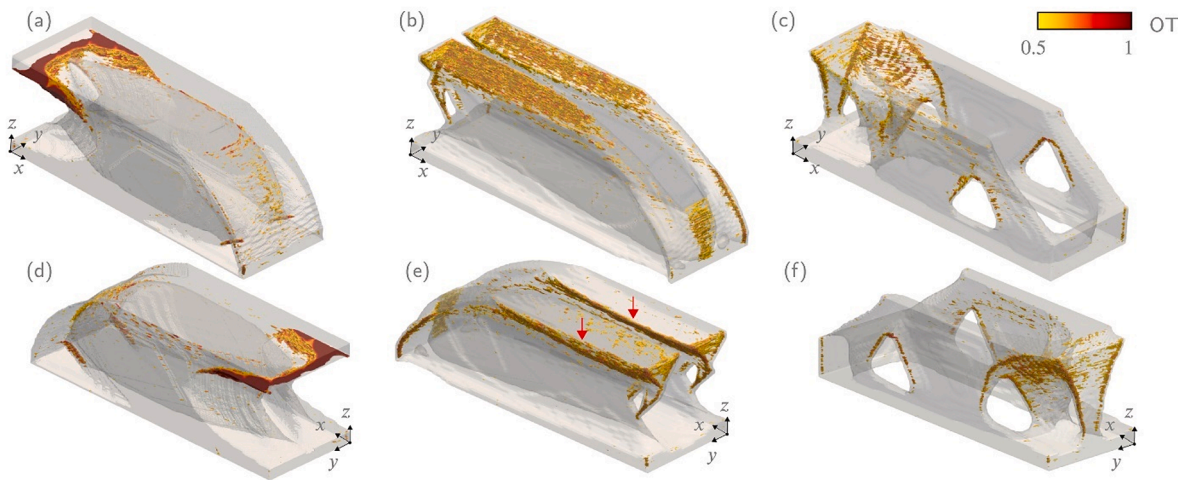


Fig. 17. Convolutional OT data visualized on parts built by LPBF from (a) and (d) standard TO design, (b) and (e) TO with geometric overhang restrictions and (c) and (f) TO with physics-based overheating restrictions [480].

set framework was presented by [490]. Amir et al. [491] extended the formulation of [489] to accommodate 3D high-resolution designs for AM problems enabled by a scalable parallel computational framework.

Pellens et al. [433] utilized the inherent strain method (described in section 4.4) to project the thermally induced distortions during metal AM by applying an experimentally determined initial strain to each deposited layer. For this purpose, layer deposition is modeled by activating new layers of finite elements (the element birth technique [492]) perpendicular to the build direction, and strains corresponding to thermal shrinkage are prescribed for calculating the distortion of the part. Incorporated into TO, this model was used to find the optimal support structure while keeping the maximum vertical displacement of the part below a user-defined tolerance on each layer (i.e. to prevent recoater collisions). With a 3D example, it was demonstrated that material and printing time reductions could be achieved using the optimized supports instead of uniformly distributed supports typically used in industrial practice. Integrating a similar purely mechanical prediction of AM distortions with TO, Misiun et al. [493] obtained designs optimal for minimum compliance which, at the same time, are also manufacturable through AM without exhibiting recoater collision or excessive distortion. During the build AM simulation, the finite element degrees of freedom of the bottom layer of nodes are suppressed to specify no displacement at the part base plate interface. When they are subsequently released as when the manufacturing is complete, the residual stresses in the part cause additional distortions. The gradients of the distortions with respect to the design variables have been formulated using the adjoint method. Density-based TO using SIMP was performed both in 2D and 3D.

More recently, instead of distortion control, the layer by layer inherent strain method has been utilized to evaluate and constrain the residual stresses in a Princess part [494]. In this metal AM-oriented TO study, an aggregated residual stress constraint and an overhang filter are used concurrently. [495] also use the inherent strain method to capture and constrain manufacturing defects such as deformations and residual stresses and perform topology optimization of support structures for this distortion minimization. This study also includes experimental validation. It is worth mentioning the accuracy of the stresses predicted by their inherent strain method is not guaranteed, as plastic deformations due to accumulated stress are not accounted for [496]. Furthermore, given the vast amounts of heating cycles during LPBF they yield the strength of the material is knocked down when the temperature increases contributing to the frequent occurrence of plastic deformation during the process. It remains a challenge to adequately include the effect of plastic deformation on residual stress formation in a sufficiently computationally efficient manner suitable for design optimization.

It is important to note all layer deposition steps during the building stage can be treated as independent linear problems appealing to the superposition principle when treating the mechanical boundary value problems as linear [496]. Consequently, all layer deposition steps and adjoint systems for sensitivity analysis can be solved in parallel, allowing to address 3D problems with this TO scheme.

A 2D example from [493] is depicted in Fig. 18 and Fig. 19. In the conventional topology optimized designs, recoater collision is expected to occur in elements colored with red (Fig. 18), while the structure is predicted to undergo considerable distortion when analyzed with the AM simulation. When the optimization is performed with AM constraints, the recoater collisions are prevented, and the final distortion is below the specified value at the nodes of interest. The optimized designs feature many auxiliary intermediate density features that effectively play no role in the minimum compliance objective, which can be interpreted as lattice-type support structures routinely used in practice. No overhang or feature size considerations were applied in this study (see Fig. 19).

Integration of a simplified thermo-mechanical AM model with density-based TO to reduce part distortions was studied by Wildman et al. [497]. For approximating the thermal history, a linear temperature decrease was assumed; therefore, the effect of part layout on the part's thermal behavior was not fully captured. Allaire et al. [498] presented a thermo-mechanical AM model incorporated into the level-set TO method to minimize thermal stresses and deformations. The AM model comprises the coupling of the heat conduction

equation with a quasi-static thermo-elastic constitutive equation and equilibrium. However, it was reported that the associated computational cost when incorporating a complete layer-by-layer model which accounts for build history was very high.

This subsection started with an overview of studies focusing on AM process parameter optimization using thermal and thermo-mechanical AM process models for fixed geometries. Recent developments reviewed above combine such models with TO of the part itself, while assuming constant AM process settings. We foresee increased efforts towards further refinement and efficiency improvement of the AM process models involved, e.g. through model order reduction, as well as the combination of geometry (TO) and AM process parameter optimization. Considered parameters range from global process settings (i.e. constant during the process and the same for each layer) to fully adaptive and location- and layer-specific settings, e.g. local laser power. Such added process flexibility may render previously unprintable geometries manufacturable, and will allow the optimization process to further maximize the design performance. The first instances of such approaches are discussed next.

2.2.2.3. Integrated part, process and property optimization. The section above described physics-based models in TO to control geometric part layout to reduce overheating, distortions, and residual stresses. It remains to present a few recent TO schemes that account for the AM process parameters. The key bottleneck here is again the computational cost and complexity of the physical AM models, for instance, to describe the scanning strategy, compounded by the large number of iterations usually required for the optimization process.

Wire and arc additive manufacturing (WAAM) is an AM method suitable for large-scale structures. In some WAAM setups, a robotic arm can continuously rotate the part during construction, giving flexibility to the fabrication sequence. The optimization of this fabrication sequence was addressed by [499]. In their *Space-time TO* framework, two design variable fields, pseudo-density and time, describe the geometric layout of the part and its intermediate forms during the fabrication. The fabrication sequence was concurrently optimized for a given density distribution by maximizing the stiffness of all intermediate production instances against the gravity loads. The proposed formulation is also particularly suitable for investigating the dependence of part distortions and residual stresses on the fabrication sequence [500]. An illustration of the latter is given in Fig. 20.

Boissier et al. [501] have considered the optimization of the scanning path to ensure melting while avoiding overheating using a shape optimization approach. The shape of the scanning path is not restricted *a priori* while the part geometry is fixed. The steady state heat conduction equation is solved to estimate the temperature field when the heat energy is applied to the entire scanning trajectory. The path length is then minimized under the constraints of ensuring melting and a maximum temperature. A descent gradient method is applied to the scanning path represented as a curve discretised by iteratively updated nodes to improve the objective. The method is demonstrated on 2D numerical examples revealing computational efficiency. Identified challenges are the problem's non-convexity and dependence of the optimized path on the chosen initialization. This method has been extended to a concurrent optimization of the path and the topology of a single layer represented by a level set function for minimum compliance [502]. A clear relation between scanning path and layer's topology has been observed. Temperature constraints associated with the path optimization are satisfied partially by the adaptation of feature thicknesses in the layer's shape, since the outcome of the AM process is not only determined by the process parameters, but the part geometry also plays a crucial role [503]. This concurrent part-path optimization scheme is reminiscent of the deposition path optimization coupled to structural TO [463] described in the section about process aspects: orientation. However, while that approach included the anisotropy induced by the deposition direction, the current approach involves actual simulation of the LBPf process physics. More recently, the concurrent scanning path and layer topology optimization accounting for the time dependence of the moving heat source has been reported by [504]. However, it is expected that the computational cost of such a model will remain high, especially in 3D.

Finally, taking the integration of AM process physics into TO yet a step further, [505] have included the thermally induced evolution of the material microstructure in a TO process. By integrating a layer-by-layer thermal model to TO that evaluates the time spent during a critical heating and cooling cycle during AM, (material dependent critical temperature range for a high strength steel is typically between 800 and 500 C⁰) $t_{8/5}$ of all FE nodes were calculated in a continuous and differentiable manner, and the mechanical properties of the design can be estimated. TO for desired mechanical properties at a specific location was performed. To simplify the problem, one layer of deposition was considered, and the $t_{8/5}$ of that particular layer was controlled through TO. In the 2D discretized design domain, a structural load case was combined with the heat input representing the AM layer deposition at the top of the design domain. The heat input was applied for a specified period, and the structure was subsequently allowed to cool. The bottom boundary of the design domain acts as a heat sink to represent the substrate generally used in the WAAM process. It can be observed in Fig. 21 that

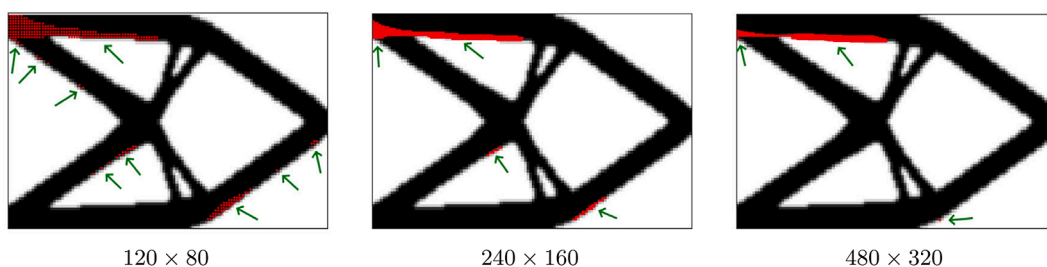


Fig. 18. Recoater collision for different domain discretisation. Red areas and green arrows indicate regions where collision occurs.

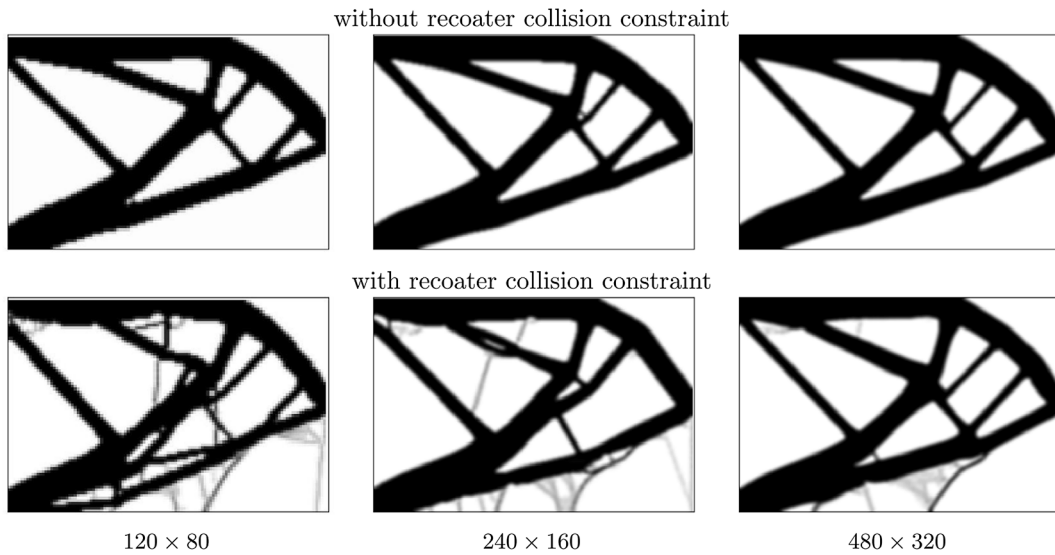


Fig. 19. Optimal designs for different domain discretization.

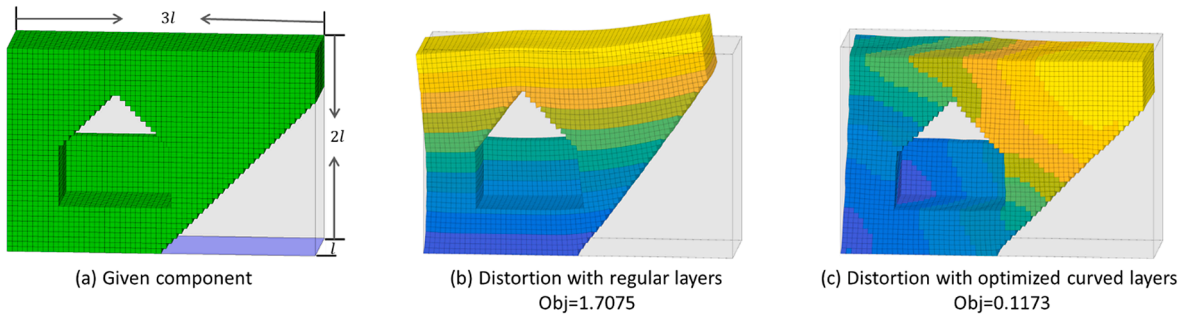


Fig. 20. Optimization of the fabrication sequence of (a) given component (b) with a deposition sequence along the vertical direction and (c) with an optimized deposition sequence for minimum part distortion due to the AM process [500].

to reduce the average $t_{8/5}$ in the control domain, the optimizer puts more material beneath the control domain to better facilitate heat evacuation. More material was placed beneath the control domain when the constrained value of $t_{8/5}$ was decreased.

3. Multi-physics modelling

3.1. Simulation of non-metallic additive manufacturing processes

Various manufacturing technologies have been developed to additively produce non-metallic components. Two of the most widely-used AM processes for non-metallic materials are material extrusion additive manufacturing and vat polymerization additive manufacturing (i.e., stereolithography, digital light processing (DLP) printing, and volumetric additive manufacturing). This subsection sequentially reviews numerical models developed for these two AM processes at the deposition-scale.

3.1.1. Material extrusion AM at deposition-scale

Material extrusion additive manufacturing (MEX) is an umbrella term for AM processes that apply extrusion to 3D print a part or a structure. General for all MEX processes is that a material is extruded through a nozzle and deposited on a substrate or a previously printed layer [506]. The material behaves like a fluid during deposition after which it solidifies or cures into a solid. Similar to most other AM processes, MEX produces one layer at the time and it is the accumulation of these 2D layers that eventually turns into a 3D object [507]. The first and most famous MEX process is Fused Deposition Modelling (FDM), see process illustration in Fig. 22, which was invented by S. Scott Crump in 1988 [508]. Here, a solid thermoplastic filament is led into the print head, where it is heated before it is deposited in the fluid state. Later, MEX has been applied to print other materials such as thermosets [509], concrete [510], ceramics [511], and hydrogels [512] to name a few. This subsection is subdivided into two parts, in which descriptions are provided of how materials behave inside print heads as well as during the deposition.

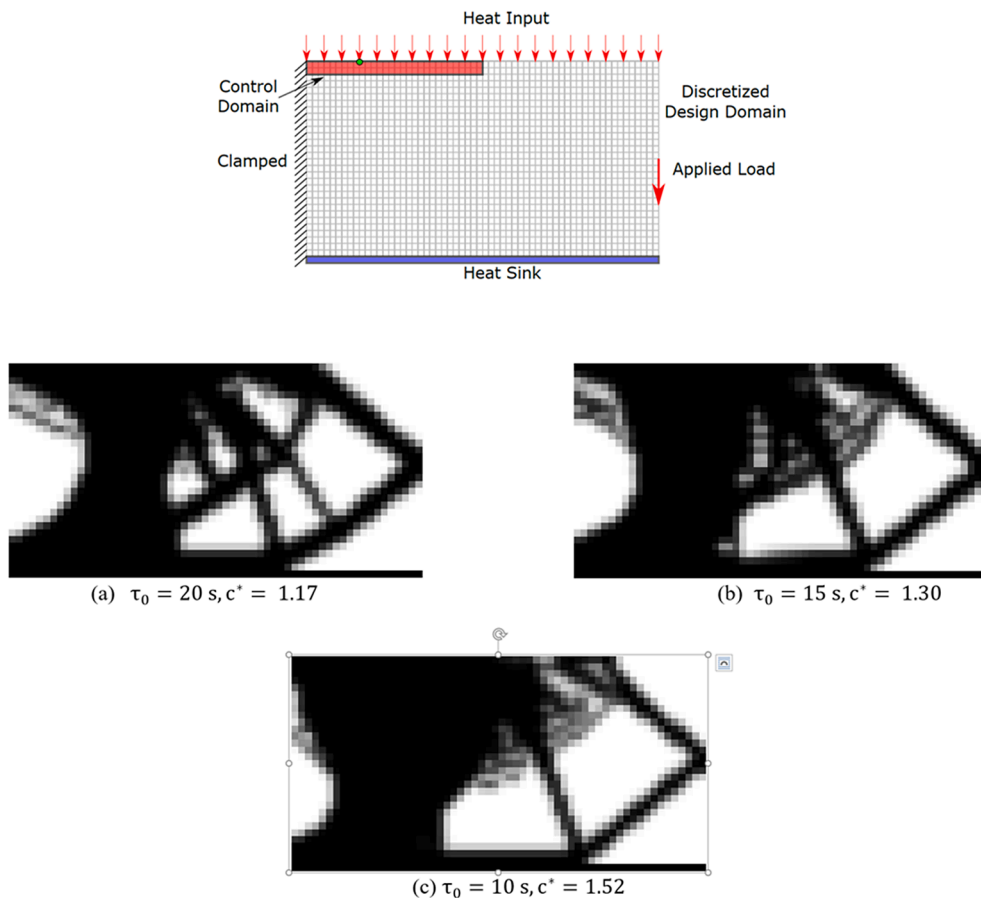


Fig. 21. Optimized design where the average cooling time in the control domain depicted is constrained to (a) 20 s, (b) 15 s and (c) 10 s.

3.1.1.1. Material behavior inside the print head. One of the most important aspects of MEX is the material behavior inside the print head as this has a direct influence on the print speed and geometrical fidelity [513]. There is no visible access to the printing head and there are limited possibilities for extracting physical properties from this key component; thus, multi-physics modelling is an important tool to advance MEX as it provides a virtual window into the process and this allows for mapping central field variables [514].

In filament-based MEX (i.e., FDM or Fused Filament Fabrication (FFF)), the solid part of the thermoplastic filament inside of the printing head acts as a piston on the fluid part of the filament, which enables the material to be extruded out through the orifice of the nozzle. The shape of the beads (or strands) that are extruded dictates the *meso*-structure formation [515], porosities [516], and width between beads [517]; all of which are paramount for the eventual mechanical performance of the component [518–520]. The restricting factors for the building speed in MEX are: 1) the maximum speed of the system positioning the printing head, 2) the maximum rate at which heat can be transferred in the hot-end (i.e., the part of the print head where the filament is melted, called the liquefier, and the extrusion nozzle), and 3) the maximum force the extruding system can apply on the filament [521]. The two latter are interlinked via the rheological behavior of the thermoplastic, which is both temperature- and shear-rate-dependent; thus, making the heat and mass transfer in the printing head a coupled and non-trivial problem to solve. In fact, several researchers have pointed out that there is a lack of understanding of the polymer flow inside the hot-end [522–524].

A number of analytical solutions have been derived to analyze the flow inside the print head [525–527]. The solutions apply different assumptions about the material behavior, the velocity profile in the print head, and the place at the hot-end where the thermoplastic liquefies. The analytical models are in relatively good agreement with experimental results at low filament feeding rates, but at higher feeding rates the models deviate from empirical findings [528]. In addition, the models are not able to predict the shift between the linear and non-linear extrusion regimes (i.e., stable and unstable extrusion). In the same study [528], a simple thermal model is developed to estimate this transition point by assuming that non-linear extrusion happens when the filament feeding rate is so high that the heating of the filament in the liquefier becomes insufficient and thus one ends up trying to force a solid filament through the contraction section of the hot-end. The model is able to predict the maximum feeding rate in the linear regime with high accuracy, when compared to experimental results made with both PLA and ABS [528].

With multi-physics models, on the other hand, it is possible to obtain a deeper and more detailed insight into the thermal and flow behavior of the material inside the hot-end [521,524,529–531] by solving the heat transfer equation together with the mass and momentum balance equations. When accounting for: 1) the liquefier is not fully filled (i.e., via free surface modelling), 2) the material

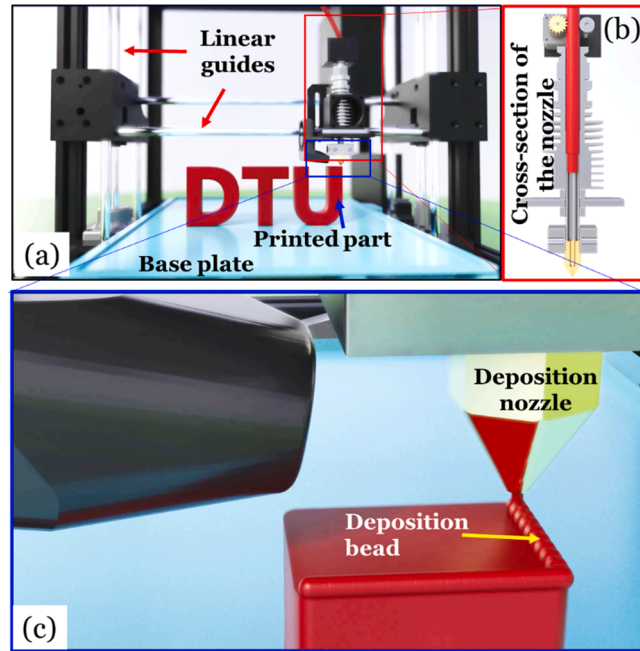


Fig. 22. Illustration of the FDM process given by an overview of the printer (a) and a snapshot of the cross-section of the nozzle (b) where the filament is heated as well as a zoom/in view of the deposition of a bead (c). The illustration is made by Sina Jafarzadeh.

behaves as a generalized Newtonian Fluid in the form of a temperature-dependent power-law cf. equations in Table 2, and 3) the heat transfer coefficient along the liquefier wall can be found by an inverse analysis; then such model is capable with reasonable accuracy to predict the feeding force at various feeding rates [532]. In Fig. 23, a snapshot of the simulated material behavior inside the print head is presented. The results of the numerical model support the assumption regarding the transition point between the linear and non-linear

Table 2

A brief overview of some of the rheological models used to simulate MEX.

<p>Generalized Newtonian Fluid in the form of the Bingham material modelThe constitutive stress tensor that is used in the momentum equation for a Generalized Newtonian Fluid is modelled as $\bar{\tau} = \eta \bar{S}$ Where η is the apparent viscosity and \bar{S} is the deformation rate tensor given by $\bar{S} = (\nabla u + \nabla u^T)$ Where u is velocity vector. For a Bingham material model, the apparent viscosity function yields $\eta = \frac{\tau_Y}{\dot{\gamma}} + \eta_p$ Where τ_Y is the yield stress and η_p is plastic viscosity. The strain rate magnitude, $\dot{\gamma}$, is calculated as $\dot{\gamma} = \sqrt{\bar{S} : \bar{S}}/2$</p>
<p>Generalized Newtonian Fluid in the form of a temperature-dependent power-lawThe apparent viscosity function for the temperature dependent power-law is modelled as $\eta = K(T_{ref})\dot{\gamma}^{n-1}H(T)$ Where K is the consistency index, T_{ref} is reference temperature, n is the power law index, T is the temperature, and $H(T)$ is the shift factor function defined as $\log H(T) = -\frac{C_1(T - T_{ref})}{C_2 + (T - T_{ref})}$ Where C_1 and C_2 are material dependent constants</p>
<p>Viscoelastic fluid with temperature dependencyFor a viscoelastic fluid, the constitutive stress tensor is decomposed into $\bar{\tau} = \bar{\tau}_V + \bar{\tau}_E$ Where $\bar{\tau}_V$ is the viscous stress component and $\bar{\tau}_E$ is elastic stress component. For a polymer this equation can be expressed as $\bar{\tau} = \bar{\tau}_S + \bar{\tau}_P$ Where $\bar{\tau}_S$ and $\bar{\tau}_P$ are the solvent and polymer stress contribution, respectively. The first can be modelled as $\bar{\tau}_S = \eta_S \bar{S}$ Where η_S is the solvent viscosity contribution. The polymer stress contribution, $\bar{\tau}_P$, can be written as $\bar{\tau}_P = \sum_{i=1}^n \bar{\tau}_{p,i}$ Where i is the mode index, n is the number of modes, and $\bar{\tau}_{p,i}$ is the polymer stress contribution of a single mode that can be calculated using the Giesekus differential viscoelastic model: $\bar{\tau}_{p,i} + \lambda_i \hat{\tau}_{p,i} + \alpha_i \frac{\lambda_i}{\eta_{p,i}} (\bar{\tau}_{p,i} \cdot \bar{\tau}_{p,i}) = \eta_{p,i} (\nabla u + \nabla u^T)$ Where λ_i is the relaxation time for each mode i, α_i is the mobility factor for each mode i, $\eta_{p,i}$ is the polymer viscosity contribution for each mode i, and $\hat{\tau}_{p,i}$ is the upper-convected time derivative of $\bar{\tau}_{p,i}$ given by $\hat{\tau}_{p,i} = \frac{D\bar{\tau}_{p,i}}{Dt} + u \cdot \nabla \bar{\tau}_{p,i} - \bar{\tau}_{p,i} \cdot \nabla u - \nabla u^T \cdot \bar{\tau}_{p,i}$ The temperature dependency on the rheological parameters can be modelled by $\lambda_i(T) = \lambda_i(T_{ref}) \cdot H(T) \eta_{p,i}(T) = \eta_{p,i}(T_{ref}) \cdot H(T) \eta_S(T) = \eta_S(T_{ref}) \cdot H(T)$</p>
<p>Elasto-visco-plastic material modelThe constitutive stress tensor is also for this material model given by $\bar{\tau} = \bar{\tau}_V + \bar{\tau}_E$ The viscous stress is given by $\bar{\tau}_S = \eta_V \bar{S}$ Where η_V is the viscosity of the material. In an Eulerian framework, the elastic stress tensor of the unyielded material can be written as a partial differential equation: $\frac{D\bar{\tau}_E}{Dt} + \nabla \cdot (u \bar{\tau}_E) - (\bar{\tau}_E \cdot \bar{W} + \bar{W}^T \cdot \bar{\tau}_E) = G \bar{S}$ Where \bar{W} is the vorticity tensor: $\bar{W} = 1/2(\nabla u - \nabla u^T)$ The material yields based on von Mises yield criteria, and the equivalent von Mises stress is given by: $\tau_{vM} = \sqrt{\frac{2}{3} II_{\bar{\tau}_E}}$ Where $II_{\bar{\tau}_E}$ is the second invariant of the elastic stress tensor. The material yields when $\tau_{vM} \geq \tau_Y$ Where τ_Y is the yield stress of the material. The elastic stress component of the yielded material is scaled by: $\bar{\tau}_E = \min\left(1, \frac{\tau_Y}{\tau_{vM}}\right) \bar{\tau}_E^*$</p>

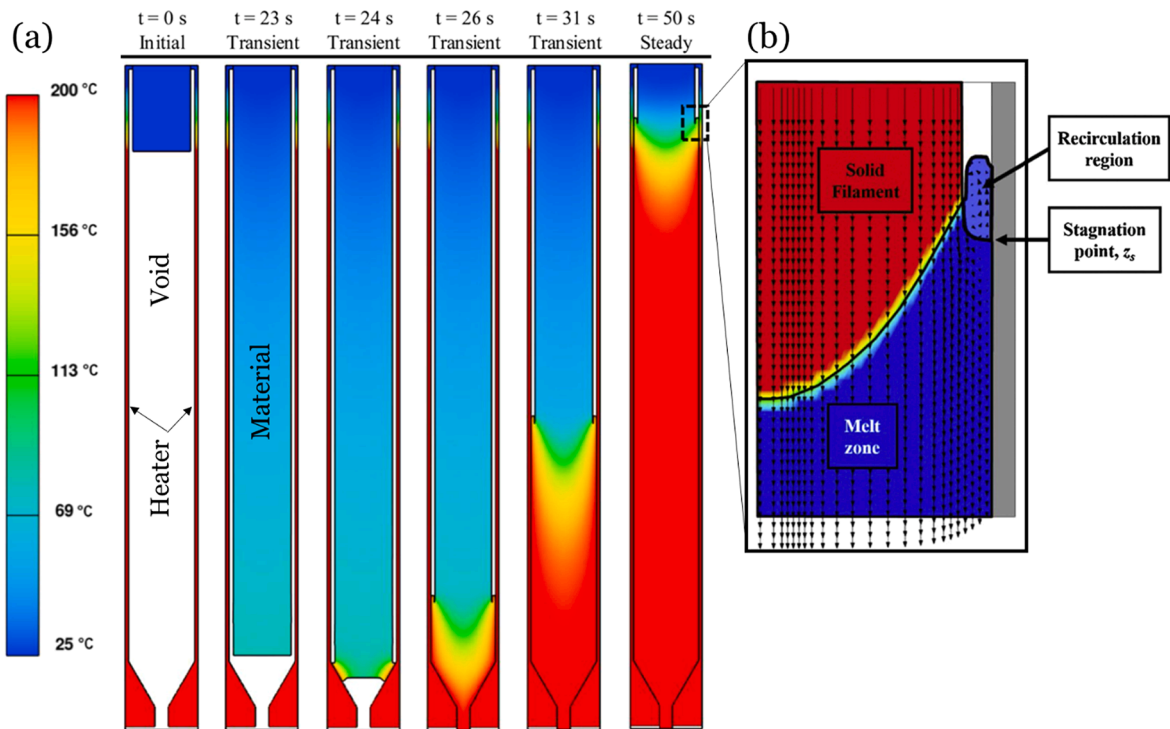


Fig. 23. Simulation of the material behavior inside the print head during MEX. (a) Temperature profile of the material at different times. At $t = 50$ s, the simulations reach steady state. (b) Sketched zoomed of a part of the hot-end where the material changes from solid to fluid. The zoom also shows a material recirculation region and a stagnation point where the vertical velocity component changes sign. The figure is adapted from [532].

extrusion regime that is applied in the analytical model in [528]. The numerical model also captures the trends seen in experiments when varying the liquefier temperature and geometry, but there are differences in the absolute feeding force values [532]. In another study, it is found that more accurate numerical results can be obtained when applying a temperature-dependent viscoelastic model instead of a Generalized Newtonian Fluid modelled as a temperature-dependent power law [533], see rheological equations in Table 2. This model also highlights how the feeding force can be reduced by choosing the right liquefier diameter. In future research, it would be interesting to develop a model that both accounts for the thermal aspects, viscoelasticity and extensional viscosity as well as free surface modelling, as this potentially could further improve the numerical predictions. Such a model will have the potential to be exploited to find optimal hot-end designs.

3.1.1.2. Material flow during deposition. Slicing software assumes simple bead geometries (e.g., elliptical or rectangular) when producing print paths for full-scale components. However, it is essential to have information at the mesostructure level in order to understand and predict the mechanical properties of the component [518–520]. Computational fluid dynamics (CFD) models have thus been developed to simulate the material flow during deposition with the objective of predicting the local bead geometry [534,535]. A 3D CFD model that assumes an isothermal Newtonian fluid and a creeping laminar flow is able to resolve the shape of the cross-section of single thermoplastic beads produced on a desktop printer with high accuracy [30]. The numerical results of such a model also underline that the cross-section of the bead is dominated by two non-dimensional parameters: 1) a normalized gap: the diameter of the orifice of the nozzle divided by the gap distance between the nozzle and substrate, and 2) the velocity ratio: the printing speed divided by the extrusion velocity [536]. The shape of the cross-section of the beads varies from circular, when printing fast with a large gap, to rectangular with round edges when printing slow with a small gap, see Fig. 24 (a)–(b). The latter, especially, deviates from the idealized cross-sections. The numerical model is also capable of predicting the printing pressure on the substrate. The pressure changes both magnitude, distribution, and position depending on the two mentioned non-dimensional parameters; e.g. when depositing with a low normalized gap and velocity ratio, the distribution of the printing pressure is relatively axisymmetric with the highest pressure centered below the orifice of the nozzle [536].

Another strength of 3D CFD models simulating material flow during deposition is that they can assist in finding an improved motion planning and deposition strategy at corners [537], see Fig. 24 (d). The simulations show that the underfill and overfill, which are often seen locally in corners, can be reduced with the right extrusion- and acceleration-sequence [538]. However, the numerical results also highlight that with a circular nozzle, it is inevitable not to end up with some rounding of material in the corners due to the round edges of the cross-section of the deposited bead. An example of a corner defects is illustrated in Fig. 24 (d). Obviously, these models are not able to simulate the printing of entire components, but they can simulate multi-bead prints (i.e., both inter- and interlayer connected beads) within a reasonable time [539]. Numerically a representative volume element (RVE) of the meso-structure can be obtained by

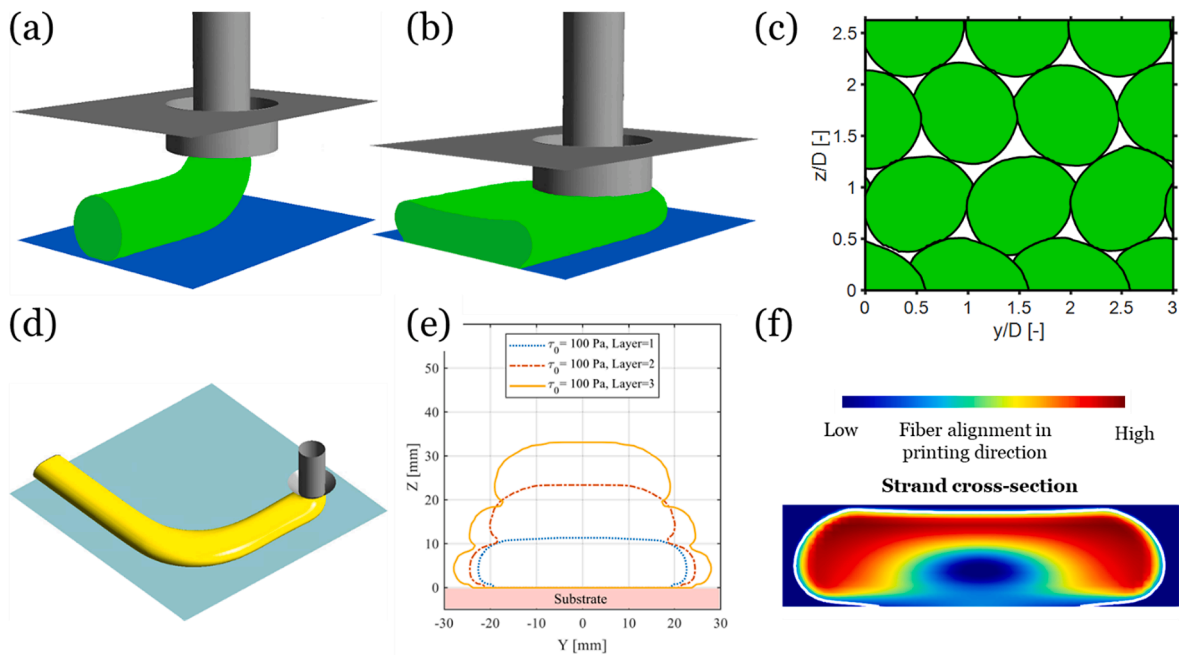


Fig. 24. Simulations of material flow during MEX deposition. (a) Printing with a large normalized gap and velocity ratio [30]. (b) Printing with a low normalized gap and velocity ratio [30]. (c) Mesostructure when printing with a skewed deposition strategy [540]. (d) Material deposition during corner printing - adapted from [538]. Multi-layer wet-on-wet printing [541]. (f) Fiber orientation in a bead - adapted from [542].

simulating the deposition of a bead and subsequently considering this bead as a solid when printing the next bead [540], see Fig. 24 (c). Although this methodology does not account for the new beads' effect on the previously deposited bead, it still provides numerical results that are comparable to experimental findings. The attractiveness of these simulations is that they predict porosities, inter- and intra-layer bond line densities as well as surface roughness.

3.1.1.3. Thermoset and concrete MEX. In contrast to thermoplastic printing where the material solidifies quickly after it has been deposited, MEX of thermosets or concrete can often be classified as wet-on-wet printing or wet-on-semisolid printing. This means that material is deposited on top of a previously printed layer that is either not changing over time (in terms of rheology) or is not fully solidified yet and thus still can deform under the force applied by the newly deposited layer [543]. In this regard, it is important to highlight that even a small deformation in a layer can accumulate over a number of layers and lead to substantial alteration of the cross-section of subsequent layers, if not taking into account in the tool path planning [544]. CFD models are able to quantify the stability and deformation in multi-layer MEX prints [541], see Fig. 24 (e). Stable printing is achieved when the material can withstand the hydrostatic pressure as well as the extrusion pressure. Simulations of wet-on-wet printing with a Bingham material show that by increasing the yield stress one can reduce the deformation in the print, while an increase in plastic viscosity negatively affects the stability, as it will increase the extrusion pressure. In addition, increasing the printing speed or reducing the extrusion velocity leads to improved prints in terms of stability as the extrusion pressure reduces. Even though deformations can be reduced, it is difficult to fully eliminate any deformation when printing wet-on-wet – especially when printing many layers. Therefore, the material needs to develop a certain yield stress in order for the print to be stable. A conservative estimate of this yield stress can be obtained by performing wet-on-dry simulations [541], while wet-on-semisolid models can provide a more nuanced evaluation of the needed yield stress [545]. Specifically for 3D concrete printing (3DCP), both particle finite element and finite volume based CFD models have been developed [546–548]. A quite good agreement between numerical and experimental 3DCP results is achieved when applying an elasto-viscoplastic material behavior [549], see rheological equations in Table 2. This is valid both for single layer beads produced with different processing parameters and for multi-layer prints [550]. An interesting avenue to follow is to exploit these models to come up with printing strategies for how to integrate steel reinforcement bars with 3DCP [551]. This is important, because most printed concrete structures, as of right now, are not reinforced and therefore not load-carrying, and this limits their applicability.

3.1.1.4. Fiber reinforced MEX. For some applications, it is an attractive option to include fibers in the material that is deposited via MEX as it enables anisotropic mechanical and thermal properties of the final component [552,553]. Simulating the fiber flow during deposition can ensure that fibers end up with the intended orientation [554]. Several numerical methods have been employed to simulate fiber orientation during MEX: the finite element method (FEM) [555–557], finite volume method (FVM) [558], and smooth-particle hydrodynamics [559–561]. In order to quantify the fiber orientation, continuum models typically apply Advani and Tucker's tensor approach [562], which is based on the famous Jeffery model that considers an ellipsoid in a Newtonian fluid [563]. The tensor

approach provides a macroscopic statistical measure for the fiber orientation in the three directions, which enables the method to cover a relatively large volume without becoming too computational heavy. In Fig. 24 (f), simulation results of the fiber orientation in a deposited bead are presented when applying this approach. Information on a local fiber level can also be retrieved e.g. by usage of the discrete element method [564], but that comes at a computational expense. The fiber orientation MEX models have a huge potential in producing born qualified composite components, but these numerical models are yet to be validated against experimental MEX results, which must be considered the first point on the to do list for researchers working within this field.

3.1.2. Vat photopolymerization at the deposition-scale

The concept of additive manufacturing first emerged with vat photopolymerization (VPP) [565]. The term VPP refers to a group of additive manufacturing methods in which a liquid photopolymer inside a vat is exposed to the curing light -mostly ultraviolet (UV) and near-UV- and solidifies to form the desired geometry. The photosensitive liquid contains monomers, oligomers, and photo-initiators. Upon exposure to the curing light, photo-initiators release free radicals that trigger a chain of reactions inside the resin and crosslinks the monomers together to form polymers.

Depending on how the photopolymerization process in the photo-sensitive resin is achieved, VPP can be categorized into three groups. The desired part can be formed in a point-wise manner, in which the points inside the resin are cured one after the other, as in Stereolithography (SLA) and two-photon polymerization (2PP). It can be formed in a plane-wise manner, in which each plane or cross-section of the whole geometry solidifies at the same time by receiving 2D light intensities, as in digital light processing (DLP) and continuous liquid interface production (CLIP), or the whole geometry can form at the same time as in volumetric additive manufacturing (VAM) and Xolography.

To further improve the competence of the additive manufacturing methods, it is important to better understand the physics behind the process and to optimize the different parameters playing role in the process. Similarly, a shorter print time demands a combination of optimized parameters. Furthermore, due to the part shrinkage in photopolymerization, it is still challenging to acquire the as-designed shape. Theoretical and numerical studies are efficient yet unexpensive methods that can improve the efficacy of VPP processes. Finally, model-based control loops can be incorporated into the VPP fabrication setups to improve their efficacy and reproducibility. In what follows, the models that have been developed in the field of vat photopolymerization additive manufacturing will be discussed in four sections, after a brief introduction in each section.

3.1.2.1. Photopolymerization. During the photopolymerization (PP), when the resin is exposed to the curing light, the photo-initiators inside the resin decompose to free radicals (Table 3-Eq. (1)). The free radicals, which are not stable, attack the monomers, react with them, and convert them to radical monomers (Table 3-Eq. (2)). The first and second stages are usually called photo-initiator decomposition and initiation step, respectively. The radical monomers, in turn, react with other monomers and grow in a stage that is called propagation, shown in Table 3-Eq. (3). The growth of polymeric chains can be terminated through combination or disproportionation mechanisms in the termination stage. While in combination, one inert chain will be formed after the reaction, two inert chains are the result of disproportionation mechanism [566]. Both of these mechanisms are usually active in the termination stage, however, it has been shown that combination is dominant for acrylate monomers [567] (Table 3-Eq. (4)–(6)).

Acrylates, which contain a vinyl group, are the most common materials used in VPP. An inhibitor or quencher such as molecular oxygen for acrylates have a much faster reaction rate with radicals compared with that of monomers with radicals. So, as long as the inhibitor is locally present in the resin, the monomers have little chance of reacting with radicals [568], and photopolymerization process cannot proceed (Table 3-Eq. (7)–(8)). In Table 3, PI , M , R^* , P^* , \bar{P} , and \bar{R} stand for the photo-initiator, monomer, primary radical, polymeric radical, stable polymer molecule, and stable radical, respectively. k_d , k_i , k_p , k_t , k_o are the reaction constants for the photo-initiator decomposition, initiation, propagation, termination and inhibition reactions, respectively. The evaluation of these constants are further discussed in [566,569,570].

Different approaches have been adopted to model the photopolymerization process [570]. In continuous approach, reaction equations are defined and solved to track the concentration of each species introduced in Table 3. On the other hand, in the stochastic and discrete models, which can be spatial (lattice-based) or non-spatial, stochastic methods such as Monte Carlo method are used to simulate the reactive physics on the basis of the possibility of each event. Here, only the continuous models are explained.

Table 3
Stages and reactions in an acrylate-based photopolymerization process.

Stage	Expression	Eq. NO.
Photo-initiator decomposition	$PI \xrightarrow{k_d} 2R^*$	(1)
Initiation	$R^* + M \xrightarrow{k_i} P^*$	(2)
Propagation	$P^* + M \xrightarrow{k_p} P^*$	(3)
Termination	$R^* + R^* \xrightarrow{k_t} 2\bar{R}$	(4)
	$P^* + P^* \xrightarrow{k_t} \bar{P}$	(5)
	$R^* + P^* \xrightarrow{k_t} \bar{P}$	(6)
Inhibition	$R^* + O_2 \xrightarrow{k_o} \bar{R}$	(7)
	$P^* + O_2 \xrightarrow{k_o} \bar{P}$	(8)

Table 4
Set of ODEs (Eq. (1)–(6)) to model the reactions. The 7th equation also accounts for the oxygen diffusion.

$\frac{d[PI]}{dt} = -k_d[PI]$	(1)
$\frac{d[R^*]}{dt} = 2k_d[PI] - k_i[M][R^*] - 2k_t[P^*][R^*] - 2k_r[R^*]^2 - k_o[O_2][R^*]$	(2)
$\frac{d[M]}{dt} = -k_i[M][R^*] - k_p[M][P^*]$	(3)
$\frac{d[P^*]}{dt} = k_i[M][R^*] - 2k_t[P^*]^2 - 2k_r[P^*][R^*] - k_o[O_2][P^*]$	(4)
$\frac{d[\bar{P}]}{dt} = k_t[P^*]^2 + 2k_r[P^*][R^*] + k_o[O_2][P^*]$	(5)
$\frac{d[O_2]}{dt} = -k_o[O_2][R^*] - k_o[O_2][P^*]$	(6)
$\frac{d[O_2]}{dt} = -k_o[O_2][R^*] - k_o[O_2][P^*] - \nabla \cdot (D_o \nabla [O_2])$	(7)

Jakobs [571] presented one of the most fundamental models for PP process which is still in use and has proven to be fast and efficient. Considering a gaussian beam for SLA that follows the Beer-Lambert law, he obtained simple relations for the actinic energy within the photopolymer, the cure profile, and the cure depth. While Jakobs' model, also known as energy exposure threshold model, is simple and efficient to provide approximate predictions about the PP outcome, it does not consider the kinetics of the reactions, it cannot predict the impact of many reaction parameters, and it is deficient when high accuracy is important [569]. Afterwards, many researchers have tried to somehow account for the reactions that take place in the photopolymerization process. Based on the simplified kinetics of the photopolymerization process, Lee et al. [572] developed a single ordinary differential equation (ODE) to relate the extent of polymerization, which is calculated from monomer concentration, to the properties of the resin and characteristics of the laser. After verifying the results of the model with experiments, they concluded that for each energy dose of the laser, there exists an optimum photo-initiator concentration that optimizes the cure depth. Later studies on PP [570,573–575] have solved a set of ODEs for the concentrations of the species that are present in the PP process, Table 4 - Eq. (1)–(6). Each ODE presents an equation for the rate of change of a specie's concentration based on its production or consumption in the different reactions that were introduced in Table 3. In some studies, Eq.6 in Table 4 has been modified to account for the diffusion of oxygen, shown in Eq. (7). In the equations of Table 4, $[X]$ represents the concentration of component X, in which X is one of the species introduced in Table 3.

Based on the equations in Table 4, Jariwala et al. [573] developed a 2D model to simulate the VPP process for a micro-stereolithography printing method. By comparing their results with experiments, they showed that their model can effectively predict the cured depth until 70 μm . Some other studies have further extended the model to incorporate the diffusion of the species and thermal effects [566,569,576]. By employing this extended model, Goodner and Bowman [566] showed that the presence of the heat generation can accelerate the PP process and increase the conversion degree close to 100 percent. Using the same framework, O'Brien and Bowman [576], modeled a resin vat that was exposed to air from the top. They studied how the thickness of a thin film, in which the photopolymerization is inhibited, changes with the concentration of oxygen and initiation rate.

Recently, a few studies have targeted the full VPP process. Wu et al. [577] combined the first-order chemical reactions, shown in Table 4, with a multibranch nonlinear viscoelastic model to simulate the property variation during curing. After validating their simulation results with experiments, they studied how some factors such as initiator concentration and light intensity can affect the printed material properties. Westbeek et al. [578] put forth a 3D chemo-mechanical model to predict the output shape of the DLP process. In their framework, they considered a rectangular gaussian function for each pixel, instead of a circular one which is common in SLA. By considering the total strain to be composed of the elastic and chemical strains and using a simple phenomenological function to model the photopolymerization, they produced results comparable with experiments, seen in Fig. 25 (a). In a similar fashion, Rehbein et al. [579] used a phenomenological function for photopolymerization and a viscoelastic model for the rheological behavior to conclude that ambient temperature and light intensity play an important role in crosslinking reactions, with an increase in both of them will expedite the photopolymerization process. In a 1D model taking advantage of a simple function to account for the kinetics in a VPP process, Classens et al. [580] decomposed the total strain into thermal, chemical, and elastic ones. They implemented the relevant boundary conditions to complete their model and used it in a state-space control paradigm capable of controlling the material properties in VPP.

3.1.2.2. Point-wise VPP. In SLA, shown in Fig. 25 (d), a platform is immersed inside the photo-resin and a laser scans the resin surface, curing point-by-point to form a layer equivalent to a section of the desired geometry. Depending on the configuration of the setup, i.e. top-down or bottom-up, the platform, with previously formed layers stuck to it, moves upward or downward with an amount equal to the height of a layer, to allow the fresh resin fill the space so that a new layer can be printed on top of the previous one. This process continues until the whole shape is formed [565,583,584].

In 2PP, two focused femtosecond near-infrared (NIR) laser beams target a point inside the resin and trigger the photopolymerization process in that point. Compared to other VPP methods, 2PP can provide a higher resolution up to 100 nm. Also, compared to SLA, which can only print on the surface of the resin vat, 2PP can print inside the resin volume because of the low absorptivity of the resin towards NIR light [583–585].

Most of the simulations on stereolithography have already been pinpointed under the broad section of photopolymerization. Some

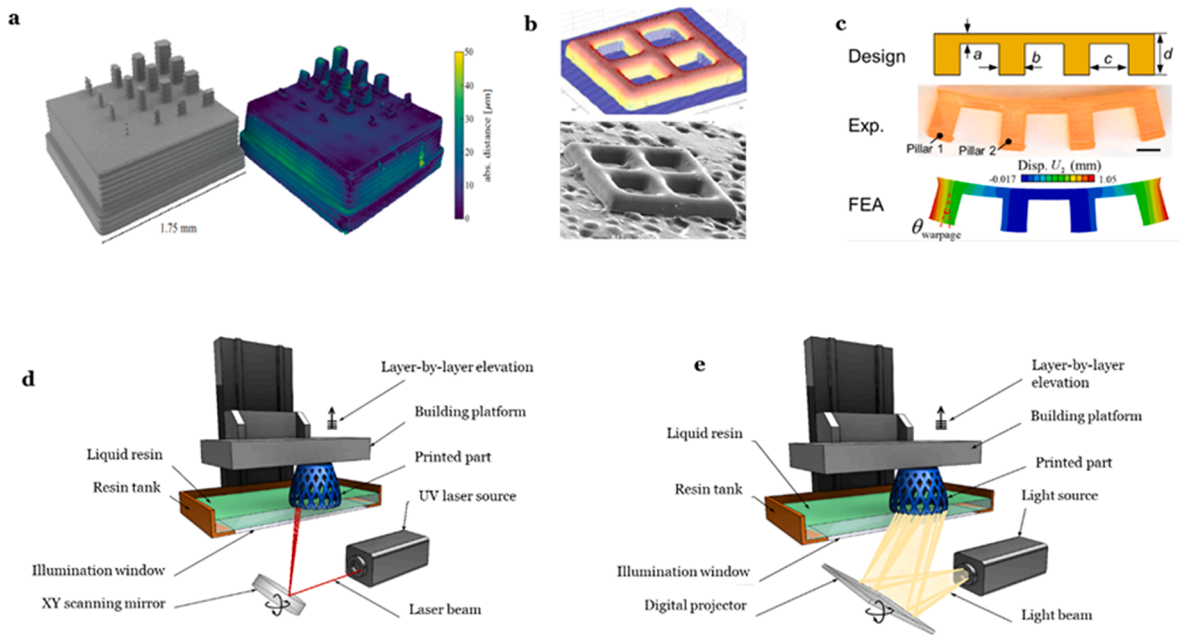


Fig. 25. a- comparison between the experimental and numerical results in which the left image is the simulation result and the color bar of the right image illustrates the discrepancy between the experiment and the simulation for a DLP setup [578]. b- comparison between fabrication (top) and simulation (bottom) of a lattice pattern made with projection-based stereolithography [581], c- comparison between design, fabrication, and finite element simulation of a bridge-like structure made with DLP [582]. d- SLA configuration [565], and e- DLP configuration [565].

more recent studies are brought here. Employing photopolymerization equations backed with experiments for dental materials, Gao et al. [586] implemented a layer-by-layer stereolithography model capable of providing the print preview. Wang et al. [587] developed an elastoplastic constitutive model to study the effects of the printing angle and layer thickness on the elastic modulus and ultimate tensile strength of the final products. They reported that a rise in the layer thickness reduces the elastic modulus and ultimate tensile strength. Additionally, an increase in the printing angle from 0 to 40° leads to an increase in ultimate tensile strength and a decrease in elastic modulus. This effect is reverse for the print angle from 40° to 90°.

3.1.2.3. Plane-wise VPP. Unlike SLA, in DLP, which is also known as mask projection-based vat polymerization, a whole layer of the photo-resin is printed at a time by exposing it to the UV light coming from a projector, see Fig. 25 (e). Accordingly, DLP, compared to SLA, provides a higher speed, while compromising resolution and printable area, which are limited by the resolution and size of the digital micro-mirror device [565,583,584,588]. In DLP, when a new layer is formed between the illumination window and the previous layer, it sticks to the window. To tear it apart, the platform moves the printed part away from the window all the way to the end of the resin container and then brings it back to have a distance of one layer-height from the projection window. This process takes a lot of time. CLIP method, however, taking advantage of a dead zone, in which oxygen concentration is high and the inhibition effect hinders the photopolymerization, considerably reduce the force to separate the newly formed layer from the illumination window. Accordingly, in CLIP the extra up and down movement of the platform is omitted and it continuously moves upward, leading to its higher speed, 25 to 100 times compared to DLP [565,574,584,589].

Some numerical studies have targeted the plane-wise VPP to further optimize these processes. Wang et al. [590] employed a coarse-grid molecular dynamic approach to shed light on the factors affecting the quality of the CLIP method. Taki [574] numerically studied the photopolymerization in the CLIP method, without considering the thermal and flow effects, and explored how the inhibition effect can influence the results to predict the final shape. Modeling the photopolymerization process in a CLIP setup, Wang et al. [575] explored different factors such as PDMS film's features and substrate's micropore array characteristics on the thickness of the inhibition zone. Using energy threshold theory, Kang et al. [581] proposed a model to predict the printed shape during the projection-based stereolithography. They compared the results of their simulations with experiments for a lattice pattern shown in Fig. 26 (b). Combining experiments, theory, and simulation, Zhang et al. [582] developed a model to capture the residual stress and shape distortion that are induced by volume shrinkage in the DLP process. They carried out experiments to measure the constants of the reactions and cure-induced property variations. After solving the equations in Table 4 to model the photopolymerization stage, they used the degree of cure obtained from this stage in their finite element code to find the stresses and strains. Their simulation and experimental results, shown in Fig. 26 (c), were consistent. Hofstatter et al. [591] developed a finite element model to predict the fiber-orientation during VPP process. Based on the results of their model, they suggested a design for a top-down DLP device to achieve better mixing of fibers in the building area.

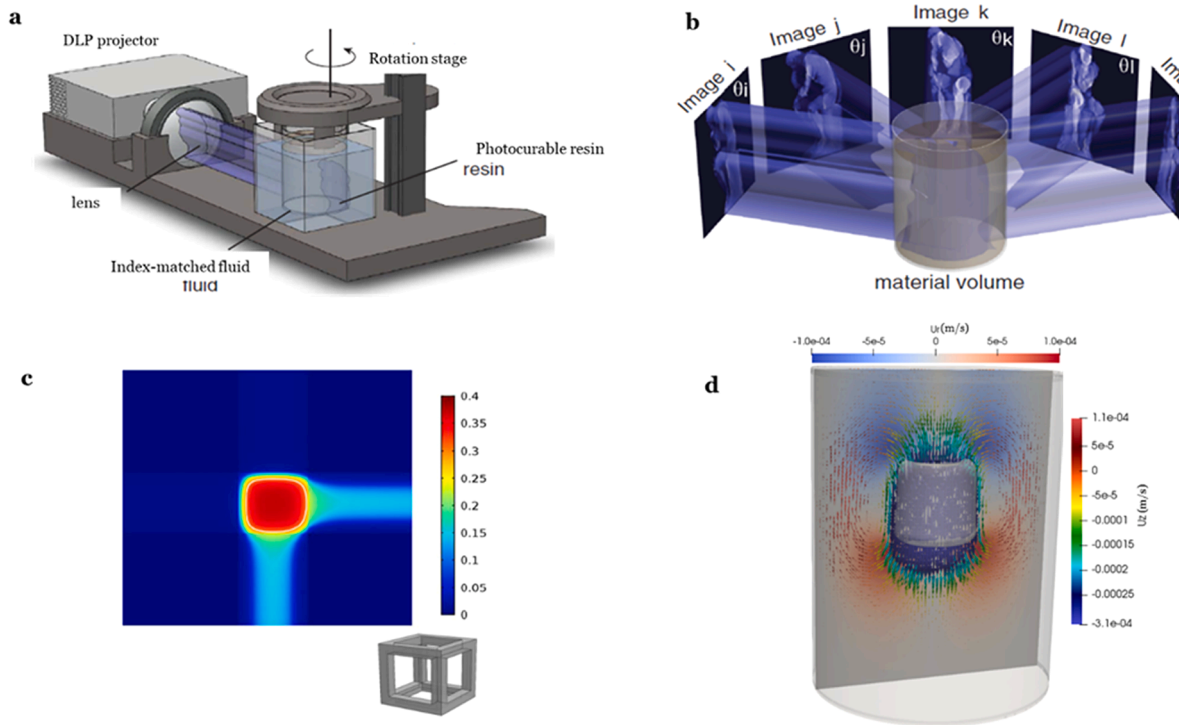


Fig. 26. A & b- principle of vam [595]- c- degree of polymerization in the domain for a semi-3D simulation of the three-beam holographic method to obtain the structure shown in the inset [598]. d- simulation of printed part sedimentation in VAM [599].

3.1.2.4. Volumetric VPP. So far, two methods have been proposed to simultaneously build the whole volume of the printed part. In the first method, shown in Fig. 26 (a) and (b), which is called computed axial lithography (CAL) and also volumetric additive manufacturing (VAM), the photo-sensitive resin is constrained within a cylindrical container that is rotating at a constant rotational velocity. Based on the principles of the computed tomography, intensity-modulated images are generated from the input geometry, which are illuminated on the resin, synchronized with its rotation rate. Due to the inhibition effect that intentionally exist in the resin, the energy from each image is not enough to cure the resin, rather it is the accumulated energy from different frames that can develop the required energy dose in the shape of the desired geometry [592–596].

Xolography is another volumetric method, in which intersecting light beams from different sources form the geometry. The first source, creating a thin light sheet, excites the photo-initiators within this thin film, and convert their state from inactive to a latent one. At the same time, the other light source with a different wavelength illuminates a section of the desired geometry into the domain, which can be absorbed only by the photo-initiators in the latent state, to start the photopolymerization process. The movement of the first light source is synchronized with the sectional image projected by the second light source to create the whole geometry [597].

Since volumetric VPP is quite a new field, there are very limited numerical simulations on this topic. Shusteff et al. [598] worked on a precursor of VAM method, in which the 3D geometry formed based on three intensity-modulated projections of the desired geometry from the three main directions. They also conducted a numerical simulation to further explore the factors that can affect the final shape quality. In their semi-3D finite element simulation, they modeled the photopolymerization process and explored the effects of light intensity and inhibitor concentration on the sharpness of the edges of the geometry. Fig. 26 (c) demonstrates the degree of polymerization for the structure model shown in the inset of this image. Using a finite volume approach, Salajeghe et al. [599] investigated the different parameters affecting the sedimentation, a potential threat in VAM (see Fig. 26 (d)). Later, exploiting a similar approach, they explored the effects of cure-induced heat generation on the sedimentation of the printed part, and explained that the thermal gradients during the photopolymerization process can mitigate the sedimentation [600].

3.2. Simulation of metallic additive manufacturing processes

Powder bed fusion (PBF) and directed energy deposition (DED) are the two most widely-used metal additive manufacturing (MAM) processes [601] and as a result, the majority of the research works, including both numerical and experimental studies, are related to these two processes. Therefore, we will cover the state-of-the-art literature mainly for these two MAM processes and go through their relevant physics and modelling frameworks. MAM processes started from arc welding of primitive multi-layer structures in the 1930 s [602] and evolved into welding based additive manufacturing in the 1960 s and 1970 s [603]. Two separate patents were published in 1981 and 1982, detailing the concept of PBF-based [604] and DED (wire-based) [605] MAM processes, respectively. Whereas the concept of DED at present is more or less the same as documented by [605], current modern PBF machines are based on a later patent

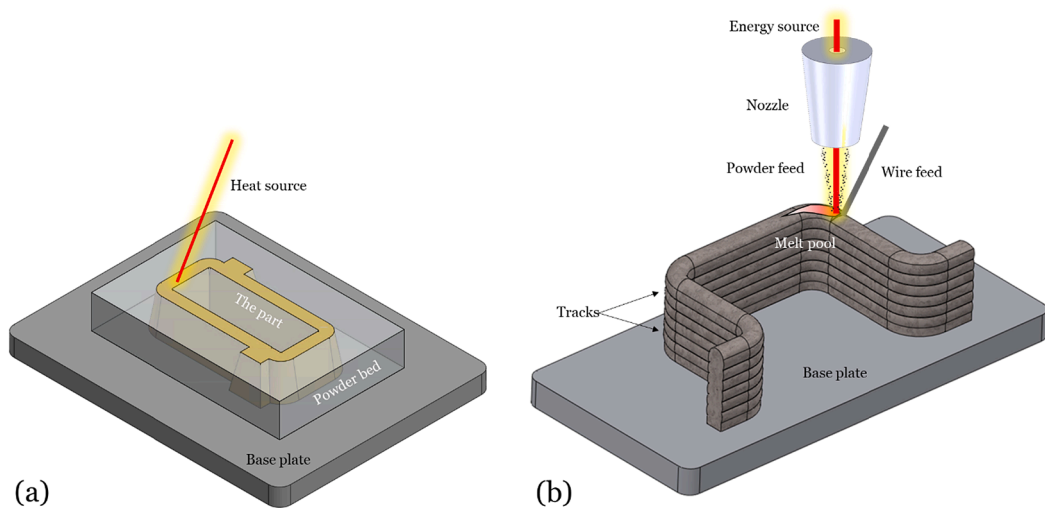


Fig. 27. (a) A schematic of PBF and (b) DED processes. Note that in (b), the feedstock is both in the form of powder and wire.

written in the late 1990 s by [606].

A schematic view of the PBF and DED processes are shown in Fig. 27 (a) and (b), respectively. In the PBF process, initially the powder table moves a certain distance vertically upwards and at the same time the build table moves almost the same distance and in the opposite direction. Then in the third step, the coating tool shown in Fig. 27 (a) translates the powder layer lying on the powder table horizontally and onto the build table. After this, the energy source starts heating specific coordinates which are constantly being provided by the PBF machine computer and based on the G-code generated by the machine's software. In both electron beam PBF (EB-PBF) and laser PBF (L-PBF), the input power must be sufficient to heat up the powder particles above their melting point. After the first layer of the part is solidified and manufactured, a few seconds of cooling time is allocated allowing for the overall temperature of the component to decrease and therefore to reduce the residual heat effect.

As opposed to the step-wise PBF processes, in DED, material deposition and melting occur at the same time, meaning that the energy source heats up the feedstock material while it is being delivered to the deposition zone. Similar to PBF, there are several types of input energy sources ranging from a massively-used laser beam (L-DED) [607,608], to electron beam (EB-DED) which requires a vacuum build chamber in the same way as the EB-PBF process and plasma arcs [609]. Another way of sub-categorizing DED is based on the type of feedstock. The feeding material could be in the form of powder, wire or combination of powder and wire, see Fig. 27 (b).

During the material deposition in MAM, several physical phenomena occur simultaneously and within very short time-scales. Melting and solidification, evaporation, ablation, thermo-capillarity, surface tension, laser-material interaction, turbulent flow, laser attenuation, grain growth and nucleation are just some of these taking place while the material is being deposited in MAM. Furthermore, these phenomena have direct impact on both the involved fluid dynamics as well as heat transfer within the liquid melt pool during the process and thus they can affect the final mechanical, microstructural and surface properties to a large extent.

The coexistent of these physical phenomena, makes MAM a very complex and delicate process to control and therefore even a slight lack of balance between these physics, which in essence originates from an improper selection of the input process parameters, could lead to a highly unstable process which is virtually impossible to control. An unstable process could potentially result in unwanted defects that disqualify a component for its final use, defects such as cracks, surface irregularities, porosities, overheating, anisotropic microstructural and mechanical properties, inclusions and deformations see Fig. 28.

These potential defects obviously link closely to the long list of input process parameters available for MAM processes [610] and it is in general possible to optimize the quality of the manufactured components and mitigate most forms of possible defects. Going one step further, it is possible to make use of these input parameters as a means to tightly control the deposition process and therefore pave the way for achieving a part with site-specific tailored properties (density, bulk morphology, microstructure, etc.).

It is currently very well established in literature that advanced numerical simulations are very useful for predicting the final properties of a component made by MAM [611], as opposed to the time- and material-consuming trial-and-error qualifications [45] which is currently well accepted in industry. Thus, advanced high-fidelity numerical simulations play a pivotal role in the overall picture of the holistic computational design of AM components and these process models can be used to manipulate the process in such a way that a part with targeted location-specific properties can be manufactured. An example of the application of high-fidelity simulations of the L-PBF process is given in Fig. 29 where it is shown that MAM simulations can predict important phenomena such as microstructures, material morphology and porosities, surface conditions, powder denudation, overhang defects, etc.

However, despite the massive increase in the computational power over the past decade, it is still not feasible to carry out a so-called full-scale, full-physics simulation of MAM, meaning a simulation that at the same time can capture all the physics and at all scales, and this is due to the highly prohibitive computational requirements that such a hypothetical simulation still would pose. This is why goal-oriented numerical simulations are typically used to study and investigate a certain aspect of a given MAM process. These

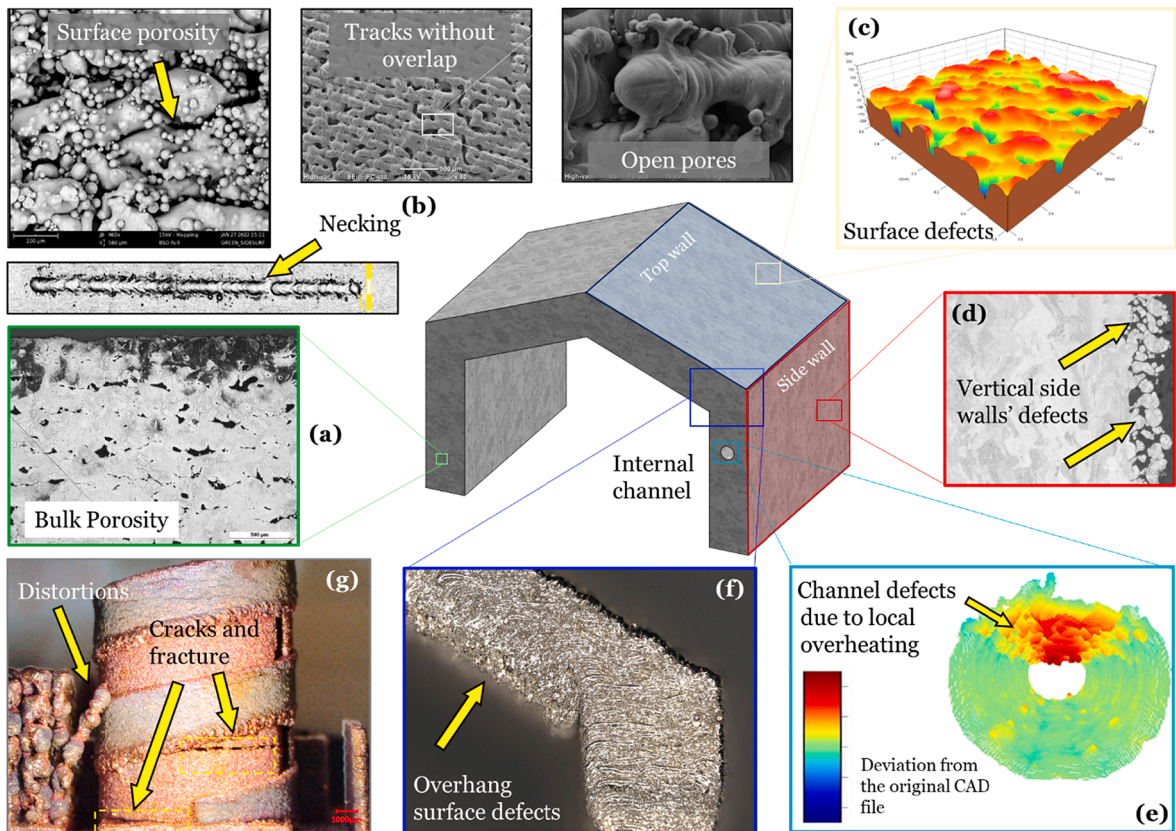


Fig. 28. An overview of a number of most important defects in PBF-made metallic parts; (a) internal porosities, (b) surface defects, open porosities and track nonuniformities, (c) side-wall defects and surface unevenness, (e) dross formation due to localized heating in internal channels (taken and adapted from [43] from DTU - Denmark), (f) dross formation at overhang surfaces and (g) crack, delamination and distortion in a full-size part made of copper.

goal-oriented models are typically categorized based on different criteria; length-scale, physics, type of coupling, type of framework, etc.

In this section we will go through the most important models presented in literature for simulating MAM processes and we will divide them into two sub-sections, namely micro-scale models and deposition-scale models, where during the former we will go through the state-of-the-art and numerical approaches used for predicting grains and dendrites formation along with their evolution, while in the latter, we will cover deposition-scale models, which simulate the manufacturing conditions and their associated physics within the area-of-influence of the heat source and the melt pool.

3.2.1. Micro-scale modelling of MAM processes

The microstructure of materials has a pivotal role in the final quality of additively manufactured products, defining their properties and performance. Furthermore, MAM offers unique opportunities for design of advanced materials in terms of alloy composition, morphology, and texture to produce parts having site-specific microstructures and enhanced properties, challenging or even not accessible for conventional manufacturing. In this context, modeling and simulations enable us to deepen our fundamental understanding of the relations between the process parameters and microstructures and facilitate time-efficient and sustainable material design and development.

An accurate prediction of additively manufactured microstructures aiming at materials engineering represents a grand challenge within MAM. It requires multiscale simulation tools to be developed and coupled with materials characterization for calibration and validation of models. The articles focused on the development of microstructure models for MAM began to appear in the literature around 2016, mainly in a 2D setting [612–614]. However, some earlier studies presented macroscale models of the evolution of material's internal structure during MAM estimating phase distribution, average grain size and/or the type of grain morphology [615–617]. While these characteristics could be instrumental in our general understanding of material microstructure and could serve as input to mechanical calculations yielding the homogenized response, macroscale models are beyond the scope of this section and are discussed in section 4. Their review in application to MAM might be found in [618].

The numerical methods currently available for description of the microstructure evolution during MAM (see Fig. 29) represent the result of tremendous progress made in microstructure modeling in directional solidification and welding [619–621]. Moreover,

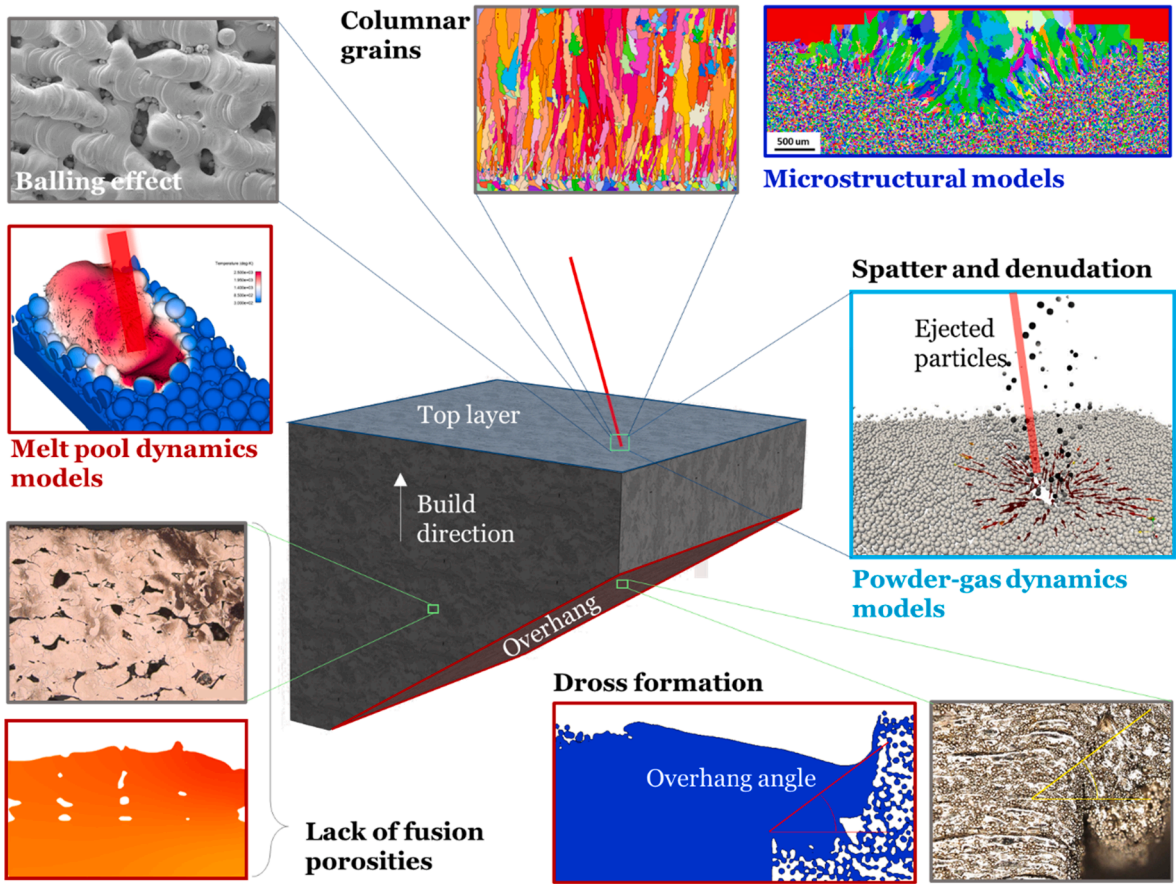


Fig. 29. An overview of the simulations of MAM (here as an example, PBF). Deposition-scale models are shown with dark red color and micro-scale models with blue borders. The figure shows how deposition-scale models could be implemented for simulating melt pool conditions as well as defect formations at various locations belonging to a metallic component.

microstructure modeling for MAM is rapidly developing field, which is supported by the fast growing number of research articles and reviews in this area. For example, the recent review on modeling of microstructure formation in MAM by Gunasegaram and Steinbach presents a general overview of the field, discussing some recent studies in the field as well as outlining research gaps [622]. This work, however, does not consider the numerical methods applied for prediction of additively manufactured microstructures. Li et al. [38] discussed the progress made in the field of microstructure simulations for MAM but limited their review to the Ti-6Al-4 V alloy. Reviews by Körner et al. [623] and Tan et al. [624] published in 2020 and 2019, respectively, comprehensively summarized microstructural models along with thermal ones reported for MAM simulations but were limited to solidification only. Hence the present section focuses on the numerical approaches enabling prediction of MAM microstructures at the grain and substructure scales and summarizes the recent progress in the field not just limited to solidification. The methods discussed include cellular automata

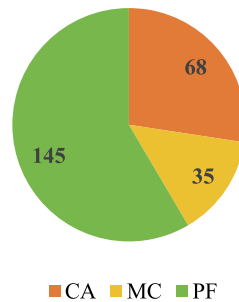


Fig. 30. Pie chart showing the number of articles from the Web of Science Core Collection mentioning ‘additive manufacturing’ and ‘microstructure’ together with each of microstructure simulation approaches. Proceeding papers are not taken into account. For CA both terms ‘cellular automata’ and ‘cellular automaton’ were used.

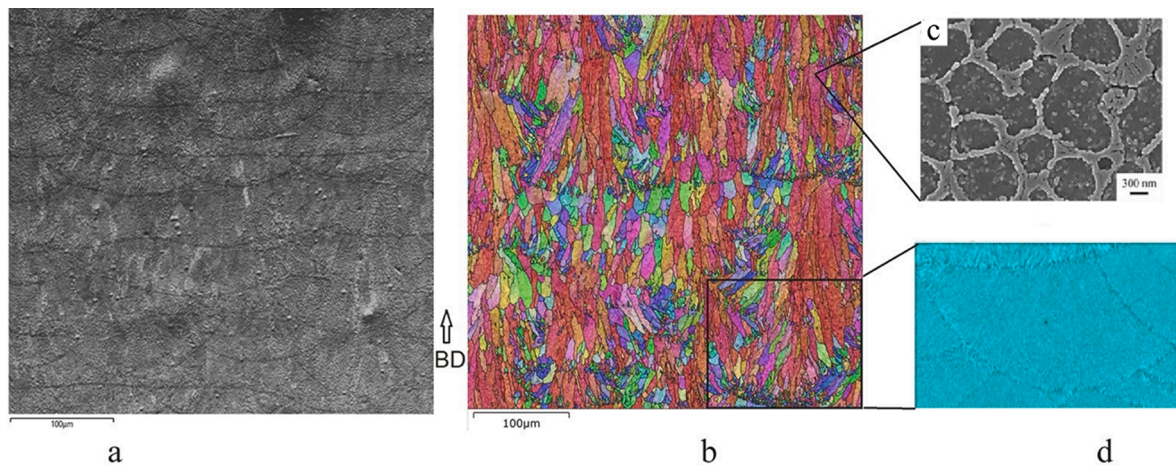


Fig. 31. Hierarchical microstructure of a LPBF AlSi10Mg alloy [628]: (a) a forward scattered electron (FSE) image showing a fish-scale structure, (b) an orientation map demonstrating a grain structure, (c) a cellular-dendritic substructure [636], and (d) an energy dispersive spectroscopy (EDS) map illustrating Si distribution in a melt pool. BD stand for the build direction..

(CA), the kinetic Monte Carlo (kMC) method, and the phase field (PF) approach, which are considered as the most widely used methods for this purpose [625]. Fig. 30 outlines the search results in the Web of Science database for articles from the Web of Science Core Collection mentioning ‘additive manufacturing’ and ‘microstructure’ together with the aforementioned methods. While this section addresses microstructure simulation models for MAM at the microscale, the interested reader could find a more general discussion of space scales and approaches in materials modeling in the seminal work of Raabe [626].

Note that we consider the approaches describing the microstructure evolution during the MAM process and accounting for physical processes involved. Another category of methods, which is not discussed in this section but is used in microstructure-based mechanical simulations of additively manufactured materials [627,628], enables fast generation of synthetic microstructures similar to those produced by MAM by grain morphology (e.g., Voronoi tessellation [629], or the method of step-by-step packing [630]). The methods from both categories applied to additively manufactured grain structures are discussed in [631].

3.2.1.1. Experimental backgrounds. Metal additive manufacturing implies the simultaneous production of a part and a material in a single print, involving many heating and cooling cycles characterized by rapid and localized melting, remelting, high cooling rates, and

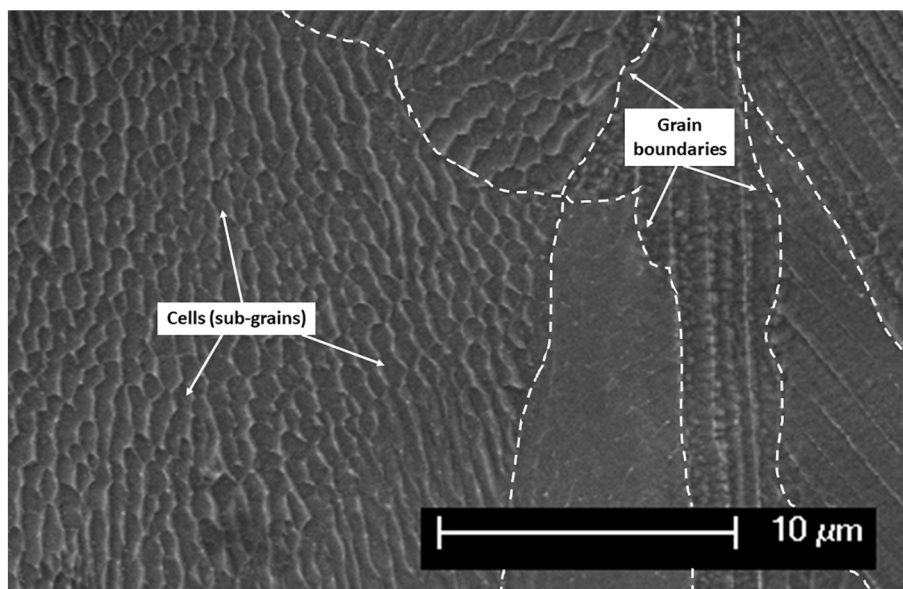


Fig. 32. Two length scales of microstructure considered in this section: the grain scale structure where white dashed lines mark grain boundaries and the cellular dendritic substructure of LPBF 316L steel as an example [58]. Different morphology of cells reflects their orientation relative to the considered cross section. The substructure elements within one grain are usually characterized by semi-identical orientations.

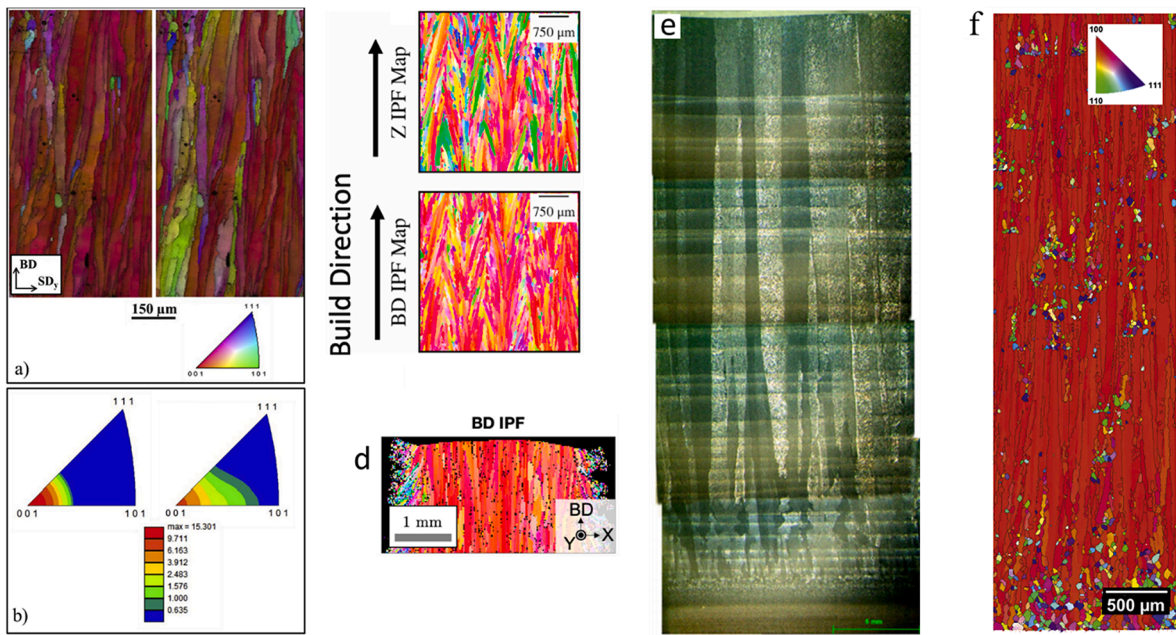


Fig. 33. Examples of ‘classic’ MAM-produced columnar grain structures: L-PBF produced high-silicon (6.9%wt. Si) steel – (a) orientation maps and (b) inverse pole figures [638]; (c, f) EB-PBF fabricated IN718 [639,641] and (d) Haynes 282 nickel based superalloys [640]; (e) direct current pulsed GTAW AM Ti6Al4V alloy [633].

steep temperature gradients. Complex thermodynamics of the MAM process results in unique microstructures, significantly different from those observed in parts produced using subtractive techniques. MAM microstructures exhibit a pronounced hierarchy, which may span up to six orders of magnitude [632], from nanoscale impurities and precipitates (<1 nm and 10–150 nm, respectively, for 316L steel as an example [632]) through micron sized cellular structures (<1 μm for 316L steel [632]) up to millimetric grains (up to 0.2 mm for 316L steel [632]) that may be even larger in DED processes [633,634]. Researchers also distinguish a melt pool pattern (Fig. 31) referred to as a fish-scale structure [634,635] as a separate microstructural element due its contribution into the mechanical behavior of a part [628]. Fig. 31 illustrates the microstructural hierarchy of an LPBF fabricated AlSi10Mg alloy. This section considers two length scales of microstructure: grain level structure shown in Fig. 31 b and intra-granular substructure illustrated in Fig. 31 c and Fig. 32.

Typically, MAM microstructures consist of large columnar grains grown epitaxially from a base plate and, in case of PBF, from powder through many layers in the build direction (BD). They predominantly have close crystallographic orientations. Therefore, MAM parts are often characterized by a process-induced morphological and crystallographic texture resulting in a pronounced anisotropy of their mechanical properties [618,619,633,637–641]. Fig. 33 illustrates the examples of ‘classic’ MAM microstructures. Some combinations of MAM process parameters may lead to the formation of certain grain patterns. For instance, a number of researchers analyzing LPBF produced cubic materials observed bimodal grain structures consisting of $\langle 110 \rangle \parallel$ BD coarse columnar grains separated by $\langle 100 \rangle \parallel$ BD narrow columnar grains with a period of one hatch distance, see Fig. 34. These microstructures were characterized by a bicomponent crystallographic texture with a pronounced $\{011\} \langle 100 \rangle$ Goss component and a weak $\{001\} \langle 100 \rangle$ cube component, which was reported for 316L austenitic stainless steel [642–644], nickel-based alloys [645–647], and copper-based alloys [648] printed with different parameters but a bidirectional (or alternating) scanning strategy. Overall, both spatial grain arrangement and crystallographic texture of an as-built part are determined by the local thermal conditions which, in turn, depend on process parameters. Process-microstructure relations define the idea of microstructure tailoring described earlier in the section; and modeling methods enabling the microstructure prediction in MAM, which are discussed in this section, are the key tools to support manufacturing in microstructure tailoring in parts to be produced, minimizing the currently exploited time- and recourse-consuming trial-and-error approach.

Previous research on microstructure development during MAM has identified epitaxial solidification and competitive grain growth as the main mechanisms yielding a highly textured columnar grain structure in MAM produced alloys without noticeable nucleation in front of the solid–liquid interface [628,633,634,636,642–648]. Epitaxial solidification (epitaxial nucleation or growth are two other terms for this process) implies extending existing grains of a partially melted material being in contact with a molten material through addition of atoms from the melt. In case of MAM, a base plate, powder particles, and already solidified layers might be identified as a partially melted material. An important condition of epitaxial solidification is a similar composition of molten and base materials, which enables complete interaction of a nucleus of atomistic dimensions with the base material, minimizing nucleation barrier, i.e., the critical nucleation undercooling $\Delta T_n \approx 0^\circ$. The newly formed crystals inheriting the crystallographic orientations of their ‘parent’ grains grow along their preferred growth directions: $\langle 100 \rangle$ for cubic materials, $\langle 10\bar{1}0 \rangle$ and $\langle 11\bar{2}0 \rangle$ for those with hexagonal symmetry

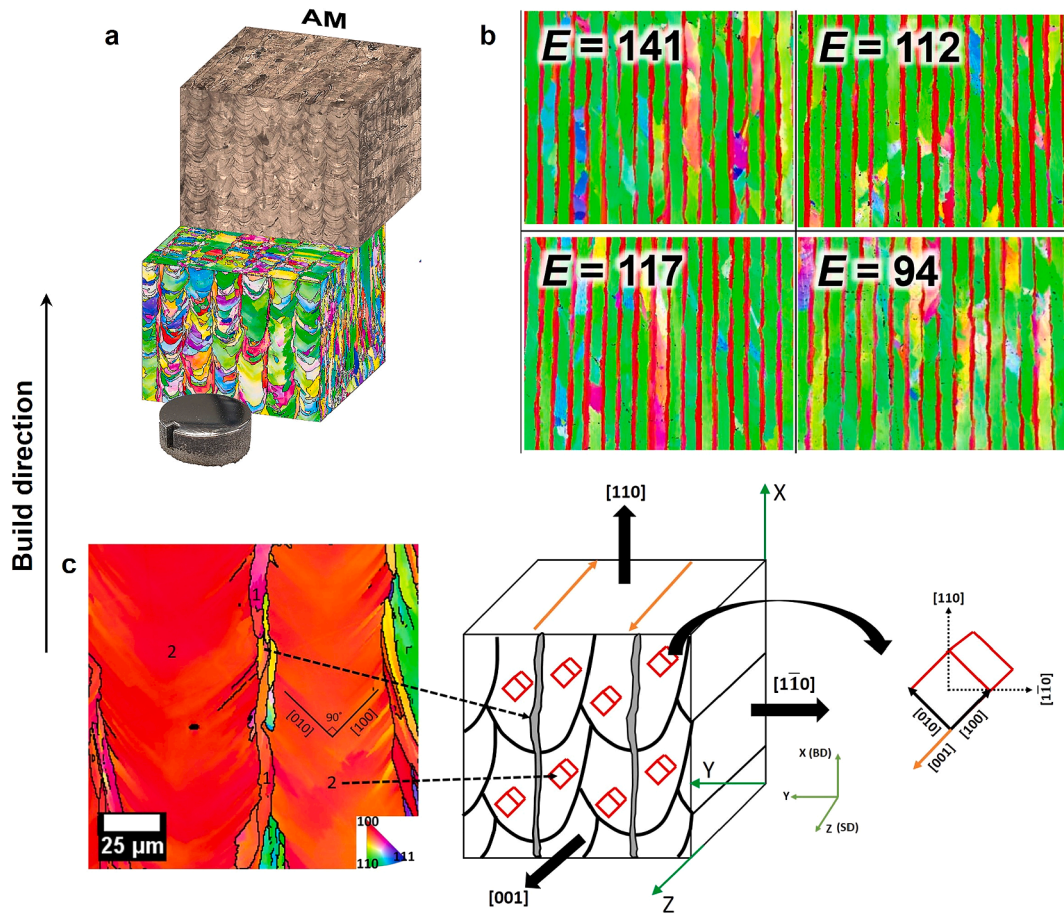


Fig. 34. Bimodal grain structures of (a) LPBF 316L steel [649], (b) IN718 [645], and (c) Ni-25 at.% alloy [644] printed with the bidirectional scanning strategy. Subfigure (c) also schematically illustrates alternating $\langle 110 \rangle \parallel$ BD and $\langle 100 \rangle \parallel$ BD columnar grains as opposed to the melt pool pattern.

[650]. The closer their preferred growth directions are aligned with the local maximum temperature gradient, the more likely the grains will ‘survive’ in the final microstructure, outgrowing those that are not so favorably oriented. In such a way, the growth is competitive, with favorably oriented crystals growing at the expense of their misoriented neighbors. Seminal works [621,651] provide more detailed description of these phenomena.

Growth competition of grains defines the effects a melt pool shape has on a microstructure. Their early analysis might be found in the seminal welding research [621,652]. A moving melt pool leads to a constantly changing direction of the local temperature gradient. As the average growth direction is roughly perpendicular to the solid–liquid interface, a growing crystal does not remain favorably oriented during the entire solidification, experiencing different degrees of ease or difficulty of growth. A number of growing grains that were misoriented with respect to the temperature gradient at the beginning might become more favorably oriented and survive in the final microstructure. However, the fact that MAM represents kilometers of a heat source path and implies multiple remelting in a single build makes the understanding of microstructure formation in MAM even more challenging.

For instance, in the earlier described case of the bicomponent Goss and cube texture in LPBF produced cubic materials, narrow $\langle 100 \rangle \parallel$ BD grains tend to grow vertically, along the centerline of a melt pool, passing through its deepest region Fig. 34 (c), which is explained by the co-directionality of their preferred growth directions with the local steepest temperature gradient (see, e.g., [642–646]). Large $\langle 110 \rangle \parallel$ BD grains form at the side boundaries of melt pools and their overlaps, occupying a part of two adjacent melt pools. These grains first grow to one side, following the temperature gradient induced by a moving heat source. With the next hatch, when a laser beam moves in the opposite direction, they grow to another side, thus changing the growth direction by $\sim 90^\circ$ [642,653]. Due to the symmetry of the cubic crystal lattice, there is no change in crystal orientation. The material microstructure is hypothesized to solidify by epitaxial growth of primary dendrite arms in the current layer on secondary dendrite arms formed in the previously solidified layer and serving as a growth front [654]. While the preferred growth directions of $\langle 110 \rangle \parallel$ BD grains are not always perpendicular to the liquidus line, $\langle 100 \rangle$ growth at $\sim \pm 45^\circ$ to BD seems the most energetically efficient [655].

Nucleation is another crucial aspect to consider when analyzing microstructure formation. Two types of nucleation are considered in theory, homogenous and heterogenous, with epitaxial nucleation being a special case of the latter, with no barrier to nucleation.

While epitaxial solidification occurs on a fusion line, grains can also nucleate in front of a solid–liquid interface, in an undercooled melt. Overall, nucleation ahead of an advancing solidification front in MAM remains a black box, and its description in microstructure modeling is the subject of considerable discussion and debate.

On the one hand, Tan and colleagues in their review on microstructure modeling for MAM [624] argue that lack of nucleation ahead of a solidification front ‘leads to inaccurate grain structure’ that might differ from the experimental results. On the other hand, a number of experimental and numerical studies indicate small probability of nucleation in front of a solid–liquid interface happening during MAM [612,613,641,643,645,647,653,656–661].

Steep temperature gradients and high cooling rates inherent in MAM are known to favour the formation of cellular-dendritic columnar microstructures by creating a very narrow mushy zone [653,659,662], which minimizes the possibility of the formation of new, equiaxed grains within the fusion zone by mechanisms, specific to weld pool solidification. Among them are dendrite fragmentation and grain detachment, both presuming the presence of respective microstructure elements in the fusion zone serving as sites for heterogeneous nucleation [621]. Secondly, in several alloys, common for MAM, the main alloying elements have a high solubility in the base metal, which is reflected in high partition coefficients ($k \approx 1$) [653,659,663,664]. This leads to a low growth restriction factor, $Q = m_L C_0 (k - 1)$ and, thus, to the slow buildup of constitutional undercooling in front of an advancing solid–liquid interface [663]. Here m_L is the liquidus slope, and C_0 is the solute concentration. The slower the development rate of a zone of constitutional undercooling, the later nucleation ahead of a solidification front can potentially occur. Even if some new equiaxed grains appear in the later stage of melt pool solidification, which is supposed to be sometimes observed in single tracks [660,665] and is related to decreasing temperature gradients and cooling rates, they are subsequently remelted and resolidified as columnar crystals.

Considering nucleation in front of a solid–liquid interface in their cellular-automata finite-volume simulations of LPBF single tracks, Panwisawas et al. [666] concluded on the difficulty of new crystal formation within a melt pool. The results of numerical studies performed for additively manufactured Ti-6Al-4 V titanium alloy [664,667–670], 316L steel [643,653,656] IN718 [613,641,647,658] and CMSX-4 [657] nickel-based superalloys and validated by experimental data support the suggestion of Koepf et al. [657] on the reasonable robustness of a microstructure printed virtually with no nucleation ahead of a solidification front taken into account. Considering only epitaxial growth from a base plate and powder, Zinovieva et al. [653] simulated 3D LPBF microstructures containing fine grains of random crystallographic orientations within the main columnar grain pattern Fig. 35. As highlighted in [653,671], it is necessary to interpret 2D experimental cross sections with caution, since the appearance of columnar grains (or cellular dendrites) growing out of plane can be easily confused with equiaxed grains (or equiaxed cells). This is well illustrated in [672].

In some cases, however, not considering nucleation ahead of a solid–liquid interface will result in an inaccurate microstructure prediction. For instance, Al-Si-(Mg) alloys or high-temperature precipitation strengthened alloys such as Al-Mg alloys modified with Sc

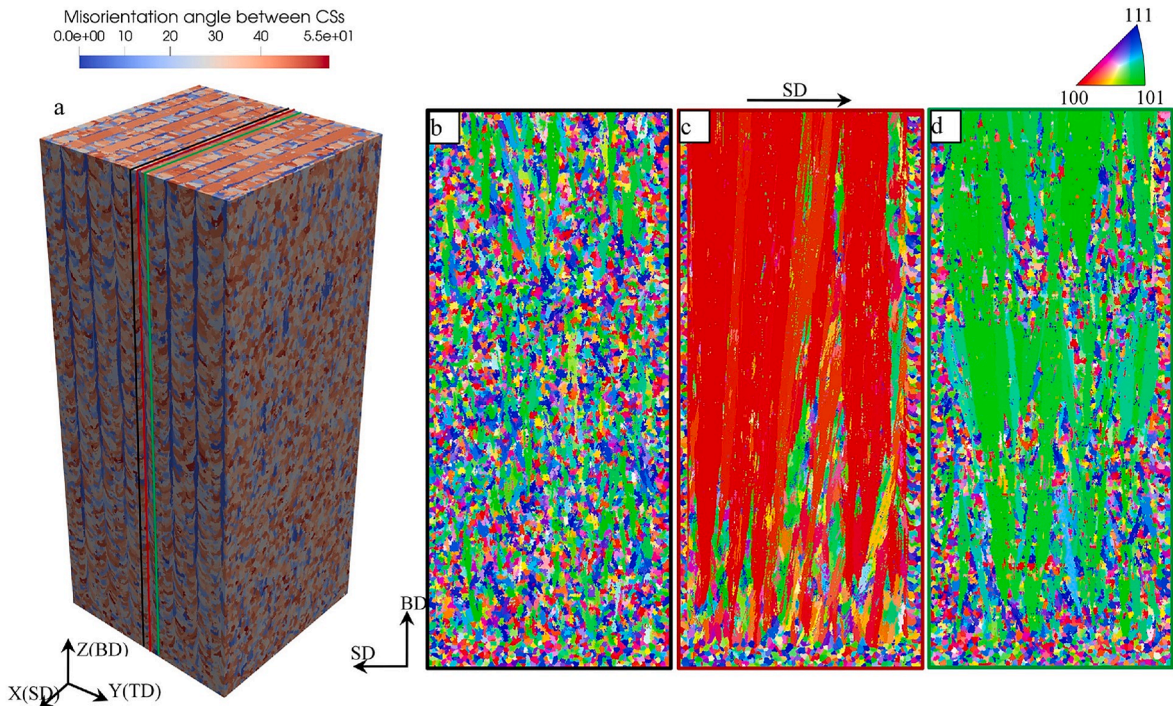


Fig. 35. (a) Model predicted grain structure of LPBF 316L steel and (b-d) orientation maps in the BD-SD cross sections showing that no nucleation ahead of a solidification front might be required to obtain fine grains in additively manufactured microstructures [653]. The calculations in [653] have been performed using a cellular-automata finite-difference model.

(Scalmalloy[®] [673]) or Zr (Addmalloy[®] [674]) are characterized by a bimodal ‘fan-shell’ grain structure consisting of fine equiaxed grains in the vicinity of melt pool boundaries and columnar grains forming a radial pattern in the central region of the melt pools Fig. 31. In the follow-up sections we go through the three microstructural modeling approaches of MAM processes.

3.2.1.2. Cellular automata simulations. CA treat an object as a set of interacting elements, with their dynamics in time and space defined by a set of transition rules. The concept was introduced in 1940 s by von Neumann and Ulam [675–677] and approximately 50 years later it was adopted to simulate microstructure evolution in recrystallization [678] and solidification of metallic materials [651]. Over the past two decades, CA have been widely employed in simulations of the microstructure evolution during various manufacturing processes, such as casting [679,680], welding [681], and hot working [682]. To the extent of our knowledge, the first studies applying cellular automata to MAM emerged in the past seven years [612,613]. Fig. 36 demonstrates some examples of model predicted grain structures using CA as compared to experimental observations.

CA are defined by four main elements. First, the computational domain is discretized by a mesh (usually regular) with cells of certain geometry. Secondly, each cell (automaton) has a predefined neighborhood, over which the cell has a direct influence. In the case of a 2D square mesh, the neighborhood typically consists of four or eight adjacent cells and is referred to as cubic von Neumann or cubic Moore neighborhood of first order, respectively, Fig. 37 (a), (b). Different neighborhood orders are considered as well [678,683]. For instance, Fig. 37 (c) illustrates the Moore third order neighborhood. The neighborhood definition might be changed by introducing weights affecting the neighbor influence [684]. Thirdly, a number of states are identified and attributed to each cell. In solidification modeling, the state is related to that of the matter, namely ‘liquid’ (occupied by the melt), ‘solid’, or ‘growing’/‘interface’ (lies at the solid–liquid interface or is occupied by an evolving mushy zone). In addition, the ‘gas’ state is introduced in some CA simulations for MAM [685] or similar manufacturing processes [686] where the consideration of a gas-metal interface is important, for instance, to take the formation of gas trapped pores into account. Some intermediate states might be considered as well [667,684]. In addition, each cell is characterized by field variables (e.g., temperature) impacting the system evolution. Fourthly, the model evolves by applying the set of rules, which needs to be defined. Table 5 represents an example of the transition rules for the i^{th} automaton for CA modeling of the grain structure evolution during LPBF.

Generally, the microstructure evolution comprises nucleation and growth of grains or substructure elements (e.g., dendrites). Within the CA approach, nucleation in the bulk of the melt is often simulated with the use of a continuous nucleation model assuming a continuous dependency of the number of grains per unit volume, N (m^{-3}), on temperature T (K). The continuous nucleation model correlates nucleation velocity with undercooling ΔT (K), cooling rate, or temperature. The first model of this kind suggesting the power law relationship,

$$N = \mu_1 (\Delta T)^n \text{ or } \frac{dN}{dt} = -n_N \mu_1 (\Delta T)^{n-1} \frac{dT}{dt} \quad (16)$$

in a differential form, was offered by Oldfield in 1966 [687], where μ_1 and n_N are fitting parameters defined based on an experimental N - ΔT dependency. The parameter n is between 1 and 2; μ_1 varies with an alloy [625]. Based on Oldfield’s pragmatic approach [687],

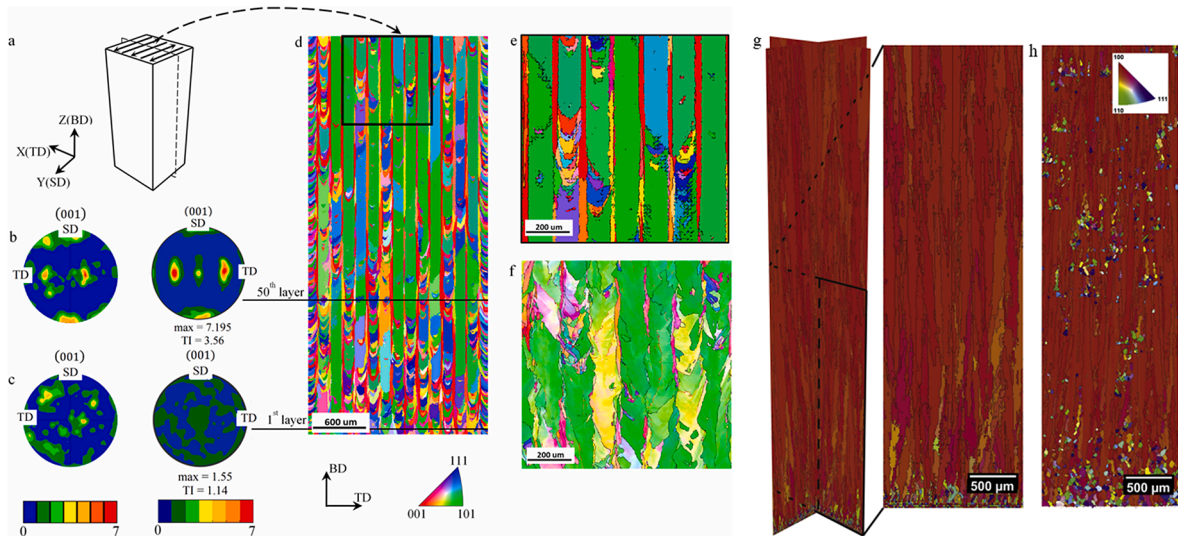


Fig. 36. Examples of CA simulations of AM microstructures in comparison with the experimental data. Subfigures a-f are related to LPBF 316L stainless steel [642,643]; subfigures g-h, to EPBF Inconel 718 [641]. (a) Schematics of the calculation domain and scan strategy applied; (b, c) experimental [642] (left column) and model predicted (001) pole figures [643] (right column) taken close to 50th and 1st layers; (d, e) model predicted orientation maps [643] and (f) experimental orientation map of LPBF 316L steel [642]; (g) simulated and (h) experimental orientation maps for EPBF Inconel 718 [641].

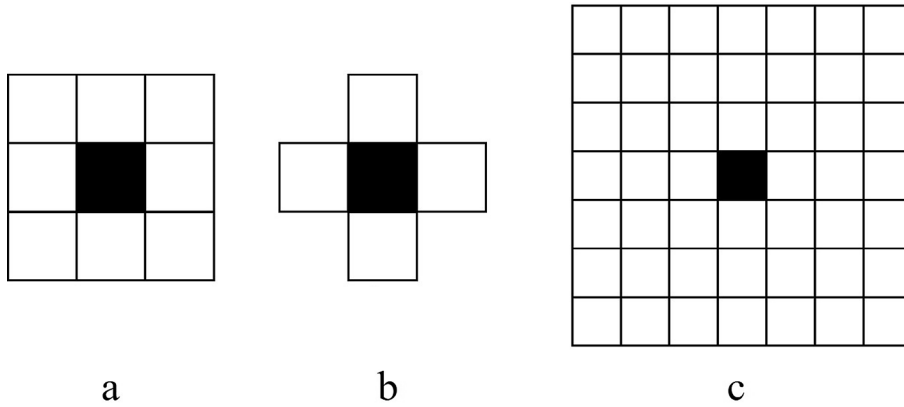


Fig. 37. (a) Cubic Moore and (b) von Neumann neighborhoods of the first order and Moore third order neighborhood.

Thévoz [688] later offered a Gaussian distribution

$$\frac{dN}{d(\Delta T)} = \frac{N_{\max}}{\Delta T_{\sigma} \sqrt{2\pi}} \exp \left[-\frac{1}{2} \left(\frac{\Delta T - \Delta T_N}{\Delta T_{\sigma}} \right)^2 \right] \tag{17}$$

to relate the density of grains to undercooling they were formed at. The temperature distribution of nuclei yields the number of potential nucleation sites per unit volume activated between certain undercooling values. Thévoz’s continuous nucleation model employs standard distribution parameters, namely the mean undercooling, ΔT_N (K), corresponding to the maximum of the distribution, standard deviation ΔT_{σ} (K), and the maximum density of nuclei, N_{\max} (m^{-3}). These parameters are derived from differential thermal analysis experiments measuring the density of grains (grain size in other words) and corresponding maximum undercooling at recalescence under various cooling conditions [689,690]. In a 2D setting, the maximum nucleation density is defined as

$$N_{\max} = \sqrt{\frac{\pi}{6} [N_{\max}^*]^3} \tag{18}$$

Here N_{\max}^* (m^{-2}) denotes the sought-for nucleation density value in the 2D case.

The continuous nucleation model, Eq. (17), was spearheaded by Rappaz and his colleagues [651,681,690] and is often used in CA simulations for MAM [612,666,685,691–695] and similar processes such as multipass arc welding [686]. Some authors employed this model to describe nucleation both within the melt pool in an additively manufactured material and when generating the base plate [666,685,691]; others considered nucleation in the base plate only [612,686,694]. Other nucleation approaches adopted in CA simulations of the microstructure evolution during MAM comprise the aforementioned Oldfield’s model [687], Eq. (16), modified so as to take into account the fraction of solid as suggested by Nastac [696] (see [697–699]), or simple approximations where nucleation proceeds at a constant rate [700] or seeds are placed in the computational domain simultaneously with their number estimated from experiments [613,643,653,658,664]. For more information on heterogeneous nucleation models, see the seminal book by Stefanescu [625].

There exist different approaches to virtually ‘nucleate’ the number of grains calculated with the chosen model. Often nucleation cells are randomly distributed within a computational domain, although some studies limited the possibility of nucleation in MAM materials to a fusion line [695]. Once the local temperature of a potential seed cell which is still in a liquid state becomes lower than the critical nucleation temperature derived from the chosen nucleation model, a new grain forms [692,694]. A number of authors [612,685,691,693,698,700] introduced an additional stochastic condition as a trigger for the nucleation event in the cell under consideration.

Once a new crystal is nucleated in a CA cell either epitaxially or ahead of an advancing solid–liquid interface, the cell becomes ‘growing’ with its index changed accordingly and is assigned a crystallographic orientation. While in epitaxial solidification a new

Table 5
Set of rules for the i th CA cell. adopted from [653]

Transition rule for	State before transition	Transition rule	State after transition
Melting	Not liquid	$T_i \geq T$	Liquid
Nucleation (base plate, powder)	Liquid	A crystal is nucleated in the i^{th} cell.	Growing
Capture	Liquid	The i^{th} cell is captured by a neighboring growing cell.	Growing
Cessation of the i th cell growth	Growing	There are no liquid cells in the neighborhood of the i^{th} cell.	Solid
Becoming partially melted during LPBF due to remelting	Solid	The i^{th} cell has a liquid cell in the neighborhood.	Growing

grain inherits the orientation of its parent grain, in the case of nucleation within the melt the orientation is usually set in a random way, with several approaches offered for this purpose in a 3D setting [653,664,693].

If the grain scale is considered, the approximative concept of a dendrite envelope [651] is employed. The envelope represents a surface that separates the inner space of a dendrite, including the solid and intra-dendritic liquid, from the exterior (Fig. 38). For materials with a cubic crystal lattice, the dendrite envelope is a square in 2D or an octahedron in 3D, with its half diagonals corresponding to the preferred growth directions of the grain. Approaches of this kind are also referred to as volume averaged models [625].

The evolution of the envelope is governed by the growth rate of the dendrite tip, v , that is computed based on the growth kinetics model. The latter considers a simplified isolated dendrite tip that is described by a hemisphere [701,702] or a paraboloid of revolution [703] and grows with a constant rate v defined as a function of a local undercooling, ΔT , that reflects the behavior of the tip region. During the dendrite growth in alloys, heat and solute are rejected in the melt changing the temperature of the solid-liquid interface, which is reflected in thermal ΔT_t (K) and solutal ΔT_c (K) undercooling terms in Eq. (19). Furthermore, in a general case, the temperature difference caused by the tip curvature, ΔT_r , and by atom attachment, ΔT_k (K) should be taken into account. The two latter contributions are referred to as the curvature undercooling and kinetic undercooling, respectively.

$$\Delta T = \Delta T_t + \Delta T_c + \Delta T_r + \Delta T_k \tag{19}$$

When defining the growth kinetics model, one defines the undercooling terms and/or omits some of them from consideration based on some assumptions. Among the dendrite tip growth models most widely adopted in CA simulations of the grain structure evolution in MAM are those offered by Kurz et al. [704] and Lipton et al. [705] abbreviated as KGT and LGK models, respectively. As a rule, their solutions are fitted by simple polynomial functions to minimize computational cost of CA calculations. Examples of fitting functions employed in CA simulations for MAM include $v_k = B\Delta T^b$ [613,641,656–658,664,685,695,706], $v_k = a_2\Delta T^2 \pm a_3\Delta T^3$ [643,653,666,670,692,694,707], $v_k = -a_0 + a_1\Delta T + a_2\Delta T^2 - a_3\Delta T^3$ [693], $v_k = -a_1\Delta T + a_2\Delta T^2$ [691]. Here a_k , B , and b stand for fitting coefficients. Some researchers introduce more complex approximations [612,697,698,700], e.g.

$$v_k = \frac{D_l}{5.51\pi^2(-m_L(1-k))^{1.5}\Gamma} \left(\frac{\Delta T^{2.5}}{C_0^{1.5}} \right) \tag{20}$$

Here D_l (m²/s) is the solute diffusion coefficient in the liquid and Γ (K·m) is the Gibbs-Thomson coefficient. Aiming to add more physics-based fidelity in microstructure simulations, Liu and Shin [667] calculated the growth rate for their CA model using a phase field method.

The growth rate function $v_k(\Delta T)$ (m/s) defines the position of apices of the dendrite envelope sometimes referred to as growth vectors [612,680], which correspond to the dendrite tips (Fig. 38). Once the square/octahedron is large enough, it captures the neighboring liquid cell. The following evolution is defined according to the transition rules (e.g., Table 5).

Another key point worth mentioning about cellular automata is the artificial anisotropy induced by a regular mesh. The mesh anisotropy results in the artificial texture formation where the simulated dendrites are aligned with the global coordinate system and are characterized by the same orientation (Fig. 39). Alternatively, the grain shape may vary depending on the grain orientation (Fig. 40). A 3D decentred octahedron (or 2D decentred square) algorithm proposed by Gandin and Rappaz [708] along with its

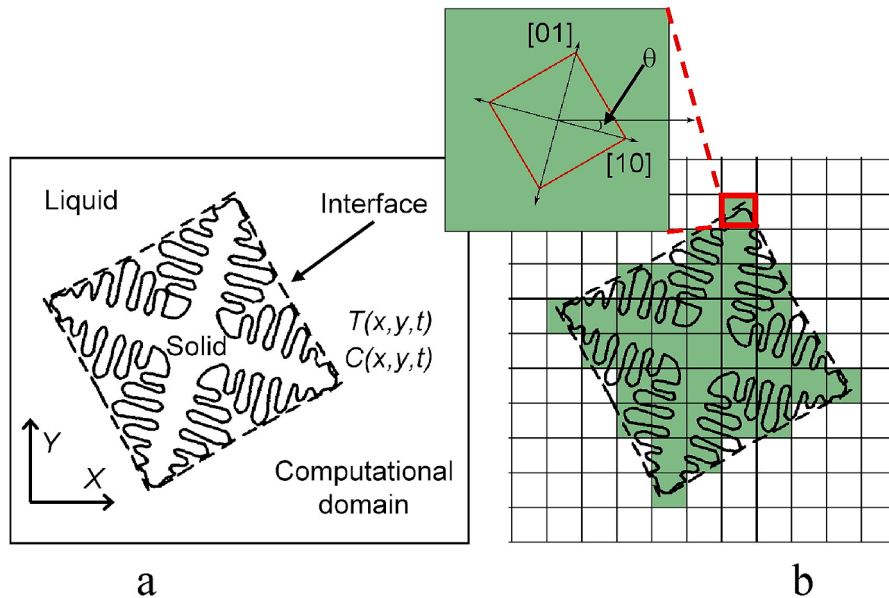


Fig. 38. Schematic representation of a 2D computational domain [612]: (a) the growth of a dendrite in the melt and (b) its representation with CA following the concept of a dendrite envelope.

modification [709] are often applied in CA simulations of the grain structure evolution in MAM [643,653,664,694,700].

As might be seen in Fig. 39, cellular automata can also be applied at the substructure scale, enabling the prediction of the complex substructure morphology and chemical microsegregation. In this case, the evolution of concentration fields should be calculated in addition to the evolution of temperature fields. For this purpose, the solute diffusion equation should be used

$$\frac{\partial C}{\partial t} = D \nabla^2 C \quad (21)$$

supplemented by the boundary conditions at the interface, including solute conservation

$$(C_l - C_s)v_n = D_l \nabla C|_{\text{liquid}} \cdot \vec{n} - D_s \nabla C|_{\text{solid}} \cdot \vec{n} \quad (22)$$

and solute partitioning between liquid and solid phases

$$C_s = kC_l \quad (23)$$

The solute diffusion equation is formulated for solid and liquid and derived from conservation of species assuming the partition coefficient $k < 1$, no source term, constant density and diffusivity, and the velocity vector $\vec{v} = 0$ for solute transport. Here C (wt%) stands for the solute concentration, D (m^2/s) is the solute diffusion coefficient, the subscripts l and s represent the values of respective variables and coefficients in the liquid or solid, respectively, \vec{n} is the normal unit vector to the interface oriented from solid to liquid, and v_n (m/s) denotes the normal interface velocity. The interface is also assumed to be in a local equilibrium with liquid and solid phases, with the equilibrium temperature defined taking into account undercooling contributions discussed above in Eq. (4). Particular attention is paid to the interface curvature calculation, where different approaches are considered [625,684,711].

While CA substructure models are widely used in microstructure modeling for conventional manufacturing processes such as casting or welding [625,684,711,712], few published studies employed them in MAM simulations [699]. For example, instead of using an analytical growth kinetic function Rolchigo et al. [713,714] assumed that local interface kinetics dominates the driving force for free energy and considered the proportionality between the driving free energy and an interfacial velocity. The local solute concentration in [713,714] was calculated using the Lattice Boltzmann (LB) method. Models of this type are of relatively high computational cost and are thus applied to small volumes (Fig. 41).

Note that despite being less efficient than grain scale CA models, substructure-scale CA models are more cost effective than PF models discussed as will we discussed in its pertinent sub-section. Aiming at combining advantages of both methods, Liu and Shin [667] developed a 2D CA substructure model where a 1D PF component was integrated to predict the growth kinetics law depending on the local solidification conditions. They reported that the 2D CAPF model improved the computational efficiency by more than 5 orders of magnitude in comparison with a pure PF model. Later the 2D CAPF model was extended to 3D [670].

Table 6 summarizes some of the major contributions within CA models for MAM, along with their highlights.

3.2.1.3. Kinetic Monte Carlo simulations. Being employed in engineering since the 1950 s [715], the Monte Carlo method has been adopted for simulations of the microstructure evolution since the 1980 s [716–720]. For this purpose, the Monte Carlo approach was formulated for the multistate kinetic Potts model [721], with the applications devoted to normal and abnormal grain growth [716,719,720,722,723], nucleation and static primary recrystallization [724,725], dynamic recrystallization [726,727], etc. In MAM, the kMC Potts model is applied to describe solidification [728–733], solid state transformation [730] and solid state grain growth due to heat exposure [732–734]. Some examples of model predicted grain structures using the kMC Potts approach along with

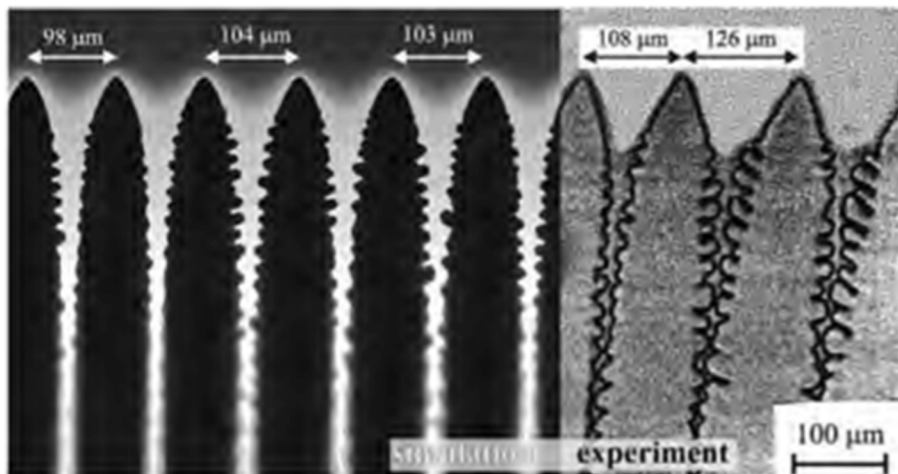


Fig. 39. CA model predicted (left [684]) and experimental (right [710]) substructures of $\text{CBr}_4 - 8 \text{ mol}\% \text{C}_2\text{Cl}_6$ alloy.

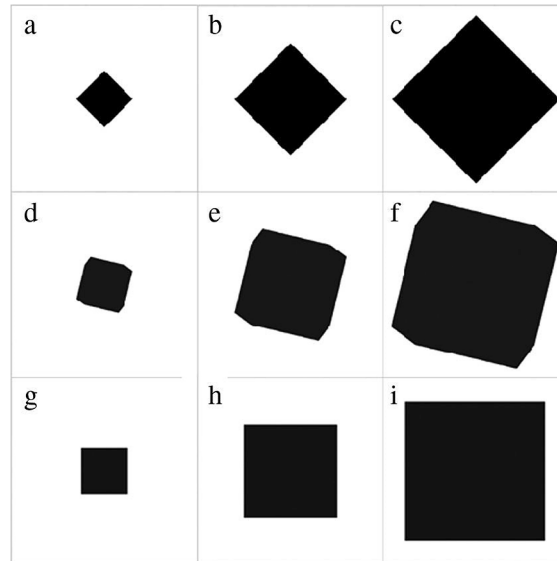


Fig. 40. Single grain growth simulated using cellular automata without corrections for mesh anisotropy [683]. The easy growth direction makes an angle of (a–c) 0°, (d–f) 30° and (g–i) 45° to the horizontal axis.

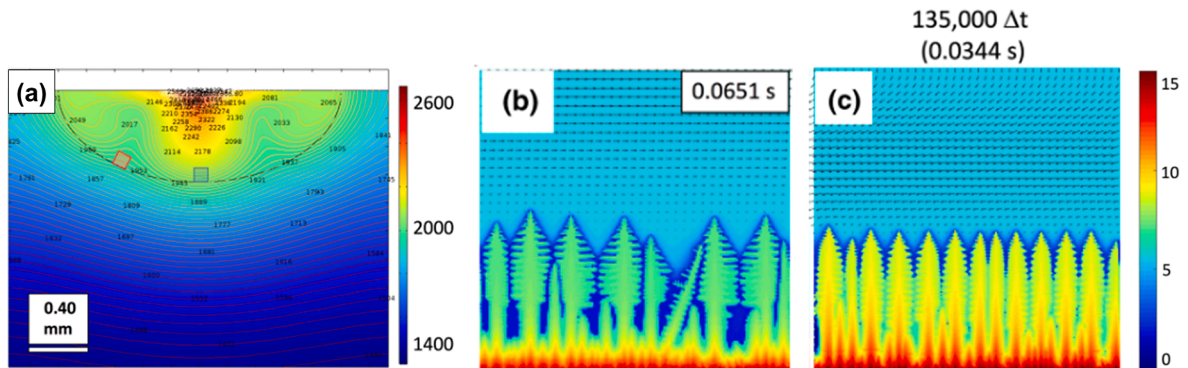


Fig. 41. (a) Thermal simulation results under conditions representative of the Laser Engineered Net Shaping (LENS) process with the domains chosen for microstructure simulations, (b) and (c) solute concentration profile in the domains of Ti-W alloy single track denoted by red and blue in subfigure (a). In subfigures (b) and (c) arrows show fluid velocity for non-solidified cells and the color bar represents the concentration of W in wt pct.

experimental grain structures are illustrated in Fig. 42.

The concept of the kMC approach is based on the minimization of the excess energy of grains in a polycrystalline material. The latter is considered as a spectrum of states or spins s (sometimes referred to as grain indices or orientations), where the regions of identical state represent grains with the grain boundary lying between sites of unlike states (Fig. 43). The grain boundary energy is determined by specifying an interaction between neighboring elements of the spectrum using the Hamiltonian, which can take different forms depending on the problem under consideration and thus define many systems. In the general case, the total energy of the polycrystalline system to be minimized sums all interfacial and volumetric contributions and reads [735]

$$E = \sum_{i=1}^K \left[\sum_{j=1}^{\Lambda} E_{gg}(s_i, s_j) + F(s_i) \right] \quad (24)$$

Here E represents the energy of a boundary unit between sites with spins s_i and s_j , $i \neq j$, F stands for the volumetric energy of a site with a spin s_i , Λ is the number of neighbors at each site ($\Lambda = 26$ in 3D or 8 in 2D, respectively [728]), and K represents all sites considered.

For instance, the Hamiltonian defined for simulating recrystallization and curvature driven grain growth accounts for the grain boundary energy (interfacial term) and stored elastic energy due to stored dislocations in the system (volumetric term) [725,736]. The ratio between these terms determines the balance between the two simulated phenomena: curvature driven grain coarsening and

Table 6
A brief overview of CA modeling of the microstructure evolution during MAM.

Topic and highlights	Coupling	Scale	Volume simulated	Ref.
Scan pattern effects on the grain structure and elastic properties of LPBF 316L stainless steel in a 3D setting	FD pure thermal model; the local steady-state temperature field translates through the domain; in-house code	grains	$2.198 \times 2.198 \times 4.53 \text{ mm}^3$; $2.7 \cdot 10^9$ CA cells; multiple passes in each powder layer, multiple layers	[643]
3D model of an LPBF single track for 316L steel	FE pure thermal model; the Cast3M software	grains	$2.5 \times 0.25 \times 0.12 \text{ mm}^3$; $7.5 \cdot 10^7$ CA cells; single track	[656]
3D model of EPBF IN 718 superalloy	analytical solution; only the remelted zone at the top of the sample is considered	grains	$2.4 \times 2.4 \times 10 \text{ mm}^3$; $\sim 5.8 \cdot 10^7$ CA cells; multiple passes in each powder layer, multiple layers	[641]
Scan speed and line offset effects on the grain structure of EPBF IN 718 superalloy in a 2D setting	LB multi-physics CFD model; in-house code	grains	$4 \times 2.5 \times 10 \text{ mm}^3$ (maximum); multiple passes in each powder layer, multiple layers	[658]
3D model of LPBF Ti-6Al-4 V alloy (β grains)	FV multi-physics CFD model; OpenFOAM	grains	single track	[666]
2D CAPF microstructural model of DED Ti-6Al-4 V alloy compared with a grain scale 3D CA and 2D PF models (β grains)	FV multi-physics CFD model; in-house code	dendrites, grains	$0.548 \times 1.508 \text{ mm}^3$; $\sim 2.1 \cdot 10^7$ CA cells (CAPF); $3 \times 0.6 \times 1.7 \text{ mm}^3$, $2.45 \cdot 10^7$ CA cells; 3 tracks in one layer (maximum)	[667]
Effects of layer thickness, laser power, inter-layer time, and the preheating temperature of the substrate on the grain structure of Ti-6Al-4 V alloy produced with wire laser additive manufacturing (WLAM) in a 3D setting (β grains)	FV pure thermal model, in-house code	grains	single track	[668]
Effects of laser beam shape on the grain structure of LPBF 316L steel in a 3D setting	multi-physics CFD model; in-house ALE3D code based on hybrid FE and FV methods	grains	$0.86 \times 0.3 \times 0.3 \text{ mm}^3$; $9.7 \cdot 10^6$ CA cells; single track	[685]
Effects of thermal gradient, solidification rate, solute concentration, alloying addition, and nucleation parameters on the grain structure of binary β -Ti alloy systems under conditions similar to LENS		grains	$0.4 \times 0.4 \times 0.625 \text{ mm}^3$; 10^8 CA cells	[693]
2D model of IN 718 superalloy under conditions similar to laser cladding	FE pure thermal model	dendrites	$0.8 \times 0.8 \mu\text{m}^2$;	
3D model of LPBF 316L stainless steel + scan pattern effects on the grain structure	analytical, series solution; the local steady-state temperature field translates through the domain	grains	$0.75 \text{ mm} \times 0.75 \text{ mm} \times 0.5625 \text{ mm}$; multiple passes in each powder layer, multiple layers	[700]

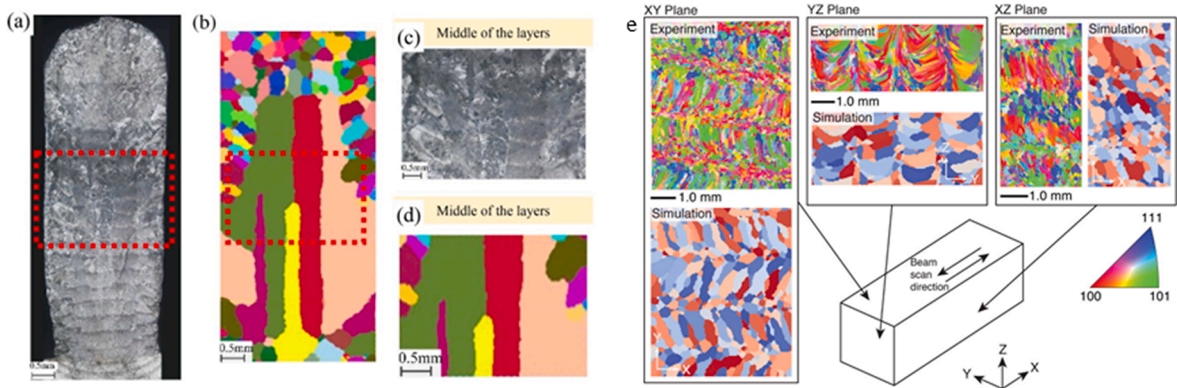


Fig. 42. Examples of kMC simulations of AM microstructures in comparison with the experimental data. Subfigures a-d are related to DED produced Ti-6Al-4 V titanium alloy [730]; subfigure e, to LENS fabricated 304L stainless steel [728].

recrystallization, respectively [725,735,736].

In microstructure simulations for MAM, the kMC Potts model takes into account boundary energy terms only ($F = 0$ in Eq. (9), reproducing curvature driven grain growth

$$E = \sum_{i=1}^K \sum_{j=1}^{\Lambda} \frac{\gamma}{2} [1 - \delta(s_i, s_j)] \quad (25)$$

Here γ^* (J/m^2) represents the specific grain boundary energy per unit length, which is often taken to be 1 [728,729,734], and δ

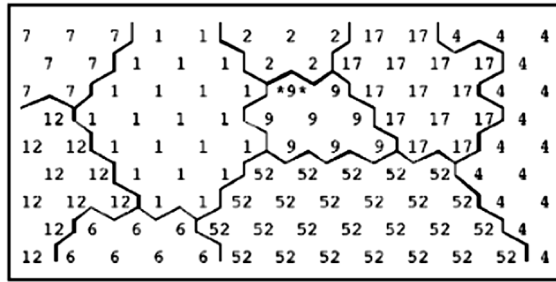


Fig. 43. A grain structure defined on a 2D triangular mesh also referred to as lattice [735].

stands for the Kronecker delta with $\delta(s_i = s_j) = 1$ and $\delta(s_i \neq s_j) = 0$.

The grain structure evolution is simulated by choosing a site and selecting its new state s from the possible states of the system (referred to as site flips [736]), both at random, which results in a change in the overall system energy calculated using Eq. (10). The new state assignment is accepted or rejected based on the Metropolis algorithm [715] where a random number $r \in [0; 1]$ is compared to the transition probability defined as

$$P = \begin{cases} M(T)\exp\left(-\frac{\Delta E}{k_B T_{MC}}\right) & \text{if } \Delta E > 0 \\ M(T) & \text{if } \Delta E \leq 0 \end{cases} \tag{26}$$

Here ΔE stands for the change in the system energy caused by the state change of the site under consideration and calculated with Eq. (10). The function $M(T)$ denotes the temperature-dependent mobility and k_B ($m^2 \text{ kg s}^{-2} \text{ K}^{-1}$) is the Boltzmann constant. The product $k_B T_{MC}$ defines the thermal fluctuations of the simulation and T_{MC} represents the so-called ‘simulation’ (or ‘absolute’) temperature, which is not related to a real physical temperature in contrast to T . For example, Rodgers et al. [734] set $T_{MC} = 0.66$, following [737], while researchers [728,729] suggest that the product $k_B T_{MC}$ can be set to 0. The transition probability might be defined in a different way [735].

In some works [716,730], the temperature-dependent mobility $M(T)$ is set to 1. In general, the mobility function might be introduced in the kMC Potts model to yield different rates of grain growth in calculations. Apparently, if this case considers the zero limit of the simulation temperature, all state assignments that decrease or do not change energy are accepted whereas those resulting in the energy increase get declined and the previous state configuration is kept.

In their kMC simulations for PBF, Rodgers et al. [728] integrated the mobility function to differentiate the microstructure evolution in the melt and heat-affected zone. They assigned spins at random to sites located in the melt and suggested that the grain boundary mobility follows an Arrhenius relationship with temperature in the heat affected zone

$$M(T) = M_0 \exp\left(-\frac{Q}{RT}\right) \tag{27}$$

Here Q (J/mol) represents the activation energy that was assumed constant in [728], R (J/K mol^{-1}) denotes the gas constant, and M_0 stands for a material-specific Arrhenius prefactor that is often set constant [728,731,734] or can be defined as $M_0 = \frac{d^4 \nu_D}{k_B T_{MC}}$ [732]. Here d represents the interatomic spacing and ν_D is the Debye frequency. However, Ge et al. [732] did not integrate the mobility into the transition probability but used it to determine the interface moving velocity. In [647], the mobility was suggested to be a function of the smallest available misorientation angle θ between any $\langle 001 \rangle$ axis of the site-candidate for switching the state and the solidification direction

$$M(\theta) = c_0 + c_1 \cos(c_2 \theta) \tag{28}$$

Simulation time in kMC modeling is quantified by Monte Carlo steps (MCS)

$$t_{MC} = n/K \tag{29}$$

where K is the number of sites in the computational domain considered, and n stands for the number of trial switches. In other words, 1 MCS corresponds to K reorientation attempts. Note that Δt_{MC} has the unit of MCS.

Among the advantages of the kMC Potts model are its flexibility, computational simplicity, and relatively short calculation times. The absence of spatial and kinetic scaling along with the challenge of accounting for the crystallographic orientations of grains represent the weaknesses of the approach.

The integration of an adequate physics-based model of the described situation into Monte Carlo simulations is required to introduce scaling. For example, describing recrystallization and curvature driven grain growth, Raabe [736] offered to scale the model using the phenomenological rate theory of grain boundary motion [738] mapped on a simulation mesh (often referred to as a lattice in numerical studies applying the Monte Carlo Potts approach). He stated the equivalence of spin flips in the kMC Potts model and real grain boundary motion, which yielded the following expression for the real time during many MCS

$$t_{\text{real}} = \frac{\lambda_p}{t_{\text{MC}} M p} = \frac{\lambda_p}{t_{\text{MC}} M_0 (p_c + p_s)} \exp\left(\frac{Q}{k_B T_{\text{MC}}}\right) \quad (30)$$

Here λ_p (m) represents the jump width or lattice parameter of the Potts model, p stands for the driving force, where subscripts c and s denote configurational contributions (for instance, through grain boundary curvature) and scalar contributions to the driving force (for example, through the elastic energy related to stored dislocations). M_0 is the pre-exponential factor defined in [736] as $M_0 = \frac{v_D b \Omega}{k_B T_{\text{MC}}} \exp\left(\frac{\Delta S_f + \Delta S_m}{k_B}\right)$ following [738], where b represents the magnitude of the Burgers vector, Ω denotes the atomic volume, ΔS_f and ΔS_m are the entropy of formation and of motion, respectively. t_{real} has the unit of [s/MCS].

Some authors [739,740] assume that an MCS is linearly proportional to the real time

$$t_{\text{MC}} = C t_{\text{real}} \quad (31)$$

and the fitting parameter C can be determined by comparing simulation results with experimental data. In his study [736], Raabe also discussed previous scaling approaches to relate an MCS Δt_{MC} to the real time step Δt_{real} suggested in [741,742].

MCS are considered in some kMC simulations for MAM [647,728,729] without being related to the real time. Simulating the grain structure evolution in Ti-6Al-4 V alloy during DED in a 2D setting, Zhang et al. [730] suggested the following relationship between the MCS and real time

$$t_{\text{MC}}^{(n+1)n_1} = \left(\frac{d_0}{K_1 \lambda}\right)^{n+1} + \frac{(n+1)\alpha_{\text{mcs}} C_1^n}{(K_1 \lambda)^{n+1}} \sum_{i=1}^{n_1} \left[\exp^n\left(-\frac{Q}{RT_i}\right) t_{\text{real},i} \right] \quad (32)$$

Here d_0 stands for the initial grain size, K_1 and n_1 represent two simulation constants calculated with regression analysis, α_{mcs} and n' denote the scale factors. The offered dependence (32) follows the experimental data based model proposed in [743] and was adopted to determine the relationship between the phase transformation time and real time. A similar time model was adopted in [734]:

$$t_{\text{real}} = \frac{dx^2 K_{\text{MC}}}{K_0} \exp\left(\frac{Q}{RT}\right) \Delta t_{\text{MC}} \quad (33)$$

where dx (m) is the mesh element size (also referred to as lattice spacing) and K_0 and K_{MC} are the simulation parameters. The latter parameter is calculated by fitting the equation defining the mean grain size, d_{MC} , with respect to Monte Carlo time

$$d_{\text{MC}}^2 = K_{\text{MC}} t_{\text{MC}} \quad (34)$$

This equation defines grain growth in isothermal kMC simulations. The model (33) comes from the assumption on the linearly proportional simulation length scale to the experimental scale

$$d = dx \cdot d_{\text{MC}} \quad (35)$$

substituted to grain growth kinetics

$$d^n = K_0 \exp\left(-\frac{Q}{RT}\right) t \quad (36)$$

Here the parameters n and K_0 and the activation energy Q are determined by fitting to the data of isothermal grain growth experiments [734,743]. For this purpose, the average grain size is measured at multiple times in a sample held at a constant temperature.

The numerical studies considered demonstrate that the kMC Potts approach can efficiently describe the grain structure evolution in a multitrack and multilayer component. However, some researchers remain rather skeptical about the capabilities of the kMC Potts model for microstructure prediction. According to Rollett and Manohar [744], the kMC method should be applied to 'gain insight into a physical system' rather than 'interpreting the results as being directly representative of a particular material'. Rodgers et al. [734] point out the absence of a rigorous quantitative kinetic relationship between the kMC Potts model and physical parameters and the trial-and-error calibration of simulation kinetics with materials and manufacturing process. Furthermore, the kMC simulation results significantly depend on the size of a simulation domain and of temperature zones (melt pool and region around it referred to as a heat affected zone [728]) and laser scanning parameters [731]. Sunny et al. [731] summarized six limitations of the kMC Potts model applied to describe the grain structure evolution during MAM. Körner et al. [623] highlight that the current kMC approach 'is not able to predict grain structure evolution' due to the failure of the underlying mechanism (curvature driven grain growth) to represent the real one (competitive grain growth) and do not recommend to use the kMC Potts model to simulate the microstructure evolution during MAM.

3.2.1.4. Phase field simulations. The origins of the PF approach are summarised in the seminal work of Karma and Rappel [745], referring to studies published in the 1980 s [746–748]. This method belongs to a larger class of approaches considering a microscopically sharp interface as a diffuse region of finite thickness evolving in the simulation domain. For this purpose, a variable φ is introduced as a function of time and spatial coordinates. The variable φ smoothly varies between two integer values over the continuous transition region and could also describe the distribution of interfacial forces in this region. In the PF approach, φ is referred to as the PF variable and describes the state of the matter, liquid or solid. Similar to other microstructure modeling approaches

discussed above, the PF method has been applied to describe solidification, solid state transformation, recrystallization, solid state grain growth [749], and even the evolution of defects to describe the dynamics of fracture [750].

Similar to many physical processes, the driving force for microstructure evolution is the opportunity to reduce the free energy of a system. The development of a typical PF model begins with the definition of the free energy F that is formulated as a functional of the set of PF variables φ and their gradients. The functional might include different energy contributions, e.g. bulk free energy, interfacial energy, elastic energy, and energy terms related to magnetic, electrostatic or electrochemical interactions [751–753]. The bulk free energy, also referred to as the chemical free energy [753], describes the compositions and volume fractions of the equilibrium phases [751]. The interfacial and strain energy contributions influence the equilibrium compositions and phase volume fractions and determine the morphology and mutual arrangement of the phase locations. The formulation of a particular free energy functional depends on a specific problem. For example, when temperature, pressure and molar volume are assumed constant and the problem does not consider elastic, magnetic or electric fields, the total free energy of the system,

$$F(\varphi, \eta_k) = \int_V f(\varphi, \eta_k, \nabla\varphi, \nabla\eta_k) = \int_V \left[f_0(\varphi, \eta_k) + \frac{\epsilon}{2}(\nabla\varphi)^2 + \sum_k \frac{\kappa_k}{2}(\nabla\eta_k)^2 \right] dr \quad (37)$$

is defined by a concentration field φ and an array of order parameter fields η_k , $k = 1 \dots p$ [751]. Here $f_0(\varphi, \eta_k)$ (J/m³) represents the classical thermodynamic free energy density of a homogeneous system described by the local values of PF variables and refers to the bulk equilibrium conditions of the coexisting regions. The local free energy density of a heterogeneous system characterized by diffuse interfaces is defined by $f(\varphi, \eta_k, \nabla\varphi, \nabla\eta_k)$. The second and third terms on the right hand side of Eq. (22) define the diffuse behavior of the interfaces, ϵ and κ_k are the gradient energy coefficients related to the interfacial energy and thickness.

The PF method describes the evolution of a PF variable with two parabolic partial differential equations, the PF evolution equation and either solute or heat conservation equation, depending on the process controlling solidification. These equations are derived from thermodynamics under the assumption of an expression for the entropy distribution in the system and of positive generation of entropy [625].

In front-tracking approaches to solve the full time-dependent free-boundary problem [754–757], interfacial boundary conditions should be applied to define the match between individual solutions of transport equations at the interface between the bulk phases. As opposed to front-tracking approaches, the PF model avoids explicit tracking of an interface whose location is a part of the solution searched for (Stefan problem). Interfacial boundary conditions are not required in the PF method, which is considered its main advantage [758,759]. While other diffuse interface approaches (e.g., the level set method [760]) still require accurate calculation of interface normals and curvatures [758], the PF approach defines the interface evolution by solving the PF equation.

As highlighted by Boettinger et al. [761], PF models can be subdivided into several classes, including models involving a single scalar order parameter and those considering multiple order parameters, models derived from a thermodynamic formulation and those built based on geometrical arguments. Some formulations are better suited for large deviations from the local equilibrium; others are not. Some PF models reflect physics, while others should be considered as merely a calculation technique. A summary of PF modeling might be found in seminal works [749,751,758,759,761].

As shown in Fig. 30, the PF method is the most widely mentioned in conjunction with ‘additive manufacturing’ and ‘microstructure’. The MAM community uses a number of different PF models: some of them employ complex thermodynamics-based formulations [614,753,762,763] limiting the computational possibilities due to high cost, while others try to adapt the mathematics so as to consider several layers at least in a 2D setting [764,765]. Some of them consider the microstructure evolution only during solidification [614,753,762,764], while others incorporate solid state phase transformations [766] or solid state grain coarsening [765] as well. Both grain scale [764,765] and substructure scale modelling [614,762,763] for MAM is conducted using the PF approach.

Grain scale PF methods typically consider two kinds of non-conservative PF variables to define the state of the matter and grains. The latter are defined through a set of order parameter fields. For example, in their PF formulation, Lu et al. [764] considered the phase field φ^k to identify the state of the matter (where k might be l, s, v, b that stand for liquid, solid, gas, and base metal, respectively) and the grain field φ^{si} to define grains with different crystallographic orientations ($i = 1, 2, \dots, \text{NG}$, where NG is the number of crystallographic orientations considered in the simulation). A similar approach was adopted in [765] but only liquid and solid states were considered.

Instead of adopting a thermodynamics-based expression, Lu et al. [764] adopted a simple interpolation to define free energy to deal with the solid–liquid transformation. The evolution of the composition field was omitted from consideration in [765], in the assumption that the composition distribution would not significantly affect grain growth. These simplifications enabled simulations of the grain structure evolution in multiple layers of LPBF fabricated Ti-6Al-4 V alloys in 2D [764] and in three-layer three-track LPBF of 316L steel [765]. Furthermore, while Lu and colleagues [764] considered 20 different crystallographic orientations in the PF formulation, neither grains of different orientations were observed in their study, nor the texture analysis of virtually printed Ti-6Al-4 V samples was conducted.

Other researchers [614,762,763] integrated the composition field in their PF models by means of the solute concentration c (wt. %) described with a generalized supersaturation field U (-) to simulate the complex solidification substructure and resolve concentration distribution. Such formulations are limited by high computational costs and allow only small regions containing a few dendrites (e.g., small selected areas in the melt pool) to be considered, which is not representative of the MAM process. In single scale approaches, therefore, substructure simulations should be treated as tools enabling the microstructure prediction in conditions similar to MAM ones. However, substructure models enable the evolution of complex microsegregation patterns to be analyzed. This is vital, e.g., to study precipitation [766] playing a key role in the mechanical response of a MAM produced material. Furthermore, the substructure

Table 7

A brief overview of PF modeling of the microstructure evolution during MAM.

Topic, highlights and reference	PF model
Effects of scanning speed and laser power on the grain structure and porosity of LPBF Ti-6Al-4 V titanium alloy using a 2D grain-scale model. Multilayer simulations.[764]	<p>Free energy functional: $F = \int_V \left\{ f_{\text{phase}} + (\varphi^s)^2 \cdot f_{\text{grain}} + (1 - \varphi^s)^2 \sum_{i=1}^{\text{NG}} (\varphi^{si})^2 + f_{\text{grad}} \right\} dV$. (1) f_{phase} is the free energy density for phase transformation without taking the grain structure into account; f_{grain} is the free energy density for grain evolution; f_{grad} is the gradient energy density (contributions of phase-phase boundaries and grain-grain boundaries); φ^k is the phase field, where k might be l, s, v, b that stand for liquid, solid, gas, and base metal, respectively; φ^{si} is the grain field, each superscript i stands for a crystallographic orientation; NG is the number of crystallographic orientations considered in the simulation; $f_{\text{phase}} = \rho^2 (\varphi^b - 1)^2 \left[(\varphi^s - 1)^2 \cdot \Phi(\tau) + (\varphi^l - 1)^2 \cdot \{1 - \Phi(\tau)\} \right] + (\rho - \varphi^s \rho^s - \varphi^l \rho^l - \varphi^b \rho^b)^2 (\varphi^v - 1)^2 + \omega \cdot \sum_{i \neq j} (\varphi^i \varphi^j)^2$. (24) $\tau = T/T_L$; T_L is the liquidus temperature; $\Phi(\tau)$ is the interpolation function; $\Phi(\tau) \rightarrow 1$ when $\tau < 1$; $\Phi(\tau) \rightarrow 0$ when $\tau \geq 1$. $f_{\text{grad}} = \frac{1}{4} \sum_{i=1}^{\text{NG}} \left[(\varphi^{si})^2 - 1 \right]^2 + \frac{3}{4} \sum_{i < j}^{\text{NG}-1} (\varphi^{si} \varphi^{sj})^2 - \frac{\text{NG} - 1}{4}$. (2) $f_{\text{grad}} = -\sum_{i < j}^4 k_{ij} \nabla \varphi^i \nabla \varphi^j - \sum_{i < j}^{\text{NG}} k_g \nabla \varphi^{si} \nabla \varphi^{sj}$.</p> <p>(3) k_p and k_g are the gradient energy coefficients for phase and grain boundaries, respectively; Governing (kinetic) equations (time-dependent Ginzburg-Landau equations): $\frac{\partial \rho}{\partial t} = \nabla M(\varphi^k, T) \nabla \frac{\delta F}{\delta \rho}$, (4) $\frac{\partial \varphi^k}{\partial t} = -L(\varphi^j, T) \cdot \frac{\delta F}{\delta \varphi^k}$, (5) $\frac{\partial \varphi^{si}}{\partial t} = -L_g^i(\varphi^j, T) \cdot \frac{\delta F}{\delta \varphi^{si}}$. (6) M, L, and L_g^i are the temperature-dependent kinetic coefficients; $M = M_0 \exp[-Q_M/RT]$, $L = L_0 \exp[-Q_L/RT]$, $L_g^i = L_{g0}^i \exp[-Q_g/RT]$. M_0, L_0, L_{g0}^i are constant pre-exponential coefficients; Q_M, Q_L, Q_g are the activation energies.</p> <p>Free energy functional: $F = \int_V \left\{ f_{\text{phase}} + f_{\text{grain}} + f_{\text{grad}} \right\} dV$, (7) $f_{\text{phase}} = m_p \left\{ (1 - \varphi)^2 \times \Phi(\tau) + \varphi^2 [1 - \Phi(\tau)] \right\}$. (8) φ is the phase field; $\varphi = 0$ in the liquid phase and 1 in the solid phase. $m_p = \frac{3}{4} \frac{\sigma_p}{(\Delta f_p) l_p}$ is the pre-coefficient, where σ_p denotes the solid liquid interfacial energy assumed isotropic and constant, and l_p is the solid liquid interfacial width (adjustable variable). $\Phi(\tau) = \frac{1}{2} \{1 - \tanh[\vartheta \times (\tau - 1)]\}$, ϑ is the constant assigned to ensure that $\Phi(\tau)$ tends to be 0 when $\tau > 1$ and 1 when $\tau < 1$. Thus, $\Phi(\tau) = 0$ in the liquid phase and 1 in the solid phase. This allows to consider the temperature field influence on liquid to solid transformation. $f_{\text{grain}} = m_g \left[\sum_{i=1}^{\text{NG}} \left(\frac{(\varphi^{si})^4}{4} - \frac{(\varphi^{si})^2}{2} \right) + \gamma \sum_{i=1}^{\text{NG}} \sum_{j \neq i} (\varphi^{si})^2 (\varphi^{sj})^2 + \frac{1}{4} (1 - \varphi)^2 \sum_{i=1}^{\text{NG}} (\varphi^{si})^2 \right]$.</p> <p>(9) $m_g = \frac{3}{4} \frac{\sigma_{g0}}{(\Delta f_g) l_g}$ is the pre-coefficient, where σ_{g0} is the constant, l_g denotes the grain boundary width set as $l_g = l_p, \Delta f_p$ and Δf_g are the maximum height of the barrier in the free energy density between two minima; γ is the model parameter, its value is determined by grain boundary energy and width. $f_{\text{grad}} = \frac{\kappa_p}{2} (\nabla \varphi)^2 + \frac{\kappa_g}{2} (\nabla \varphi^{si})^2$. (10) $\kappa_p = \frac{3}{4} \sigma_p l_p$ and $\kappa_g = \alpha_k \sigma_g l_g$ are the gradient term coefficients for solid liquid interface and grain boundary, respectively. $\sigma_g = \sigma_{g0} \{1 + \epsilon (\cos^4 \theta_{\text{inc}} + \sin^4 \theta_{\text{inc}})\}$ is the grain boundary energy, ϵ is the phenomenological parameter that controls the anisotropy strength, θ_{inc} is the inclination angle, which is the minimum angle between the normal direction of the grain boundary and the (001) orientation. Governing equations (time-dependent Ginzburg-Landau equations): $\frac{\partial \varphi(r, t)}{\partial t} = -L_p \frac{\delta F(\varphi, \varphi^{si}, T)}{\delta \varphi(r, t)}$, (11) $\frac{\partial \varphi^{si}(r, t)}{\partial t} = -L_g^i \frac{\delta F(\varphi, \varphi^{si}, T)}{\delta \varphi^{si}(r, t)}$. (12) t is time; r is the coordinate vector; L_p and L_g denote the temperature-dependent kinetic coefficients related to mobility of the solid liquid interface and grain boundary; $L_g = \frac{D_g}{\alpha_k l_g}$, where $D_g = D_0 \exp\left(-\frac{Q_g}{RT}\right)$ is the grain boundary mobility; D_0 is the constant pre-exponential coefficient.</p>
2D substructure-scale model describing the evolution of Ti-6Al-4 V titanium alloy in conditions similar to EPBF[762]	<p>Total free energy density: $f(c, \varphi) = h(\varphi) f^s(c_s) + \{1 - h(\varphi)\} f^l(c_l) + \omega \cdot g(\varphi)$, (13) $c = h(\varphi) c_s + \{1 - h(\varphi)\} c_l$, (14) $\mu^s(c_s) = \mu^l(c_l)$, (15) $h(\varphi) = \varphi^3 (6\varphi^2 - 15\varphi + 10)$; $g(\varphi) = \varphi^2 (1 - \varphi)^2$; c is the solute concentration. The chemical potentials μ^l and μ^s of liquid and solid phases, respectively, can be found from the respective free energy densities f^l and f^s. As in the previous row, the phase field $\varphi = 0$ in the liquid phase and 1 in the solid phase. Governing equations (PF and diffusion equations): $\frac{\partial \varphi}{\partial t} = M \left[\epsilon^2 \nabla^2 \varphi - h'(\varphi) \{f^s - f^l\} - \omega \cdot g'(\varphi) \right]$, (16) $\frac{\partial c}{\partial t} = \nabla \cdot \left[\frac{D(\varphi)}{\partial^2 f / \partial c^2} \nabla \frac{\partial f}{\partial c} \right]$. (17) M is the PF parameter; D is the solute diffusion coefficient; ϵ is the gradient energy coefficient; ω is the height of double potential.</p>
2D substructure-scale model describing the evolution of IN718 nickel-based superalloy in conditions similar to EPBF[763]	<p>Governing equations for PF and concentration variables[759]: $\tau_0 \alpha(\bar{n}) \left[1 - (1 - k) \frac{z - V_p t}{l_T} \right] \frac{\partial \varphi}{\partial t} = \nabla \cdot \left[W(\bar{n})^2 \nabla \varphi \right] + \varphi - \varphi^3 - \lambda g(\varphi) \left[U + \frac{z - V_p t}{l_T} \right]$, (18) $\left(\frac{1+k}{2} - \frac{1-k}{2} \varphi \right) \frac{\partial U}{\partial t} = \nabla \cdot \left[D_L q(\varphi) \nabla U + a(\bar{n}) W \{1 + (1 - k) U\} \frac{\partial \varphi}{\partial t} \frac{\nabla \varphi}{ \nabla \varphi } \right] + \frac{1}{2} [1 + (1 - k) U] \frac{\partial \varphi}{\partial t}$. (19) The solute concentration c is described with a generalized supersaturation field $U = \frac{1}{1 - k} \left(\frac{2kc/c_{\infty}}{1 + k - (1 - k)\varphi} - 1 \right)$.</p>

(continued on next page)

Table 7 (continued)

Topic, highlights and reference	PF model
2D substructure scale non-equilibrium model describing the rapid solidification microstructure of Ni-Nb alloy in conditions similar to LPBF [753]	<p>(20)$a(\hat{n}) \equiv a(\theta) = 1 + \epsilon' \cos 4\theta$ is the <u>fourfold surface energy anisotropy function for cubic crystals, with the inclination angle</u> $\theta = \arctan(\partial_z \varphi / \partial_x \varphi)$; c_∞ is the average solute concentration far from the solid-liquid interface. The phase field $\varphi = -1$ in the liquid phase and 1 in the solid phase. k is the partition coefficient; $g(\varphi) = (1 - \varphi^2)^2$ is the double-well function that stabilizes the two phases φ ensuring that $g(-1) = g(1) = 0$; $q(\varphi) = (1 - \varphi)/2$ ensures zero solute diffusivity in solid; D_L is the solute diffusivity in the liquid; $l_T = m_L c_\infty(1 - k)/kG$ is the thermal length; m_L is the liquidus slope; $W = d_0 \lambda / a_1$ is the interface width (length scale); a_1 and λ are constants; $d_0 = \Gamma / m_L (1 - k)c_l$ is the capillary length; Γ is the Gibbs-Thomson coefficient; $c_l = c_\infty/k$ is the concentration in the liquid at the interface. $\tau_0 = a_2 \lambda W^2 / D_L$ is the relaxation time; a_2 is the constant. The model considers the 'frozen temperature approximation', which translates the temperature gradient G along the vertical z axis following $T = T_0 + G(z - V_p t)$; $T_0(z = 0, t = 0)$ is a reference temperature. The main variables φ and U are related to the temperature T through the term $(z - V_p t) / l_T$ in Eq. (21) where V_p can be found from the melt pool solid liquid interface determined from thermal simulations.</p> <p><u>Free energy functional:</u> $F = \int_V \{ f_{int} + f_{chem} \} dV$, (22) $f_{int} = \frac{4\sigma_{\alpha\beta}}{\eta} \left\{ \frac{\eta^2}{\pi^2} \nabla \varphi_\alpha \cdot \nabla \varphi_\beta + \varphi_\alpha \varphi_\beta \right\}$, (23) $f_{chem} = \varphi_\alpha f_\alpha(c_\alpha) + \varphi_\beta f_\beta(c_\beta) + \lambda \{ c - (\varphi_\alpha c_\alpha + \varphi_\beta c_\beta) \}$. (24) $\sigma_{\alpha\beta}$ is the interfacial energy between α and β phases; η is the <u>interface width</u>; $\varphi_{\alpha/\beta}$ is the phase fraction of a corresponding phase, $\varphi_\alpha + \varphi_\beta = 1$; $c_{\alpha/\beta}$ is the <u>concentration of a corresponding phase</u>; c is the overall concentration; $f_{\alpha/\beta}$ is the free energy density of a corresponding phase derived within the CALPHAD formalism [768]; λ is the Lagrange multiplier needed to ensure the solute conservation constraint $c = \varphi_\alpha c_\alpha + \varphi_\beta c_\beta$. At the alloy composition $c_{alloy} = 3.2$ (at% Nb), <u>two phases (liquid and γ) read</u> $f_\alpha V_m = c_\alpha G_{Nb}^0 + (1 - c_\alpha) G_{Ni}^0 + RT \{ c_\alpha \ln(c_\alpha) + (1 - c_\alpha) \ln(1 - c_\alpha) \} + c_\alpha (1 - c_\alpha) \sum_{i=1}^n G_i (2c_\alpha - 1)^i$, (25) V_m is the molar volume; G_{Nb}^0 and G_{Ni}^0 are the reference states of constituent elements; G_i are coefficients that contribute to excess Gibbs energy. <u>Governing equations for the phase concentrations (obtained using variational principles):</u> $\varphi_\alpha \dot{c}_\alpha = \nabla(\varphi_\alpha D_\alpha \nabla c_\alpha) + P^{int} \varphi_\alpha \varphi_\beta \left(\frac{\partial f_\beta}{\partial c_\beta} - \frac{\partial f_\alpha}{\partial c_\alpha} \right) - \varphi_\alpha \dot{\varphi}_\alpha (c_\beta - c_\alpha)$, (26) $\varphi_\beta \dot{c}_\beta = \nabla(\varphi_\beta D_\beta \nabla c_\beta) + P^{int} \varphi_\alpha \varphi_\beta \left(\frac{\partial f_\alpha}{\partial c_\alpha} - \frac{\partial f_\beta}{\partial c_\beta} \right) - \varphi_\beta \dot{\varphi}_\beta (c_\alpha - c_\beta)$, (27) $D_{\alpha/\beta}$ is the chemical diffusivity in the respective phase; $P^{int} = 8M/a\eta$ is the interface permeability; M is the atomic mobility; a is the lattice constant. <u>Governing equations for the phase fractions (obtained using variational principles):</u> $\dot{\varphi}_\alpha = K \left\{ \sigma_{\alpha\beta} \left[\nabla^2 \varphi_\alpha + \left(\frac{\pi}{\eta} \right)^2 \left(\varphi_\alpha - \frac{1}{2} \right) \right] - \frac{\pi^2}{8\eta} \Delta g_{\alpha\beta}^{\sigma} \right\}$, (28) $K = \frac{8P^{int} \eta M_{\alpha\beta}}{8P^{int} \eta + M_{\alpha\beta} \pi^2 (c_\alpha - c_\beta)^2}$, (29) $\Delta g_{\alpha\beta}^{\sigma} = f_\alpha - f_\beta + \left(\varphi_\alpha \frac{\partial f_\alpha}{\partial c_\alpha} - \varphi_\beta \frac{\partial f_\beta}{\partial c_\beta} \right) (c_\beta - c_\alpha)$, (30) $M_{\alpha\beta}$ is the interfacial mobility; $\Delta g_{\alpha\beta}^{\sigma}$ is the chemical driving force. K is the kinetic coefficient showing the effect of finite diffusion and redistribution at the interface. The governing equation for φ_β can be derived from $\varphi_\beta = 1 - \varphi_\alpha$. For the solid-liquid interface characterised by <u>fourfold anisotropy, the interfacial energy and interface mobility are approximated as</u> $\sigma_{\alpha\beta}(n) = \sigma_{\alpha\beta}^0 (1 - \epsilon [3 - 4(n_x^4 + n_y^4)])$, (31) $M_{\alpha\beta}(n) = M_{\alpha\beta}^0 (1 - \epsilon [3 - 4(n_x^4 + n_y^4)])$, (32) $\sigma_{\alpha\beta}^0$ is the interfacial energy coefficient; ϵ is the anisotropy coefficient; $M_{\alpha\beta}^0$ is the interface mobility coefficient; $n = (n_x, n_y)$ is the interface normal vector defined as $n = \nabla \varphi_\alpha / \nabla \varphi_\alpha \cdot \alpha$ represents a solid phase.</p>

scale modeling is helpful for the identification of dendrite tip growth rate, which might be integrated into grain scale front tracking approaches.

As mentioned above, the PF approach is very flexible depending on the modelling intent and is mathematically rigorous, which requires profound expertise in the area. Table 7 serves for illustrative purposes to demonstrate a wide variety of the PF mathematical formulations available in the MAM space, both for the grain and substructure scales. As might be seen from Table 7, PF models require a number of different material and model parameters, which induces uncertainty related to the choice/identification of each parameter, in particular considering that the material parameters might be unknown (e.g., temperature-dependent mobility coefficients [623]). On the other hand, atomistic simulations help obtain material parameters (e.g., kinetic coefficients) [767], which highlights the need for multiscale modeling for MAM. Fig. 44 shows some examples of model predicted microstructures using the grain scale and substructure scale PF models.

In summary, the PF approach has a profound physics-based fidelity in describing microstructure features and the composition evolution but requires an accurate consideration due to uncertainty related to a variety of necessary material and model parameters, the very mathematics and the required profound expertise in the area. Körner et al. [623] highlight the importance of the PF method in bridging between atomistic and grain scale approaches to simulate microstructure evolution. However, as compared to CA and kMC Potts methods, the PF approach still requires considerable computational time. Even at the grain scale, it is capable to simulate few tracks and few layers in a 3D setting, and a search of the literature revealed very few studies capable of such simulations.

3.2.1.5. *Challenges and future directions.* Due to extreme process conditions, additively manufactured metals and alloys considerably differ in their microstructure from those fabricated by casting, mechanical working and subtractive machining techniques. Back in

2017, Francois and colleagues in their seminal perspective paper [769] highlighted that AM microstructures provide ‘a rich avenue’ for research into ‘into the long-standing endeavor of understanding and quantifying the process-to-performance linkage for material response’. This remains particularly relevant now.

New microstructure modeling approaches and further development of the existing ones remain an important priority for better process and performance representation and optimization. We outline some of the challenges below.

The continuous nucleation models employed to describe the generation of new crystals in front of a solid–liquid interface are empirical in essence and thus rely heavily on experimental data. These models use parameters that are supposed to be derived from experiments, as it was done for microstructure simulations of casting [651,770,771]. To our knowledge, however, currently parameters are either some random parameters, in particular where a model is presented without validation or phenomenon analysis, or are based on some earlier published literature where they are adjusted to obtain final microstructures similar to those observed experimentally in another manufacturing process [667,691,707,772] and sometimes they are chosen mistakenly. Admittedly, Boettinger [773] emphasized the difficulty of estimating the nucleation temperature because of poorly known materials parameters and potency of catalytic nucleation sites. In many processes, including MAM, very little is known about the temperature distribution of nuclei $dN/d(\Delta T)$. That is why sometimes researchers tend to use even simpler functions than Eq. (17) to describe nucleation.

Overall, research applying physics-based nucleation models supported by experiments will be helpful, in particular in computational materials design for MAM and in the prediction of AM microstructures of metallic materials with pronounced nucleation tendency (e.g., aluminum alloys [628,774]). While the research community is still on the way to the former direction, microstructures of AM materials with pronounced nucleation tendency are currently simulated either with artificial generation methods [628] or based on calibration [706]. We believe that the solution of this challenge might be found in applying multiscale microstructure modeling approaches.

Furthermore, it is common practice for many microstructural models to approximate complex multi-component alloys as binary ones (e.g. [641,643,653,657,775]) to decrease the model complexity and computational cost. This approach is rational; however, it involves a number of assumptions that might not accurately approximate the reality and thus bring inaccuracy and uncertainty in microstructure simulations. In the future, this issue should be carefully analyzed.

3.2.2. Deposition-scale MAM models (heat transfer, CFD, spatter, stresses, etc.)

In this sub-section and as mentioned in the prelude to section 3.2 on modelling of MAM processes, simulation platforms that model the melt pool and/or its surrounding’s conditions will be covered. The current sub-section is sub-divided into three different modelling groups of; I) powder-gas dynamics models, II) melt pool evolution models and finally, III) fully coupled powder-gas–melt pool simulations. The first group of deposition-scale models, simulates the aerodynamic conditions evolving around the deposition zone and capture the powder-gas interaction in both L-PBF and DED processes and does not take the melt pool’s internal fluid dynamics into consideration. The second group, the melt pool evolution models, simulate the melt pool’s evolving temperature field, velocity field and ultimately, the hydrodynamic conditions of the surface of the melt pool in MAM processes. The last group, the fully coupled models, simulate the entire powder-gas and melt pool conditions at the same time and thus the mutual impact of the surrounding gas dynamics and the adjacent moving powder particles on the melt pool’s internal heat and fluid flow. Especially contributions in the second group are more frequent in literature and this will to some extent also be reflected in our presentation, whereas the scarcity of the latter group of deposition-scale models means that we will treat the relatively few available models more in depth.

3.2.2.1. Powder-gas dynamics simulations. As per their name, powder-gas models are used to predict the aerodynamics conditions of surrounding or shield gas near the melt pool borders. Depending on their complexity, these models can simulate the powder particles’ trajectory, their motion dynamics as well as their temperature and fusion conditions, see Fig. 29.

In the L-PBF process, these models (see Fig. 45) can be used for simulating the cold spatter phenomenon i.e. the dislocation and

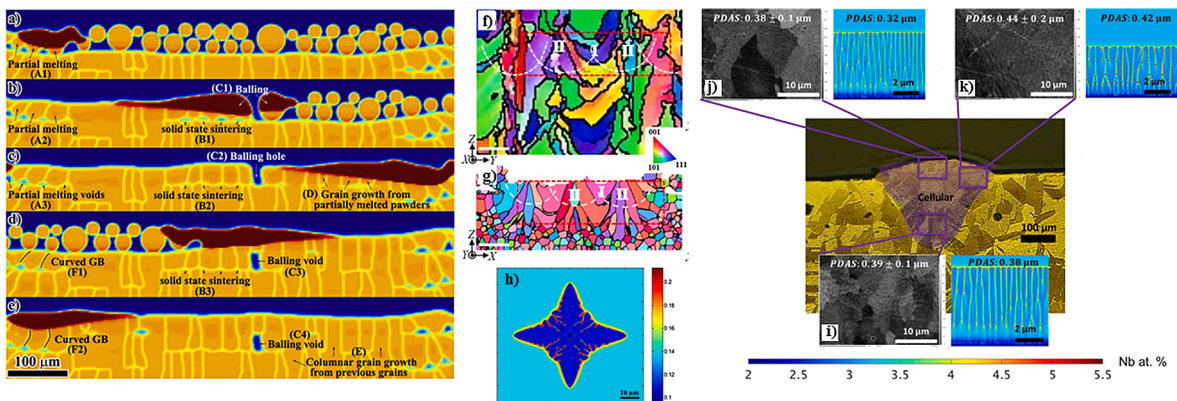


Fig. 44. Examples of PF simulations of AM microstructures: subfigures a-e are related to the PBF fabricated Ti-6Al-4 V [764]; subfigures f-g to LENS fabricated 304L stainless steel [728].

ejection of nearby solid-state powder particles close to the melt pool location (there has also been some attempts to model hot spatter [776] by [777]). When the amount of input energy delivered to the scanning area is sufficiently high, evaporation of the metallic phase initiates and this leads to the ejection of vaporized metal where an upwards jet stream forms and this jet tends to create a local low-pressure zone that drags the adjacent powder particles in and then carries them almost vertically up into the chamber [778,779].

Early examples of such simulations are the works by Masmoudi, Bolot and Caddet [780] and Bidare et al. [781] where in the former, the vapor plume forming in L-PBF of 316-L is simply modelled via adding a mass source into the mass balance equation, and in the latter, the Knudsen layer's assumption [782,783] is used to obtain the temperature-dependent vapor jet's velocity. Furthermore, in both of these works [780,781] the concentration of the evaporated metal in the surrounding is also calculated as a separate field variable. Bidare et al. [781] specifically reported a plume velocity of 800 m.s^{-1} based on their 2D finite element simulation. In both simulations [780,781], the powder layer is modelled as a continuum domain with effective properties. Therefore, a major drawback of this type of continuum-based powder layer assumption is that the explicit powder-powder as well as the powder-gas interaction is not simulated and these models can only model the plume formation in the presence of a resting surrounding gas. In a recent publication from the same group, Bitharas et al. [784] extended their previous 2D model to a 3D to study the influence of cross flow in L-PBF of 316-L steel, still assuming a continuum domain for powder particles. However, still the major drawback of this model is its inability to explicitly track the powder particles' motion as well as their flying distance and relocation on the powder bed.

Li and Tan [785] developed a 2D computational fluid dynamics (CFD) simulation coupled with a Lagrangian particle tracking (LPT) solver to simulate the interacting powder-gas conditions in the L-PBF process of Ti6Al4V. The vapor plume was explicitly modelled by adding a jet-like boundary condition with an experimentally-found [20] inlet velocity of 500 m.s^{-1} with a width of $200 \mu\text{m}$ [785]. Furthermore, the pressure- and velocity-related forces from the CFD simulation of the hosting fluid were calculated and then mapped to the Lagrangian points of the powder particles to find their linear as well as angular velocities. In [786] a 3D coupled finite volume (FVM) discrete element method (DEM) model was developed to simulate cold spatter during L-PBF of 316-L stainless steel. In a similar manner to [785], in [786] a localized moving jet boundary condition with prescribed velocity of 150 m.s^{-1} and temperature of 3080 K was added to account for the plume's thermo-aerodynamics impacts on the powder particles. Very recently, a somewhat similar methodology was applied in [787] where the focus is more on how different jet angles could lead to the denudation. In [788] a 2D axis-symmetric model of the vapor plume formation as well as the subsequent spatter was developed using a particle-based gas kinetic direct simulation Monte Carlo method. Like the previous works by [785,786], in [788] the plume was simplified by simulating it with an inlet boundary condition with prescribed temperature. This assumption would give satisfactory results while predicting the powder particles' motion, but it lacks the ability of taking the unsteady and highly transient behavior of the vapor plume, as triggered by melt pool's instability, into account.

In contrast to the very recent L-PBF models discussed above, powder-gas simulations of powder DED processes have been under constant development well over 20 years, therefore they are more matured. Powder-gas simulations of powder DED are made mainly numerically and to a lesser extent and mostly in the 2000's, analytically, with the primary goal of predicting the powder particles' concentration at different cross-sections of the powder stream and along the injection direction. In another analytical model in [789] it was assumed that the powder concentration is inversely related to the width of the powder streams during powder DED. In another analytical model presented in [790] it was shown that the powder concentration profile transforms from an annular shape to a nearly Gaussian shape at the convergence point of the streams. Furthermore, they simulated the attenuation of the laser beam based on the Beer-Lambert law while using the analytically-derived powder particles' concentration profile mentioned earlier. In a later work, an analytical model was used to predict the powder particles' temperature while accounting for laser attenuation [791]. In their thermal model, they assumed that laser attenuation is proportional to the total area occupied or shadowed by the powder particles and they finally reported a laser attenuation of 7%, 28% and 39% at the focal point of powder streams, -1.00 mm and -2.00 mm below this

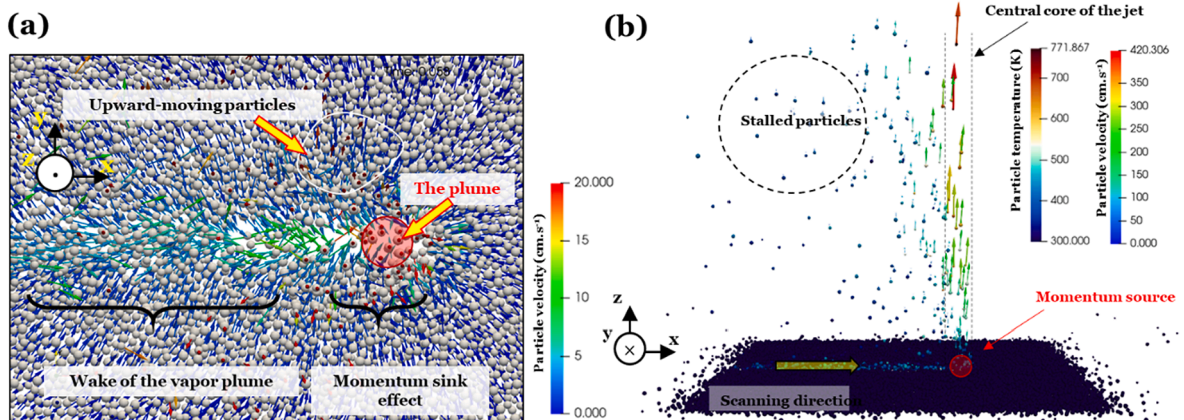


Fig. 45. Two snapshots of an powder-gas dynamics simulations of the spatter phenomenon from: (a) top view and (b) side view. The plume's motion dynamics is explicitly modelled via adding a momentum source with prescribed temperature and velocity magnitude (see (b)). Spatter simulations developed based on FVM-DEM at DTU.

plane, respectively. Finally in the analytical work [792], the influence of the angle between the powder jet and the laser beam in powder DED on the temperature of the powder cloud was studied and it was reported that the maximal attenuation is achieved under the perfect alignment, as expected.

Although analytical models of powder DED give a quick and approximate estimate of the powder-gas conditions along with the particles' evolving temperature, they have limited applications as they neglect important physical phenomena such as turbulence, stochastic motion of powder particles and their shadowing effects. Therefore, analytical models could be considered as a simple estimation tool that could replace advanced and time-consuming numerical simulations for industrial purposes and mainly for parameter adaptation.

Due to the mentioned limitations of analytical models, the focus of the more recent research works within the field has shifted towards numerical simulations, especially since they better resemble the real manufacturing conditions and have fewer fundamental assumptions. One of the earliest CFD simulations with an isothermal assumption was done by Lin [793] in 2000 and in this model, the powder-gas mixture was treated as a separate phase with its dispersion in the primary phase, i.e. the ambient gas being simulated with the dispersed phase method (DPM). Furthermore, Lin [793] accounted for turbulent flow and as a result solved the conservation of turbulent kinetic energy and its dissipation rate along with the continuity and linear momentum balance partial differential equations (PDEs). Table 8 lists the most important PDEs that describe this class of numerical simulations for powder DED as well as L-PBF processes. Note that the turbulence terms typically apply to powder DED simulations only.

In this type of powder-gas dynamics simulations, the Reynolds averaged Navier-Stokes (RANS) equations are solved in a Eulerian framework, while the DPM equation is solved via a force balance for the individual particles and on a Lagrangian framework. Flow compressibility, mutual powder-gas momentum coupling and finally turbulence are the three major physical phenomena in powder-gas aerodynamics models of powder DED processes and the complexity and accuracy of such models will be distinctly different depending on the inclusion or exclusion of these three types of physics. For instance, Zekovic et al. [797] developed an FVM-based 3D isothermal incompressible turbulent CFD model to simulate the aerodynamics conditions of powder streams during co-axial powder DED of H-13 tool steel. In their work, they considered the mutual momentum impact between powder particles and the carrying gas flow via introducing the $\Phi_{P-F,i}$ ($N.m^{-3}$) term in the RANS momentum equation (see Table 8), whereas in the earlier work of Lin [793] only the drag force from the host fluid on the powder particles was considered and as a result, the $\Phi_{P-F,i}$ ($N.m^{-3}$) term was set to zero. Moreover, Zekovic et al. [797] predicted the transformation in the shape of the powder concentration profile and subsequently identified the location of maximum powder concentration. In another work, Zhang et al. [798] developed a 2D axis-symmetric isothermal turbulent FVM-based CFD simulation with one-way coupling between the powder particles and carrier flow gas in the commercial software package ANSYS Fluent and reported that the powder concentration profile closely follows a Gaussian distribution near the focal plan where the powder streams converge and this is in agreement with widely-observed experimental investigations as well. In [799] a 2D thermo-aerodynamics compressible CFD simulation of powder DED with laminar flow assumption was developed and similarly to [793], DPM was used to calculate the powder particles' motion in [799]. As an entirely new feature as compared to [793], in [799], the temperature of the powder particles was determined based on a lumped thermal capacity analysis while accounting for laser absorption, radiative and convective heat transfer to the ambient as well as the particles' latent heat of fusion. Furthermore in [799] it was noticed that even though the Mach number is below 0.1 in all the simulations, the compressibility assumption is still valid since the gas density could change due to temperature changes during the laser heating step. This conclusion underlines the fact that the isothermal flow assumption could lead to inaccurate results, especially since the temperature rise due to laser heating is so significant that assuming incompressible flow is not valid.

Similar models but with the inclusion of turbulence were made in [800–802] where their salient features were including the shape-dependent drag coefficient in [800] (see Fig. 46 (b)), the particles' restitution coefficient in [801] and finally the laser attenuation effect in [803]. According to [801] a lower restitution coefficient of 0.91 leads to a more focused and less dispersed powder stream, compared to the case with 0.99 restitution coefficient.

Taberero et al. [802] simulated the powder concentration profile at different lengths along the deposition direction and they noticed that the maximum powder concentration level gradually drops due to damping of the streams into the resting host fluid. In their later model [803], they also accounted for laser attenuation and assumed that this only occurs after the focal plane [805], while

Table 8

List of PDEs describing powder-gas dynamics simulations of MAM processes [794–796]. Superscript O^F denotes fluid. ρ ($kg.m^{-3}$) is the density of the fluid.

Continuity	$\frac{\partial(\rho u_i^F)}{\partial x_i} = 0,$
Momentum balance	$\rho \left[\frac{\partial}{\partial t} u_i^F + \frac{\partial}{\partial x_j} (u_j^F u_i^F) \right] = -\frac{\partial p}{\partial x_i} + \rho g_i + \frac{\partial}{\partial x_j} (\sigma_{ij} + \tau_{ij}) + \Phi_{P-F,i},$
Conservation of turbulence's kinetic energy	$\rho \left[\frac{\partial}{\partial t} k + \frac{\partial}{\partial x_j} (u_j^F k) \right] = \frac{\partial}{\partial x_j} \left[\left(\mu_f + \frac{\mu_{nrb}}{\sigma_k} \right) \frac{\partial k}{\partial x_j} \right] + \tau_{ij} \frac{\partial u_i^F}{\partial x_j} - \rho \epsilon,$
Conservation of the dissipation rate of turbulence's kinetic energy	$\rho \left[\frac{\partial}{\partial t} \epsilon + \frac{\partial}{\partial x_j} (u_j^F \epsilon) \right] = \frac{\partial}{\partial x_j} \left[\left(\mu_f + \frac{\mu_{nrb}}{\sigma_\epsilon} \right) \frac{\partial \epsilon}{\partial x_j} \right] + \frac{\epsilon}{k} \left(C_{\epsilon 1} \tau_{ij} \frac{\partial u_i^F}{\partial x_j} - \rho \epsilon C_{\epsilon 2} \right),$
Stokes stresses	$\sigma_{ij} = \mu_f \left(\frac{\partial u_i^F}{\partial x_j} + \frac{\partial u_j^F}{\partial x_i} \right)$
Turbulent stresses	$\tau_{ij} = \mu_{nrb} \left(\frac{\partial u_i^F}{\partial x_j} + \frac{\partial u_j^F}{\partial x_i} \right) - \frac{2}{3} \rho k \delta_{ij}$

the laser attenuation is proportional to the projected area of powder particles. A more advanced thermal model that included both laser's initial and its subsequent back-reflection from the base plate impact on the powder particles, in addition to the initial laser irradiation by the laser for particles' temperature calculation was developed in [806] using the CFD-ACE + software package. It should be noted, however, that the fluid flow of the gaseous phase in [806] was considered to be laminar, as opposed to the earlier mentioned works accounting for turbulence. The laser beam attenuation was modelled in [807] and was set proportional to the total number of powder particles overshadowing the laser beam column. One of the most recent and most advanced aerodynamics simulations is presented in [804] which entails a two-way coupled turbulent flow CFD simulation of powder DED, see Fig. 46 (a). As was the case in [793] dated back from 2000, DPM was also used to model the powder particles' motion dynamics in [804]. Moreover, as a completely new feature, an advanced laser model was added where the transport of the Gaussian laser as well as its attenuation was modelled by introducing a PDE in the convective-diffusive form.

It is worth mentioning that the extent to which the major physical phenomena of turbulence, compressibility, base plate reflection and powder-gas momentum coupling, affect the powder-gas thermo-aerodynamics conditions is not clear, and literature lacks a dedicated work on how these influence the accuracy of powder-gas dynamics models of MAM.

The powder-gas dynamics models are well-suited for obtaining the location of impact of injected powder particles especially during the powder DED process in which its heat source has a small effective diameter. In this situation, it would be very cumbersome to establish the exact location of impact of the incoming powder particles experimentally, and hence powder-gas dynamics models could be implemented to pre-check how different nozzle designs and input parameters affect the dispersion of powder streams thus acting as a tool to tweak the process parameters to result in the highest powder catchment efficiency possible. However, it must be emphasized that standalone powder-gas simulations of powder DED processes are not able to give any indication of melt pool morphology and as such they are only used for the external flow analysis outside the melt pool. Hence, in order to model the entire process more realistically, they must be augmented by including melt pool simulation as well resulting in fully coupled powder-gas–melt pool models.

As regards the powder-gas models of the L-PBF process, such as the works by Chen and Yan [786] and Li and Tan [785], even though they do not simulate the melt pool evolution and the resultant transient behavior of the plume, these models are still very useful for predicting the denudation that could potentially lead to big surface defects when printing multiple tracks and layers. Further works are required to study how chambers with low pressure (near to vacuum) and at high Knudsen numbers could change the resulting denudation pattern.

3.2.2.2. Melt pool evolution simulations. Melt pool models constitute the largest part of the available simulations related to MAM and as their name also suggests, this type of models are used for predicting the transient evolution of different field variables related to the melt pool, and depending on the type of model, these variable could be liquid metal velocity, pressure, surface deformation, stresses, phase fraction, temperature, etc., see Fig. 29. Melt pool simulations of MAM processes in the broadest form could be divided into the two primary groups of conduction-based and transport-based simulations. The main distinction between these two types of simulations is whether they account for the fluid flow inside the melt pool. In this respect, conduction-based models only solve the PDE for energy

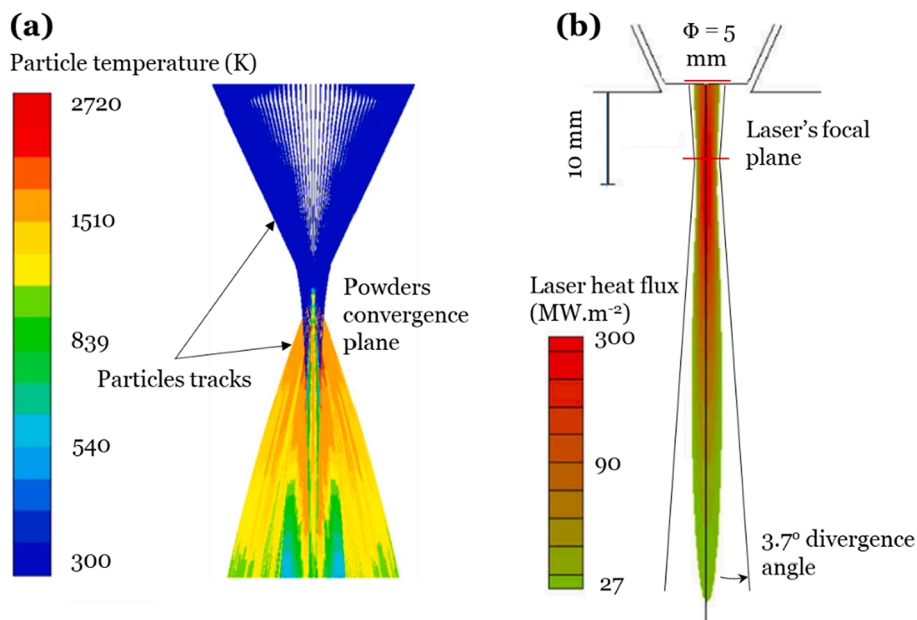


Fig. 46. (a) Simulated trajectory of ejected powder particles during powder DED of stellite 6 using the DPM method colored with calculated temperature [804]. (b) Predicted laser heat flux along the irradiation axis [800]. Note that in the latter, the laser heat flux attenuation is triggered by the beam's defocusing with 3.7° divergence angle.

balance with an assumed velocity of zero, while transport-based models apart from solving the energy balance also obtain the velocity and pressure fields from solving the coupled continuity and linear momentum balance together.

Although a significant amount of work has been done on numerical modelling of MAM processes, many research groups have also attempted to obtain the evolving temperature fields in these processes via various analytical models. This was for instance shown in the work of Kar and Mazumder [808] who solved the 1D transient temperature field during DED via a multi-region analytical model inspired by the classical textbook by Carslaw and Jaeger [809]. Bontha et al. [810] used the 2D version of the Rosenthal’s solution to obtain the temperature field around the melt pool in MAM of Ti6Al4V. They subsequently compared their calculated solidification parameters with the ones determined by an FEM thermal simulation and they could observe a very good agreement. Later on, Bontha et al. [811] extended their model to 3D and simulated the temperature field over an entire part during MAM. Other than Rosenthal’s solution, there are also different types of analytical models, like the Eager-Tsai [812] distributed heat source model, which is primarily developed for welding applications but are also applicable to MAM processes. El Cheikh et al. [813] (see Fig. 47 (a)) and Lalas et al. [814] made analytical-geometrical models to predict the shape of the tracks during DED and in the former, they described the shape of DED tracks with a semi-circular cross-section with radius and distance from the base plate defined as inputs. In [815] and [816] a closed-form mathematical formulation for predicting the evolution of temperature around the melt pool during MAM of 316-L steel and In625 was presented (see Fig. 47 (c)). Important solidification parameters such as cooling rate and temperature gradients were then determined in [815] by simply extracting spatial and temporal derivatives from the model.

However, similar to the shortcomings of the analytical powder-gas dynamic models, analytical melt pool models have fairly little application as they ignore a long list of important physics such as melting, fluid flow, surface deformation, thermo-capillarity, etc. These major assumptions render such easy-to-use models inadequate when it comes to understanding sophisticated mechanisms behind defect formation. Therefore, numerical simulations are comparatively a much better platform for involving the interacting physics occurring during MAM processes.

3.2.2.3. Conduction-based models. A large portion of thermal models of MAM processes in literature are conduction-based FEM simulations. In these, the transient temperature as well as the liquid fraction, are the two most important field variables which are obtained by solving the energy balance PDE which is coupled with a melting model that defines the change of liquid fraction with temperature, see Table 9. Except from perhaps a few 2D thermal simulations of MAM processes, e.g. [817], the majority of conduction-based models are 3D FEM-based simulations [818–821]. One could also point out to the works by Hoadley and Rappaz [822] and Kumar and Roy [823] who modelled the thermal conditions of DED while considering its longitudinal cross-section using the FEM and FVM, respectively, and the work by Ya, Pathiraj and Liu [824] (see Fig. 48 (a)), who simulated the temperature field at the frontal cross-section of DED while using an adaptive re-meshing technique for the material addition.

The FEM-based thermal model of the L-PBF process of In625 of Criales, Arisol and Özel [825] is another rare example of a 2D simulation of MAM processes (see Fig. 48 (b)). Such 2D simulations are of limited use when it comes to modelling sophisticated scanning patterns or complex geometries and due to this, such models are now considered obsolete.

Fig. 49 (a) shows a 3D view of a typical conduction-based thermal model of the PBF process. As observed in Fig. 49 (a), the computational domain is divided into two continuum regions with the upper thinner domain representing the powder layer while the bigger underlying domain is the already-manufactured or so-called bulk region. In almost all of the conduction-based models of the PBF processes, a volume-averaging or mass-averaging is carried out to obtain the effective thermo-physical properties such as thermal conductivity, density, specific heat capacity and effective surface emissivity. As earlier mentioned, such purely conduction-based models assume the velocity field and hence the convective terms in the PDE for energy conservation to be zero.

The assumption of using a continuum domain with effective properties is mainly due to the fact that explicit representation or modelling of individual powder particles in conduction-based simulations makes fairly little sense, especially because the powder particles cannot flow even after melting and therefore their non-ideal point-contacts (see Fig. 49 (b)) would make the conduction heat transfer extremely difficult and as a result, the temperature field could be highly overestimated.

There is a wide range of empirical equations which express average thermal properties based on porosity and the powder bed properties, see Table 10. In [818] as an example, the thermal conductivity of the powder layer was approximated based on a power-law given in Table 10 while also incorporating two material phase changes into the FEM model; an irreversible phase change for simulating the powder-to-bulk transition and a reversible phase change model for simulating the solid-to-liquid transition.

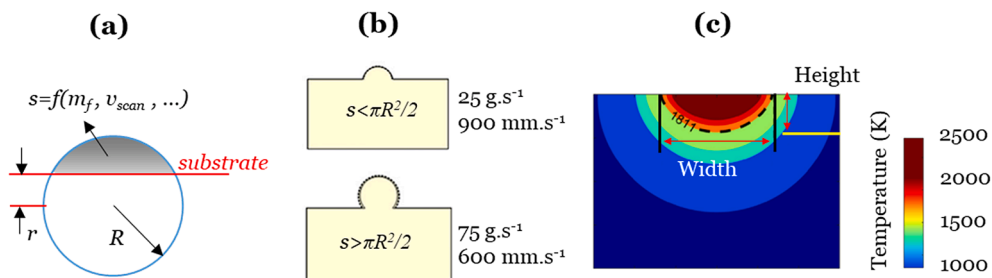


Fig. 47. (a) Schematic of the analytical-geometrical model developed in [813] and (b) the resulting predicted cross-sections. (c) Front view of the temperature field within the melt pool calculated with the analytical formulation derived in [815].

Table 9

PDE of energy balance in its general form in addition to a set of boundary conditions typically used for melt pool evolution models.

Energy conservation	$\frac{\partial}{\partial t}(\rho h) + \frac{\partial}{\partial x_j}(\rho u_j h) = \frac{\partial}{\partial x_k} \left(k \frac{\partial T}{\partial x_k} \right) + \sum \dot{q}_v^s$
Exposed surface boundary condition	$-k \frac{\partial T}{\partial x_n} \Big _{\Omega} = \epsilon \zeta [T^4 - T_{surr}^4] + h_{conv} [T - T_{surr}] + \sum \dot{q}_{\Omega}^s$
Enthalpy definition	$h(T) = h_{ref} + \int_{T_{ref}}^T \rho c_p(T) dT + f_l(T) \cdot \Delta H_{sl}$

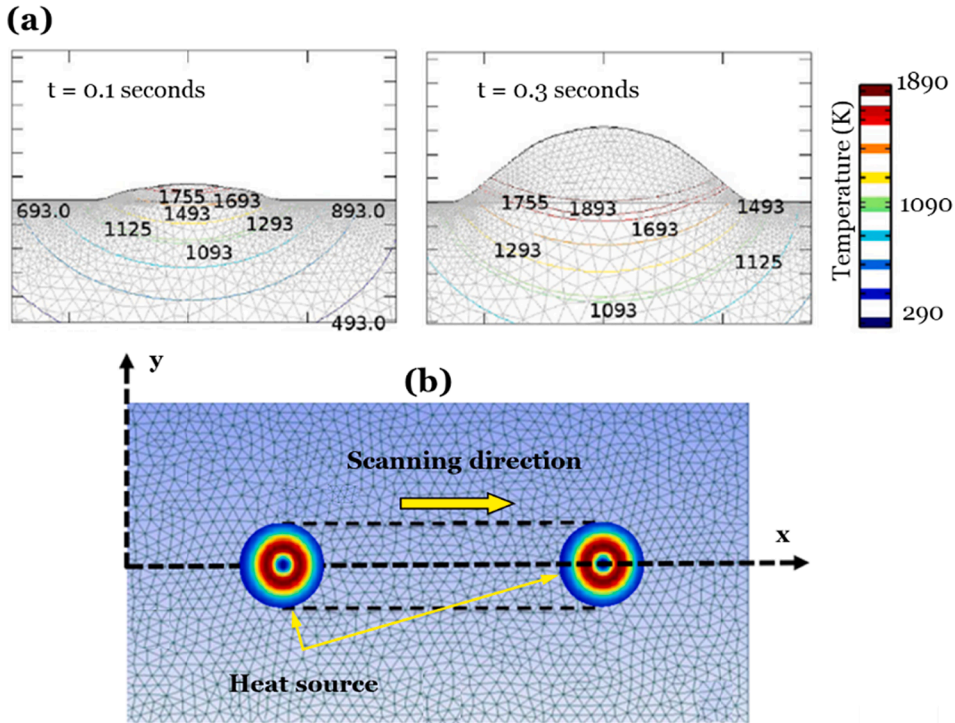


Fig. 48. (a) The 2D profile model with re-meshing of DED [824] (b) The 2D conduction-based model for the L-PBF process of In625 [825].

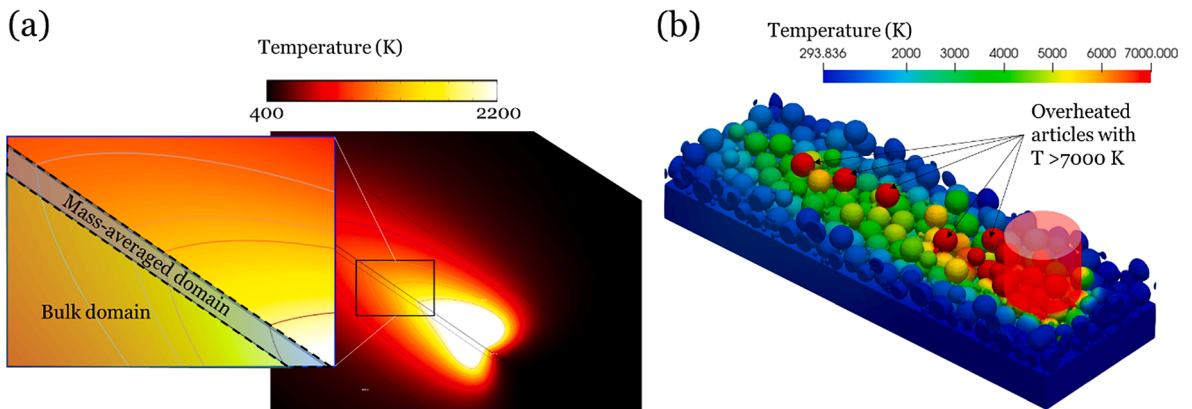


Fig. 49. (a) Predicted temperature of the L-PBF process using a conduction-based FEM model developed in COMSOL Multiphysics, where the powder domain is simulated with a mass-averaging method. (b) Predicted temperature contours from a conduction-based FVM thermal model (developed in Flow-3D) in which the powder particles are resolved explicitly. Since there are small point contact areas in between particles, temperatures are overestimated as heat cannot be dissipated properly by conduction only. Both of the figures are produced internally at the Technical University of Denmark, DTU.

As also given in Table 9 and shown in Fig. 49 (a), the thermal impact of the laser in the L-PBF process is typically simulated via a moving Gaussian heat flux. [836,837] used this type of thermal boundary condition to simulate the melt pool evolution during L-PBF of AlSi10Mg and commercially pure titanium and they studied the change in instantaneous cooling rate during the process. While most of the conduction-based thermal models use a fixed domain size, [838,839] took the layer height reduction into consideration in their FEM models.

Conduction-based thermal simulations of L-PBF have been mainly used for identifying the best set of process parameters for achieving a sound and smooth track or bulk morphology [830,832] and this was mainly before 2017 from when the transport-based melt pool models gradually started to replace conduction-based models for PBF simulations in literature. Furthermore, conduction-based simulations are not well-suited candidates for predicting the track quality, as these models do not account for the two important physical phenomena of surface tension and overall fluid dynamics that eventually decide the final shape of a track.

Aside from single-track defects, the gradual temperature increase of the part due to heat accumulation is another phenomenon occurring in almost any MAM process [478,840–842] potentially changing the metallurgical phase of the already-printed layers. Roberts et al. [843] did one of the earliest studies related to this heat accumulation and simulated the temperature field during the printing of 5 layers of Ti6Al4V with L-PBF and they noted that the temperature at the already-manufactured layers continues to grow due to the subsequent thermal loads while new layers are being printed. Along the same line, Liu, Zhang and Pang [844] simulated the temperature field during L-PBF of 3 single tracks of 316-L, which were directly made on top of each other, and they observed that the melt pool size grows monotonically at later layers and they mainly ascribed this to the gradual heat accumulation.

Compared with PBF processes, the heat accumulation effect is substantially more pronounced in DED processes. Based on the process specifications given in Table 11 and by doing a rule-of-thumb calculation, the linear energy density (LED) for a typical DED process is at least 1 [852] and normally between 2 and 3 orders of magnitude larger than the LED typically used in a PBF process. Manvatkar et al. [853] for instance developed an FEM-based thermal model and predicted both the melt pool growth and solidification cooling rates during DED of 316-L stainless steel and they noticed a continuous melt pool growth while printing subsequent layers.

One of the main advantages of conduction-based MAM simulations is their lower computational requirements when compared to simulations with higher fidelities such as transport-based models. This advantage of shorter runtimes consequently makes it easier to couple thermal models to any possible subsequent solver, such as a metallurgical, kinetic or mechanical model. For instance, Costa et al. [854] presented an FEM-based conduction model coupled to a kinetic model to predict spatial phase transformation during powder DED of AISI 420. They found that two distinct regions, one predominantly martensitic on the upper half and the other, mainly tempered martensite and on the lower half, form during the process. In their thermal model they assumed that an element or a block of deposited material is activated at an initial temperature equal to the liquidus temperature mainly inspired by the work by Neto and Villar [855]. Suarez et al. [856] and Lakhkar et al. [857] developed relatively similar thermo-kinetic models where in the former, Suarez et al. [856] implemented the Johnson-Mehl-Avrami equation to predict the phase fraction transformations during DED of Ti6Al4V. As an example within PBF processes, Raghavan et al. [858] made a thermo-metallurgical model of the EB-PBF process of IN718 and they ultimately predicted the impact of four main input process parameters on important solidification parameters such as the morphology factor and the solidification cooling rate. Yin et al. [859] studied the change in dendrites growth direction during multi-layer L-PBF of Ti6Al4V with their thermo-metallurgical model where they finally reported the growth direction converges to a

Table 10
Selected effective thermo-physical properties of the powder bed for PBF simulations.

Property	Expression	Refs.
ρ (kg.m ⁻³)	$\frac{\rho_{bulk} - \rho}{\rho_{bulk}}$	[826]
k (W.m ⁻¹ .K ⁻¹)	$k_s(1 - \phi)$	[827]
	$k_s(1 - \phi)^n$	[818,828]
	$k_f \left\{ (1 - \sqrt{1 - \phi}) \left(1 + \frac{\phi \left(\frac{4}{3} \sigma T_p^3 D_p \right)}{k_f} \right) + \sqrt{1 - \phi} \left\{ \left(\frac{2}{1 - \frac{k_f}{k_s}} \right) \left(\frac{\ln \left(\frac{k_s}{k_f} \right)}{\left(1 - \frac{k_f}{k_s} \right)} - 1 \right) + \frac{4}{3} \frac{\sigma T_p^3 D_p}{k_f} \right\} \right\}$	[829–831]
	$\frac{\rho_{relative} k_s}{1 + \frac{(0.02 \times 10^{1.4 - 2\rho_{relative}})(k_s)}{k_f}}$	[832–834]
c_p (J.kg ⁻¹ .K ⁻¹)	$k_f \frac{\eta N}{2} \left[0.5 \ln(1 + L^*) + \ln(1 + \sqrt{L^*}) + \frac{1}{1 + \sqrt{L^*}} - 1 \right]$	[827]
	$\frac{\rho_s c_{p,s} \phi + \rho_f c_{p,f} (1 - \phi)}{\rho_s \phi + \rho_f (1 - \phi)}$	[835]
$\epsilon_{surface}$ (-)	$A_H^* \epsilon_H + (1 - A_H^*) \epsilon_s$	[830]
	$A_H^* = \frac{0.908 \phi^2}{1.908 \phi^2 - 2\phi + 1}$	
	$\epsilon_H = \frac{\epsilon_s \left[2 + 3.082 \left(\frac{1 - \phi}{\phi} \right)^2 \right]}{\epsilon_s \left[2 + 3.082 \left(\frac{1 - \phi}{\phi} \right)^2 \right] + 1}$	

Table 11
A short list of typical input process parameters used for MAM processes.

Input parameter	Process	
	PBF	DED
Input power	< 500 W	< 3000 W
Scanning velocity	< 2700 mm.s ⁻¹	< 20 mm.s ⁻¹
Beam size	< 100 μm	< 5000 μm
Powder size	< 60 μm	< 150 μm
references	[619,845–849]	[850,851]
Build size	300 by 350 by 300 mm ³	3200 by 3670 by 300 mm ³
reference	[1]	

certain value after printing a couple of layers. Zhang et al. [860] made an attempt to couple their FEM-based thermal model to a subsequent CA-based microstructural simulation for the DED process of Ti6Al4V.

As also given in Table 9, there are at least two possibilities of including the thermal effects of heat sources in MAM into the energy balance equation, one via modelling the laser as a moving heat flux ($\sum \dot{q}_v''$ (W.m⁻²)) and hence imposing it as a surface boundary condition and another by including it as a source term on the right hand side of the energy balance PDE ($\sum \dot{q}_v'''$ (W.m⁻³)). According to literature, the laser in L-PBF is mostly simulated as a heat flux on the top exposed boundary of the computational domain whereas for the EB-PBF process, the electron beam's thermal impact is directly modelled as a volumetric heat source. This could most certainly be argued from a physical point since the laser's energy gets absorbed at the surface under irradiation while for EB-PBF, the kinetic energy of electrons is transformed into internal energy of the material within the irradiated zone [861,862].

Although the majority of the L-PBF thermal models represent the laser with a surface heat flux, a few contributions can actually be found in which the authors simulate the laser/material interaction via a volumetric heat source. [863] and [864] for instance modelled the thermal influence with volumetric heat sources. In the former, [863], they expressed the laser's thermal impact with a Gaussian-cylindrical heat source in which its depth, more specifically the optical penetration depth, needed to be calibrated against experiments. In the latter, [864] used a rather sophisticated approach and instead of applying a pre-determined vertical distribution function, they ran an a-priori Monte-Carlo-based ray-tracing simulation [865] to find the correct vertical distribution.

For DED processes, the heating step could be simulated with either an initial elevated temperature assumption for activated cells, heat sources and heat fluxes, or a combination of both initial liquid temperature and heat sources. [866] modelled the temperature field while activating the newly-deposited regions at the liquidus temperature during DED of 316-L while [867] and [868] used a moving heat flux to simulate the heating process during DED.

In these works [866–868] the track profile is rectangular Fig. 50 (a) which is far from the actual smooth surface of a DED track. Such an assumption could lead to errors in the predicted temperature, mainly because the heat flux is distributed over a flat surface and this results in a more uniform temperature field, as compared to the case with a curved surface. Another approach would be to approximate the actual shape of the experimentally-observed track profile based on predefined functions Fig. 50 (b) and (c). [869] for instance represented the track shape of H-13 DED tracks via a semi-cylinder for simplicity. [870] approximated the track shapes from prior experiments via an arced surface and then subjected their activated cells to a moving spherical heat source. A similar approach was adopted by [871] who developed an FE-based thermal model with an arced free surface. In a more recent work by [872], the free surface of the DED track is predicted by a transport-based model and then the information regarding the position of this free surface is fed to a subsequent conduction-based thermo-mechanical model.

Conduction-based thermal models have been extensively used for predicting the evolving transient temperature field required for thermo-mechanical analysis in MAM processes. The main PDEs for thermo-mechanical models of MAM processes are given in Table 12.

According to Table 12 and based on the standard linear strain decomposition rule, the total incremental strain tensor is defined as the sum of elastic, plastic, thermal and metallurgical incremental strain tensors [875]. Nevertheless, since a full thermo-metallurgical-

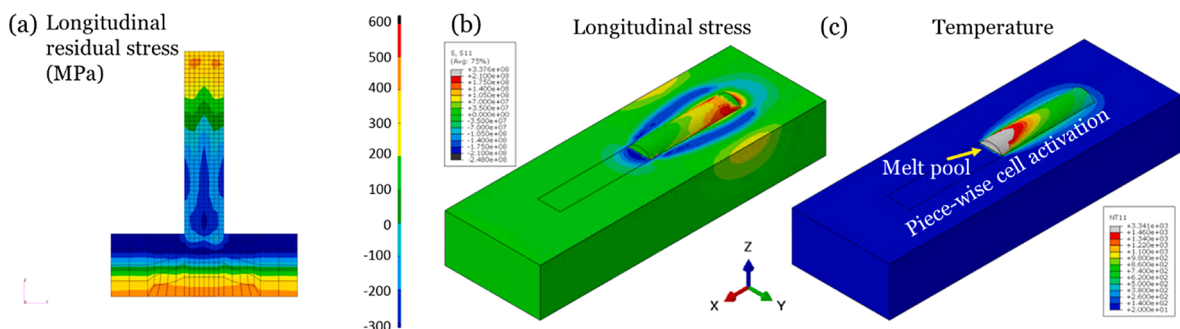


Fig. 50. (a) Predicted longitudinal residual stresses for multi-layer DED of In625 with flat surface assumption [873] (b) and (c) show calculated longitudinal stress as well as temperature development during powder DED of stainless steel 316 – L with curved free surface. (b) and (c) are based on in-house FEM models where the free surface is taken from optical microscopy [874].

mechanical analysis for MAM processes is relatively computationally heavy, most of the stress analyses given in literature are thermo-mechanical simulations without any metallurgical analysis. Labudovic and Kovacevic [876] for instance predicted the temperature field during powder DED of Monel 400 on AISI 1006 and they noticed increasing residual stresses along the height of the build. Kamara, Marimuthu and Li [877] made a thermo-mechanical model of the powder DED process of Waspaloy on IN718 with 6 tracks and 20 layers and they used a uniform moving heat flux to model the laser heating. Farahmand and Kovacevic [878] developed a thermo-mechanical model based on FEM for powder DED of AISI H13 on ASTM A36. In their simulation, they represented the track cross-sectional profile with a curved surface and they furthermore reported that the residual stress magnitude decreases at lower scanning speeds. One of the major issues which has not been investigated sufficiently in the literature is the impact of the choice of material model on the final stress results. The power-law and bilinear material models shown in Fig. 51 (a) and (b), respectively, are the two most employed stress-strain relationships used in thermo-mechanical models of MAM.

Johnson Cook's material model given in Table 13 is a closed form stress-strain relationship that expresses stress as a function of plastic strain, plastic strain rate and temperature.

Yang et al. [879] simulated the progressive stress formation during manufacturing of a thin-walled component made of Ti6Al4V and with a rectangular cross-section. In their work, the transformation or metallurgical strain was entirely ignored, therefore the residual stresses were found via a pure thermo-mechanical analysis. Although the impact of metallurgical phase transitions is often ignored in research works related to thermo-mechanical modelling of MAM, the inclusion of phase transformation-induced strains in mechanical simulations of MAM is actually very important for Ti6Al4V. Also for other alloys it is very well proven in literature that neglecting these strains could lead to severe underestimation of residual stresses in H-13 and AISI 410 [880,881].

Heigel, Michaleris and Reutzler [882] developed a somewhat similar thermo-mechanical model of powder DED of Ti6Al4V to that of Yang et al. [879] and simulated the evolution of residual stresses as well as the temperature field during manufacturing of single and double walls. They furthermore accounted for the stress relaxation and hence set all the remaining process-induced strains to zero, for those elements whose temperature went above 640 °C. In a later work and from the same research team, Denlinger and Michaleris [873] made a thermo-mechanical model of powder DED of the two alloys In625 and Ti6Al4V. In this work, the stress relaxation was modelled by setting the remaining plastic strain to zero to model the erasing of the crystals' dislocations above 640 °C, see Fig. 50 (a). They ultimately showed that ignoring stress relaxation causes minimal changes in the final stress magnitudes for In625, whereas for Ti6Al4V on the other hand, ignoring this phenomenon leads to an overestimation of residual stress seven times the experimentally-observed values. In a more recent work from the same team, Li et al. [883] added a new re-meshing feature, denoted octree mesh-coarsening, to the model. This re-meshing technique logically refines the mesh near the deposition zone which is exposed to high temperature gradients.

Similar to DED, deposition-scale thermo-mechanical simulations have been used to predict the formation of residual stresses during the L-PBF process. There is a significant resemblance between the setup of thermo-mechanical models for DED and L-PBF processes. The main differences that distinguish the two are first, the huge ratio between the overall size of the sample and the melt pool in PBF and second, its sophisticated and sometimes layer-wise altering scanning strategies. These two factors along with relatively fine mesh requirement for resolving the melt pool geometry, make deposition-scale PBF models solely applicable to computational domains which are confined to a few tracks and layers [884,885].

Representative examples are the thermo-mechanical models of L-PBF of AlSi10Mg and stainless steel 316-L by Wu, Wang and An [886] and Hussein et al. [887]. In the work by Cheng, Shrestha and Chou [888], an FEM-based thermo-mechanical model was developed and used for studying the role of scanning patterns on the maximum residual stress levels during three layers L-PBF of In718, and it was concluded that the out-in pattern causes the highest residual stresses. In another work, Parry, Ashcroft and Wildman [889] simulated the evolution of residual stresses forming during a multi-track L-PBF process of Ti6Al4V using an FEM-based model. They ultimately reported that there is a direct correlation between the residual stress level and the scan length and they furthermore underlined that lower temperature gradients potentially lead to lower stress level, which is in agreement with the TGM theory [31]. In a more recent work, Chen et al. [890] have investigated how the overlap ratio between neighboring tracks would affect stresses in L-PBF of Ti6Al4V. They came up with the final conclusion that higher overlap ratios lead to larger normal stresses parallel to the scan pattern while lower overlap ratios gives rise to larger normal stresses perpendicular to the scan path. It must be noted that none of the above mentioned thermo-mechanical models of L-PBF considered the contribution of the phase transformation-induced strains on the mechanical conditions. Tan et al. [891] on the other hand developed a fully coupled thermo-metallurgical-mechanical model for multi-track-layer L-PBF of Ti6Al4V and they calculated residual stresses in two different scenarios, one with and one without accounting for solid state phase transformation. They found that compared to the case ignoring solid state phase transformation, the magnitude of

Table 12

The main governing equations used for thermo-mechanical simulation of MAM processes.

Force equilibrium	$\frac{\partial \sigma_{ij}}{\partial x_j} = 0,$
Hooke's law	$\sigma_{ij} = \frac{E}{1+\nu} \left[\frac{1}{2} (\delta_{ik} \delta_{jl} + \delta_{il} \delta_{jk}) + \frac{\nu}{1-2\nu} \delta_{ij} \delta_{kl} \right] \epsilon_{kl}^{el}$
Linear strain decomposition	$\dot{\epsilon}_{ij}^{total} = \dot{\epsilon}_{ij}^{el} + \dot{\epsilon}_{ij}^{pl} + \dot{\epsilon}_{ij}^{th} + \dot{\epsilon}_{ij}^{tr}$
Plastic strain from J2 flow theory	$\dot{\epsilon}_{ij}^{pl} = \frac{9}{4} \left[\frac{1}{E_i} - \frac{1}{E} \right] \frac{s_{kl} \dot{\sigma}_{kl}}{\sigma_e^2} s_{ij}$
Small total strain	$\epsilon_{ij}^{tot} = \frac{1}{2} \left[\frac{\partial u_i}{\partial x_j} + \frac{\partial u_j}{\partial x_i} \right]$

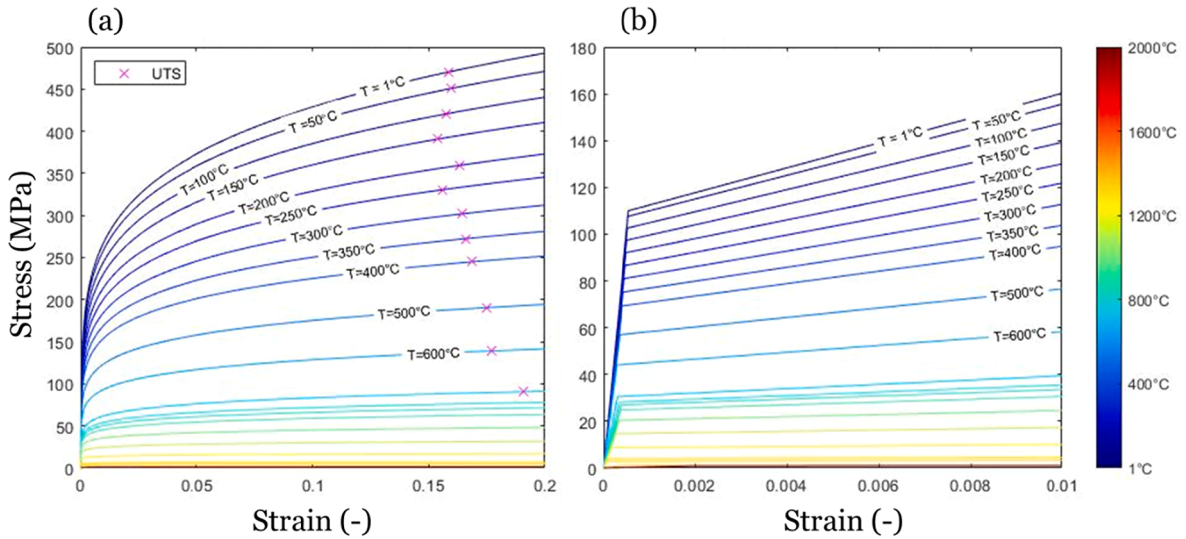


Fig. 51. Stress–strain curves for stainless steel 316-L; (a) power-law model and (b) bi-linear model.

Table 13
Expressions for stress-stress relationships.

Power-law	$\epsilon =$	$\begin{cases} \frac{\sigma}{E(T)} & \sigma \leq \sigma_Y(T) \\ \frac{\sigma_Y(T)}{E(T)} \left[\frac{1}{n} \left(\frac{\sigma}{\sigma_Y(T)} \right)^{n(T)} - \frac{1}{n(T)} + 1 \right] & \sigma > \sigma_Y(T) \end{cases}$	
Ramberg-Osgood	$\epsilon = \frac{\sigma}{E(T)} + \kappa \frac{\sigma_Y(T)}{E(T)} \left(\frac{\sigma}{\sigma_Y(T)} \right)^{n(T)}$		
Johnson-Cook	$\sigma = (A + B\epsilon_{p,avg}^{m_{JC}}) \left(1 + C \cdot \ln \left(\frac{\dot{\epsilon}_{p,avg}}{\dot{\epsilon}_0} \right) \right) \left(1 - \left(\frac{T - T_{ref}}{T_{melt} - T_{ref}} \right)^{m_{JC}} \right)$		

compressive stresses was higher in the case including of phase transformation.

It is virtually impossible to model the entire stress evolution during L-PBF of a whole part with such detailed deposition-scale models that eventually also resolve the melt pool geometry. This is the reason why process multi-scaling techniques are typically used for modelling the part-scale conditions and these methods will be covered in section 4.2.1. However, in DED, the ratio of the component size to the melt pool size is much bigger than that of L-PBF and hence, deposition-scale models of DED can reliably predict the thermal and mechanical conditions of a complete component within a feasible computational time. But as will be shown in section 4.2.1, detailed deposition-scale models of PBF processes, are very useful for calibrating part-scale simulations that use for example inherent strain as the multi-scaling technique. The main drawback of conduction-based models is on the other hand, their inability to capture the melt pool temperature and this is because the fluid flow motion and convection are ignored. This typically leads to overestimation of peak temperatures. There have been some works to circumvent this by applying updated [892], non-isotropic thermal conductivity [893–895] or by doing inverse analysis [896] to find effective thermal conductivity values. But these methodologies are mainly applicable when the melt pool is in a stable regime.

3.2.2.4. *Transport-based models.* In transport-based melt pool models, as opposed to conduction-based models, the fluid dynamics inside the melt pool during the deposition and melting processes is simulated, thus accounting for the other major heat transfer mechanism, namely, the advection, which was neglected in conduction-based models. The main governing PDEs for transport-based melt pool evolution simulation of MAM processes are listed in Table 14 where the velocity and pressure fields are determined from solving the coupled PDEs for continuity and linear momentum balance or in other words the Navier-Stokes equations. Consequently, the temperature field obtained from the energy balance PDE given in Table 9 will be highly dependent on the velocity field from the fluid dynamics analysis. In this case, heat transfer takes place due to conduction as well as transport/advection.

The majority of transport-based melt pool evolution simulations are assuming incompressibility, in which case, the source term in the continuity equation would become zero in Table 14. One of the few exceptions is the work by Bellet’s group at MINES ParisTech who used a compressible flow assumption in their simulation [897] and mainly because they modelled the powder layer using averaging methods similar to the ones discussed in the section for conduction-based simulations, and hence it was required to consider compressibility to allow for the powder layer’s shrinkage after melting. $\dot{S}_{mass}^{\prime\prime}$ ($\text{kg}\cdot\text{m}^{-3}\cdot\text{s}^{-1}$) and $\dot{S}_{mom,i}^{\prime\prime}$ ($\text{N}\cdot\text{m}^{-3}$) in the PDEs expressed in

Table 14 are mass and momentum sources terms respectively, which represent the impact of external forces or internal agents. An example of a transport-based melt pool evolution simulation of the L-PBF process is shown in Fig. 52. Physical phenomena such as wetting, solidification and surface hydrodynamics within the melt pool are considered in this model. These phenomena are typically modelled via adding certain equations to the two source terms (i.e. in mass and momentum PDEs), depending on the type of the transport-based model. In this respect, these two terms will be expanded in the upcoming sections while describing different classes of transport-based MAM models.

The Marangoni effect (mostly the thermo-capillarity effect) is one of the main drivers of the fluid flow inside the melt pool in MAM processes. For most metals and alloys employed in MAM processes, the Marangoni effect leads to flow of the liquid metal from the hotspot with lower surface tension to the cooler rims of the melt pool where surface tension is higher [898,899]. In some rare cases, for instance when a surface active element is added to the metal, the flow direction is inverted and this leads to a situation called the inverse Marangoni effect [900,901]. Two of the most widely used surface tension expressions in MAM transport simulations are given in Table 15.

The first expression in Table 15 is used for sulfur-iron systems [902] and with some modification, it could also be applied to silver and nickel [903,904]. The second expression [905] in this table is a simplified representation of the non-linear expression given in the first row and it needs updating of the differential term depending on the sulfur content, while the first equation in Table 15, already contains a term that accounts for the sulfur impact. The derivative is in essence the main factor deciding the direction as well as the magnitude of the Marangoni effect, where a positive value for $d\gamma/dT|_{ref}$ ($N.m^{-1}.K^{-1}$) leads to a melt pool with a radially inward flow (see Fig. 53 (c)) denoted inverse Marangoni, while a negative sign results in a flow with the opposite direction, known as normal Marangoni [906] (see Fig. 53 (b)). It must, however, be mentioned that for most metals and alloys, $d\gamma/dT|_{ref}$ ($N.m^{-1}.K^{-1}$) is negative [907], which results in a normal Marangoni condition.

In terms of complexity, transport-based melt pool simulations with flat surfaces are considered to be the simplest ones. Therefore, since there is no curvature involved in the calculations, only the Marangoni effect is taken into account whereas capillarity, which is entirely dependent on the surface curvature, is ignored. Table 16 gives an overview of the boundary conditions as well as the expanded form of the mass and linear momentum source terms for flat surface models.

According to Table 16, the source term in the continuity equation is set to zero and a drag-based function is used to simulate the fluid dynamics impact on melting and solidification [908,909]. The second source term for the Navier-stokes equation given in Table 16 expresses the buoyant forces based on the Boussinesq assumption [910,911]. It must be noted that, here, both the solidification drag together with buoyancy are imposed over the entire computational domain, hence being added as global source terms to the model.

In flat surface transport-based models of the L-PBF process, with no surface-tracking solver involved [912], the powder layer is modelled via averaging techniques [913] as listed earlier in Table 10. Mukherjee et al. [914–916] from Debroy's group at Penn State University developed a series of CFD simulations of the L-PBF process while using the flat surface assumption. They modelled the heat, fluid flow and solidification conditions during L-PBF of different alloys using their in-house FVM-based solver. [917] and [918] developed similar CFD simulations of the L-PBF process using FVM and FEM, for inverse and normal Marangoni cases, respectively. [919] presented an FE-based CFD model and concluded that convective heat transfer is one order of magnitude stronger than conduction in L-PBF of In718.

One of the main drawbacks of transport-based models with a flat surface is that they are in general unable to predict any type of porosity formation during the course of L-PBF, although Mukherjee et al. [916] considered the non-sintered regions of the domain as lack of fusion porosities. Such porosities in reality occur due to improper melting of the powder bed which eventually entraps air and ultimately results in some remnant voids [920]. Thus, these porosities, especially the keyhole pores, can only be properly and realistically tracked with a two-phase flow solver. Hence, ideally, flat surface models should be used for MAM processes with stable melt pools without any keyhole or surface instability formation. Other types of surface defects such as balling cannot be modelled with these models, although.

The same issue also applies to flat surface transport-based models of DED processes, since these models are unable to predict any inter-track or inter-layer porosity formation when big hatch distances or high material flows are employed. Manvatkar, De and Debroy [921] predicted the melt pool's temperature and its internal fluid dynamics via an FVM-based CFD model during powder DED of stainless steel 316-L. As they accounted for convection inside the melt pool, they reported more realistic solidification cooling rates about half the ones calculated with their conduction model. This model was later and with a number of minor modifications applied to simulate the thermal, fluid flow and metallurgical conditions of powder DED of In718 and SS 316-L [922,923]. In transport-based models with flat surfaces, it is assumed that the melt pool forms within the most recently-activated block in which its height in

Table 14

List of main PDEs for transport-based melt pool evolution simulations of MAM processes. F stands for fluid.

Continuity	$\frac{\partial \rho u_i^F}{\partial x_i} = \sum \dot{S}_{mass}^*$
Linear momentum balance	$\rho \left[\frac{\partial}{\partial t} u_i^F + \frac{\partial}{\partial x_j} (u_j^F u_i^F) \right] = -\frac{\partial p}{\partial x_i} + \rho g_i + \frac{\partial}{\partial x_j} (\tau_{ij}) + \sum \dot{S}_{mom,i}^*$
Stokes stresses	$\tau_{ij} = \mu_f \left(\frac{\partial u_i^F}{\partial x_j} + \frac{\partial u_j^F}{\partial x_i} \right)$

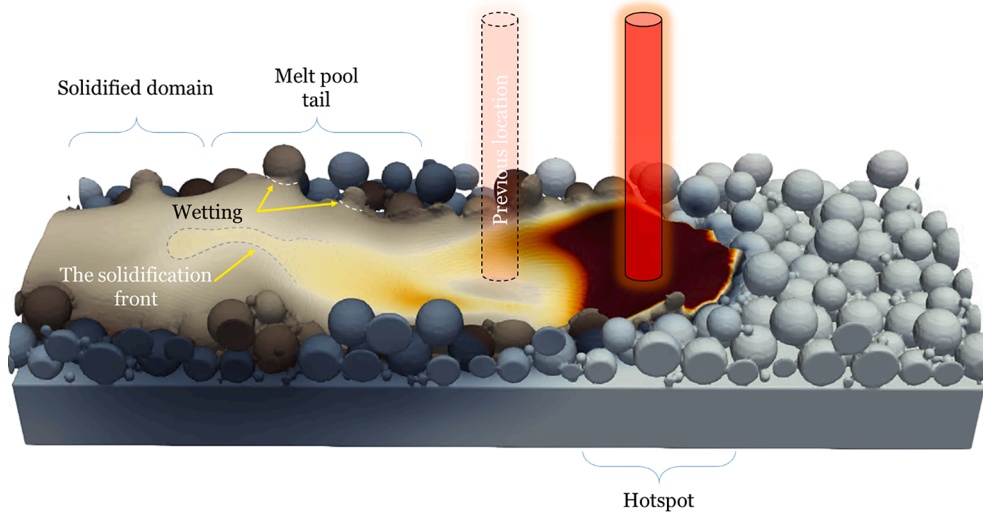


Fig. 52. Predicted temperature contour and melt pool’s surface hydrodynamics in L-PBF. The arrows show the local wetting near the solid particles alongside with the progressive solidification front. Snapshot taken for the FVM model made at DTU.

Table 15

Two of the most widely-used surface tension expressions used for MAM transport simulations.

Sahoo-Debroy-McNallan expression	$\gamma(T) = \gamma_{ref} + \frac{d\gamma}{dT}\bigg _{ref} (T - T_{ref}) - RT_s \ln(1 + A \cdot w_{sulfur} \exp(\Delta H_0 / RT))$
Linearized form	$\gamma(T) = \gamma_{ref} + \frac{d\gamma}{dT}\bigg _{ref} (T - T_{ref})$

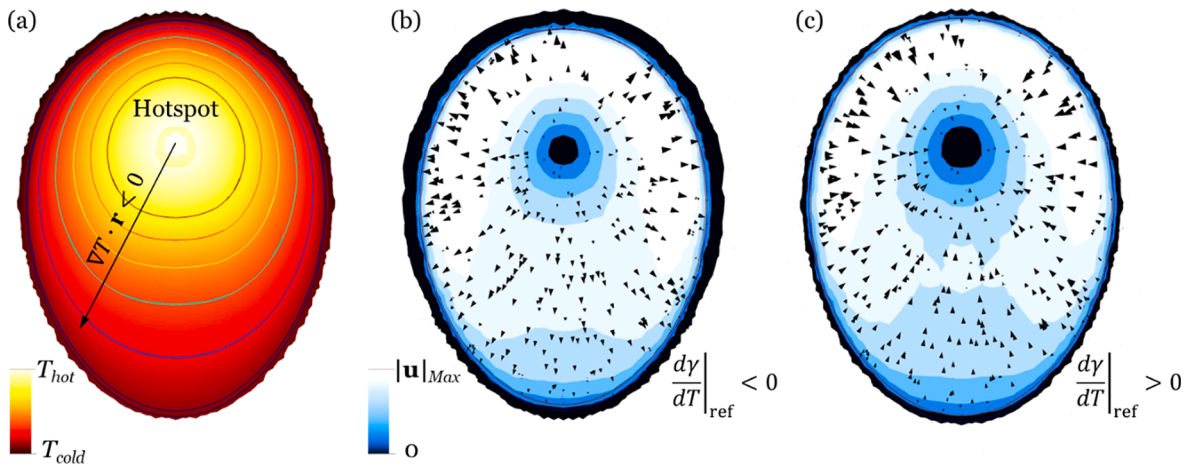


Fig. 53. Contours of (a) temperature, and velocity magnitude of (b) normal and (c) inverse Marangoni predicted by FEM-based transport model of L-PBF developed at the Technical University of Denmark – DTU.

most cases is predetermined (based on *ex-situ* experiments or nominal input values) and then fed as an input to the model. In reality, and especially for DED processes with higher heat-to-mass ratio, the melt pool gets well-distributed over the previously-fabricated track and its size could highly deviate from the nominal input values. Despite all these limitations, flat surface transport-based melt pool models are still applicable for understanding how input parameters could alter the thermal and metallurgical conditions during powder DED and an example of this is the recent work by Singh et al. [924] who made an FVM-based model for powder DED of Al-0.5Sc-0.5Si, see Fig. 54 (a). Although in all these CFD simulations, element-activation is made to account for the material deposition, Jiang et al. [925] did the simulation without such an element-activation and instead, used a continuum powder bed averaging approach to model the melt pool.

In a relatively similar manner to conduction-based melt pool simulations, there is also a branch of transport-based models which

Table 16
Fluid dynamics boundary condition and the expanded form of source terms for the mass and linear momentum balance equations used for transport-based MAM simulations with fixed surfaces.

Boundary condition at top	$\frac{d\gamma}{dT} [\nabla T_i - n_i (\nabla T_k n_k)]$
$\sum \dot{S}_{mass}^*$	0
$\sum \dot{S}_{mom,i}^*$	$\frac{K_c (1 - f_{liq})^2}{C_k + f_{liq}^3} u_i^F + \rho g_i \beta \Delta T$

use a pre-determined curved surface for representing the track profile in DED processes. Here, the same governing equations as earlier mentioned in Table 16 are applied, therefore, despite a curved surface is considered, the surface tension is not taken into account. Knapp et al. [926] modelled the front section of the track as a 3D ellipsoid (see Fig. 54) and the rest of the bead by an extruded ellipse, inspired by the work [927]. In [926] it was required to obtain the geometrical constraints describing the ellipsoid by fulfilling the mass balance arising from the deposition. Wei et al. [733] further employed this model for modelling the heat and fluid flow together with the microstructural conditions of DED of In718, where a combined CFD and Monte-Carlo grain growth model was used. A comparison between flat and curved surface assumptions was carried out in [926] and it was shown that the solidification cooling rates are not significantly affected by the shape of the track profile. And in agreement with the second comparison between a conduction-based and a transport-based model in [926], it was demonstrated that the inclusion of the fluid flow has a significant impact on the solidification cooling rates. In a recent work [928] and from the same research group, a version of this transport-based model is coupled to a Johnson-Mehl-Avrami kinetic model [929,930] to predict the spatio-temporal variations of different field variables including the martensitic phase fraction as well as hardness for powder DED-processed H13 tool steel.

According to the previous section, the inclusion of the fluid flow in the melt pool is a major factor that highly influences the solidification cooling rate, whereas, under the assumption of a fixed surface, does not have a significant impact on the solidification cooling rates. However, for microstructural simulations, the curvature of the melt pool affects both the grain growth as well as the solidification pattern [931], and therefore it is generally highly recommended to include the real shape of the track into the models.

In relatively more advanced transport-based models, and especially for DED processes, the free surface of the deposition is tracked via mathematical expressions which are primarily based on either a force balance or mass conservation within the tracks. [932] predicted the evolving free surface of the deposited track using an arbitrary Lagrangian-Eulerian (ALE)-based remeshing technique for DED of a cobalt-based alloy on steel. The growth of free surface of the deposit in [932] is in general attributed to two velocity components at the liquid-gas interface; i.e. the liquid velocity at the free surface calculated from the CFD analysis and the prescribed Gaussian velocity due to the addition of powder particles, see Table 17.

[934] employed also ALE-based remeshing and applied it to DED of Co-Cr-W powder on 38MnVS baseplate with 0.04 wt% of sulfur. It was found that at higher mass flow rates of 6 g/min, the sulfur concentration drops to 0.005 wt% from 0.035 wt% at 0.1 g/min and mainly due to dilution. This in turn led to a change in the direction of the melt pool flow from an inward flow to a normal outward flow. Similarly to [934,935] used a similar ALE-based remeshing technique and modelled powder DED with both Gaussian and super Gaussian laser profiles.

It is also possible to model the free surface of a track in DED by fulfilling the balance of all active forces on the L/G interface [937]. [938] simulated the growing free surface of multiple powder DED-made tracks being deposited on top of each other also via minimizing the total energy of the liquid-gas interface of the melt pool. They observed grain-coarsening in the subsequent tracks of the multi-layer samples and this was caused by the residual heat effect discussed earlier. Finally, [939] applied a procedure in which they

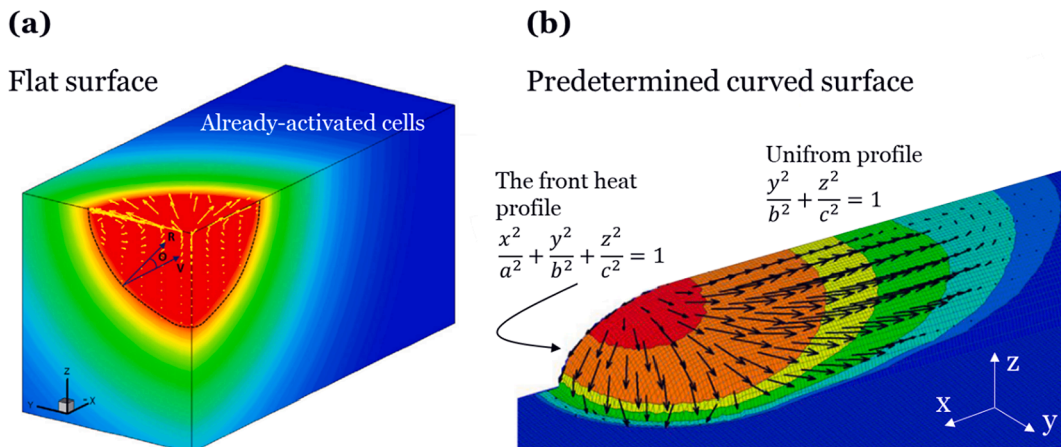


Fig. 54. Examples of fixed surface powder DED simulations with (a) flat surface [924] and (b) predetermined curved surface [926].

minimized the sum of gravitational potential energy and surface energy, while fulfilling the mass conservation constraint and assuming a uniform profile over the length of the track, see Table 18.

According to Table 18, the integral equation is a simplified form of the total energy function given in the first row and ψ (m) is the height function that due to the uniform track deposition along the deposition axis x , will only be dependent on a single variable, y (m). In the next step, the Navier-Stokes and energy conservation were solved using the variational multi-scale formulation [939]. The surface energy minimization approach was used in [936] as well (see Fig. 55), where the track shape, size and dilution were simulated for 60 different tracks with several combinations of different input variables for powder DED on In718. [936] showed that the dilution percentage increases with increasing the energy per unit mass while the dendritic arm spacing becomes lower. It was also shown that the impact of nickel concentration on the final microhardness is significantly higher than that of the solidification cooling rate. This well-tested surface-tracking method has also been recently applied to wire DED in [940] as well. One major issue associated with surface energy minimization-based methods is that they are not able to predict porosity formation and are therefore only applicable to stable melt pool conditions.

The majority of transport-based melt pool simulations use an independent PDE for resolving the dynamic growth of the free surface. The level set (LS) [941] and volume of fluid [942] (VOF) methods are the two main surface-tracking methods used for predicting the surface hydrodynamics of melt pools during MAM processes. The full form for both of these two surface-tracking algorithms is given in Table 19.

This class of transport-based models is sometimes referred to as multiphysics simulations in literature as well, mainly because they entail a long list of physical phenomena. One of the earliest multiphysics simulations of MAM was made by [943] who modelled the heat and fluid flow as well as the surface hydrodynamics of DED of the stellite 6 alloy. The free surface conditions of the melt pool were modelled by solving an advection-like PDE of a flag variable that tracked the free surface hydrodynamics whilst the melt pool was moving. [944] and [945] used a combination of CFD and the LS method to predict the melt pool's thermo-fluid-hydrodynamic conditions during single track powder DED of H-13. One of the unique features of the former work is the implementation of a lever-rule liquid fraction function, as opposed to the bulk of literature in modelling MAM which assumes a linear correlation between the liquid fraction function and temperature for simplicity. An updated FVM-based version of this model with a modified mesh was used by [946], for modelling double-track DED. [947] also used LS to predict the hydrodynamics and surface conditions of single-tracks made with DED where TiC reinforcing particles were embedded in a 316-L stainless steel matrix and the concentration of the reinforcing particles was modelled with a passive scalar field.

As compared to what is the case for DED as outlined above, the LS method has been used considerably less for surface-tracking during PBF processes. [948] is an example which in a similar manner to [897] uses averaged powder layer properties, and thus individual particles are not explicitly resolved, see Fig. 56 (a). Furthermore, to account for the layer height reduction due to melting, a compressible flow assumption was used. The LS method has also been used in transport simulations of higher heat inputs that lead to keyhole and keyhole induced porosities. One of these simulations is given in [949] which was based on Tan et al.'s earlier transport-based welding simulations [950–952]. Here the sharp interface method was applied when imposing the triple interface boundary conditions, namely surface tension, the Marangoni effect and the recoil pressure see Fig. 56 (b), as opposed to the alternative continuum surface force (CSF) model.

The majority of transport-based melt pool simulations use VOF to track the melt pool's surface conditions. One of the big advantages of VOF and LS is that, with some modifications, the field output from these techniques (the flag variables φ (-) and F (-), for LS and VOF, respectively) could be used as a tool to find the thermo-physical properties at the liquid–gas interface, see Table 20 and Fig. 57.

According to Table 20, in the LS method, the Heaviside function of the distance flag variable φ (m) is used to interpolate the material properties over the interface region which has a thickness of 2ϵ (m). Whereas in VOF, the material properties are linearly dependent on the flag variable F (-), see Fig. 57.

In transport-based melt pool simulations, surface boundary conditions are typically transformed into volumetric forces or source terms via the continuum surface force method i.e. CSF [954]. The CSF technique transforms a two-dimensional surface force or surface heat flux into a corresponding volumetric force or heat source, respectively, see Table 21. In the VOF method, the gradient operator of the flag variable acts like a pulse function which is only active over the interface region and is then zero over the rest of the gaseous or metallic domain, as there is no gradient of the flag variable outside the interface region. In this way it is guaranteed that the force or the heat flux is only imposed on a very specific and limited interface region.

The transformation of 2D boundary conditions into volumetric source terms via the CSF method for LS and VOF are elucidated in Table 21. The sum of all thermal as well as fluid dynamics source terms will be inserted into the right hand side of the energy and linear momentum balance PDEs (\dot{q}_{Laser}^v (W.m⁻³) and $\dot{S}_{mom,i}^v$ (N.m⁻³)) as given in Table 9 and Table 14, respectively. In Table 21 and Fig. 57 it is observed that there are three interfacial boundary forces active at the exposed surface of the melt pool. \dot{F}_{Cap} (N.m⁻²) is due to the capillary forces and these forces act perpendicularly to the free surface of the melt. The third interfacial boundary force is due to the

Table 17

The liquid/gas velocity calculation used for the prediction of the deposition shape in [932] and [933].

The liquid–gas interface velocity	$u_{LG} = u_i^l n_i + V_i^p n_i$
Prescribed velocity due to mass addition	$V_i^p(x, y) = \frac{2m\eta_m}{\rho_p \pi r_p^2} \exp\left(-\frac{2r^2}{r_p^2}\right) X_i, i = 3$

Table 18

The total energy function in its general and subsequently in its simplified integral form as well as the mass conservation constraint used in [939] for predicting the free surface of DED tracks.

Total energy function	$E_{total} = \int_{\Gamma_{L-g}} \gamma d\Gamma + \int_{\Omega_{melt}} \rho g z d\Omega$
Integral form of the total energy function	$E_{total}(\psi) = \int_{-1/2}^{+1/2} (\gamma \sqrt{1 + \psi_y^2} + \frac{1}{2} \rho g \psi^2) dy$
The mass conservation constraint	$\rho_m v_{scan} \int_{-1/2}^{+1/2} \psi dy = m_f \eta_m$

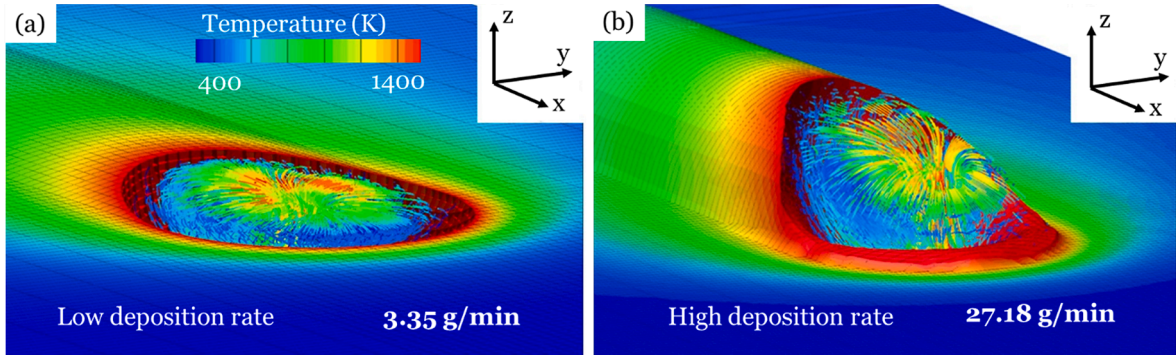


Fig. 55. Predicted track shapes along with calculated temperature and velocity of the melt pool during (a) low and (b) high material deposition rates from [936]. The shape of the deposits in [936] are modelled via surface energy minimization.

Table 19

PDEs expressing the LS and VOF methods along with the definition of their associated flag variables.

LS	$\frac{\partial \phi}{\partial t} + \frac{\partial}{\partial x_j} (u_j^{L/G} \phi) = \sum S_{LS,i}''$		
	$\phi < 0 : \text{solid}$	$\phi > 0 : \text{void}$	$\phi = 0 : \text{interface}$
VOF	$\frac{\partial F}{\partial t} + \frac{\partial}{\partial x_j} (u_j^F F) = \sum S_{VOF,i}''$		
	$F = 1 : \text{solid}$	$F = 0 : \text{void}$	$0 < F < 1 : \text{interface}$

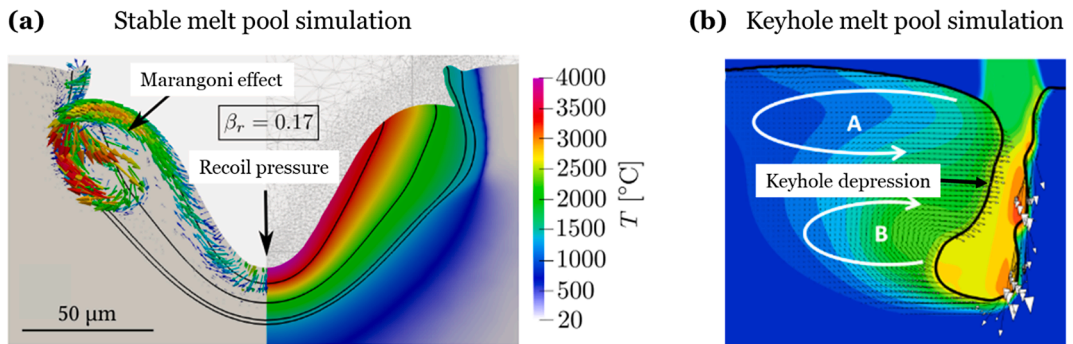


Fig. 56. Two examples of transport-based L-PBF simulations of (a) stable melt pool [948] and (b) keyhole melt pool [949] conditions with LS as the surface-tracking algorithm.

evaporation of the metallic phase which leads to a normal pressure that in a similar way to the capillary forces, acts perpendicularly to the free surface of the melt pool. Furthermore and as seen in Table 21, in the CSF method for both LS and VOF, there is a stabilizing multiplier. These stabilizers, as per their name, are supposed to smoothen the transition of the volumetric forces over the interface region to avoid severe numerical instabilities [954,955]. Furthermore, the stabilizing term used for the heat sources are also supposed to add a larger weight on the metallic phase and therefore they involve additional parameters.

Even though the majority of both transport- and conduction-based models use a Gaussian heat flux to simulate the laser heating process, there is currently no consensus about the choice of q_{ν}^{ν} ($W \cdot m^{-3}$) and this is especially the case in DED simulations. In powder or wire DED processes, the energy is delivered to the sample in a direct way, where the laser irradiates the surface of the sample and at the

Table 20
Interpolation functions and derivative forms of flag variables for the LS and VOF methods [686,953].

Property	LS	VOF
Flag scalar	$\phi(m)$	$F(-)$
Interpolation function	$H(\phi) = \begin{cases} 1 & \phi < -\epsilon \\ \frac{1}{2} \left[1 + \frac{\phi}{\epsilon} + \frac{1}{\pi} \sin\left(\frac{\phi\pi}{\epsilon}\right) \right] & \phi \leq \epsilon \\ 1 & \phi > \epsilon \end{cases}$	$F(-)$
Material property $\chi^*(-)$ over interfaces	$\chi^*(H) = \sum H_k \chi_k^*$	$\chi^*(F) = \sum F_k \chi_k^*$
Derivative form	$\delta(\phi) = \frac{\partial H}{\partial \phi} = \begin{cases} 1 & \phi < -\epsilon \\ \frac{1}{2\epsilon} \left[\cos\left(\frac{\phi\pi}{\epsilon}\right) \right] & \phi \leq \epsilon \\ 1 & \phi > \epsilon \end{cases}$	∇F

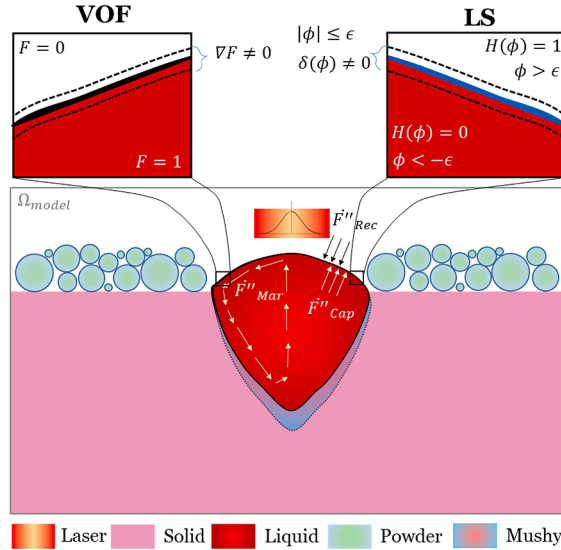


Fig. 57. Schematic figure of the melt pool from front view to show the difference between VOF and LS at the metal-gas interface.

Table 21
Transformation of 2D fluxes and forces into corresponding volumetric forms via the CSF method for LS and VOF.

Flux / force	The original 2D form Definition	Volumetric term via the CSF method		Stabilizer term
		LS	VOF	
$\dot{q}_{Laser} (W.m^{-2})$	$\frac{2\eta_L P_L}{\pi r_b^2} \exp\left(-\frac{2r^2}{r_b^2}\right)$	$\dot{q}_{Laser} \cdot \delta(H)$	$\dot{q}_{Laser} \cdot \nabla F$	$\frac{2\overline{\rho c_p}}{\rho c_p _{metal} + \rho c_p _{air}}$
$\dot{q}_{evap} (W.m^{-2})$	$(1-\beta_r) \sqrt{\frac{M}{2\pi RT}} p_0 \exp\left(\frac{\Delta H_{lv} M}{RT_{vap}} \left(\frac{T-T_{vap}}{T}\right)\right) \Delta H_{lv}$	$\dot{q}_{evap} \cdot \delta(H)$	$\dot{q}_{evap} \cdot \nabla F$	
$\dot{F}_{Cap} (N.m^{-2})$	$\kappa \sigma n_i$	$\dot{F}_{Cap} \cdot \delta(\phi)$	$\dot{F}_{Cap} \cdot \nabla F$	$\frac{2\overline{\rho}}{\rho _{metal} + \rho _{air}}$
$\dot{F}_{Mar} (N.m^{-2})$	$\frac{dy}{dT} [\nabla T_i - n_i (\nabla T_k n_k)]$	$\dot{F}_{Mar} \cdot \delta(\phi)$	$\dot{F}_{Mar} \cdot \nabla F$	
$\dot{F}_{Rec} (N.m^{-2})$	$p_0 \exp\left(\frac{\Delta H_{lv} M}{RT_{vap}} \left(\frac{T-T_{vap}}{T}\right)\right) n_i$	$\dot{F}_{Rec} \cdot \delta(\phi)$	$\dot{F}_{Rec} \cdot \nabla F$	

same time in an indirect way, in which, the energy is transported by molten powder particles or the feeding wire. Therefore, there are several ways to model the energy delivery in DED processes and Table 22 lists a number of such expressions together with their corresponding mass source terms.

According to Table 22, Gan et al. [932] used a streamlined way of modelling the heating process during DED and assumed a Gaussian heat flux for the laser beam, whereas Singh et al. [924] used a somewhat more advanced heat flux with a Gaussian distribution and included the bulk energy delivery from the powder particles as well as the surface heating due to direct laser irradiation. [923], however, divided the heat flux used by Singh et al. [924] by the nominal track height t (m) and derived a volumetric heat source instead. Knapp et al. [926] simulated the heating process with a combination of heat source and heat flux, where the former represented the indirect heating due to powder particles collision with the melt pool, and the latter represented the direct attenuated laser

Table 22
Different types of mass and energy heat sources used in transport-based DED models.

	$\sum \dot{S}_{mass}$	\dot{q}_{Laser}	$\dot{q}_{v, Laser}$
Gan et al. [932]	0	$\frac{f_H P_L \eta_{liq}}{\pi r_b^2} \exp\left(-f_H \frac{r^2}{r_b^2}\right)$	0
Singh et al. [924]	0	$\frac{f_H P_L (\eta_p + \eta_{liq} (1 - \eta_p))}{\pi r_b^2} \exp\left(-f_H \frac{r^2}{r_b^2}\right)$	0
Manvatkar et al. [923]	0	0	$\frac{f P_L (\eta_p + \eta_{liq} (1 - \eta_p))}{\pi r_b^2 t} \exp\left(-f \frac{r^2}{r_b^2}\right)$
Knapp et al. [926]	0	$\frac{f_H (\eta_p P - m_f c_p (T_{sol} - T_{amb}))}{\pi r_b^2} \exp\left(-f_H \frac{r^2}{r_b^2}\right)$	$\frac{f (m_f c_p (T_{sol} - T_{amb}))}{\pi r_b^2 c} \exp\left(-f \frac{r^2}{r_b^2}\right)$
Wei et al. [956]	$\frac{\eta_c m_f}{n_{cells} V_{cell}}$	0	$\left(\dot{Q}_p + \dot{Q}_s\right) \nabla F,$ $\dot{Q}_p = \frac{\eta_c m_f [c_p (T_{sol} - T_{amb}) + \Delta H_{sl}]}{\pi r_b^2},$ $\dot{Q}_s = \frac{\eta_s \left(P - \frac{\eta_c m_f}{\eta_p} [c_p (T_{sol} - T_{amb}) + \Delta H_{sl}]\right)}{\pi r_b^2}.$

Table 23
Bramson and Hagen-Rubens relationships for calculating the liquid metal absorptivity for laser heating.

Bramson's model [853]	$\eta_{liq} = 0.365 \left(\frac{R(T)}{\lambda}\right)^{0.5} - 0.067 \left(\frac{R(T)}{\lambda}\right) + 0.006 \left(\frac{R(T)}{\lambda}\right)^{1.5}$
Hagen-Rubens model [957]	$\eta_{liq} = (8 \epsilon_0 \omega R(T))^{0.5}$
Electrical resistivity for Ni-based alloys [958]	$R(T) = 1.251 + 1.346 \times 10^{-4} T$

irradiation.

$\eta_{liq} (-)$ in Table 22 is the laser absorption coefficient for liquid metal. The expanded form of a number of laser absorption coefficients used for melt pool simulations of MAM are given in Table 23.

Based on Table 23, Bramson's model is a function of the wavelength of the laser whereas the Hagen-Rubens expression is suited near infrared laser absorptions [938].

Furthermore, it is noted in Table 22 that the mass source term in [924,923] and [926] are set to zero and this is because all these models have fixed surfaces and therefore their surface shape is prescribed a-priori, as opposed to more advanced simulations with surface-tracking modules [956]. Similar transport-based models have also been used to a large extent to simulate the thermal and fluid dynamics conditions during PBF processes. [959] and [960] developed FVM-based CFD simulations of the L-PBF process of AlSi10Mg and In718, respectively, and used the VOF method to model the surface hydrodynamics. They moreover assumed a very primitive powder layer configuration, which only involved a single layer of powder particles. Furthermore, they assumed a uniform size distribution for the powder particles. In their later work, [961] added the recoil pressure contribution in addition to the Marangoni effect and capillarity and they reported a higher level of surface porosity at a scanning speed of 500 mm.s⁻¹, in contrast to almost no surface porosity observed at a lower speed of 200 mm.s⁻¹.

Transport-based simulations with surface-tracking algorithms are ideal for predicting defect formation during the course of the process. The two most widely-observed defects in MAM processes are surface irregularities and porosities. In a recent study, it was clearly shown by means of an FVM-based multiphysics simulation that depending on the scanning speed, a track with uniform morphology, necking defects or apparent balling defects could form [962]. Similar FVM-based models were developed to predict the depression zone using VOF as the surface-tracking method [963–965]. There is a possibility of lack-of-fusion porosity formation during PBF processes which operate under low linear energy densities or bigger hatch spacing [966]. [967] simulated the formation of inter-layer and inter-track lack-of-fusion porosity formation during L-PBF of In718 with an FVM-based CFD model, see Fig. 58 (c). However, the computational domain included only three layers without accounting for the intra-track cooling time which is the time that takes for the laser to reach the start of the second track after scanning the part of the first track which is outside the model domain. On the other hand, under higher laser power-to-speed ratios, there is a likelihood of porosity formation due to a deep keyhole formation [968]. Prediction this requires a more advanced heat source model involving multiple reflections and ray-tracing. Although [969,970] managed to successfully simulate the keyhole porosity via using a complex moving volumetric heat source, it is currently well-established in literature that keyhole undulations are predominantly caused by multiple reflections and instantaneous entrapment of laser rays inside the cavity of the depression zone [971] (see Fig. 58 (d)). The ray-tracing method has been used in [972,973] for investigating different types of keyholes as well as the effect of the previous tracks' morphology on the porosity formation of the most recent track, respectively.

Similar models were adopted for investigating how the balling effect could form during EB-PBF. In [974] a CFD model of the EB-PBF of Ti6Al4V with a physically-informed heat source model was used to find the most influential parameters that cause balling (see Fig. 58 (a)). It was reported that a higher power along with lower layer thicknesses result in least balling. In a follow-up work [978],

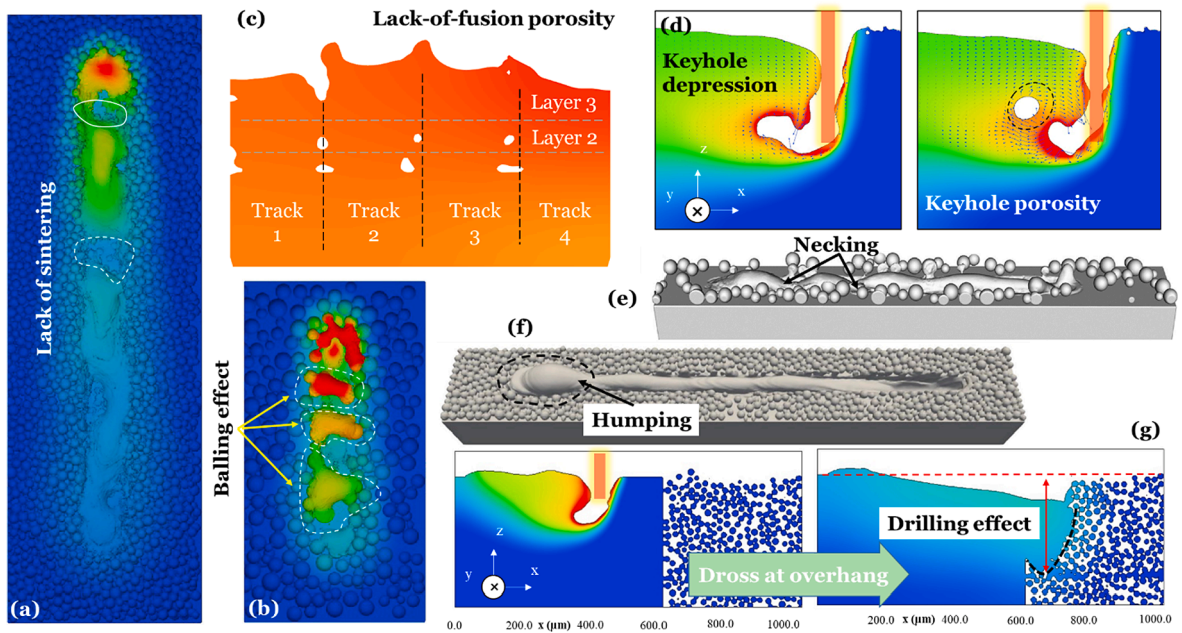


Fig. 58. Transport-based simulation of PBF processes showing (a) lack of sintering, (b) balling effect [974], (c) lack of fusion porosity [967], (d) keyhole formation and keyhole-induced porosity [971], (e) necking [975], (f) humping [976] and (g) dross formation [977]. Note that (a) and (b) are EB-PBF and the rest belong to the L-PBF process.

different scanning patterns were examined in order to find the best scanning strategy resulting in the lowest lack-of-fusion porosity possible. Overhang defects formation for downfacing surfaces were studied and modelled in [977] in which an FVM-based model was used to analyze the seldomly dross defect during L-PBF (see Fig. 58 (g)). In this work it was revealed that the melt pool depression turns into a drilling mode when it enters the powder domain at the end of the track and this leads to dripping-like defects denoted dross. In [979] different scanning directions on the edge of overhangs were tested but the melt pool regime was only in the conduction regime without any depression formation. The mechanism behind the formation of bulges at the beginnings of tracks, the so-called humping effect, was elaborated with a CFD model and it was concluded that at fixed linear energy densities, bigger humps form at higher scanning speed as more material will be re-distributed at the tail of the melt pool since bigger channels form [976], see Fig. 58 (g).

Such CFD simulations were also employed for more fundamental studies in [980–982]. Bayat et al. [980] investigated the role of positive and negative thermo-capillarity during the L-PBF process and concluded that regardless of the direction of the Marangoni effect, the melt pool temperature becomes lower and gets distributed more uniformly as the magnitude of this effect increases. In the work by Wu et al. [982] the impact of evaporation as well as the evaporation pressure on the melt pool was studied using an FVM-based model. Similar FVM-based transport models with minor modifications [983–988] have been developed mainly for understanding how changes in different input process parameters affect the defect formation as well as the melt pool dynamics.

Apart from the bulk of the melt pool simulations which are carried out with the FVM method, there are also some contributions based on the Lattice-Boltzmann (LB) method which predicts the fluid dynamics condition of a fluid, based on collision and streaming. Several works from Körner's group at FAU Erlangen are based on the LB method and mainly developed for the EB-PBF process of Ti6Al4V both in 2D [989,990] and 3D [991]. [975,992] also based their CFD model on the LB method and modelled single track continuous and pulsed L-PBF processes with this procedure. In a recent work from Körner's group [993], a 2D transport-based model of the PBF process of a bi-material alloy is developed using LB, where important material properties get actively updated based on the information from the phase diagram. The composition functionally graded materials (FGM) are receiving increasing attention in academia and the abovementioned CFD models are useful for identifying the distribution of an alloy over the other alloy. Depending on the shape of the compositional gradient, whether the transition occurs over two layers or 10 layers, there is a risk of micro-crack formation in locations with sharp compositional transitions, see Fig. 59 (a). In [994] the melt pool dynamics during L-PBF of In718/Cu10Sn was modelled using FVM model and it was observed that the melt pool size is significantly smaller over regions which were rich in Cu10Sn. Similar observations were reported in [995] and the reduced melting detected in the simulation results was ascribed to regions with higher Cu10Sn content which had higher thermal conductivity. In a more recent work [996], the L-PBF process of In718 powder on 316-L stainless steel was analyzed and it was noted that the interface between these two alloys, under some specific process parameters, resembles fish-scale morphologies, see Fig. 59 (b). That being said, it is important to emphasize that [994–996] simulated the second material phase fraction with a passive scalar field, rather than modelling it as an active variable from which the material properties of the entire FGM material could be updated and changed, as done in [993].

The Arbitrary Lagrangian Eulerian (ALE) method is another approach to model the fluid dynamics of the melt pool and it has been

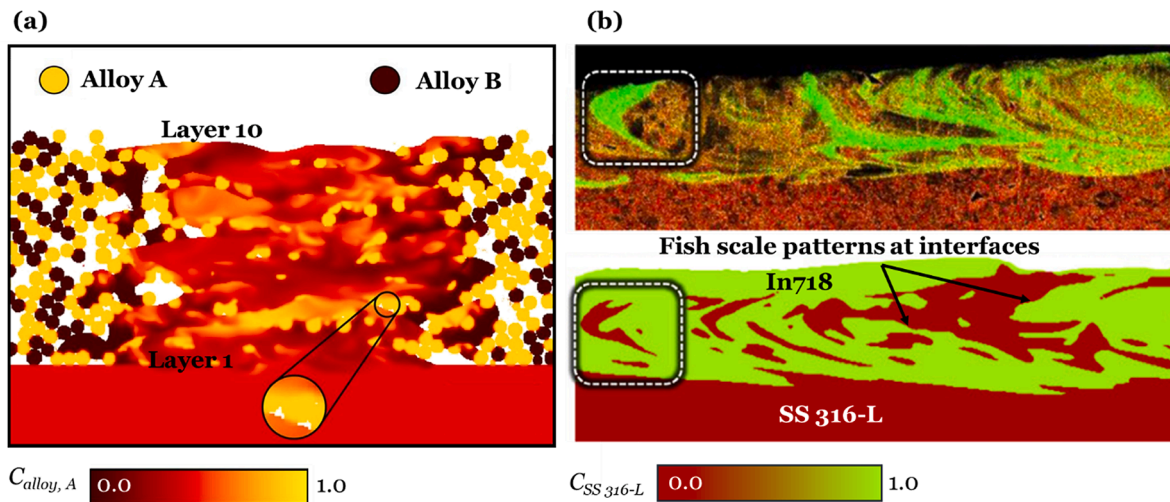


Fig. 59. Compositional FGM material simulation for (a) EB-PBF process of hypothetical materials A and B [993] and (b) L-PBF process of In718 on stainless steel 316-L base [996].

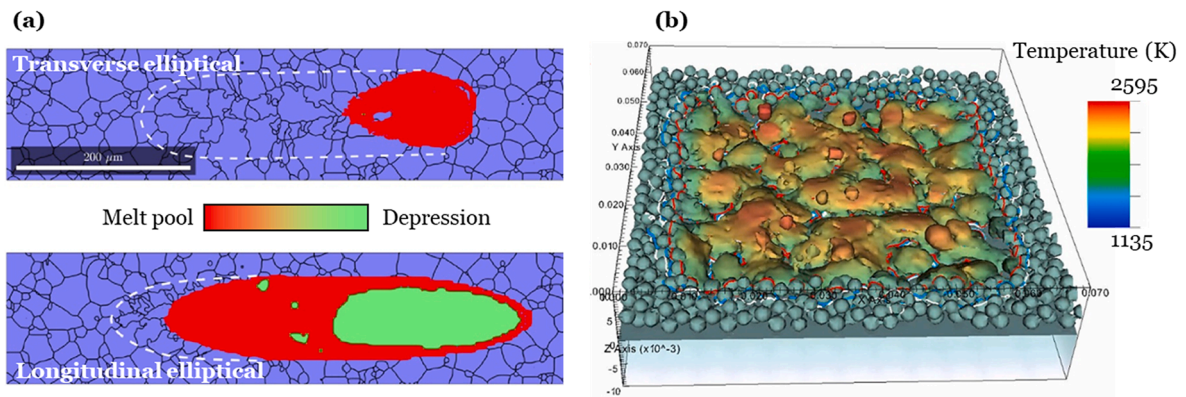


Fig. 60. Predicted melt pool shape using ALE3D for (a) single track L-PBF with transverse elliptical and longitudinal elliptical beam shapes [685] and for (b) large area pulsed L-PBF [1001].

successfully employed by the simulation research team at the Lawrence Livermore National Laboratory (LLNL) for the purpose of modelling PBF processes. The ALE-based numerical code at LLNL is ALE3D that uses a hybrid FEM and FVM formulation and the domain discretization is carried out on unstructured grid [997,998]. ALE3D has so far been used for modelling the melt pool conditions [999,1000] and in one case the spatter formation [777] during L-PBF. In more recent works from the MAM simulation group at LLNL, the impact of beam shaping, on the melt pool as well as the microstructure was modelled [685] see Fig. 60 (a). Moreover, Roehling et al. [1001] used this code in a recent study to model the large-area L-PBF process of 316-L stainless steel with a pulsed laser beam, see Fig. 60 (b).

Despite the different frameworks applied to the modelling of PBF processes, i.e. LB, FEM, FVM, ALE, or smoothed particle hydrodynamics [1002,1003] (SPH), most of the transport-based DED models are based on the FVM method and this is mainly due to the fact that the robust VOF surface-tracking algorithm is a perfect together with the FVM. This combination of VOF and FVM has also been applied to powder DED processes of In718 [956], In625 [1004], iron-sulfur compounds [1005], 316-L stainless steel [1006], 1045 steel [1007,1008], etc. In most of these simulations, the focus is on how the change in the mass or energy per unit length could alter the dilution rate or potential inter-track porosity formation (Fig. 61).

One major drawback of such DED models which do not explicitly model the powder injection step, is that they entirely ignore the momentum effect of the high-velocity powder particles that impact the melt pool. In a recent study by Bayat et al. [1010] it is demonstrated how the collision of the powder particles with the melt pool, inverts the fluid direction from outwards to inwards. The significance of the particles' linear momentum and thermal condition could be better understood when looking at the powder-gas dynamics models mentioned earlier in this section, where it was shown these particles could obtain high temperatures as well as very high momentums depending on the input process parameters. Therefore, it is ideal to couple a powder-gas dynamics or aerodynamics model to a subsequent transport-based model, in order to capture the thermo-fluid effect of incoming particles on the melt pool. Despite requiring extra computational resources, such works give better predictions of the temperature and hydrodynamics

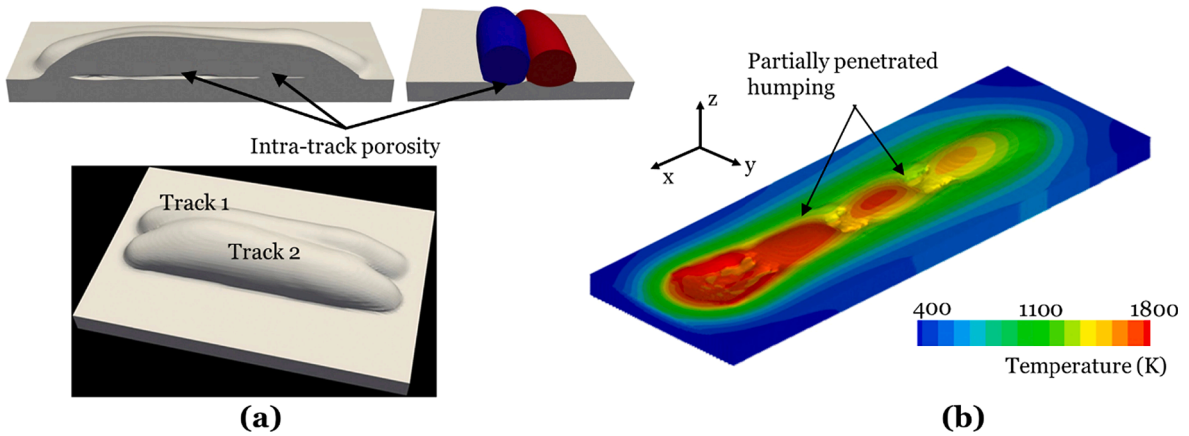


Fig. 61. (a) 3 different views of the calculated track shape for powder DED of In718 where intra-track pores are formed between the two tracks [956]. (b) Predicted shape of the surface of a track for wire DED process where observable humps and discontinuities are shown [1009].

Table 24

2D and 3D forces in wire DED simulations. Note that for the 2D forces, the CSF/VOF method is used to convert them to volumetric forces. The last three lines relate to the electro-magnetic, solidification drag and buoyancy forces which are all global, in contrast to the first four forces which are applied to the melt pool interface [1009,1011,1012].

Force	The original 2D form Definition	Volumetric term via the CSF method in VOF	Stabilizer terms
$F_{Cap}^f (N.m^{-2})$	$\kappa \sigma n_i$	$F_{Cap}^f \cdot \nabla F$	$\frac{2\bar{\rho}}{\rho_{metal} + \rho_{air}}$
$F_{Mar}^f (N.m^{-2})$	$\frac{d\gamma}{dT} [\nabla T_i - n_i (\nabla T_k n_k)]$	$F_{Mar}^f \cdot \nabla F$	
$F_{Rec}^f (N.m^{-2})$	$\rho_0 \exp\left(\frac{\Delta H_{lv} M}{RT_{vap}} \left(\frac{T - T_{vap}}{T}\right)\right) n_i$	$F_{Rec}^f \cdot \nabla F$	
$p_{arc} (N.m^{-2})$	$P_{max} \exp\left(-\frac{r^2}{2r_p^2}\right) n_i$	$F_{Cap}^f \cdot \nabla F$	
$F_{EM}^f (N.m^{-3})$	$-\left(\frac{\Omega_{x1}}{r}\right) \exp\left(-\frac{r^2}{2r_p^2}\right) \left(1 - \exp\left(-\frac{r^2}{2r_p^2}\right)\right) \left(1 - \frac{x_3}{z_0}\right)^2 \left[\frac{(x_1 - x_{1,arc})}{r}\right]$ $-\left(\frac{\Omega_{x2}}{r}\right) \exp\left(-\frac{r^2}{2r_p^2}\right) \left(1 - \exp\left(-\frac{r^2}{2r_p^2}\right)\right) \left(1 - \frac{x_3}{z_0}\right)^2 \left[\frac{(x_2 - x_{2,arc})}{r}\right]$ $-\left(\frac{\Omega_{x3}}{r}\right) \exp\left(-\frac{r^2}{2r_p^2}\right) \left(1 - \frac{x_3 - x_{3,arc}}{z_0}\right)$		
$F_{CK}^f (N.m^{-3})$	$\frac{K_c (1 - f_{liq})^2}{C_k + f_{liq}^3} u_i^F$		
$F_{\beta}^f (N.m^{-3})$	$\rho g_i \beta \Delta T$		

conditions of the melt pool. These two-way coupled or fully coupled models will be discussed shortly after this section.

One-way coupled melt pool models have been widely applied to wire DED processes due to their less complexity as compared to powder DED processes. The relevant source terms added to the linear momentum PDE for wire or wire arc DED processes are given in Table 24.

In contrast to powder DED where powder particles collide with the melt pool at a very high speed and thus to a large extent affect the internal fluid flow, the melt pool and the entire deposition process is more stable in wire DED as the material gets continuously fed into the melt pool at a controlled and relatively slow speed. A multiphysics simulation of wire DED of Ti6Al4V was developed in [1013] and a significant growth of the melt pool length from about 10 mm to 16 mm was noticed after printing 21 layers on the top of each other. Moreover, similar to L-PBF, depression zones form at the front part of the melt pool and this is caused by the arc pressure and the overall impact of the electromagnetic forces, see Table 24. In a more advanced model, the impact of liquid metal droplet due to feeding and on the melt pool’s dynamics is also captured [1014]. Larger printing volumes consisting of multiple layers and with more complicated helical scanning paths was modelled in [1015] In a more recent work, the impact of ultrasonic vibrations on the melt pool’s shape during wire DED of 1045 steel was investigated in [1016] and it was shown that the melt pool’s width-to-depth ratio increases in the case of vibrations.

3.2.2.5. Fully coupled powder-gas–melt pool simulations. Fully-coupled powder-gas–melt pool simulations are in essence a combination of the powder-gas dynamics models and melt pool evolution models discussed earlier. In contrast to the previously presented powder

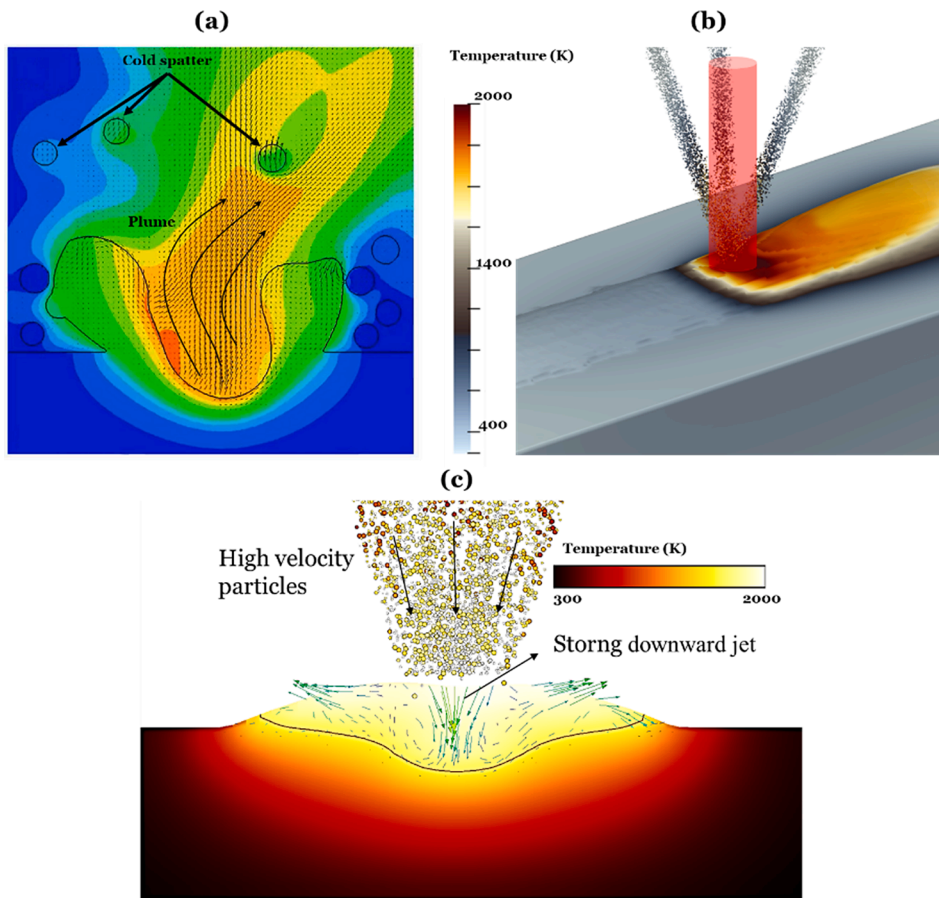


Fig. 62. Two-way coupled simulation of (a) the L-PBF process [1017] and (b) and (c) powder DED [1010].

gas dynamics simulations, which only simulate the interaction between the powder particles' motion and the jet plume in L-PBF or the shielding gas in powder DED, the fully coupled MAM simulations take into account the impact of the melt pool on the departing particles in L-PBF. Likewise the thermal and momentum impact of the incoming particles on the melt pool dynamics in powder DED are captured by such fully coupled models. However, the mutual impact between the melt pool condition and powder particle conditions differ in terms of main direction in these two MAM processes. More specifically, in L-PBF, the powder particle motion is triggered by the evaporation-induced vapor plume that originates from the melt pool, and hence the main direction of influence goes from the melt pool to the powder particles. However, in powder DED, it is the collision between the incoming powder particles and their subsequent effect on the melt pool condition which is the main direction of influence.

In [1017] the LS was implemented to identify the interface between the condensed (C) (metallic) and the gaseous phase (G) and, the ghost fluid method used to split these two regions into a C-mesh and a G-mesh region, respectively - see Fig. 62 (a). The fluid flow variables are solved with CFD assuming incompressibility inside the C-mesh region within the so-called real C-mesh and the interface cells in the C-mesh are designated ghost cells, while the rest of the cells are deactivated. The flow conditions of the gas phase are determined assuming high-speed compressible flow as well as an ideal gas and including the surface tension forces, the Marangoni effect as well as the laser heating via ray-tracing in the gas-condensed (G/C) interface cells. Finally, in order to calculate the motion dynamics of the powder particles, gas-induced forces from the CFD simulation calculated on the gaseous phase are then interpolated on Lagrangian points of powder particles and subsequently the motion of every individual powder particle is simulated based on Lagrangian particle tracking (LPT). At least four modes of powder-gas conditions could be identified, i.e. the recoil mode, the entrainment mode, the elevation mode and finally the expulsion mode.

Jakumeit et al. [1018] developed a fully coupled powder-gas-melt pool simulation of the L-PBF process of In718 and Ti6Al4V and solved the gas and metallic phases' fluid dynamics conditions with an FVM-based Eulerian multiphase approach and like [1017] used the ideal gas model to predict the gaseous phase's variables. The LPT method was used to predict the trajectory and position of the particles. Volume-averaged drag forces were calculated by Schiller-Neumann's drag coefficient expressions thereby obtaining the net force and ultimately the acceleration of powder particles and it was reported that the calculated particles' acceleration for various powder sizes, matches the theoretical values.

As for the powder DED process, the main coupling is the other way around, hence powder particles carried with the shielding gas that impact the melt pool dynamics. Wen and Shin [1019] coupled their previous powder-gas dynamics model with a transport-based

Table 25

The volumetric force and heat generation source terms expressing the momentum and thermal impact of the powder particles on the melt pool.

$F_{particles}^v (N.m^{-3})$	$\left[\frac{3\mu C_{Drag} Re}{4\bar{\rho}_p \bar{D}_p^2} (u_p - u_F) \right] \frac{\Delta t \dot{N}_p \bar{m}_p \cdot \nabla F}{\Delta V_{cell}}$
$q_{particles}^w (W.m^{-3})$	$\frac{c_p \Delta T_p \dot{N}_p \bar{m}_p \nabla F}{\Delta V_{cell}}$

melt pool for powder DED with a co-axial nozzle and used the LS method to capture the free surface of the melt pool. In [1020], the same authors applied this methodology to high powder diode laser off-axis powder DED and modelled both the particles trajectory and the evolving melt pool dynamics. This procedure was questioned by Ibarra-medina, Vogel and Pinkerton [1021] who believed that the coupling strategy was not clearly defined in the work by Wen and Shin.

A sophisticated and multi-step modelling strategy was proposed in [1022,1023] where different physics were sequentially coupled with each other. In these two works, separate models for gas dynamics, particle movement and finally the free surface evolution were developed and linked together. In [1024] and [1025] fully integrated modelling frameworks were developed to simulate both the powder particles' movement and their subsequent impact on the melt pool dynamics for powder DED of maraging steel MS-01 and In718, and see Fig. 62 (b) and (c). The thermal and momentum impact of injected particles on the melt pool was established by inserting the volumetric heat and source terms given in Table 25 into the linear momentum and energy balance PDEs listed in Table 9 and Table 14, respectively.

In Fig. 62 (c) one can see that due to collision of high-velocity powder particles with the melt pool, an inward fluid flow is formed. In Fig. 62 (c) it is further noticed that by increasing the overall particles' temperature, the fluid again reverts to a radially outward flow where the Marangoni effect dominates the particles' impact.

A simpler modelling approach was introduced in [1026,1027] where instead of calculating the particles' temperature as well as their motion dynamics during the ejection process, liquefied particles with initial melt temperatures were directly inserted into the melt pool. This method could represent a much cheaper, but also less accurate alternative as compared to the works [1024] and [1025], since there is no need to calculate the laser-particle interaction. This simplification was tested in earlier works in the 2000's in 2D melt pool simulations [1028]. Finally, the most complex and advanced model of the powder DED process has been given in [1029] where a DEM model for simulating the particles' conditions is coupled with a CFD model for predicting the melt pool dynamics. It was specifically shown in [1029] that the influence of the particles momentum on the melt pool dynamics is far larger than the Marangoni effect inside the melt pool.

4. Multi-scaling and reduction techniques

As discussed earlier, the properties of an AM component, observed at the macroscale, are dictated by processes and structural features at much smaller scales such as meso- and micro-scale. Hence, a holistic optimized design approach for AM requires a fine control over all different length scales involved both in the design of a component and in the manufacturing process. This section reviews the most important research efforts towards including all relevant interdependencies across scales in a computationally feasible manner.

4.1. Structural and material multi-scaling

Depending on the scale and the physics under consideration, relevant multi-scaling techniques can be divided into three categories:

- Homogenization and de-homogenization methods which deal with architected materials that are characterized by geometrical features defined at *meso*-scale.
- Integrated computational material engineering (ICME) dealing primarily with the material microstructure at the micro-scale level [1030].
- Process multi-scaling methods which also aim at the micro-scale level but deal specifically with the solidification and subsequent thermal cycles occurring during the AM process. These models are in essence reduced-order models of the advanced process simulations discussed in section 3 and are therefore ideal for being involved in the physics-based TO methods introduced in section 2.2.

Fig. 63 presents an overview of the various mechanical aspects that can be involved in a multi-scale analysis and optimization of an AM component. The figure also clarifies the terminology regarding the macro-, meso- and micro-scale, used in the following discussion of multi-scaling techniques. Moreover, it exemplifies the use of ICME and homogenization.

4.1.1. Homogenization

Homogenization methods constitute the core of multi-scaling. Based either on a periodic unit-cell or a so-called representative volume element (RVE), homogenization methods extract constitutive laws or parameters for a homogeneous material

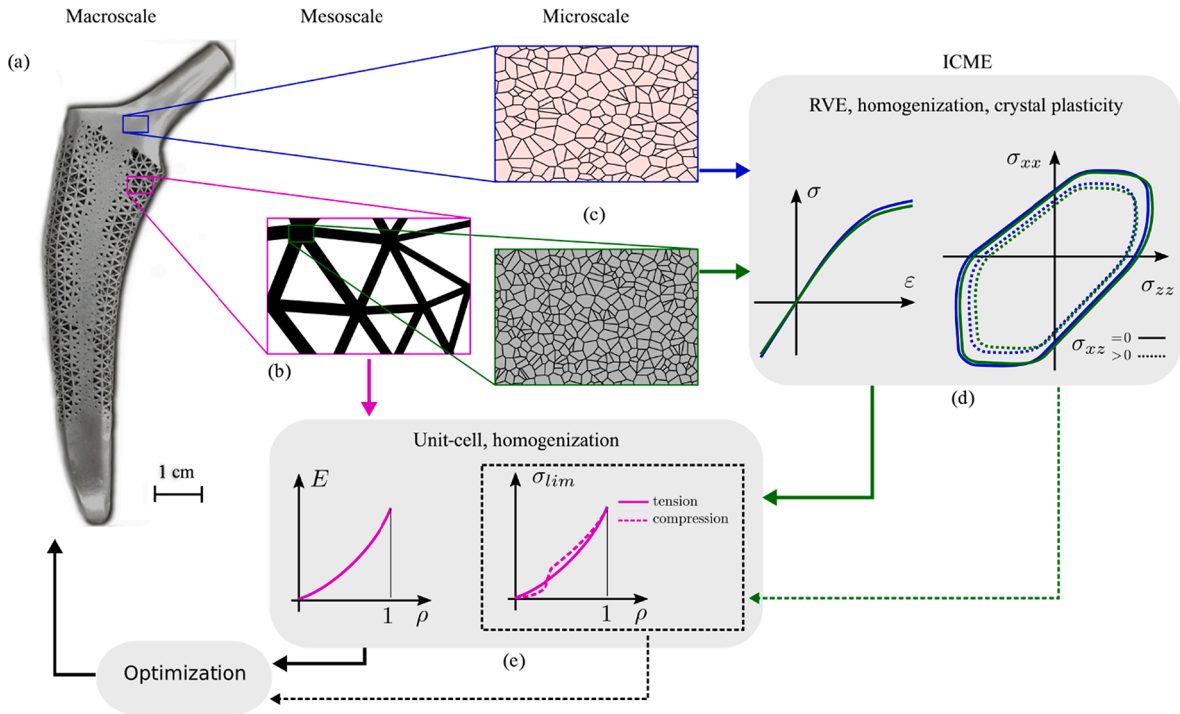


Fig. 63. Overview of mechanical multi-scaling methods. (a) 3D printed hip implant with functionally graded lattice [1031], (b) meso-scale architected structure, (c) material microstructure (d) homogenized elastoplastic behavior of a solid AM material depending on the actual microstructure and including anisotropy, (e) homogenized elastoplastic behavior of an architected AM structure as a function of the material volume fraction ρ (for $\rho = 1$ the solid material case is recovered).

Table 26

Overview of homogenization literature and terminology relevant for upscaling micro- and meso-scale features at various levels of fidelity. FE² is denoted finite element squared.

Homogenization methods	asymptotic/linear	nonlinear, FE ² , etc.
1st order / separation of scales	[1032,1033]	[1034–1037]
higher order / nonlocal / size effects	[1038,1039]	[1040–1042]

which represents a real material with an underlying heterogeneous structure. Applying homogenization to a unit-cell for an architected material, as e.g. the meso-scale lattice of Fig. 63 (b), can provide elasticity and plastic yield parameters as a function of the lattice volume fraction (cf. Fig. 63 (e)). Such functions are in turn essential for optimizing the lattice volume fraction distribution over the component domain (cf. Fig. 63 (a)). The main difference between unit-cells and RVEs, is that the latter only statistically represent the real materials, in contrast to unit-cells which are one-to-one representations of perfectly periodic structures. RVEs typically represent a statistically sufficient portion of the polycrystal micro-structure of metals, see Fig. 63 (c). They are used in ICME for predicting the material behavior as a function of the material microstructure, even accounting for anisotropies (Fig. 63 (d)).

Table 27

Fundamental equations for 1st order homogenization ().

Equation	Description
$\bar{P} = \frac{1}{ RVE } \int_{RVE} P dV$	Averaging of micro-scale (or meso-scale) 1st PK stress tensor P to the homogenized tensor \bar{P}
$\bar{F} = \frac{1}{ RVE } \int_{RVE} F dV$	Averaging of the micro-scale (or meso-scale) deformation gradient F to the homogenized tensor \bar{F}
$\delta\bar{P} = \bar{C} : \delta\bar{F}$	Homogenized tangent (fourth-order) stiffness tensor \bar{C}

adapted from [1046]

The term “homogenization” is often considered equivalent to first order asymptotic homogenization, which is used for example to extract linearized elasticity parameters, i.e. Young's modulus and Poisson's ratio, for a heterogeneous or porous material. However, higher order and nonlinear methods are also important and useful for multi-scaling in the AM context. Table 26 shows an overview of the different types of homogenizations available in the literature based on the two categorizations.

For the classical first-order homogenization theory, [1032], to be applicable, one must ensure a sufficient separation of scales. Unit-cell parameters and orientation are assumed to change slowly, and macroscale stress gradients are assumed to be small enough for changes at the unit-cell scale to be insignificant [1038,1043]. The classical FE^2 method is a numerical solution to this problem for a micro-structure with a general nonlinear behavior [1044]. When separation of scales between the unit-cell scale and the component scale is not granted, more specialized methods are necessary such as multiscale FEM [1045] and higher order homogenization approaches [1038,1040,1043]. In addition, Table 26 distinguishes between asymptotic homogenization applied for linear problems, and nonlinear homogenization [1034], for unit-cells or representative volume elements involving material and kinematic nonlinearities. The latter is for example relevant for obtaining stress strain curve as those shown in Fig. 63 (d). Table 27 shows the most fundamental equation for 1st order nonlinear homogenization of an RVE.

4.1.2. Integrated computational material engineering (ICME)

At length scales similar or lower than the AM process resolution, AM materials are heterogeneous. Material mechanics at these scales and homogenization, are therefore essential for a series of macroscopic mechanical properties. Elastic and plastic anisotropy, yield and ultimate tensile strength, as well as toughness are the most important ones, studied in the literature.

In the context of a holistic computational design approach for AM, linking the material micro-structure (or *meso*-structure) to macroscopic properties is not only essential for assessing the performance of a given component but also for tailoring its material micro-structure (or *meso*-structure) towards a specific application. In that sense, the material microstructure is not necessarily treated as a given condition but it can also be subject to optimization. This possibility is addressed in the research field of ICME [1030]. ICME is typically applied to metals, but it can also be applied to polymer AM [1047]. Fig. 64 demonstrates how an ICME model can reflect the actual interdependencies between process, microstructure and material properties in a computational environment.

Multiphysics simulations at deposition-scale, such as the ones discussed in section 3.2.2 coupled with the microstructural simulations i.e. CA, MC and PF described earlier in section 3.2.1 can be used in order to obtain essential microstructural data such as grain morphology and texture. This kind of data, which are necessary for creating a statistically representative volume for the material of interest, were traditionally obtained experimentally requiring considerably larger effort as compared to computationally generated RVEs. Process simulations can also provide essential information about the morphology of porosities, which is highly relevant for parts made through MEX processes, discussed in section 3.1.1. Such RVE models are the most fundamental tool within ICME for bridging the micro-scale with the continuum scale. For computational reasons they represent a small volume of the material in question, sufficiently large though to statistically represent the actual microstructure in terms of grain morphology, properties and orientation [1049,1050] (cf. Fig. 64 (d)). The most simple form of upscaling from the RVE scale to the meso- or macro-scale is based on asymptotic homogenization [1032]. RVE models for metals typically involve rather complex elasto-plastic anisotropic constitutive laws within each grain of the RVE [1051], or they can be created based on a rectilinear grid mesh, simulated either with FE or spectral solvers [1052], or they can be based on grain conforming meshes and simulated with FE solvers [1053]. Publicly available software (open source) such as DREAM3D [1054] and Neper [1053] are extremely valuable tools used in a large portion of the available AM literature for the creation

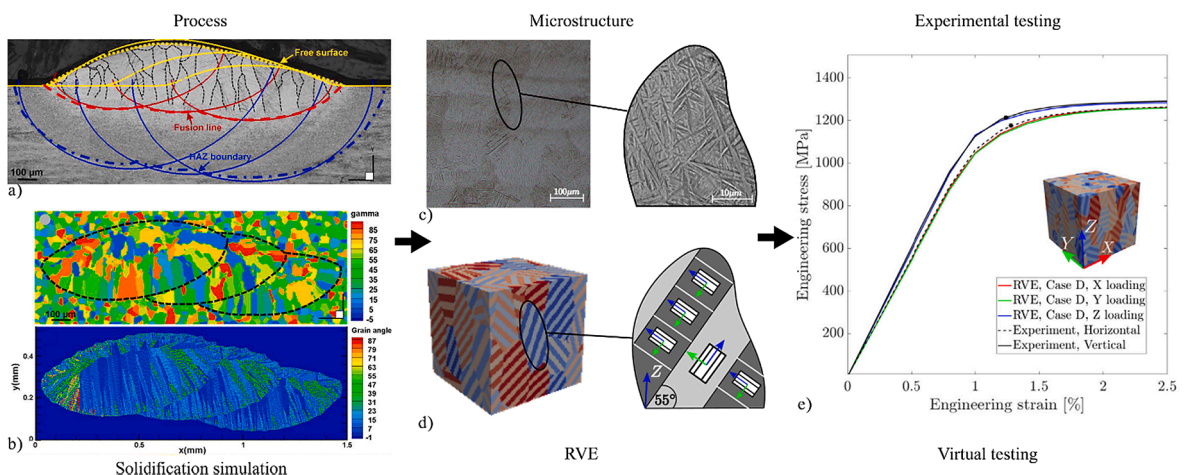


Fig. 64. Demonstration of the ICME concept for AM Ti6Al4V. Like the real AM process (a) leads to a characteristic martensitic microstructure (c) [1048], a cellular automata simulation of the solidification process (b) can provide grain structure and texture information for the creation of an equivalent RVE (d) [1048]. The RVE model is verified when it can reproduce the experimentally observed mechanical behavior through an equivalent virtual experiment (e) [1048]. The verified ICME model can then be used to study the effect of process parameters on the mechanical behavior of the printed material numerically.

Table 28

Crystal plasticity equations used in a classical ICME model.

$F = I + \nabla u = F_e F_p$	Deformation gradient for the displacements field u and its decomposition into an elastic and a plastic part
$S = \mathbb{C} : (F_e^T F_e - I)/2$	Commonly used constitutive law providing the second Piola-Kirchhoff stress (valid for large rotations and small elastic strains)
$\dot{F}_p = \sum_i \dot{\gamma}_i s_i \otimes n_i F_p$	Temporal rate of the plastic part of the deformation tensor as a function of the slip rates $\dot{\gamma}_i$ of all slip systems i characterized by a slip direction s_i and a slip plane normal n_i
$\dot{\gamma}_i = \frac{\dot{\gamma}_{ref}}{\tau_{i,crit}^n} \tau_i ^{n-1} \tau_i$	Slip rate for slip system i as a function of the resolved shear stress τ_i (written in a form free of the nondifferentiable sign function). $\dot{\gamma}_{ref}$ and $\tau_{i,crit}$ are crystal specific parameters.

and analysis of RVEs. The RVE creation in such software is a first step based on statistical input (expected value and variance) regarding the grain size and aspect ratio. A second essential step consists in assigning a crystallographic orientation to each grain that is in accordance with texture measurement or process simulation. The last important step is to assign crystal plasticity parameters to each type of crystal in the RVE. The main crystal plasticity equations used in the modelling of individual RVE grains are summarized in Table 28, along with necessary crystal plasticity parameters.

In connection to AM, the vast majority of RVE models for ICME deal with two metals of interest, Titanium alloys and steel. An excellent demonstration of RVE modelling for accurately reproducing the experimentally observed anisotropic hardening of AM of high manganese steel, has been provided by Motaman et al. [1055]. Similar numerical investigations were made for AM stainless steel 316L by Charmi et al. [1056] and for Ti-6Al-4 V by Riyad et al. [1057], and by Somlo et al. [1048]. All these works rely to some degree on experimental data, used either for model calibration or validation. They all recognize the strong impact of crystallographic texture on the macroscopically observed anisotropic yielding behavior. In that sense, such RVE models can contribute to a holistic computational design by providing e.g. anisotropic yield surfaces for any crystallographic texture obtained by AM process simulations (Fig. 63 (d) and Fig. 64 (e)).

Pressure-independent anisotropic yield surfaces [1058–1060], generated from RVE models, can adequately describe the yield limit of the represented material microstructure. In this context, the process for extracting macroscopic yield surfaces from RVE models is referred to as virtual testing [1061–1063]. This homogenization approach has been successfully applied to AM metals e.g. in [1064] and [1065]. The latter work demonstrates also that apart from the anisotropy it may also be necessary to consider non-quadratic yield surfaces [1066], to accurately represent the yield limit of the RVE under general loadings. Although virtual testing is extremely valuable for substituting tedious and expensive, or impractical experimental tests, a certain amount of experimental testing is still necessary for calibrating the numerical RVE models used in the virtual testing. Typical examples of such fundamental experimental testing of AM metals can be found in [1067–1071]. Some of these experimental works include also important discussions about the possible links between the printing process as well as subsequent heat treatment, and the obtained microstructure.

One area where AM related ICME literature is rather scarce, concerns the role of micro-residual stresses on the macroscopically observed behavior of 3D printed metals. Micro-residual stresses occur at the grain level during solidification and thermal cycling during printing and have a large impact on the yielding and fracture resistance behavior of the produced metal. Some preliminary works in this area can be found in [1072,1073]. AM-process induced residual stresses at the component level are easier to address than micro-residual stresses, and they are therefore much more studied in the available literature [1074,1075].

4.1.3. Architected materials

One of the main strengths of AM is its freedom of producing complex geometries with a very fine spatial resolution. Architected materials exploit this freedom for achieving tailored mechanical properties by means of a complex porous geometry at the mesoscale [1076–1080], with a characteristic dimension comparable to the spatial resolution of the AM method in use. The fine spatial resolution of modern AM, makes the use of multi-scaling methods imperative in order to avoid a prohibitive computational load and still harvest the full potential of architected materials within an optimization based holistic design approach.

There are two general approaches for the use of architected materials in the design of AM components. The first approach concerns components consisting of a constant periodic lattice structure over their entire volume or over an interior infill volume (cf. Fig. 65 (a)). The second approach deals with components made of spatially varying lattice structures, where the mesoscale architecture is tailored to the specific loading conditions at each individual point over the component geometry [1081] (cf. Fig. 63 (a) and (b) and Fig. 65 (b)). Such functionally graded material designs can be obtained by simply varying the material volume fraction of the lattice over space, or even by adapting the lattice orientation locally in order to exploit its anisotropy.

Periodic architected materials have been studied and optimized with regard to stiffness [1082], buckling resistance [343], dynamic properties [1083,1084] and energy absorption [1085]. Normally, a compromise is necessary between buckling strength and stiffness, because these two properties are inherently in competition, although considerable buckling strength improvement at little decrease in stiffness can be achieved by introducing hierarchy [345] (see section 2.1.2). Independent of whether a periodic material architecture is optimized or not, the process of upscaling from the mesoscale to the component scale is based on the mathematical theory of homogenization [1032,1046] as earlier discussed. Analytical or computational homogenization, applied to the unit-cell of an architected material, is employed for obtaining macroscopic properties such as stiffness, plastic yield, and buckling limit.

For components made of spatially constant periodic lattices, homogenized mechanical properties of the lattice are used directly, as constitutive properties of an equivalent solid material, in the analysis and optimization of a component [1086]. For functionally graded components, the volume fraction and the orientation of the architected material unit-cell, varies spatially [1087,1088]. Hence, the architected material homogenized properties, typically the stiffness tensor, need to be obtained as a function of the material volume

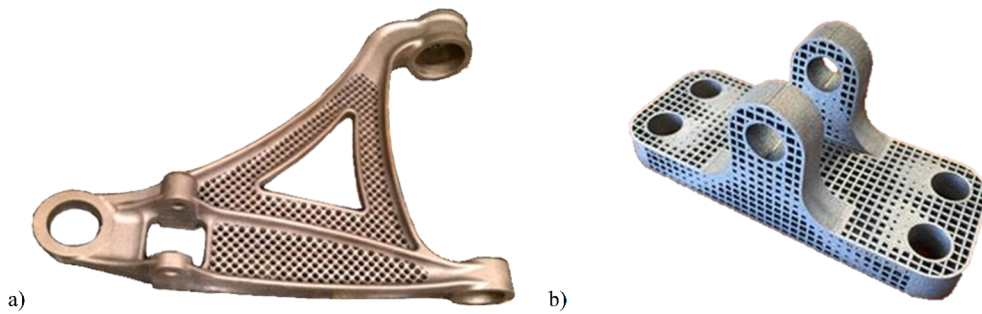


Fig. 65. Metallic AM components with infill lattice of (a) constant and (b) variable volume fraction (reproduced from [460]).

fraction and the orientation. This approach was in fact the foundation of the original homogenization based topology optimization method [1088], discussed in section 2.1.

Architected materials are inherently anisotropic. Nevertheless, they can be designed so that they have an initially isotropic elastic response at small deformations [1089,1090]. Elastically isotropic lattice structures, although in general not stiffness optimal, are yet of great interest in the context of AM design, because of their very simple representation at the macroscale, based on only two fundamental elasticity parameters, i.e. bulk and shear moduli, or Young's modulus and Poisson ratio. In the general case, homogenization of periodic architected materials or materials with a heterogenous micro-structure requires an anisotropic and possibly nonlinear description of their elastic response [1034], as well as anisotropic yield surfaces with regard to plasticity. It is important to note that classical pressure-independent yield surfaces [1058–1060] are not suitable for highly porous architected materials. Instead, pressure dependent anisotropic yield surfaces need to be employed [1091,1092]. Once such anisotropic yield surfaces are obtained, for certain lattice structures of interest, as a function of the volume fraction [1093,1094], (cf. right hand side diagram in Fig. 63 (e)), they can in principle be used in stress constrained optimization, as it is currently done for isotropic materials [1095]. This is an open research area, where currently available literature is rather scarce.

Apart from using homogenization to create a link between the architected lattice scale, i.e. the *meso*-scale, and the component scale, it is also possible to create designs with multiscale geometry, purely based on geometrically constraining the design space of the optimization procedure. The purely geometric approach has been successfully applied for generating structures with bone-like infill, even in 3D, [1096]. As another alternative to homogenization, the multi-scale finite element method can be used for resolving the mechanics in both small and large scales simultaneously. This approach has so far been demonstrated for 2D design problems [1097,1098]. Another alternative to physics-based homogenization is to apply data driven homogenization as in [1099].

Another means of obtaining multiscale geometry is de-homogenization, introduced earlier in section 2.1. Dehomogenization methods aim at reconstructing the fine structure at the mesoscale, based on optimization results obtained in a homogenized model at the component level. Typically these results include volume fraction and unit-cell orientation distributions over the entire component volume. So far, de-homogenization methods have been developed and have been successfully applied for compliance minimization problems and simple lattice structures in 2D and 3D [214]. Extension to more complex unit-cells and consideration of lattice yielding and buckling aspects are emerging research fields of high interest.

4.2. Multi-scaling and reduced order modelling for process simulations

As noticed in section 3, multiphysics simulations of AM processes at micro- or deposition-scale are typically carried out over limited computational domains that in most cases do not exceed a handful of tracks and layers. For instance, the deposition-scale model developed in [967] involved four tracks and three layers and the overall size of the domain was 1.50 mm by 1.0 mm by 1.0 mm. However, in reality, the size of a typical sample made by PBF processes could be around a few up to 10 or 15 cm. Moreover, the multiphysics models discussed in section 3 require very fine mesh and cell sizes in order to fully resolve the melt pool or strand shape in metal and non-metal AM processes, respectively. Typical element or cell sizes employed in multiphysics simulations are about 5 μm [1100] and a rule of thumb calculation shows that to mesh a cubic component with a characteristic length of 1.0 cm would need 8×10^9 cells in order to properly capture and resolve the laser and melt pool which are in the order of order (10) – order (100) μm for PBF processes. Therefore, carrying out such multiphysics simulations on real-size parts is in general unfeasible due to huge computational requirements. Thus model reduction techniques are increasingly being applied to AM process simulations as well.

In the following sub-sections, the multi-scaling approach is addressed first, followed by an introduction to machine learning techniques and their application for AM process model reduction.

4.2.1. Process multi-scaling methods

Process multi-scaling is a solution to the large computation requirements of AM process models since such methods allow for modelling a certain condition or variable (for instance temperature or stress) during the course of AM processes over an entire part within an acceptable time. Process multi-scaling methods aim at the micro-scale level but they deal specifically with the solidification and subsequent thermal cycles occurring during the AM process. These models are in essence reduced-order models of the advanced process simulations discussed in section 3 and are therefore ideal for being involved in physics-based TO methods introduced in section

2.2. There are few number of process multi-scaling techniques and they are mostly devised for PBF processes where the ratio between the sample and the melt pool size is quite substantial, hence, process multi-scaling is crucial.

One of these methods is the adaptive mesh refinement (AMR) technique in which the mesh around regions experiencing bigger gradients of a certain variable is refined [1101]. Denlinger et al. [1102] adopted an element-coarsening method in their thermal simulation of the L-PBF process where they ultimately managed to model the temperature field during the manufacturing of 38 layers comprising 3400 laser tracks. Olleak and Xi [1103] used a scan-wise AMR method in which refined the mesh along the scan path of the laser over a certain length variable, denoted the refinement length, while elements outside this zone retained their size and shape. Li et al. [883] developed an AMR using an Octree mesh for their transient thermo-mechanical analysis of metal AM of Ti6Al4V and In625. They carried out two levels of Octree mesh coarsening using hex8 hexahedral elements. With more levels of mesh coarsening, the regions farther from the laser irradiation have increasingly coarser meshes. Finally, they reported that two levels of mesh coarsening shortened the calculation time compared to a static mesh by about 66%. [1104,1105] approximated the temperature field to be composed of an analytical solution and a subsequent correcting numerical FEM solution and by applying AMR, they managed to simulate the transient temperature field of 1313 layers in half of the actual printing time of the same sample in reality. A novel hybrid methodology was introduced in [1106] and [1107] for modeling the temperature field via analytical point and line heat sources, respectively, in combination with a numerical correction field to simulate the in a computationally efficient manner. This approach gave a unique way to account for the laser scanning patterns in an explicit manner in a part-scale model. In [1108], a semi-analytical thermal method was coupled to an elasto-plastic mechanical boundary value problem that computes the thermal stresses and distortions for WAAM and the model has been validated by comparing the predictions with experimental measurements and simulation results obtained by a non-linear transient model from the literature.

Flash heating (FH) is another process multi-scaling method that is typically used for metal AM processes. In this method, first, the part is sliced into a number of *meta*-layers, which are in essence multiple actual layers merged into a single layer. Then the overall input energy from the heat source required for printing a layer is calculated and subsequently released within each of these *meta*-layers and over a certain time period, called activation or on-time. According to [1109], the final temperature of a *meta*-layer could drastically be affected by this parameter. For instance, [1110] and [1111] applied this method with very short activation times and this led to a peak temperature over the melting point. In contrary, [1112] employed extended on-time periods, namely the gradual heating method, that eventually resulted in peak temperatures in the order of few hundred degrees Celsius. [1113] released the heat source in multiple shots in a so-called multi-shot method. Fig. 66 (a) gives an overview of the three different temporal distributions for flash heating, multi-shot heating and gradual heating. [1114] came up with a more advanced way of activating the *meta*-layers and instead of simply activating

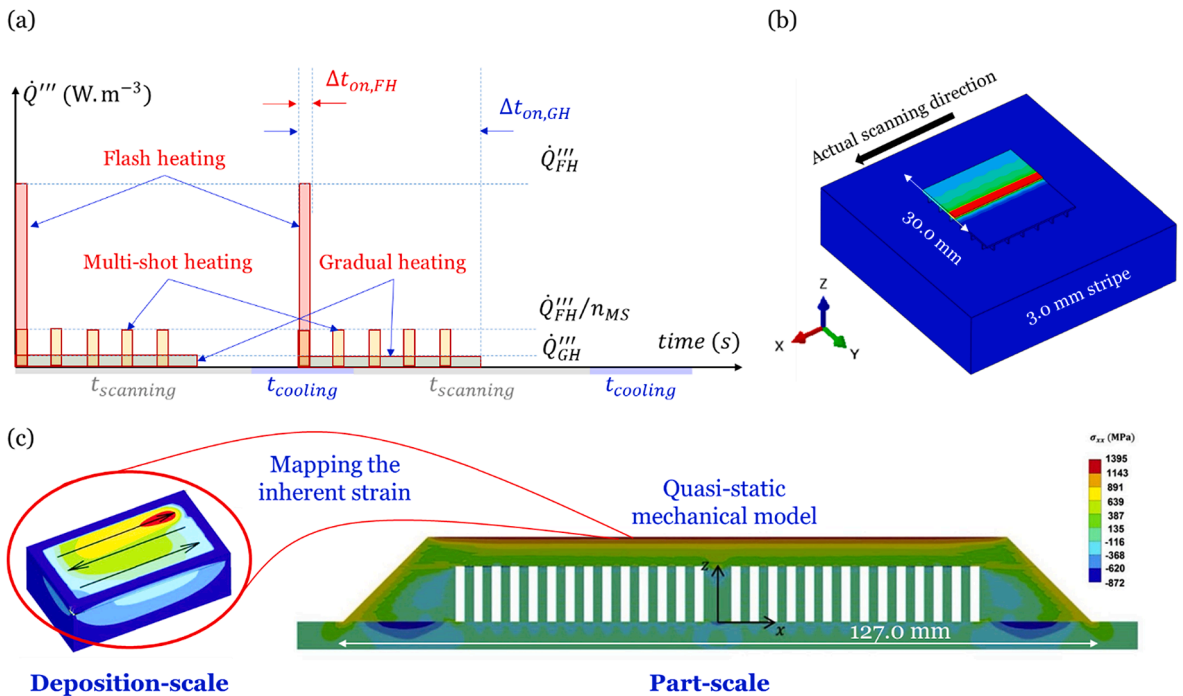


Fig. 66. An overview of two process multi-scaling techniques, (a) and (b) flash heating and its variants and (c) the inherent strain method. (a) Shows the temporal distribution of the heat sources for flash heating, multi-shot flash heating [1113] and gradual heating [1115]. Δt_{on} (s) is the activation or on-time period of the heat source and the multiplication of the heat source and Δt_{on} must be the same for flash and gradual heating. (b) is a snapshot of the temperature contour for sequential flash heating [1116] and (C) is the inherent strain method where the inherent strain components are found in the deposition-scale thermo-mechanical model on the left and then these components are mapped to the *meta*-layers in the quasi-static mechanical model at part-scale on the right [1117].

the energy within a whole *meta*-layer, they adopted sequential activation (so-called sequential flash heating) which is in a much better agreement with reality both in terms of respecting the actual scan pattern as well as the current laser beam location, see Fig. 66 (b). The FH method represents one of the best options for doing physics-based TO at part-scale and the simulations carried out by Ranjan et al. [478] described in section 2.2.2 are all based on or inspired by this process multi-scaling method. And as earlier pointed out, it would have been virtually impossible to couple multiphysics deposition-scale models to physics-based TO due to the computational requirements and this once more underlines the importance of process multi-scaling for achieving reduced-order and fast-responding models.

FH being a thermal model at part-scale, is very suitable for providing input to a subsequent mechanical analysis also at part-scale, consequently resulting a thermo-mechanical analysis which was done e.g. by [1116], one can also model the thermo-mechanical conditions. Another relevant process multi-scaling technique which has undergone continuous progress since the 1970's in the welding literature [1118,1119] is the inherent strain (IS) method. Unlike FH which typically is a single-scale fully or sequentially-coupled thermo-mechanical model, the IS method is rather a hierarchical multi-step method which normally is composed of a deposition-scale thermo-mechanical model (similar to the ones described in section 3.2.2) and a subsequent part-scale mechanical model. The averaged process-induced strains are first calculated via the deposition-scale model and then these strains are fed and applied to *meta*-layers in a quasi-static mechanical model at part-scale, see Fig. 66 (c). [1120] applied this methodology and obtained the inherent strains numerically and then fed them to their part-scale mechanical models where they validated the model against multiple benchmark artifacts. [1121–1124] also did a series of relatively similar hierarchical simulations and coupled three different length-scales together.

The IS method in its original form had a number of drawbacks (including inaccurate residual stress prediction) when applied to metal AM processes and it has ever since gone through multiple improvements to improve its stress prediction accuracy. [1117,1120,1125] came up with a more advanced version of this approach, i.e. the modified IS (MIS) method, which yields more accurate results when it comes to prediction of the final deformation of an AM part. One major disadvantage of the original MIS method is, nevertheless, that its part-scale module is an isothermal solid mechanical model, meaning that it is unable to capture the impact of significant temperature gradients as well as material's softening due to melting on the stress evolution, as opposed to the thermo-mechanical FH method that automatically accounts for these thermal effects. In an attempt to mitigate the isothermal condition of the original MIS method, Dong et al. [1126] performed a two-equilibrium procedure and applied the inherent strains at two consecutive static steps, the first one at intermediate temperature (elevated temperature resembling melting) and the second one at the steady state or room temperature, respectively. This method is shown to be superior to the original MIS method in predicting the residual stresses [1126], even though both have satisfactory distortion predictions. In a very recent work, [1127] (see Fig. 67) came up with an even more advanced hybrid version of the MIS method, where the inherent strains are temperature-dependent. This platform consists of three steps, 1) initially the detailed deposition-scale model is run at a range of interpass temperatures imposed as previous blocks' temperatures, 2) a part-scale FH model is done to find interpass temperatures to determine temperature-dependent inherent strains and 3) the same two-equilibrium part-scale mechanical simulation (as in [1126]) is done. The temperature-dependent inherent strain method is believed to be more accurate for high through-put DED-based processes where heat accumulation is substantial.

When looking at time-efficiency for mechanical simulations, MIS-based models (the part-scale modules) are quite faster than FH-based thermo-mechanical models, mainly because the former is a static mechanical model with constant material properties and this makes far less convergence issues hence less iterations, as compared to the FH method that requires very fine timesteps to converge at high temperature gradients. As an example, the runtime for the part-scale module of the most advanced IS-based model, i.e. temperature dependent inherent strain proposed in [1127], takes roughly 30 min for simulating stresses in a metallic sample with 250 mm length and 27 mm size height manufactured with wire-based DED. Whereas, according to [1128] performing a thermo-mechanical analysis for DED using FH takes between 8 h up to 100 h of runtime, depending on the scaling factor. On top of this, although

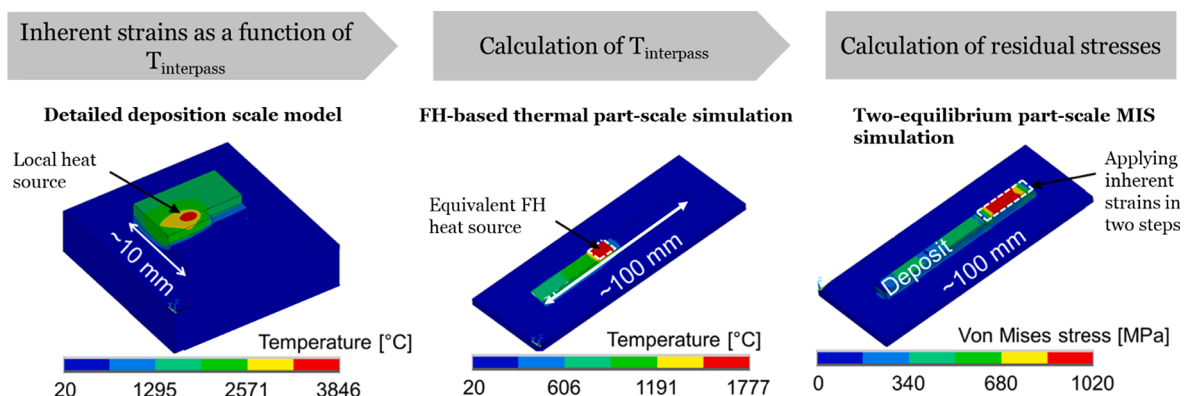


Fig. 67. The workflow of the temperature-dependent MIS method proposed in [1127]. According to the figure, first a detailed deposition-scale model is run to determine inherent strains at various imposed interpass temperatures. Then a part-scale thermal model based on the FH method is run to find $T_{\text{interpass}}$ for the entire part geometry. Then based on the calculated $T_{\text{interpass}}$ from step 2, corresponding inherent strains saved from step 1 are imposed on the final part based on the two-equilibrium strategy introduced in [1126] to find residual stresses.

compared to detailed deposition-scale process models, FH and IS multi-scaling techniques obviously boost the simulation speeds substantially, they suffer from inherent inaccuracies mainly stemming from the concept of *meta*-layers and layer lumping. This was for instance shown in [1114] where the FH method on its own significantly overestimated the final deformation due to the very coarse layer lumping carried out while the modified version, the sequential FH method, had a much better distortion accuracy but at the expense of much longer runtimes (9 h for basic FH and 65 h for sequential FH). That is therefore the reason why IS-based multi-scaling is preferred for doing structural physics-based TO [488,494,495] and thermal-only FH is an appropriate choice when performing thermal physics-based TO [480] and thermo-mechanical FH methods are not suited for physics-based TO including process constraints. The FH method with prolonged heat source activation times a.k.a. gradual heating, might also be suitable for finding necessary temperature gradients due to geometrical changes needed for physics-based TO with thermal process restrictions as discussed in section 2.2.2, thermal restrictions.

4.2.2. Machine learning based process model reduction

The growing number of contributions in recent years on modelling additive manufacturing processes is also reflected in the large number of studies focussed on application of machine learning (ML) techniques, which have become the single largest category of reduced order modelling techniques for AM. The remainder of this sub-section delves into the machine learning based methods applied to additive manufacturing, and discusses the different approaches adopted as well as the highlights the successes and challenges of these techniques. There have been over 600 publications in this field over the last decades (2004–2021), with the major findings summarized across at least 12 review articles within the period 2020–2021. Therefore, the section progresses by quickly summarizing these reviews, and then focuses on over 40 selected studies (out of 65 relevant studies) already documented over 2022, producing a detailed picture of the state-of-the-art within this field.

Machine learning is an umbrella term for a set of algorithms that primarily identify and quantify patterns across a given dataset. Depending upon how the initial data set is handled, the ML algorithms fall under four sub-categories.

- Supervised ML algorithms: The datasets are cleaned and accurately (and often painstakingly) labelled, and the algorithms are used to learn the relationship between the input and the output subsets i.e. a mapping of input data to output data is performed iteratively until the desired level of accuracy is attained. Typical applications include creation of regression models for prediction of trends as well as generation of classification models to identify and sort/categorize future data.
- Unsupervised ML algorithms: The datasets are unlabelled and the algorithms are used to identify underlying patterns, trends and groupings within and across the different data subsets. The goal is typically to identify relationship between different data points (as opposed to input to output mapping), understand the underlying structure of the data, and thereby formulate rules for automatic segmentation/clustering of the data into categories. Additional goals pertain to generation of data visualization models that provide insight into the achieved clustering via two/three dimensional plots, and to reduction of dimensionality e.g. by identifying, ranking and selecting the principal components (i.e. a mathematical combination of current data dimensions/variables) which govern the relationship across the data points.
- Semi-supervised ML algorithms: These algorithms combine aspects of both supervised and unsupervised ML techniques, wherein the dataset consists of both clean/labelled and raw/unlabelled data. The models are trained on the labelled subset of data (i.e. learn classification rules), and then used to label the remaining data (i.e. apply clustering based on learned rules).
- Reinforcement ML algorithms: Reinforcement ML uses supervised and/or unsupervised ML algorithms in an iterative manner on live datasets, whereby the models are continuously updated, created and/or discarded based on continuous feedback in terms of positive or negative rewards signals. The reward based reinforcement leads to dynamic models that make decisions/predictions based on the similarity of the current model inputs to the prior data, and thereafter update the criteria for assessing the similarity based on the now expanded prior dataset. These models are specifically applicable when decisions/predictions are to be made within scenarios that involve randomized incoming data and changing model environment.

All four sub-categories of ML techniques have been applied to additive manufacturing in recent years. Both supervised and unsupervised ML techniques have been applied at all process scales i.e. from microscale prediction of solidification [1129] and in-situ alloy formation [1130], to the deposition scale defect formation [1131] predictions based on thermal maps, melt pool dimensions and hot/cold spatter occurrence, to the mesoscale predictions of local residual strains and stresses [1132] and macro-scale predictions of the resultant final part shape deviations [1133]. The recent trends of developing physics-informed ML models [1134] at these different length scales, as opposed to traditional correlation based black-box models, has promoted their incorporation into both in-situ process control [1135–1137] investigations as well as Design for AM (DfAM) [1133,1138,1139] workflows. However, reinforcement ML techniques have found limited success as yet, owing to practical ML-specific challenges [1140] related to small available datasets, lack of proper data labeling, and insufficient application of feature engineering/selection, which continue to hinder the promulgation of these techniques at industrial production scales. In addition, other well-known challenges exist, related to overfitting/underfitting the models as well as the transfer of models developed on a specific machine-material-part design combination to other machines, materials and part designs.

A broad review by Qin et al. [1133] highlighted ML applications in AM to cover multiple AM system categories i.e. PBF, DED, ME, VP and MJ. Focusing on key studies, the review categorized the applications into domains of ML for DfAM, ML for materials analytics, ML for defect detection, ML for process control and ML for AM sustainability. Classification using supervised learning algorithms were found to be prevalent in the design and materials selection fields while regression studies using supervised algorithms dominated the defect detection and process control domain. Unsupervised learning algorithms, on the other hand, were limited to fields of defect

detection and process control, primarily aimed towards dimensionality reduction for in-situ decision making and control. A similar review by Nasiri et al. [1137] also included studies on SLA and BJ, but focused on the predictability of mechanical behaviour of AM parts i.e. shape deviation, geometric accuracy, and density prediction. Highlighting the potential usage of AM in producing functionally graded materials, the review also identified current knowledge gaps for achieving accurate model-based AM of such components. In a future-looking short review, Elambasseril et al. [1135] further highlighted the non-trivial aspects of the data flow for connecting these various domains, especially pointing at the convergent development required in the fields of AI, digital twins and data capture-n-storage to enable applications of ML models for closed-loop AM system and product development.

As highlighted in a recent review by Durodola [1129] focusing on ML applications for alloy design, the ML models are developed on an assumption that observations \times during any process can be related to the outputs y by some unknown function g such that $y = g(x)$ represents the ground reality of the process. The ML algorithms approximate this ground reality by an initial arbitrary model $F(x,w)$, wherein w corresponds to a set of adjustable variables and/or mathematical operators introduced such that $F(x,w) \approx g(x)$. The ML methods then define a minimization function, e.g. the Hankel norm or the L2 norm, with respect to the output y . The final ML model constitutes uniquely identified set of values of w and \times that result in the lowest value for the defined minimization function. Supervised ML techniques are applied when the variables constituting \times and y are known apriori, while unsupervised/semi-supervised ML techniques are used when the variables constituting y are either unknown or partially known respectively. Reinforcement ML techniques become especially relevant when the variables constituting \times and y are known to have associated uncertainties and/or stochasticity $x\theta$ and $y\theta$ such that the ML model constitutes $F(x,w, x\theta) \approx g(x, x\theta) = (y, y\theta)$. Typically, the selection of variables and operators in w is made such that the ML models can be computed significantly faster than any corresponding multiphysics model of the same process, while having similar or better accuracy than corresponding analytical models of the process. In order to ascertain the performance of the ML models, metrics such as mean absolute error (MAE), mean absolute percentage error (MAPE) or root mean squared error (RMSE) are typically utilized as show in equations (38)–(40) respectively, wherein the true value y for the error

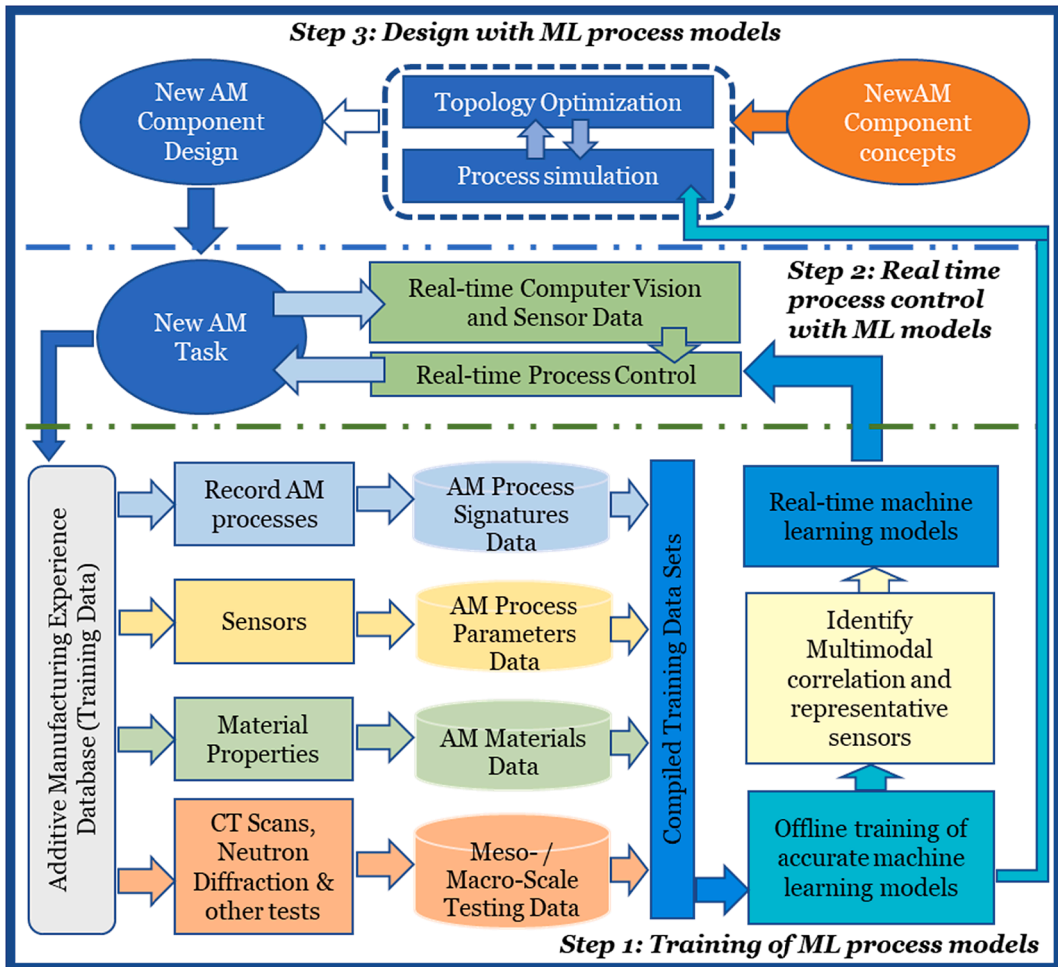


Fig. 68. Extended three step strategy for close loop ML algorithm for smart manufacturing based on review by Raza et al [1130]. Step 1(bottom) highlights how ML models are trained for real-time applications and for simulation-driven design applications. Step 2 (middle) shows the implementation in a real-time environment. Step 3 (top) shows application within component design workflow.

calculations are generated either by experiments, high-fidelity multiphysics simulations or low-fidelity analytical model evaluations.

$$\text{Meanabsoluteerror}(MAE) = \frac{1}{n} \sum_{i=1}^n |F(x, w)_i - y_i| \quad (38)$$

$$\text{Meanabsolutepercentageerror}(MAPE) = \frac{100\%}{n} \sum_{i=1}^n \left| \frac{F(x, w)_i - y_i}{y_i} \right| \quad (39)$$

$$\text{Rootmeansquarederror}(RMSE) = \sqrt{\frac{\sum_{i=1}^n (F(x, w)_i - y_i)^2}{n}} \quad (40)$$

The recent review by Raza et al. [1130] provided an overview of the steps associated with achieving ML based model reduction, focusing on the importance of selection of appropriate ML algorithms based on the problem definition, and on the subsequent integration onto a real-time AM process control scenario (see Fig. 68). The advantages and limitations of choosing naive Bayes classifier (BC) models, k-nearest-neighbor (kNN) method, Decision trees (DT) approach, kernel methods such as support vector machine (SVM), and artificial neural networks (ANN) were discussed, as applicable to the problems of material discovery/selection, alloy development, in-situ process parameter control as well as parameter optimization. The review also highlighted the usage of deep learning techniques such as convolution neural networks (CNN) across the various areas of AM aimed at establishing the process-structure-property and composition-structure-property relationships. For the latter case, the review also highlighted the various material property databases available for ML investigations, e.g. AFLOW, Open Quantum materials Database, Polyinfo Polymer Database, Crystallography Open Database, etc., containing material data ranging from elastic, thermal, electro-chemical properties to DFT-based properties and crystal structure information.

Similar prevalence of CNN based studies was also noted by Zhang et al [1141] for deposition-scale defect models, based on a review focused on combination of in-process monitoring techniques for LPBF and EBM with ML techniques. Fu et al. [1131] also reviewed application of ML algorithms for defect detection in laser-based metal AM processes, categorizing the individual investigations by the selected ML algorithm, the type of material, the types of defect, and the obtained prediction accuracy of the implementation. The defects were broadly classified into geometric and dimensional defects, cracks, and meltpool induced defects e.g. lack-of-fusion pores, keyholes pores, gas porosity, balling defects, track continuity defects, etc. The dataset for the supervised learning studies reviewed therein ranged from in-situ thermal images and pyrometry of the meltpool to layerwise optical and thermal imaging to acoustic spectroscopy during production, to post-process microscopy and metallographic images. Both LPF and DED processes were studied and the applied ML techniques involved logistic regression (LR), Gaussian process regression (GPR), SVM, naive BC, kNN, random DT, ANN, CNN or long-term recurrent CNN (RNN). High prediction accuracy of > 90% was documented for most studies while nearly all reviewed investigations achieved > 75% accuracy. The unsupervised learning studies applied techniques of k-means clustering (KMC), deep belief network (DBN) or self-organized maps (SOM), while using the datasets containing powder bed images, X-ray CT based porosity maps, optical tomography images, acoustic emissions and/or near-infrared thermal images. The unsupervised learning studies reviewed could identify recoater hopping, recoater streaking, debris, and potential keyhole and/or lack-of-fusion defects with > 80% accuracy, while no accuracy values were reported for identification of cracks and drift phenomena during production. The stated accuracy values however were brought into question within the review paper, specifically pointing to the small databases typically available for creation and testing of these ML models in the reviewed studies.

Sharma et al [1134] also pointed out the usage of ML techniques for meltpool dynamics prognosis for LPBF, as well as the growing development of Physics-informed ML models. The review also expanded upon the different modelling techniques available for the thermal modelling of PBF process, but fell short of identifying studies that could merge the two fields. Combining studies focused on in-process monitoring and defect detection with studies focused on process-thermal dynamics-structure-property relationships, Wang et al. [1132] highlighted the application of similar ML techniques and datasets across both domains of metal AM. The reviewed articles were categorized based on which part of the PTSP linkages were addressed (e.g. process-thermal, process-structure, process-property, thermal-structure, etc), and the corresponding model inputs and outputs for each category were highlighted. The studies were found to be primarily focused on more popular AM materials such as SS316L, Ti6Al4V, Inconel 718/625, SS 17-4PH and AlSi10Mg. Key questions related to designing ML models capable of handling both temporal thermal dynamics and spatial structural evolution in an effective and time-efficient manner were identified as existing knowledge gaps within the field of ML applied to process modelling.

4.2.2.1. ML driven reduced order modelling at the deposition scale. A majority of the reduced order modelling (or surrogate modelling) investigations with ML techniques has focussed on the *meso*-scale aspects of the metal AM processes i.e. the dimensions of the meltpool, the local temperature fields and the consequent formation of porosities. The applicability of such models is dependent on the complexity of the multiphysics model that ML intends to replace, and is aligned with the necessary model-fidelity schema proposed by Yan et al. [1142] (wherein the suitability of applying semi-empirical techniques based on Rosenthal solution are compared against FE based thermal models and FV based CFD models for the different regions of a typical power vs scanning speed process map). For example, Ness et al. [1143] used Extremely Randomized Decision Trees upon datasets generated via FE thermal simulations of wire arc additive manufacturing of aluminum 2319 using ABAQUS. The study introduced a generic feature set aimed at capturing the thermal process across different geometries, deposition patterns, and power intensities. The feature set contained sample time, deposition time, euclidean distance between laser and sample node, boolean value corresponding to whether the adjacent pass or layer is printed, normalized time since adjacent node deposition, normalized time since deposition within heat influence zone, power influence factor,

volume ratio of air within the heat influence zone. An aggregate of 55 decision trees constituted the overall ML model, chosen based on trade-off between accuracy and processing time. The performance of the train set was assessed through the average of the 5-fold cross-validation results, an iterative procedure wherein the entire dataset was randomly partitioned into five disjoint subsets of approximately the same size, and for each set, the mean absolute error (MAE), the mean absolute percentage error (MAPE) and the root mean squared error (RMSE) were used as the test performance. The model showed an overall performance of MAPE of 0.8% – 2.5%, it could sufficiently capture the temperature trends and peak values, and thus could be used as a surrogate for the high-fidelity ABAQUS model to predict the temperature during the production of a single layer.

Along similar routes, Liao et al. [1144] used physics-informed-neural-network models to predict the full temperature distribution within a part being produced using partial temperature data measured with an infrared camera during DED of IN718. The PINN was initially trained on FE simulation of a single pass, tested with resultant RMSE of < 4 °C and maximum error of < 100 °C, and subsequently retrained with experimental data leading to a final model RMSE of < 48 °C. Instead of using physical laws to predict temperatures, Kozjek et al. [1145] applied RF techniques to combine high-resolution coaxial Planck thermometry melt pool temperature measurements with a selected set of LPBF process parameters, in order to predict the melt pool temperatures within the next layer to be produced. In a more expansive investigation, Akbari et al. [1146] have investigated the feasibility of using processing parameters from four different metal AM methods (two PBF and two DED) across 30 materials in order to create a model capable of predicting the shape and dimensions of the resultant melt pool as well as classifying whether the resultant melt pool is within the keyhole, lack-of-fusion, balling or desirable region of the process window. A comparison of the suitability of different ML algorithms for deriving the desired meltpool model was also highlighted, as the applied techniques corresponded to Ridge linear regression, Lasso linear regression, Random Forest (RF), Gaussian process model, Support Vector Machine (SVM), classical Gradient Boost, XGBoost, Logistic regression (LR) and Artificial neural networks (ANN); with the neural networks, gradient boosting and random forest models outperforming the other models.

Estalaki et al. [1147] have used kNN, RF, DT, multi-layer perceptron (an ANN technique), LR and AdaBoost (a Gradient Boost technique) methods in order to create a model for microporosity prediction in LPBF SS304L based on in-situ thermographic sensor data and μ -CT reconstructions of porosity distributed in the experimental samples. The kNN and RF techniques were shown to consistently outperform other techniques for microporosity predictions across a series of statistically relevant validation tests, with the RF models showing $> 90\%$ Precision, Recall, Accuracy and F1 scores for 7% and 10% hold-out validation tests (the four scores of Accuracy, Precision, Recall and F1 as relate the number of on true/false positive/negative results with the ground truth corresponding to 100% on each score). Similar studies of relating meltpool information to the final local porosity in the part were performed by Gawade et al. [1148] (using XGBoost method on laser net shaping of Ti6Al4V) and Smoqi et al. [1149] (using kNN technique with LPBF of ATI 718Plus alloy). Gawade et al. [1148] combined simulation data generated from high-fidelity thermal models in AUTODESK with empirical meltpool maps extracted from pyrometry data based on approximately similar time and part of the print. The simulated melt pools helped the supervised learning model learn better to predict porosity labels by providing physics-based features to the empirical melt pools. Functional principal component analysis was used to reduce the 63 features defining each meltpool shape to 8 factors covering 98% of the variation of the data. Following the train-test 80–20 data split, the training dataset could be recreated with 99% accuracy, 98% recall and 99% precision, while the test dataset had 99% accuracy, 86.67% recall and 100% precision. The model predicted 13 out of 15 porous melt pools and 296 out of 296 non-porous melt pools correctly within the test data. Smoqi et al. [1149] compared the performance of kNN based model with deep learning based CNN models and observed similar levels of predictability - with the additional feature extraction and feature engineering performed for the kNN implementation as well as the lack of sufficiently large datasets for the CNN model being attributed as reasons for the similar performance.

Deep neural network methods, specifically convolutional neural networks (CNN), are the most adapted technique for models involving meltpool analysis/predicted due to their suitability to handle image based data, as well as the deep learning nature of the involved algorithms. Du et al. [1150] have used a combination of genetic algorithms and deep neural networks with a dataset consisting of melt pool dimensions, volumetric energy density, Richardson number, Marangoni number, solidification time and surface tension force, in order to predict the balling susceptibility index of the process-material-parameter combination. The dataset spanned across multiple materials including AlSi10Mg, A357, Co-Cr alloys, SS 316L and corresponded to 166 experiments. Zhang et al. [1151] compared the performance of RF, XGBoost and LightGBM models for predicting microhardness based on the process parameters and the measured meltpool intensity data during LPBF. In contrast to the finding of Estalaki et al. [1147] on the suitability of the techniques, XGBoost was reported to have the best comparative performance.

Pandiyan et al [1152] used long.short term memory CNN to handle combined signals from a heterogeneous time-synced sensing system (based on back reflection, visible image, IR image, and acoustic emissions) in order to classify melt pools during LPBF of 316L within the three regimes of lack-of-fusion, conduction mode and keyhole mode. A prediction accuracy of 98% was reported across the variable time scales, as well as the greater significance of back reflection and acoustic emission sensor data towards melt pool predictability. Huang et al [1153] instead used CNN to relate process parameters with the observed meltpool characteristics, while Lapointe et al [1154] further included the geometry of the part into the input features of their CNN models. Huang et al [1153] used combinations of high-fidelity FE simulations of EBAM of Ti6AL4V on ABAQUS along with low-fidelity Rosenthal-model based simulations to generate the training dataset, and applied Singular Value Decomposition based Kriging approach as well as a pointcloud CNN. Hemmasian et al [1155] used high-fidelity FLOW3D based simulations of single pass during LPBF to generate the training dataset for their CNN model, and achieved an RMSE of 2–3% for the predicted temperature field. Hosseini et al [1156] used a physics-informed neural network to predict the temperature and melt pool dimensions and benchmarked it against simulations in ABAQUS, and achieved MAE of $< 4.5\%$. Ren et al [1157] used a recurrent neural network, a deep neural network and a CNN to make thermal prediction for any arbitrary geometry and scanning strategy during DED, and utilized a FE thermal analysis to create the training data for the ML

models. A combined RNN-DNN model was reported to have the best performance of 98.09% accuracy.

4.2.2.2. *ML driven reduced order modelling at the meso/macro scale.* The recent works on ML driven reduced order modelling at the macro-scale have focused on predicting the overall part porosities coming out of the AM processes, the associated surface morphologies, the presence of near surface cracks and their impact of the strength and stiffness of the components. Ansari et al [1158] have used CNN to identify and classify porosity levels in a part based on a training dataset consisting of images taken after each layer was produced in the LPBF machine. Identified porosities in the layer images were labelled using either the original CAD file of the part or the X-CT scan data of the part, with CAD-based labelling resulting in 90% accuracy as opposed to X-CT based labelling leading to 97% accuracy.

Li et al [1159] created a nonlinear regression model of the surface morphology, flatness and near-surface crack probability as function of the process parameters using optical scanning data as well as SEM images. Phadke et al [1160] also created ML models relating the LPBF process parameters for AlSi10Mg to the roughness of a cylindrical component, but used ANN as the modelling technique and further considered the dimensional accuracy and the cylindricity as model outputs. Hu et al [1161] investigated the

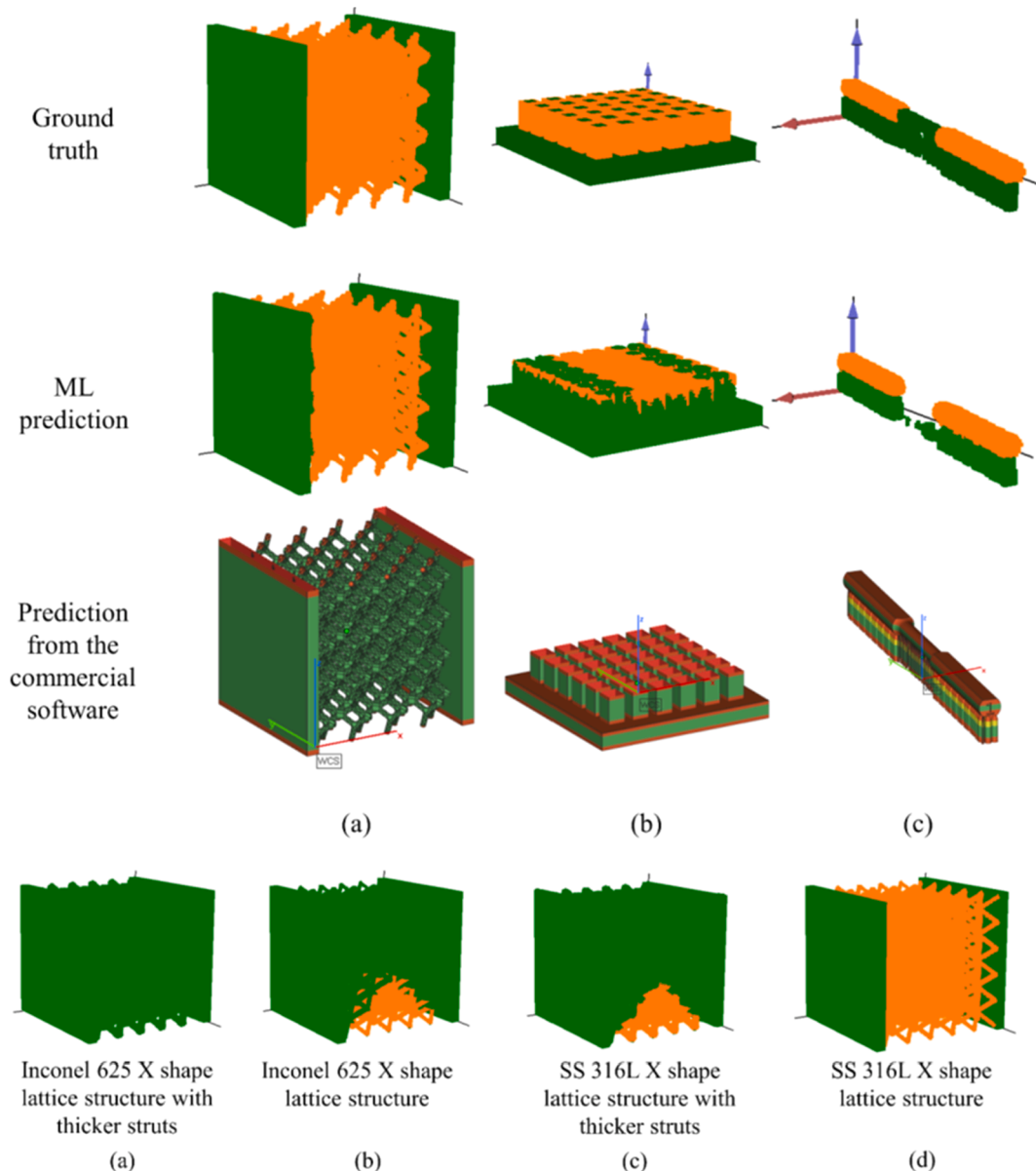


Fig. 69. Top: Test cases of the validation set. (a) A diamond lattice structure made from AlSi10Mg 5 using an EOS machine, (b) a benchmark with tiny needles, and (c) an AlSi10Mg tensile bar 6 printed using Renishaw. Bottom: Comparison of the predictions obtained using two different materials with varying strut 4 thicknesses. From Zhang et al. [1166].

impact of surface defects on the stiffness and the flexural strength of thin structures and lattice structures. The training data set was generated by simulating the mechanical behaviour of small trusses and beams with modified surfaces on the ANSYS WorkBench, corresponding to typically observed process defects. The gradient boost method with a five-fold cross-validation method was adopted for the main predictive model, while a Lasso polynomial regression model accounted for the interaction effects.

Residual stress within LPBF components was the focus of the CNN model implemented by Dong et al [1162], wherein the training dataset was generated via FE simulation of the process. The CNN utilized combinations of three geometric features, namely circular struts, square struts and walls, as the inputs to define the different training geometries, and thus could predict residual stresses within any arbitrary part geometry within 14–25% error. CNNs were also used by Fang et al [1163] to create a predictive model for the mechanical properties (UTS, YS, EI and failure stress) of Inconel 718 walls built by DED, and used measured mechanical properties with simulated thermal data from corresponding components. Yang et al [1164] instead used extensive literature sources from the period of 2010–2019 to create a training dataset of tensile properties of HIP-ed Ti6Al4V parts made of LPBF, and applied ANN to create a predictive model with ~ 5% accuracy.

Zhang et al [1165] have applied voxel-based CNN for predicting the occurrence of visual defects (e.g. distortions) during LPBF and compared their predictive model against printability analysis within the Materialise software. In follow-up studies, Zhang et al [1166] have also demonstrated the increased performance of the CNN models in predicting the shape defects of complex geometries as compared to printability analysis on commercial software (see Fig. X3). The combination of such models of geometry-based printability analysis with models for the *meso*-aspects (e.g. porosity) and macro-aspects (e.g. stresses and strength) of metal AM processes are likely to open new pathways for direct simulation-based design of optimized, printable components in the future (Fig. 69).

4.3. Reduced order modeling and multi-scaling techniques in a holistic approach

Although multi-scaling techniques are used as independent tools for understanding and improving AM process and components performance, the ultimate vision is to use these techniques as components of a holistic optimization approach for AM. This vision, addressed in general in the present review as illustrated in Fig. 63, has already been subject of several research and review

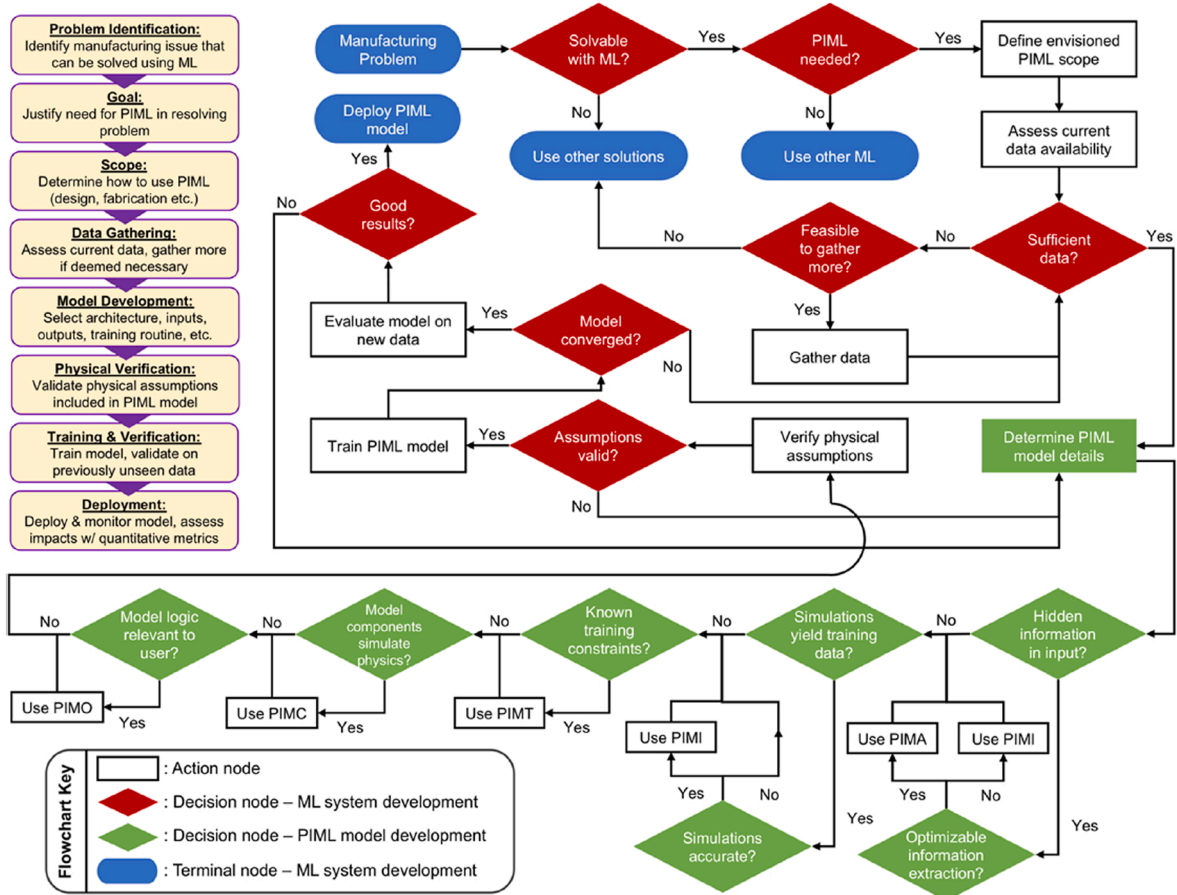


Fig. 70. Flowchart for physics informed machine learning model implementation as suggested by Guo et al[13]. Note: The difference between PIMO, PIMC, PIMT, PIMA and PIMI are highlighted and the application scenario for each is specified.

publications. Francois et al. [1167] have provided a short overview of the different challenges in the modelling of process, micro-structure and properties, as well as in the optimization of process and component topology. The paper also discussed the opportunities from combining these modelling and optimization components in a holistic manner. Yan et al. [1168] presented their implementation of a similar vision with some extra focus on data handling. In a recent comprehensive review paper [1169], Hashemi et al. have presented their vision about a computational linking of process–structure–property–performance models for AM and focused mainly on process optimization.

The various multi-scaling and reduced order modelling techniques reviewed in this section can be implemented within process simulations during topology optimization, especially at the early stages of the optimization as well as towards the later stages. Naturally, for critical components, the closer one approaches to the final design, the greater the need for using accurate, fully-resolved multiphysics models. Fortunately, as pointed out by Nasiri et al [S14], a strong complementarity exists between the typical application scenarios of multiphysics numerical modelling and ML models; with the former models challenged by the randomness/uncertainty of inputs coupled to a well-established apriori model representation, while the latter models hindered by unknown model representation prior to training but subjected to well-known inputs. Physics informed ML (PIML) models, such as those reviewed by Guo et al [S13], aim to address the overlap between these two modelling approaches, suggesting paths for integrating both in order to realize very fast process optimization cycles. Guo et al [S13] distinguished between physics informed model input (PIMI), physics-informed model architecture (PIMA), physics- informed model training (PIMT), physics-informed model components (PIMC) and physics-informed model outputs (PIMO), and suggested a detailed framework for identifying the relevant application case for each of these while combining ML with simulations (see Fig. 70). PIMI constituted preprocessing of in-situ production data (e.g. transformation of temperature data into time–frequency domain) and/or augmentation with production parameters and simulation data in order to better identify predictors of the final output variable. PIMT aimed to improve the obtained ML models by improving the weightage ascribed to the training data entities i.e. penalty factors were put on the specific training data instances if such values were deemed to be physically inconsistent/unlikely (in other words, PIMT aimed to suppress outliers within output data to get improved models). PIMC were related to the phenomena governed by activation and initialization (e.g. nucleation during solidification and grain growth), and additionally focused on minimizing meaningless fitting parameters and increased usage of meaningful physical parameters (i.e. for any given model $F(x,w)$, the number of entities in w was reduced in favor of the number of entities in x). PIMA built on the concepts of reinforcement ML and PIMI, and aimed to improve model performance by simultaneously learning appropriate input data transformations as a part of the model optimization procedure. PIMO focused on ensuring the physical consistency of the ML prediction models, by quantifying how the input features numerically affected the model output rather than suppressing the outputs for training (as in PIMT). While the PIMLs were identified to enhance model interpretability in all five modes, the overall applicability to metal AM was still found to be limited by challenges related to data availability, multiphysics model availability, data imbalance between compliant and non-compliant AM parts, data curation (cleaning, processing, alignment and fusion of data from different sources), and standardization of PIML implementation methods.

These various physics informed machine learning models can be applied in a progressive manner for process simulations (i.e. computation of process physics induced restrictions) during topology optimization, following the strategies described in Section 2.2.2, and similar to those demonstrated in 2.2.2.

5. Conclusion

AM processes have proven their capabilities in realizing complex TO'ed geometries which would have been nearly impossible to produce with well-established conventional manufacturing techniques. TO has so far been successfully applied to various design problems entailing a wide range of multiphysics problems as well as material design. Looking from a manufacturing perspective, however, TO'ed features are potentially prone to defects and anomalies that could impair the part's quality. This issue is mainly due to the fact that in TO, typically, process-related conditions are not accounted for, whereas in reality, any noticeable instability in the process conditions, could prohibit the manufacturing of the TO'ed geometry. On the other side, advanced AM process models have shown their capacities as a reliable and cheap prediction tool that can identify the best set of input process parameters needed to end up with a defect-free AM'ed component. To date, TO and process models have been implemented as two separate geometry and material design tools for AM. In this respect, process models have been used for optimizing the process conditions without optimizing the final performance of the component under manufacturing, while TO has been used to optimize the geometry to obtain the optimal performance regardless of the AM process conditions. In this work, on the other hand, the primary goal is to conceive these two as an integrated holistic computational design tool that not only optimizes the function of a certain part but also guarantees its quality while it is being manufactured via AM. This link between the two modelling and designing paradigms is materialized by incorporation of process models in TO, simply known as TO with physics and AM process constraints.

In the first part of the work in section 2.1, we reviewed the main building blocks and methods of TO, giving an overview of problems formulations, discretization and solution strategies. We then reviewed some tools, like filtering and projection methods, which were originally introduced for regularization of the TO problem, but also find wide application for implementing AM design rules. Then, we reviewed some specific, yet broadly studied TO physics applications which are particularly relevant for AM. Stress constraints due to process conditions, however, remain an inseparable part of the holistic computational design and are dealt with in physics-based TO techniques.

The account for buckling criteria within the TO process is fundamental for the stability and performance of the built part. Also, buckling can be triggered by any AM-induced imperfection or defects. Finally, we gave an extensive review of TO for thermal and thermo-fluid applications, including heat sinks, heat exchangers, and devices for fluid control. Specifically, these TO'ed thermal

management devices pose a challenge while manufacturing, especially since delicate geometrical features typically constitute these thermally TO'ed designs for achieving improved heat transfer.

Such TO'ed structures are prone to severe manufacturing defects to an extent that could disqualify the part for end-user applications. Therefore, TO methods that account for manufacturing restrictions are described and enumerated in [section 2.2](#). Regarding the development of TO methods that incorporate AM aspects, most studies thus far have focused on introducing geometric AM design rules into TO. For feature size control and overhang angle control adequate solutions have been proposed and demonstrated on large-scale industry-relevant problems. Geometrical aspects where further development and investigations are expected include suppression of enclosed voids (especially in complex large-scale cases), build orientation and trajectory optimization, in combination with anisotropy. While AM design rules are widely used and relatively inexpensive computationally, it is clear that not every relevant effect can be captured reliably through geometric rules alone.

Prevention of overheating, distortion, consideration of the effect of residual stresses after printing, and controlling local material properties through AM process parameters and geometric features require physics-based AM process simulations, discussed in [section 2.2.2](#). Integration of these into TO forms a major challenge due to both the added complexity in (sensitivity) analysis and the significant computational cost involved for simulations. Research aimed at finding and validating adequate model simplification approaches that provide sufficient physical insight at reduced computational cost is crucial in advancing TO for AM beyond direct geometric control. The first steps in this direction can already be recognized in recent literature, as discussed in this review.

AM process models have proven to be ideal tools for rapid certification as a means of bypassing expensive experimentation. AM process models have shown their strength in predicting process conditions at unmatched spatio-temporal resolutions which are sometimes impossible or at least too expensive to reveal using *in-situ* monitoring devices. Such models are typically implemented for obtaining the best set of input process parameters (process window) for achieving a high-quality component. AM process models are applied to micro- and deposition-scales. The latter are applicable to both metal and non-metal AM processes as described in sections 3.1 and 3.2.2. Depending on their fidelity and involved physics, metal AM process models are subdivided into powder-gas dynamics models, melt pool evolution models and finally, fully coupled powder-gas–melt pool models (see 3.2.2). Aerodynamics conditions of the chamber gas in L-PBF or dynamics of the shielding gas in powder DED processes are modelled with powder-gas dynamics models. Furthermore, such models can detect cold spatter that can lead to severe surface non-uniformities due to denudation of the powder particles. Melt pool evolution models, as per their name, are dedicated to simulation of various field variables evolving around the laser-material interaction regions. These models cover a wide range depending on the type of their thermal model, which could be either conduction-based or convection-based as well as depending on their coupling with a subsequent model, e.g. solid mechanics, metallurgical, etc. The most advanced melt pool evolution models at the current stage are able to predict surface or bulk porosities caused by improper selection of input process parameters. Finally, as the last and most advanced category of melt pool evolution models, fully coupled powder-gas–melt pool models obtain the entire gas- and melt pool-related field variables simultaneously. Such models, despite significant computational requirements, are conceived to be the most accurate models for temperature predictions during metal AM processes. These could provide useful input data to microstructural models for grain growth simulations. So far, the main bottleneck of these models is still the very long computational runtimes to an extent that render these models only applicable to very limited and confined domains significantly far from the actual component size. This is the main reason why shortcut process multi-scaling methods described in [section 4.2](#) are needed, since otherwise it is impractical to incorporate these models into physics-based TO.

Process models also entail microstructural simulations at micro-scale. Several modelling techniques for grain growth and nucleation simulations exist at this scale, including CA, KMC and PF. As discussed in [Section 3.2.1](#), nucleation remains a black box. Its accurate description in microstructure modeling would be a sound next step of the research community that could promote our understanding of MAM process-microstructure relationships and support materials design with MAM. Quantitative predictions of AM microstructures in large volumes in appropriate time will play a key role in yielding valuable insights for industrial applications. Further research should be undertaken aimed at the establishment of process-microstructure functions to minimize time and computational efforts in the virtual design of process-microstructure maps, with a global aim of reverse engineering.

To circumvent the very long computational times as well as small domains sizes of advanced process models discussed in [section 3](#), material and process multi-scaling are fantastic solutions ([sections 4.1 and 4.2](#), respectively). Multi-scaling is a key player in establishing the holistic computational design tool. Integrated computational material engineering (ICME in 4.1.2) is a detour multi-scaling tool to make representative volume elements which reflect an actual part's morphology at deposition- and micro-scale. ICME formulations are a material multi-scaling tool and the key enabling element of process-structure–property relationships. Furthermore, ICME formulations allow for calculating averaged material properties for part-scale simulations at macro-scale. While process multi-scaling methods given in [section 4.2](#) are used for reducing the order of advanced multiphysics models discussed in [section 3](#). Such process multi-scaling techniques allow for prediction of a specific field variable over an entire part's geometry and within affordable runtime. Thus, part-scale process models which are developed based on process multi-scaling can be readily incorporated in physics-based TO mentioned in. These part-scale models, on the other hand, lack the capability of describing the actual physics accurately and they are typically fed with ideal material properties. Hence, material multi-scaling methods could link the micro- and deposition scale models to a part-scale model where realistic and updated material properties can be derived based on ICME and then in turn fed to these part-scale models, and this can subsequently serve as an additional constraint in a more realistic, physics-based TO.

AM technologies are constantly developing, and TO methods for AM must therefore focus on the state of the art to be relevant. Here the concept of 'contactless supports' is mentioned and that this significantly changes the cost and complexity related to the realization of overhanging regions. Furthermore, AM is increasingly combined with other manufacturing processes: hybrid manufacturing, post-processing steps, assembly etc. The first studies focusing on such combinations have been identified. Consideration of this

interdependent chain of processes forms a complex but important direction for future computational design methods within the DfM philosophy.

Finally, both for the physics-based and geometry-based research directions, in order to ensure progress of the field the importance of proper validation and comparative studies is emphasized. To facilitate this, the research community is encouraged to share implementations of methods. Here also journal editors can contribute by stimulating reproducible research.

Declaration of Competing Interest

The authors declare that they have no known competing financial interests or personal relationships that could have appeared to influence the work reported in this paper.

Data availability

The authors are unable or have chosen not to specify which data has been used.

Acknowledgments

MB and JH received funding from Independent Research Fund Denmark, DIGI-3D project (Contract No. 0136–00210B). JS and RS would like to acknowledge the support of the Independent Research Fund Denmark (Contract No. 0171-00115B).

The author group highly acknowledges Wayne Edgar Alphonso for his support on providing experimental images for this paper. The authors would also like to acknowledge Berin Šeta, Raphael Comminal, Sina Jafarzadeh, Alberto Santi and Rajit Ranjan for providing useful inputs and texts in this work. The author group also highly acknowledges professor Dorte Juul Jensen for her valuable feedbacks about this paper.

References

- [1] Frazier WE. Metal additive manufacturing: A review. *J Mater Eng Perform* 2014;23:1917–28. <https://doi.org/10.1007/s11665-014-0958-z>.
- [2] Sigmund O, Maute K. Topology optimization approaches: A comparative review. *Struct Multidiscip Optimiz* 2013;48:1031–55. <https://doi.org/10.1007/s00158-013-0978-6>.
- [3] Jensen JS, Sigmund O. Systematic design of photonic crystal structures using topology optimization: Low-loss waveguide bends. *Appl Phys Lett* 2004;84. <https://doi.org/10.1063/1.1688450>.
- [4] Sigmund O. *A 99 line topology optimization code written in Matlab*. Springer-Verlag; 2001.
- [5] Sigmund O. On the usefulness of non-gradient approaches in topology optimization. *Struct Multidiscip Optimiz* 2011;43:589–96. <https://doi.org/10.1007/s00158-011-0638-7>.
- [6] Sigmund O. Design of material structures using topology optimization 1994.
- [7] Andersen MN, Wang F, Sigmund O. On the competition for ultimately stiff and strong architected materials. *Mater Des*. 2021. <https://doi.org/10.1016/j.matdes.2020.109356>.
- [8] M.; S.O. Rozvany, G. I.N.; Zhou, Topology optimization in structural design; 1992.
- [9] Ferrari F, Sigmund O, Guest JK. Topology Optimization with linearized buckling criteria in 250 lines of Matlab. *Struct Multidiscip Optimiz* 2021. <https://doi.org/10.1007/s00158-021-02854-x>.
- [10] Pingen G, Maute K. Optimal design for non-Newtonian flows using a topology optimization approach. *Comput Math Appl* 2010;59:2340–50. <https://doi.org/10.1016/j.camwa.2009.08.044>.
- [11] Dilgen SB, Dilgen CB, Fuhrman DR, Sigmund O, Lazarov BS. Density based topology optimization of turbulent flow heat transfer systems. *Struct Multidiscip Optimiz* 2018;57:1905–18. <https://doi.org/10.1007/s00158-018-1967-6>.
- [12] Dbouk T. A review about the engineering design of optimal heat transfer systems using topology optimization. *Appl Therm Eng*. 2017;112:841–54. <https://doi.org/10.1016/j.applthermaleng.2016.10.134>.
- [13] Yan S, Wang F, Hong J, Sigmund O. Topology optimization of microchannel heat sinks using a two-layer model. *Int J Heat Mass Transf*. 2019;143:118462. <https://doi.org/10.1016/j.jheatmasstransfer.2019.118462>.
- [14] Jensen JS, Sigmund O. Topology optimization for nano-photonics. *Laser Photon Rev*. 2011;5:308–21. <https://doi.org/10.1002/lpor.201000014>.
- [15] Mostafaei A, Zhao C, He Y, Reza Ghiaasiaan S, Shi B, Shao S, et al. Defects and anomalies in powder bed fusion metal additive manufacturing. *Curr Opin Solid State Mater Sci*. 2022;26:100974. <https://doi.org/10.1016/j.cossms.2021.100974>.
- [16] Martin AA, Calta NP, Hammons JA, Khairallah SA, Nielsen MH, Shuttlesworth RM, et al. Ultrafast dynamics of laser-metal interactions in additive manufacturing alloys captured by in situ X-ray imaging. *Mater Today Adv*. 2019;1:100002. <https://doi.org/10.1016/j.mtadv.2019.01.001>.
- [17] Calta NP, Martin AA, Hammons JA, Nielsen MH, Roehling TT, Fezzaa K, et al. Pressure dependence of the laser-metal interaction under laser powder bed fusion conditions probed by in situ X-ray imaging. *Addit Manuf*. 2020;32. <https://doi.org/10.1016/j.addma.2020.101084>.
- [18] Leung CLA, Marussi S, Atwood RC, Towrie M, Withers PJ, Lee PD. In situ X-ray imaging of defect and molten pool dynamics in laser additive manufacturing. *Nat Commun*. 2018;9:1–9. <https://doi.org/10.1038/s41467-018-03734-7>.
- [19] Cunningham R, Zhao C, Parab N, Kantzos C, Pauza J, Fezzaa K, et al. Keyhole threshold and morphology in laser melting revealed by ultrahigh-speed x-ray imaging. *Science* 1979;363(2019):849–52. <https://doi.org/10.1126/science.aav4687>.
- [20] Zhao C, Fezzaa K, Cunningham RW, Wen H, de Carlo F, Chen L, et al. Real-time monitoring of laser powder bed fusion process using high-speed X-ray imaging and diffraction. *Sci Rep*. 2017;7:1–11. <https://doi.org/10.1038/s41598-017-03761-2>.
- [21] Hooper PA. Melt pool temperature and cooling rates in laser powder bed fusion. *Addit Manuf*. 2018;22:548–59. <https://doi.org/10.1016/j.addma.2018.05.032>.
- [22] King W, Anderson AT, Ferencz RM, Hodge NE, Kamath C, Khairallah SA. Overview of modelling and simulation of metal powder bed fusion process at Lawrence Livermore National Laboratory. *Mater Sci Technol (United Kingdom)*. 2015;31:957–68. <https://doi.org/10.1179/1743284714Y.0000000728>.
- [23] Markl M, Körner C. Multiscale Modeling of Powder Bed-Based Additive Manufacturing. *Annu Rev Mater Res*. 2016;46:93–123. <https://doi.org/10.1146/annurev-matsci-070115-032158>.
- [24] Meier C, Penny RW, Zou Y, Gibbs JS, Hart AJ. Thermophysical phenomena in metal additive manufacturing by selective laser melting: Fundamentals, modeling, simulation and experimentation. *ArXiv* 2017. <https://doi.org/10.1615/annualrevheattransfer.2018019042>.
- [25] Brenken B, Barocio E, Favaloro A, Pipes RB, Kunc V. Fused filament fabrication of fiber-reinforced polymers: A review. *Addit Manuf*. 2018;21:1–16. <https://doi.org/10.1016/j.addma.2018.01.002>.

- [26] Al Rashid A, Koç M. Fused Filament Fabrication Process: A Review of Numerical Simulation Techniques. *Polymer*, MDPI. 2021;13:20.
- [27] Ferro P, Romanin L, Berto F. Understanding powder bed fusion additive manufacturing phenomena via numerical simulation. *Frattura Ed Integrità Strutturale*. 2020;14:252–84. <https://doi.org/10.3221/IGF-ESIS.53.21>.
- [28] Wei HL, Mukherjee T, Zhang W, Zuback JS, Knapp GL, De A, et al. Mechanistic models for additive manufacturing of metallic components. *Prog Mater Sci*. 2021;116. <https://doi.org/10.1016/j.pmatsci.2020.100703>.
- [29] Bayat M, Dong W, Thorborg J, To AC, Hattel JH. A review of multi-scale and multi-physics simulations of metal additive manufacturing processes with focus on modeling strategies. *Addit Manuf*. 2021;47. <https://doi.org/10.1016/j.addma.2021.102278>.
- [30] Serdeczny MP, Comminal R, Pedersen DB, Spangenberg J. Experimental validation of a numerical model for the strand shape in material extrusion additive manufacturing. *Addit Manuf*. 2018;24:145–53. <https://doi.org/10.1016/j.addma.2018.09.022>.
- [31] Bartlett JL, Li X. An overview of residual stresses in metal powder bed fusion. *Addit Manuf*. 2019;27:131–49. <https://doi.org/10.1016/j.addma.2019.02.020>.
- [32] Fang ZC, Wu ZL, Huang CG, Wu CW. Review on residual stress in selective laser melting additive manufacturing of alloy parts. *Opt Laser Technol*. 2020;129:106283. <https://doi.org/10.1016/j.optlastec.2020.106283>.
- [33] Bertini L, Bucchi F, Frendo F, Moda M, B. Disma Monelli, Residual stress prediction in selective laser melting A critical review of simulation strategies. *Int J Adv Manuf Technol* 2019:1–3.
- [34] Luo Z, Zhao Y. A survey of finite element analysis of temperature and thermal stress fields in powder bed fusion Additive Manufacturing. *Addit Manuf*. 2018;21:318–32. <https://doi.org/10.1016/j.addma.2018.03.022>.
- [35] Paul S. Finite element analysis in fused deposition modeling research : A literature review. *Measurement* 2021;178:109320. <https://doi.org/10.1016/j.measurement.2021.109320>.
- [36] Cook PS, Murphy AB. Simulation of melt pool behaviour during additive manufacturing: Underlying physics and progress. *Addit Manuf*. 2020;31:100909. <https://doi.org/10.1016/j.addma.2019.100909>.
- [37] Das A, Gilmer EL, Biria S, Bortner MJ. Importance of Polymer Rheology on Material Extrusion Additive Manufacturing: Correlating Process Physics to Print Properties, 2021. <https://doi.org/10.1021/acscapm.0c01228>.
- [38] Li J, Zhou X, Brochu M, Provatas N, Zhao YF. Solidification microstructure simulation of Ti-6Al-4V in metal additive manufacturing: A review. *Addit Manuf*. 2020;31:100989. <https://doi.org/10.1016/j.addma.2019.100989>.
- [39] Zhang J, Li X, Xu D, Yang R. Recent progress in the simulation of microstructure evolution in titanium alloys. *Prog Nat Sci: Mater Int* 2019:1–10. <https://doi.org/10.1016/j.pnsc.2019.05.006>.
- [40] Charles A, Elkaseer A, Thijs L, Scholz SG. Dimensional errors due to overhanging features in laser powder bed fusion parts made of Ti-6Al-4V. *Appl Sci (Switzerland)*. 2020;10. <https://doi.org/10.3390/app10072416>.
- [41] Charles A, Elkaseer A, Thijs L, Hagenmeyer V, Scholz S. Effect of process parameters on the generated surface roughness of down-facing surfaces in selective laser melting. *Appl Sci (Switzerland)*. 2019;9:1–13. <https://doi.org/10.3390/app9061256>.
- [42] Klingaa CG, Mohanty S, Hattel JH. Realistic design of laser powder bed fusion channels. *Rapid Prototyp J*. 2020;26:1827–36. <https://doi.org/10.1108/RPJ-01-2020-0010>.
- [43] Klingaa CG, Dahmen T, Baier S, Mohanty S, Hattel JH. X-ray CT and image analysis methodology for local roughness characterization in cooling channels made by metal additive manufacturing. *Addit Manuf*. 2020;32. <https://doi.org/10.1016/j.addma.2019.101032>.
- [44] Klingaa CG, Dahmen T, Baier-Stegmaier S, Mohanty S, Hattel JH. Investigation of the roughness variation along the length of LPBF manufactured straight channels. *Nondestructive Testing Evaluat* 2020;35:304–14. <https://doi.org/10.1080/10589759.2020.1785445>.
- [45] DebRoy T, Mukherjee T, Milewski JO, Elmer JW, Ribic B, Blecher JJ, et al. Scientific, technological and economic issues in metal printing and their solutions. *Nat Mater*. 2019;18. <https://doi.org/10.1038/s41563-019-0408-2>.
- [46] Wu J, Sigmund O, Groen JP. Topology optimization of multi-scale structures: a review, 2021, 1455–1480.
- [47] Liu J, Gaynor AT, Chen S, Kang Z, Suresh K, Takezawa A, et al. Current and future trends in topology optimization for additive manufacturing. *Struct Multidiscip Optim* 2018. <https://doi.org/10.1007/s00158-018-1994-3>.
- [48] Osanov M, Guest JK. Topology Optimization for Architected Materials Design. *Annu Rev Mater Res*. 2016;46:211–33. <https://doi.org/10.1146/annurev-matsci-070115-031826>.
- [49] Zhan T. Progress on different topology optimization approaches and optimization for additive manufacturing: A review. *J Phys Conf Ser* 2021. <https://doi.org/10.1088/1742-6596/1939/1/012101>.
- [50] Meng L, Zhang W, Quan D, Shi G, Tang L, Hou Y, et al. From Topology Optimization Design to Additive Manufacturing: Today's Success and Tomorrow's Roadmap. *Arch Comput Meth Eng* 2020. <https://doi.org/10.1007/s11831-019-09331-1>.
- [51] Sehmi M, Christensen J, Bastien C, Kanarachos S. Review of topology optimisation refinement processes for sheet metal manufacturing in the automotive industry. *Struct Multidiscip Optim* 2018. <https://doi.org/10.1007/s00158-017-1876-0>.
- [52] Bendsoe MP, Sigmund O. *Topology Optimization: Theory, Methods and Applications*. Springer; 2004.
- [53] Eschenauer HA, Olhoff N. *Topology optimization of continuum structures: A review*. *Appl Mech Rev*. 2001;54:331–90.
- [54] Sigmund O, Maute K. Topology optimization approaches. *Struct Multidiscip Optim* 2013;48:1031–55. <https://doi.org/10.1007/s00158-013-0978-6>.
- [55] Sigmund O. A 99 line topology optimization code written in {M}atlab. *Struct Multidiscip Optim* 2001;21:120–7. <https://doi.org/10.1007/s001580050176>.
- [56] Wang C, Zhao Z, Zhou M, Sigmund O, Zhang XS. A comprehensive review of educational articles on structural and multidisciplinary optimization. *Struct Multidiscip Optim* 2021;64. <https://doi.org/10.1007/s00158-021-03050-7>.
- [57] Hughes T.J.R. *The Finite Element Method: {L}inear Static and Dynamic Finite Element Analysis*. Prentice-Hall; 1987.
- [58] Bathe K-J. *{F}inite {E}lement procedures in engineering analysis, first*; 1982.
- [59] Crisfield MA. *Nonlinear finite element analysis of solid and structures*. Wiley; 1991.
- [60] Zienkiewicz O, Taylor R, Zhu JZ. *The Finite Element Method: its Basis and Fundamentals: Seventh Edition*; 2013. <https://doi.org/10.1016/C2009-0-24909-9>.
- [61] Oliveira HL, Leonel ED. Boundary element method applied to topology optimization using the level set method and an alternative velocity regularization. *Meccanica* 2019;54. <https://doi.org/10.1007/s11012-019-00954-z>.
- [62] Finite element approximation for optimal shape design. theory and applications. *Math Comput Simul*. 1989;31. [https://doi.org/10.1016/0378-4754\(89\)90167-5](https://doi.org/10.1016/0378-4754(89)90167-5).
- [63] Chen L, Lu C, Lian H, Liu Z, Zhao W, Li S, et al. Acoustic topology optimization of sound absorbing materials directly from subdivision surfaces with isogeometric boundary element methods. *Comput Methods Appl Mech Eng*. 2020;362. <https://doi.org/10.1016/j.cma.2019.112806>.
- [64] Abert C, Huber C, Bruckner F, Vogler C, Wautischer G, Suess D. A fast finite-difference algorithm for topology optimization of permanent magnets. *J Appl Phys*. 2017;122. <https://doi.org/10.1063/1.4998532>.
- [65] Iguchi A, Tsuji Y, Yasui T, Hirayama K. Efficient topology optimization of optical waveguide devices utilizing semi-vectorial finite-difference beam propagation method. *Opt Express*. 2017;25. <https://doi.org/10.1364/oe.25.028210>.
- [66] Groen JP, Langelaar M, Sigmund O, Ruess M. Higher-order multi-resolution topology optimization using the finite cell method. *Int J Numer Methods Eng*. 2017;110:903–20. <https://doi.org/10.1002/nme.5432>.
- [67] Chen Y, Zhou S, Li Q. Multiobjective topology optimization for finite periodic structures. *Comput Struct*. 2010;88:806–11. <https://doi.org/10.1016/j.compstruc.2009.10.003>.
- [68] Kreisselmeier G, Steinhauser R. *Systematic Control Design by Optimizing a Vector Performance Index*. IFAC Proc Volumes 1979;12:113–7.
- [69] Wrenn GA. An Indirect Method for Numerical Optimization Using the {K}reisselmeier-{S}teinhauser Function, National Aeronautics and Space Administration, Office of Management, Scientific and Technical Information Division; 1989. <https://books.google.it/books?id=LjSCAAAIAAJ>.
- [70] Kennedy GJ, Hicken JE. Improved constraint-aggregation methods. *Comput Methods Appl Mech Eng*. 2015;289:332–54.
- [71] Bertsekas DP. Necessary and sufficient conditions for a penalty method to be exact. *Math Program* 1975;9:87–99. <https://doi.org/10.1007/BF01681332>.
- [72] di Pillo G, Grippo L. Exact Penalty Functions in Constrained Optimization. *SIAM J Control Optim*. 1989;27:1333–60. <https://doi.org/10.1137/0327068>.

- [73] van Dijk NP, Maute K, Langelaar M, van Keulen F. Level-set methods for structural topology optimization: A review. *Struct Multidiscip Optim* 2013;48. <https://doi.org/10.1007/s00158-013-0912-y>.
- [74] Deaton JD, Grandhi RV. A survey of structural and multidisciplinary continuum topology optimization: post 2000. *Struct Multidiscip Optim* 2014;49:1–38.
- [75] Dilgen CB, Dilgen SB, Aage N, Jensen JS. Topology optimization of acoustic mechanical interaction problems: a comparative review. *Struct Multidiscip Optim* 2019;60. <https://doi.org/10.1007/s00158-019-02236-4>.
- [76] Rossow MP, Taylor JE. A finite element method for the optimal design of variable thickness sheets. *AIAA J* 1973;11. <https://doi.org/10.2514/3.50631>.
- [77] Osher S, Sethian JA. Fronts propagating with curvature-dependent speed: Algorithms based on Hamilton-Jacobi formulations. *J Comput Phys*. 1988;79. [https://doi.org/10.1016/0021-9991\(88\)90002-2](https://doi.org/10.1016/0021-9991(88)90002-2).
- [78] Allaire G, Jouve F, Toader AM. Structural optimization using sensitivity analysis and a level-set method. *J Comput Phys*. 2004;194. <https://doi.org/10.1016/j.jcp.2003.09.032>.
- [79] Allaire G, Jouve F, Toader A-M. A level-set method for shape optimization. *C R Math*. 2002;334:1125–30. [https://doi.org/10.1016/S1631-073X\(02\)02412-3](https://doi.org/10.1016/S1631-073X(02)02412-3).
- [80] Wang MY, Wang X, Guo D. A level set method for structural topology optimization. *Comput Methods Appl Mech Eng*. 2003;192:227–46. [https://doi.org/10.1016/S0045-7825\(02\)00559-5](https://doi.org/10.1016/S0045-7825(02)00559-5).
- [81] Sokolowski J, Zochowski A. On the topological derivative in shape optimization. *SIAM J Control Optim*. 1999;37. <https://doi.org/10.1137/S0363012997323230>.
- [82] Amstutz S. Connections between topological sensitivity analysis and material interpolation schemes in topology optimization. *Struct Multidiscip Optim* 2011. <https://doi.org/10.1007/s00158-010-0607-6>.
- [83] Garreau S, Guillaume P, Masmoudi M. The topological asymptotic for PDE systems: The elasticity case. *SIAM J Control Optim*. 2001;39. <https://doi.org/10.1137/S0363012900369538>.
- [84] Cea J, Garreau S, Guillaume P, Masmoudi M. The shape and topological optimizations connection. *Comput Methods Appl Mech Eng* 2000. [https://doi.org/10.1016/S0045-7825\(99\)00357-6](https://doi.org/10.1016/S0045-7825(99)00357-6).
- [85] Cai S, Zhang W. An adaptive bubble method for structural shape and topology optimization. *Comput Methods Appl Mech Eng*. 2020;360. <https://doi.org/10.1016/j.cma.2019.112778>.
- [86] Eschenauer HA, Kobelev VV, Schumacher A. Bubble method for topology and shape optimization of structures. *Struct Optim* 1994;8. <https://doi.org/10.1007/BF01742933>.
- [87] Thierauf G. Optimal topologies of structures: Homogenization, pseudo-elastic approximation and the bubble-method, *Engineering Computations* (Swansea, Wales). 13 (1996). <https://doi.org/10.1108/02644409610110994>.
- [88] Gangl P. A multi-material topology optimization algorithm based on the topological derivative. *Comput Methods Appl Mech Eng*. 2020;366. <https://doi.org/10.1016/j.cma.2020.113090>.
- [89] Wang Y, Yang H, Kang Z. Velocity Field Level Set Method Incorporating Topological Derivatives for Topology Optimization. *J Appl Mech*. 2022;89. <https://doi.org/10.1115/1.4053989>.
- [90] Norato JA, Bendsoe MP, Haber RB, Tortorelli DA. A topological derivative method for topology optimization. *Struct Multidiscip Optim* 2007;33. <https://doi.org/10.1007/s00158-007-0094-6>.
- [91] Allaire G, de Gournay F, Jouve F, Toader AM. Structural optimization using topological and shape sensitivity via a level set method. *Control Cybern* 2005;34.
- [92] Allaire G, Jouve F. Coupling the level set method and the topological gradient in structural optimization. *Solid Mech Appl* 2006. https://doi.org/10.1007/1-4020-4752-5_1.
- [93] Wang MY, Zhou S. Phase field: A variational method for structural topology optimization. *CMES - Comput Model Eng Sci* 2004;6.
- [94] Wallin M, Ristinmaa M, Askfelt H. Optimal topologies derived from a phase-field method. *Struct Multidiscip Optim* 2012;45. <https://doi.org/10.1007/s00158-011-0688-x>.
- [95] Burger M, Stainko R. Phase-field relaxation of topology optimization with local stress constraints. *SIAM J Control Optim*. 2006;45. <https://doi.org/10.1137/05062723X>.
- [96] Takezawa A, Nishiwaki S, Kitamura M. Shape and topology optimization based on the phase field method and sensitivity analysis. *J Comput Phys*. 2010;229. <https://doi.org/10.1016/j.jcp.2009.12.017>.
- [97] Olhoff N, Bendsoe MP, Rasmussen J. On CAD-integrated structural topology and design optimization. *Comput Methods Appl Mech Eng*. 1991. [https://doi.org/10.1016/0045-7825\(91\)90044-7](https://doi.org/10.1016/0045-7825(91)90044-7).
- [98] Bletzinger K-U, Maute K. Towards generalized shape and topology optimization. *Eng Optim* 1997;29:201–16. <https://doi.org/10.1080/03052159708940993>.
- [99] Ansola R, Canales J, Tarrago JA, Rasmussen J. On simultaneous shape and material layout optimization of shell structures. *Struct Multidiscip Optim* 2002. <https://doi.org/10.1007/s00158-002-0227-x>.
- [100] Dilgen CB, Dilgen SB, Fuhrman DR, Sigmund O, Lazarov BS. Topology optimization of turbulent flows. *Comput Methods Appl Mech Eng*. 2018;331:363–93. <https://doi.org/10.1016/j.cma.2017.11.029>.
- [101] Maute K, Schwarz S, Ramm E. Adaptive topology optimization of elastoplastic structures. *Struct Optim* 1998;15. <https://doi.org/10.1007/BF01278493>.
- [102] de Sturler E, Wang S, Paulino GH. Topology optimization with adaptive mesh refinement. In: *Proceedings of the \$6\$-Th International Conference on Computation of Shell and Spatial Structures*; 2008.
- [103] Stainko R. An adaptive multilevel approach to the minimal compliance problem in topology optimization. *Commun Numer Methods Eng*. 2006;22:109–18. <https://doi.org/10.1002/cnm.800>.
- [104] di Cristofaro D, Galimberti C, Bianchi D, Ferrante R, Ferro N, Mannisi M, et al. Adaptive topology optimization for innovative 3d printed metamaterials. In: *World Congress in Computational Mechanics and ECCOMAS Congress*; 2021. <https://doi.org/10.23967/wccm-eccomas.2020.049>.
- [105] Ferro N, Micheletti S, Perotto S. Compliance–stress constrained mass minimization for topology optimization on anisotropic meshes. *SN Appl Sci*. 2020;2. <https://doi.org/10.1007/s42452-020-2947-1>.
- [106] Misztal MK, Barentzen JA. Topology-adaptive interface tracking using the deformable simplicial complex. *ACM Trans Graph*. 2012;31. <https://doi.org/10.1145/2167076.2167082>.
- [107] Christiansen AN, Nobel-Jørgensen M, Aage N, Sigmund O, Barentzen JA. Topology optimization using an explicit interface representation. *Struct Multidiscip Optim* 2014;49. <https://doi.org/10.1007/s00158-013-0983-9>.
- [108] Lian H, Christiansen AN, Tortorelli DA, Sigmund O, Aage N. Combined shape and topology optimization for minimization of maximal von Mises stress. *Struct Multidiscip Optim* 2017;55. <https://doi.org/10.1007/s00158-017-1656-x>.
- [109] Zhou M, Lian H, Sigmund O, Aage N. Shape morphing and topology optimization of fluid channels by explicit boundary tracking. *Int J Numer Methods Fluids*. 2018;88. <https://doi.org/10.1002/fld.4667>.
- [110] Villanueva CH, Maute K. Density and level set–{XFEM} schemes for topology optimization of 3–{D} structures. *Comput Mech*. 2014;54:133–50. <https://doi.org/10.1007/s00466-014-1027-z>.
- [111] Kreissl S, Maute K. Levelset based fluid topology optimization using the extended finite element method. *Struct Multidiscip Optim* 2012;46. <https://doi.org/10.1007/s00158-012-0782-8>.
- [112] Liu P, Luo Y, Kang Z. Multi-material topology optimization considering interface behavior via XFEM and level set method. *Comput Methods Appl Mech Eng*. 2016;308. <https://doi.org/10.1016/j.cma.2016.05.016>.
- [113] Villanueva CH, Maute K. CutFEM topology optimization of 3D laminar incompressible flow problems. *Comput Methods Appl Mech Eng*. 2017;320:444–73. <https://doi.org/10.1016/j.cma.2017.03.007>.
- [114] Burman E, Claus S, Hansbo P, Larson MG, Massing A. CutFEM: Discretizing geometry and partial differential equations. *Int J Numer Methods Eng*. 2015;104:472–501. <https://doi.org/10.1002/nme.4823>.
- [115] Burman E, Elfverson D, Hansbo P, Larson MG, Larsson K. Cut topology optimization for linear elasticity with coupling to parametric nondesign domain regions. *Comput Methods Appl Mech Eng*. 2019;350. <https://doi.org/10.1016/j.cma.2019.03.016>.

- [116] Andreasen CS, Elingaard MO, Aage N. Level set topology and shape optimization by density methods using cut elements with length scale control. *Struct Multidiscip Optim* 2020;62. <https://doi.org/10.1007/s00158-020-02527-1>.
- [117] Aage N, Giele R, Andreasen CS. Length scale control for high-resolution three-dimensional level set-based topology optimization. *Struct Multidiscip Optim* 2021;64. <https://doi.org/10.1007/s00158-021-02904-4>.
- [118] Wein F, Dunning PD, Norato JA. A review on feature-mapping methods for structural optimization. *Struct Multidiscip Optim* 2020;62. <https://doi.org/10.1007/s00158-020-02649-6>.
- [119] Sun J, Tian Q, Hu H. Topology Optimization of a Three-Dimensional Flexible Multibody System Via Moving Morphable Components. *J Comput Nonlinear Dyn* 2018;13. <https://doi.org/10.1115/1.4038142>.
- [120] Zhang W, Li D, Yuan J, Song J, Guo X. A new three-dimensional topology optimization method based on moving morphable components (MMCs). *Comput Mech* 2017;59. <https://doi.org/10.1007/s00466-016-1365-0>.
- [121] Guo X, Zhang W, Zhong W. Doing topology optimization explicitly and geometrically—a new moving morphable components based framework, *Journal of Applied Mechanics*. *Trans ASME* 2014;81. <https://doi.org/10.1115/1.4027609>.
- [122] Zhang W, Yuan J, Zhang J, Guo X. A new topology optimization approach based on Moving Morphable Components (MMC) and the ersatz material model. *Struct Multidiscip Optim* 2016;53. <https://doi.org/10.1007/s00158-015-1372-3>.
- [123] Liu C, Zhu Y, Sun Z, Li D, Du Z, Zhang W, et al. An efficient moving morphable component (MMC)-based approach for multi-resolution topology optimization. *Struct Multidiscip Optim* 2018;58. <https://doi.org/10.1007/s00158-018-2114-0>.
- [124] Beekers M, Fleury C. Topology optimization involving discrete variables, in: *Proceedings of the Second World Congress of Structural and Multidisciplinary Optimization: [M]ay 26–30 1997, [Z]akopane, [P]oland, 1997: pp. 533–538*.
- [125] Beekers M. Topology optimization using a dual method with discrete variables. *Struct Multidiscip Optim* 1999;17:14–24.
- [126] Ranjbarzadeh S, Picelli R, Gloria R, Silva ECN. Topology optimization of structures subject to non-Newtonian fluid–structure interaction loads using integer linear programming. *Finite Elem Anal Des* 2022;202. <https://doi.org/10.1016/j.finel.2021.103690>.
- [127] Yan XY, Liang Y, Cheng GD. Discrete variable topology optimization for simplified convective heat transfer via sequential approximate integer programming with trust-region. *Int J Numer Methods Eng* 2021;122. <https://doi.org/10.1002/nme.6775>.
- [128] Liang Y, Sun K, Cheng GD. Discrete variable topology optimization for compliant mechanism design via Sequential Approximate Integer Programming with Trust Region (SAIP-TR). *Struct Multidiscip Optim* 2020;62. <https://doi.org/10.1007/s00158-020-02693-2>.
- [129] Bendsoe MP. Optimal shape design as a material distribution problem. *Struct Optim* 1989;1:193–202. <https://doi.org/10.1007/BF01650949>.
- [130] Rozvany GIN, Zhou M, Birker T. Generalized shape optimization without homogenization. *Struct Multidiscip Optim* 1992;4:250–2. <https://doi.org/10.1007/bf01742754>.
- [131] Bendsoe MP, Sigmund O. Material interpolation schemes in topology optimization. *Arch Appl Mech* 1999;69:635–54. <https://doi.org/10.1007/s004190050248>.
- [132] Hashin Z, Shtrickman S. A variational approach to the theory of the elastic behaviour of multiphase materials. *J Mech Phys Solids* 1963;11:127–40.
- [133] Duysinx P, Bendsoe MP. Topology optimization of continuum structures with local stress constraints. *Int J Numer Methods Eng* 1998;43:1453–78. [https://doi.org/10.1002/\(SICI\)1097-0207\(19981230\)43:8<1453::AID-NME480>3.0.CO;2-2](https://doi.org/10.1002/(SICI)1097-0207(19981230)43:8<1453::AID-NME480>3.0.CO;2-2).
- [134] Lipton R. Design of functionally graded composite structures in the presence of stress constraints. *Int J Solids Struct* 2002;39. [https://doi.org/10.1016/S0020-7683\(02\)00129-4](https://doi.org/10.1016/S0020-7683(02)00129-4).
- [135] Dzierżanowski G. On the comparison of material interpolation schemes and optimal composite properties in plane shape optimization. *Struct Multidiscip Optim* 2012;46:693–710. <https://doi.org/10.1007/s00158-012-0788-2>.
- [136] Zargham Sajjad TARRBIA. Ward, Topology optimization: a review for structural designs under vibration problems. *Struct Multidiscip Optim* 2016;53. <https://doi.org/10.1007/s00158-015-1370-5>.
- [137] Stolpe M, Svanberg K. An alternative interpolation scheme for minimum compliance optimization. *Struct Multidiscip Optim* 2001;22:116–24.
- [138] Swan CC, Arora JS. Topology design of material layout in structured composites of high stiffness and strength. *Struct Optim* 1997. <https://doi.org/10.1007/BF01198375>.
- [139] Swan CC, Kosaka I. Voigt-Reuss topology optimization for structures with linear elastic material behaviours. *Int J Numer Methods Eng* 1997. [https://doi.org/10.1002/\(sici\)1097-0207\(19970830\)40:16<3033::aid-nme196>3.3.co;2-q](https://doi.org/10.1002/(sici)1097-0207(19970830)40:16<3033::aid-nme196>3.3.co;2-q).
- [140] Christiansen RE, Vester-Petersen J, Madsen SP, Sigmund O. A non-linear material interpolation for design of metallic nano-particles using topology optimization. *Comput Methods Appl Mech Eng* 2019;343. <https://doi.org/10.1016/j.cma.2018.08.034>.
- [141] Hvejsel CF, Lund E. Material interpolation schemes for unified topology and multi-material optimization. *Struct Multidiscip Optim* 2011;43. <https://doi.org/10.1007/s00158-011-0625-z>.
- [142] Zuo W, Saitou K. Multi-material topology optimization using ordered SIMP interpolation. *Struct Multidiscip Optim* 2017;55. <https://doi.org/10.1007/s00158-016-1513-3>.
- [143] Nocedal J, Wright S. *Numerical Optimization*. New York: Springer; 2006.
- [144] Christiansen S, Patriksson M, Wynter L. Stochastic bilevel programming in structural optimization; 1999. <https://doi.org/10.1007/s001580100115>.
- [145] Kočvara M. Topology optimization with displacement constraints: A bilevel programming approach. *Struct Optim* 1997. <https://doi.org/10.1007/BF01197948>.
- [146] Herskovits J, Leontiev A, Dias G, Santos G. Contact shape optimization: A bilevel programming approach. *Struct Multidiscip Optim* 2000. <https://doi.org/10.1007/s001580050149>.
- [147] Washizu K. *Variational Methods in Elasticity and Plasticity*, {S}econd. Pergamon Press; 1975.
- [148] Ciarlet P. The Finite Element Method for Elliptic Problems. *Soc Ind Appl Math* 2002. <https://doi.org/10.1137/1.9780898719208>.
- [149] Haftka RT, Gurdal Z. *Elements of Structural Optimization*. Netherlands: Springer; 2012.
- [150] Haftka RT. Simultaneous analysis and design. *AIAA J* 1985;23:1099–103.
- [151] Haftka RT, Kamat MP. Simultaneous nonlinear structural analysis and design. *Comput Mech* 1989;4:409–16. <https://doi.org/10.1007/BF00293046>.
- [152] Shin YS, Haftka RT, Plaut RH. Simultaneous analysis and design for eigenvalue maximization. *AIAA J* 1988;26:738–44.
- [153] Maar B, Schulz V. Interior point multigrid methods for topology optimization. *Struct Multidiscip Optim* 2000;19:214–24. <https://doi.org/10.1007/s001580050104>.
- [154] Dreyer T, Maar B, Schulz V. Multigrid optimization in applications. *J Comput Appl Math* 2000;120:67–84. [https://doi.org/10.1016/S0377-0427\(00\)00304-6](https://doi.org/10.1016/S0377-0427(00)00304-6).
- [155] Hoppe R, Petrova SI, Schulz V. Primal-Dual Newton-Type Interior-Point Method for Topology Optimization. *J Optim Theory Appl* 2002;114. <https://doi.org/10.1023/a:1016070928600>.
- [156] Kočvara M, Mohammed S. Primal-dual interior point multigrid method for topology optimization. *SIAM J Sci Comput* 2016. <https://doi.org/10.1137/15M1044126>.
- [157] Rojas-Labanda S, Stolpe M. Benchmarking optimization solvers for structural topology optimization. *Struct Multidiscip Optim* 2015;52:527–47. <https://doi.org/10.1007/s00158-015-1250-z>.
- [158] Haug EJ, Rousset B. Design Sensitivity Analysis in Structural Mechanics. *J Struct Mech* 1980;8 {P}art {I}: {S}tatic response Variations 17–41, {I}.
- [159] Rousset B, Haug EJ. Design Sensitivity Analysis in Structural Mechanics (III): {E}ffects of Shape Variation. *J Struct Mech* 1982;10:273–310. <https://doi.org/10.1080/03601218208907414>.
- [160] Haug EJ, Rousset B. Design Sensitivity Analysis in Structural Mechanics. II. Eigenvalue Variations. *J Struct Mech* 1980. <https://doi.org/10.1080/03601218008907358>.
- [161] Cardoso JB, Arora JS. Variational method for design sensitivity analysis in nonlinear structural mechanics. *AIAA J* 1988. <https://doi.org/10.2514/3.9939>.
- [162] Kohn Rv, Strang G. Optimal design and relaxation of variational problems. *Commun Pure Appl Math* 1986;39. <https://doi.org/10.1002/cpa.3160390107>. Part {I}: 1–25, {P}art {II}: 139–182, {P}art {III}.

- [163] Strang G, Kohn RV. Optimal design in elasticity and plasticity. *Int J Numer Methods Eng*. 1986;22:183–8. <https://doi.org/10.1002/nme.1620220113>.
- [164] Lions JL. Optimal Control of Systems Governed by Partial. Differential Equations 1971. <https://doi.org/10.1007/978-3-642-65024-6>.
- [165] Lurie KA. Applied Optimal Control Theory of Distributed Systems; 1993. <https://doi.org/10.1007/978-1-4757-9262-1>.
- [166] Tortorelli DA, Michaleris P. Design sensitivity analysis: Overview and review. *Inverse Prob Eng* 1994;1. <https://doi.org/10.1080/174159794088027573>.
- [167] Jensen JS, Nakshatrala PB, Tortorelli DA. On the consistency of adjoint sensitivity analysis for structural optimization of linear dynamic problems. *Struct Multidiscip Optim* 2014;49. <https://doi.org/10.1007/s00158-013-1024-4>.
- [168] Tortorelli DA, Haber RB, Lu SCY. Design sensitivity analysis for nonlinear thermal systems. *Comput Methods Appl Mech Eng*. 1989;77. [https://doi.org/10.1016/0045-7825\(89\)90128-X](https://doi.org/10.1016/0045-7825(89)90128-X).
- [169] Tortorelli DA. Sensitivity analysis for non-linear constrained elastostatic systems. *Int J Numer Methods Eng*. 1992;33. <https://doi.org/10.1002/nme.1620330807>.
- [170] Carlsson J, Sandberg M, Szepessy A. Symplectic pontryagin approximations for optimal design. *Math Modell Numer Anal* 2009. <https://doi.org/10.1051/m2an/2008038>.
- [171] Othmer C. A continuous adjoint formulation for the computation of topological and surface sensitivities of ducted flows. *Int J Numer Methods Fluids*. 2008. <https://doi.org/10.1002/fld.1770>.
- [172] Evgrafov A. State space Newton's method for topology optimization. *Comput Methods Appl Mech Eng*. 2014;278:272–90. <https://doi.org/10.1016/j.cma.2014.06.005>.
- [173] Kontoleon EA, Papoutsis-Kiachagias EM, Zymaris AS, Papadimitriou DI, Giannakoglou KC. Adjoint-based constrained topology optimization for viscous flows, including heat transfer. *Eng Optim* 2013;45:941–61. <https://doi.org/10.1080/0305215X.2012.717074>.
- [174] Papadopoulos IPA, Farrell PE, Surowiec TM. Computing multiple solutions of topology optimization problems. *SIAM J Sci Comput* 2021;43. <https://doi.org/10.1137/20M1326209>.
- [175] Bluhm GL, Sigmund O, Poulis K. Internal contact modeling for finite strain topology optimization. *Comput Mech*. 2021. <https://doi.org/10.1007/s00466-021-01974-x>.
- [176] Chandrasekhar A, Sridhara S, Suresh K. AuTO: a framework for Automatic differentiation in Topology Optimization. *Struct Multidiscip Optim* 2021. <https://doi.org/10.1007/s00158-021-03025-8>.
- [177] Ma Y, Dixit V, Innes MJ, Guo X, Rackauckas C, Comparison A, et al. IEEE High Performance Extreme Computing Conference. HPEC 2021;2021:2021. <https://doi.org/10.1109/HPEC49654.2021.9622796>.
- [178] Prager W, Taylor JE. Problems of optimal structural design. *Trans Am Soc Mech Eng* 1968.
- [179] Andreassen E, Clausen A, Schevenels M, Lazarov BS, Sigmund O. Efficient topology optimization in MATLAB using 88 lines of code. *Struct Multidiscip Optim* 2011;43:1–16. <https://doi.org/10.1007/s00158-010-0594-7>.
- [180] Ferrari F, Sigmund O. A new generation 99 line Matlab code for compliance Topology Optimization and its extension to 3D. *Struct Multidiscip Optim* 2020;62:2211–28.
- [181] Fleury C. {CONLIN}: {A}n efficient dual optimizer based on convex approximation concepts. *Struct Optim* 1989;1:81–9. <https://doi.org/10.1007/BF01637664>.
- [182] Fleury C. Structural weight optimization by dual methods and convex programming. *Int J Numer Methods Eng* 1979;14:1761–83.
- [183] Fleury C, Braibant V. Structural optimization: A new dual method using mixed variables. *Int J Numer Methods Eng*. 1986;23:409–28. <https://doi.org/10.1002/nme.1620230307>.
- [184] Khot NS. Optimality Criterion Methods in Structural Optimization; 1982.
- [185] Berke L, Khot NS. Structural optimization using optimality criteria. In: *Computer Aided Optimal Design: Structural and Mechanical Systems*. Springer; 1987. p. 271–311.
- [186] Chang KJ. Optimality criteria methods using K–S functions. *Struct Optim* 1992;4:213–7.
- [187] Yin L, Yang W. Optimality criteria method for topology optimization under multiple constraints. *Comput Struct*. 2001;79:1839–50.
- [188] Patnaik SN, Gupta JD, Berke L. Merits and limitations of optimality criteria method for structural optimization. *Int J Numer Methods Eng*. 1995;38:3087–120. <https://doi.org/10.1002/nme.1620381806>.
- [189] Khot NS. Algorithms based on optimality criteria to design minimum weight structures. *Eng Optim* 1981;5:73–90.
- [190] Hassani B, Hinton E. A review of homogenization and topology optimization III - Topology optimization using optimality criteria. *Comput Struct*. 1998. [https://doi.org/10.1016/s0045-7949\(98\)00133-3](https://doi.org/10.1016/s0045-7949(98)00133-3).
- [191] Groenwold AA, Ertan LFP. On the equivalence of optimality criterion and sequential approximate optimization methods in the classical topology layout problem. *Int J Numer Methods Eng* 2008;73:297–316.
- [192] Svanberg K. The method of moving asymptotes - A new method for structural optimization. *Int J Numer Methods Eng*. 1987;24:359–73.
- [193] Svanberg K. {MMA} and {GCMMA}—two methods for nonlinear optimization; 2007.
- [194] Svanberg K. A Class of Globally Convergent Optimization Methods Based on Conservative Convex Separable Approximations. *SIAM J Optim* 2002;12:555–73. <https://doi.org/10.1137/S1052623499362822>.
- [195] Wächter A, Biegler LT. Line search filter methods for nonlinear programming: Local convergence. *SIAM J Optim* 2006;16. <https://doi.org/10.1137/S1052623403426544>.
- [196] Wächter A, Biegler LT. On the implementation of an interior–point filter line-search algorithm for large-scale nonlinear programming, *Math. Program* 2006; 106:25–57. <https://doi.org/10.1007/s10107-004-0559-y>.
- [197] Gill PE, Murray W, Saunders MA. SNOPT: An SQP algorithm for large-scale constrained optimization. *SIAM J Optim* 2002;12. <https://doi.org/10.1137/S1052623499350013>.
- [198] Rojas-Labanda S, Stolpe M. Automatic penalty continuation in structural topology optimization. *Struct Multidiscip Optim* 2015;52:1205–21.
- [199] Rojas-Labanda S, Stolpe M. An efficient second-order SQP method for structural topology optimization. *Struct Multidiscip Optim* 2016;53:1315–33. <https://doi.org/10.1007/s00158-015-1381-2>.
- [200] Kočvara M, Stingl M. PENNON. In: di Pillo G, Murli A, editors. *High Performance Algorithms and Software for Nonlinear Optimization*. Boston, MA: Springer US; 2003, pp. 303–321. https://doi.org/10.1007/978-1-4613-0241-4_14.
- [201] Kočvara M, Kočvara M. On the modelling and solving of the truss design problem with global stability constraints. *SMO* 2002; 23: 189–203. <https://doi.org/10.1007/s00158-002-0177-3>.
- [202] Ben-Tal A, Kočvara M, Nemirovski A, Zowe J. Free material design via semidefinite programming: the multiloading case with contact conditions. *SIAM Rev* 2000; 42. <https://doi.org/10.1137/S0036144500372081>.
- [203] Czarnecki S, Lewiński T. A stress-based formulation of the free material design problem with the trace constraint and multiple load conditions. *Struct Multidiscip Optim* 2014;49. <https://doi.org/10.1007/s00158-013-1023-5>.
- [204] Haslinger J, Kočvara M, Leugering G, Stingl M. Multidisciplinary free material optimization. *SIAM J Appl Math*. 2010;70. <https://doi.org/10.1137/090774446>.
- [205] Xie YM, Steven GP. A simple evolutionary procedure for structural optimization. *Comput Struct*. 1993;49. [https://doi.org/10.1016/0045-7949\(93\)90035-C](https://doi.org/10.1016/0045-7949(93)90035-C).
- [206] Young V, Querin OM, Steven GP, Xie YM. 3D and multiple load case bi-directional evolutionary structural optimization (BESO). *Struct Optim* 1999;18. <https://doi.org/10.1007/s001580050119>.
- [207] Huang X, Xie YM. Evolutionary topology optimization of geometrically and materially nonlinear structures under prescribed design load. *Struct Eng Mech* 2010;34. <https://doi.org/10.12989/sem.2010.34.5.581>.
- [208] Huang X, Xie YM. A further review of ESO type methods for topology optimization. *Struct Multidiscip Optim* 2010;41. <https://doi.org/10.1007/s00158-010-0487-9>.

- [209] Rozvany GIN. A critical review of established methods of structural topology optimization. *Struct Multidiscip Optim* 2009. <https://doi.org/10.1007/s00158-007-0217-0>.
- [210] Challis VJ. A discrete level-set topology optimization code written in Matlab. *Struct Multidiscip Optim* 2010;41:453–64. <https://doi.org/10.1007/s00158-009-0430-0>.
- [211] Woldseth Rv, Aage N, Bærentzen AJ, Sigmund O. On the use of Artificial Neural Networks in Topology Optimisation; 2022.
- [212] Groen JP, Sigmund O. Homogenization-based topology optimization for high-resolution manufacturable microstructures. *Int J Numer Methods Eng* 2018. <https://doi.org/10.1002/nme.5575>.
- [213] Jensen PDL, Sigmund O, Groen JP. De-homogenization of optimal 2D topologies for multiple loading cases. *Comput Methods Appl Mech Eng*. 2022;399:115426. <https://doi.org/10.1016/j.cma.2022.115426>.
- [214] Groen JP, Thomsen CR, Sigmund O. Multi-scale topology optimization for stiffness and de-homogenization using implicit geometry modeling. *Struct Multidiscip Optim* 2021;63. <https://doi.org/10.1007/s00158-021-02874-7>.
- [215] Bendsoe MP, Kikuchi N. Generating optimal topologies in structural design using a homogenization method. *Comput Methods Appl Mech Eng*. 1988;71:197–224.
- [216] Suzuki K, Kikuchi N. A homogenization method for shape and topology optimization. *Comput Methods Appl Mech Eng*. 1991;93. [https://doi.org/10.1016/0045-7825\(91\)90245-2](https://doi.org/10.1016/0045-7825(91)90245-2).
- [217] Olhoff N, Lurie KA, Cherkav AV, Fedorov AV. Sliding regimes and anisotropy in optimal design of vibrating axisymmetric plates. *Int J Solids Struct*. 1981;17. [https://doi.org/10.1016/0020-7683\(81\)90032-9](https://doi.org/10.1016/0020-7683(81)90032-9).
- [218] Cherkav AV. Exact estimates of the conductivity of a binary mixture of isotropic materials. *Proc Roy Soc Edinburgh: Section A Math* 1986; 104. <https://doi.org/10.1017/S0308210500019041>.
- [219] Cherkav AV, Gibiansky LV. Coupled estimates for the bulk and shear moduli of a two-dimensional isotropic elastic composite. *J Mech Phys Solids*. 1993;41. [https://doi.org/10.1016/0022-5096\(93\)90006-2](https://doi.org/10.1016/0022-5096(93)90006-2).
- [220] Cherkav AV, Gibiansky LV. Variational principles for complex conductivity, viscoelasticity, and similar problems in media with complex moduli. *J Math Phys*. 1994;35. <https://doi.org/10.1063/1.530782>.
- [221] Avellaneda M, Milton GW. Bounds on the effective elasticity tensor of composites based on two-point correlations. In: American Society of Mechanical Engineers, Petroleum Division (Publication) PD; 1988.
- [222] Lipton RP. On optimal reinforcement of plates and choice of design parameters. *Control Cybern* 1994;23.
- [223] Lipton R. Optimal design and relaxation for reinforced plates subject to random transverse loads. *Probab Eng Mech* 1994;9. [https://doi.org/10.1016/0266-8920\(94\)90002-7](https://doi.org/10.1016/0266-8920(94)90002-7).
- [224] Pantz O, Trabelsi K. Construction of minimization sequences for shape optimization. In: 2010 15th International Conference on Methods and Models in Automation and Robotics, MMAR 2010; 2010. <https://doi.org/10.1109/MMAR.2010.5587222>.
- [225] Pantz O, Trabelsi K. A Post-treatment of the homogenization method for shape optimization. *SIAM J Control Optim*. 2008;47. <https://doi.org/10.1137/070688900>.
- [226] Stutz FC, Groen JP, Sigmund O, Bærentzen JA. Singularity aware de-homogenization for high-resolution topology optimized structures. *Struct Multidiscip Optim* 2020;62. <https://doi.org/10.1007/s00158-020-02681-6>.
- [227] Stutz FC, Olsen TF, Groen JP, Trung TN, Aage N, Sigmund O, et al. Synthesis of Frame Field-Aligned Multi-Laminar Structures. *ACM Trans Graph*. 2022;41. <https://doi.org/10.1145/3516522>.
- [228] Groen JP, Stutz FC, Aage N, Bærentzen JA, Sigmund O. De-homogenization of optimal multi-scale 3D topologies. *Comput Methods Appl Mech Eng*. 2020;364. <https://doi.org/10.1016/j.cma.2020.112979>.
- [229] Groen JP, Wu J, Sigmund O. Homogenization-based stiffness optimization and projection of 2D coated structures with orthotropic infill. *Comput Methods Appl Mech Eng*. 2019;349. <https://doi.org/10.1016/j.cma.2019.02.031>.
- [230] Christensen CF, Wang F, Sigmund O. Multiscale Topology Optimization Considering Local and Global Buckling Response; 2022.
- [231] Kohn RV, Strang G. Optimal design and relaxation of variational problems. *Commun Pure Appl Math*. 39 (1986) Part {I}: 1–25, {P}art {II}: 139–182, {P}art {II}. <https://doi.org/10.1002/cpa.3160390107>.
- [232] Cheng KT, Olhoff N, Cheng G, Olhoff N. An investigation concerning optimal design of solid elastic plates. *Int J Solids Struct*. 1981;17:305–23. [https://doi.org/10.1016/0020-7683\(81\)90065-2](https://doi.org/10.1016/0020-7683(81)90065-2).
- [233] Keno-Tung C, Olhoff N, Cheng G, Olhoff N. Regularized formulation for optimal design of axisymmetric plates. *Int J Solids Struct*. 1982;18:153–69. [https://doi.org/10.1016/0020-7683\(82\)90023-3](https://doi.org/10.1016/0020-7683(82)90023-3).
- [234] Sigmund O, Petersson J. Numerical instabilities in topology optimization: A survey on procedures dealing with checkerboards, mesh-dependencies and local minima. *Struct Optim* 1998;16:68–75.
- [235] Díaz A, Sigmund O. Checkerboard patterns in layout optimization. *Struct Optim* 1995;10:40–5. <https://doi.org/10.1007/BF01743693>.
- [236] Jog CS, Haber RB. Stability of finite element models for distributed-parameter optimization and topology design. *Comput Methods Appl Mech Eng*. 1996;130:203–26.
- [237] Rahmatalla SF, Swan CC. A Q4/Q4 continuum structural topology optimization implementation. *Struct Multidiscip Optim* 2004;27. <https://doi.org/10.1007/s00158-003-0365-9>.
- [238] Paulino GH, Le CH. A modified Q4/Q4 element for topology optimization. *Struct Multidiscip Optim* 2009. <https://doi.org/10.1007/s00158-008-0228-5>.
- [239] Haber RB, Jog CS, Bendsoe MP. Variable-topology shape optimization with a control on perimeter. In: American Society of Mechanical Engineers, Design Engineering Division (Publication) DE, 1994; pp. 261–272.
- [240] Haber RB, Jog C, Bendsoe MP. A new approach to variable–topology design using a constraint on the perimeter. *Struct Multidiscip Optim* 1996;11.
- [241] Ambrosio L, Buttazzo G. An optimal design problem with perimeter penalization. *Calc Var Partial Differ Equ*. 1993;1:55–69.
- [242] Petersson J. Some convergence results in perimeter–controlled topology optimization. *Comput Methods Appl Mech Eng*. 1999;171:123–40. [https://doi.org/10.1016/S0045-7825\(98\)00248-5](https://doi.org/10.1016/S0045-7825(98)00248-5).
- [243] Petersson J, Sigmund O. Slope constrained topology optimization. *Int J Numer Methods Eng*. 1998;41:1417–34.
- [244] Sigmund O. On the design of compliant mechanisms using topology optimization. *J Struct Mech* 1997;25:493–524.
- [245] Sigmund O, Maute K. Sensitivity Filtering from a Continuum Mechanics Perspective. *Struct. Multidiscip. Optim*. 2012;46:471–5.
- [246] Bruns TE, Tortorelli DA. Topology optimization of non-linear elastic structures and compliant mechanisms. *Comput Methods Appl Mech Eng*. 2001;190:3443–59. [https://doi.org/10.1016/S0045-7825\(00\)00278-4](https://doi.org/10.1016/S0045-7825(00)00278-4).
- [247] Jansen M, Lazarov BS, Schevenels M, Sigmund O. On the similarities between micro/nano lithography and topology optimization projection methods. *Struct Multidiscip Optim* 2013;48:717–30. <https://doi.org/10.1007/s00158-013-0941-6>.
- [248] Bourdin B. Filters in topology optimization. *Int J Numer Methods Eng*. 2001;50:2143–58. <https://doi.org/10.1002/nme.116>.
- [249] Lazarov BS, Sigmund O. Filters in topology optimization based on Helmholtz–type differential equations. *Int J Numer Methods Eng*. 2011;86:765–81.
- [250] Wallin M, Ivarsson N, Amir O, Tortorelli D. Consistent boundary conditions for PDE filter regularization in topology optimization. *Struct Multidiscip Optim* 2020;62:1299–311. <https://doi.org/10.1007/s00158-020-02556-w>.
- [251] Lazarov BS, Wang F, Sigmund O. Length scale and manufacturability in density-based topology optimization. *Arch Appl Mech* 2016;86:189–218. <https://doi.org/10.1007/s00419-015-1106-4>.
- [252] Hoghoj LC, Träff EA. An advection–diffusion based filter for machinable designs in topology optimization. *Comput Methods Appl Mech Eng*. 2022;391. <https://doi.org/10.1016/j.cma.2021.114488>.
- [253] Poulsen TA. Topology optimization in wavelet space. *Int J Numer Methods Eng*. 2002;53:567–82. <https://doi.org/10.1002/nme.285>.
- [254] Poulsen TA. A new scheme for imposing a minimum length scale in topology optimization. *Int J Numer Methods Eng*. 2003. <https://doi.org/10.1002/nme.694>.
- [255] Clausen A, Andreassen E. On filter boundary conditions in topology optimization. *Struct Multidiscip Optim* 2017;56:1147–55.

- [256] Sigmund O, Jensen JS. Systematic design of phononic band-gap materials and structures by topology optimization. *Philos Trans R Soc A Math Phys Eng Sci* 2003. <https://doi.org/10.1098/rsta.2003.1177>.
- [257] Yoon GH, Jensen JS, Sigmund O. Topology optimization of acoustic-structure interaction problems using a mixed finite element formulation. *Int J Numer Methods Eng*. 2007;70:1049–75. <https://doi.org/10.1002/nme.1900>.
- [258] Sigmund O. Morphology-based black and white filters for topology optimization. *Struct Multidiscip Optim* 2007;33:401–24.
- [259] Svanberg K, Svard H. Density filters for topology optimization based on the Pythagorean means. *Struct Multidiscip Optim* 2013;48:859–75. <https://doi.org/10.1007/s00158-013-0938-1>.
- [260] Hägg L, Wadbro E. Nonlinear filters in topology optimization: existence of solutions and efficient implementation for minimum compliance problems. *Struct Multidiscip Optim* 2017;55:1017–28. <https://doi.org/10.1007/s00158-016-1553-8>.
- [261] Wadbro E, Hägg L. On quasi-arithmetic mean based filters and their fast evaluation for large-scale topology optimization. *Struct Multidiscip Optim* 2015;52. <https://doi.org/10.1007/s00158-015-1273-5>.
- [262] Zhou M, Lazarov BS, Wang F, Sigmund O. Minimum length scale in topology optimization by geometric constraints. *Comput Methods Appl Mech Eng*. 2015; 293:266–82.
- [263] Guest JK, Prévost JH, Belytschko T. Achieving minimum length scale in topology optimization using nodal design variables and projection functions. *Int J Numer Methods Eng*. 2004;61:238–54. <https://doi.org/10.1002/nme.1064>.
- [264] Belytschko T, Xiao SP, Parimi C. Topology optimization with implicit functions and regularization. *Int J Numer Methods Eng*. 2003;57. <https://doi.org/10.1002/nme.824>.
- [265] Guest JK. Imposing maximum length scale in topology optimization. *Struct Multidiscip Optim* 2009;37:463–73. <https://doi.org/10.1007/s00158-008-0250-7>.
- [266] Wu J, Clausen A, Sigmund O. Minimum compliance topology optimization of shell-infill composites for additive manufacturing. *Comput Methods Appl Mech Eng*. 2017;326:358–75.
- [267] Carstensen JV, Guest JK. Projection-based two-phase minimum and maximum length scale control in topology optimization. *Struct Multidiscip Optim* 2018;58: 1845–60. <https://doi.org/10.1007/s00158-018-2066-4>.
- [268] Xu S, Cai Y, Cheng G. Volume preserving nonlinear density filter based on {H}eaviside functions. *Struct Multidiscip Optim* 2010;41:495–505.
- [269] Wang F, Lazarov BS, Sigmund O. On projection methods, convergence and robust formulations in topology optimization. *Struct Multidiscip Optim* 2011;43: 767–84.
- [270] Lazarov BS, Schevenels M, Sigmund O. Robust design of large-displacement compliant mechanisms. *Mech Sci* 2011;2:175–82. <https://doi.org/10.5194/ms-2-175-2011>.
- [271] Lazarov BS, Schevenels M, Sigmund O. Topology optimization with geometric uncertainties by perturbation techniques. *Int J Numer Methods Eng*. 2012;90: 1321–36. <https://doi.org/10.1002/nme.3361>.
- [272] Schevenels M, Lazarov BS, Sigmund O. Robust topology optimization accounting for spatially varying manufacturing errors. *Comput Methods Appl Mech Eng*. 2011;200:3613–27. <https://doi.org/10.1016/j.cma.2011.08.006>.
- [273] da Silva GA, Cardoso EL, Beck AT. Comparison of robust, reliability-based and non-probabilistic topology optimization under uncertain loads and stress constraints. *Probab Eng Mech* 2020;59:103039.
- [274] Jansen M, Lombaert G, Diehl M, Lazarov BS, Sigmund O, Schevenels M. Robust topology optimization accounting for misplacement of material. *Struct Multidiscip Optim* 2013;47:317–33. <https://doi.org/10.1007/s00158-012-0835-z>.
- [275] Yin L, Ananthasuresh GK. Design of distributed compliant mechanisms. *Mech Based Des Struct Mach* 2003;31. <https://doi.org/10.1081/SME-120020289>.
- [276] Salazar de Troya MA, Tortorelli DA. Three-dimensional adaptive mesh refinement in stress-constrained topology optimization. *Struct Multidiscip Optim* 2020; 62. <https://doi.org/10.1007/s00158-020-02618-z>.
- [277] da Silva GA, Aage N, Beck AT, Sigmund O. Three-dimensional manufacturing tolerant topology optimization with hundreds of millions of local stress constraints. *Int J Numer Methods Eng*. 2021. <https://doi.org/10.1002/nme.6548>.
- [278] Sigmund O. Some Inverse Problems in Topology Design of Materials and Mechanisms; 1996. https://doi.org/10.1007/978-94-009-0153-7_35.
- [279] Kikuchi N, Nishiwaki S, Ono Fonseca JS, Nelli Silva EC. Design optimization method for compliant mechanisms and material microstructure. *Comput Methods Appl Mech Eng*. 1998. [https://doi.org/10.1016/S0045-7825\(97\)00161-8](https://doi.org/10.1016/S0045-7825(97)00161-8).
- [280] Ananthasuresh GK, Kota S, Kikuchi N. Strategies for systematic synthesis of compliant mems. In: American Society of Mechanical Engineers, Dynamic Systems and Control Division (Publication) DSC; 1994.
- [281] Zhu B, Zhang X, Zhang H, Liang J, Zang H, Li H, et al. Design of compliant mechanisms using continuum topology optimization: A review. *Mech Mach Theory*. 2020. <https://doi.org/10.1016/j.mechmachtheory.2019.103622>.
- [282] de Leon DM, Alexandersen J, Jun JS, Sigmund O. Stress-constrained topology optimization for compliant mechanism design. *Struct Multidiscip Optim* 2015. <https://doi.org/10.1007/s00158-015-1279-z>.
- [283] Meneghelli LR, Cardoso EL. Design of Compliant Mechanisms with Stress Constraints Using Topology Optimization. *Adv Struct Mater* 2013. https://doi.org/10.1007/978-3-319-00717-5_3.
- [284] Emmendoerfer H, Fancello EA, Silva ECN. Stress-constrained level set topology optimization for compliant mechanisms. *Comput Methods Appl Mech Eng*. 2020. <https://doi.org/10.1016/j.cma.2019.112777>.
- [285] Sigmund O. Manufacturing tolerant topology optimization. *Acta Mech Sin* 2009;25:227–39. <https://doi.org/10.1007/s10409-009-0240-z>.
- [286] Nishiwaki S, Frecker MI, Min S, Kikuchi N. Topology optimization of compliant mechanisms using the homogenization method. *Int J Numer Methods Eng*. 1998;42. [https://doi.org/10.1002/\(SICI\)1097-0207\(19980615\)42:3<535::AID-NME372>3.0.CO;2-J](https://doi.org/10.1002/(SICI)1097-0207(19980615)42:3<535::AID-NME372>3.0.CO;2-J).
- [287] Frecker MI, Ananthasuresh GK, Nishiwaki S, Kikuchi N, Kota S. Topological synthesis of compliant mechanisms using multi-criteria optimization, *Journal of Mechanical Design*. *Trans ASME*. 1997;119. <https://doi.org/10.1115/1.2826242>.
- [288] Bruns TE, Sigmund O, Tortorelli DA. Numerical methods for the topology optimization of structures that exhibit snap-through. *Int J Numer Methods Eng*. 2002; 55. <https://doi.org/10.1002/nme.544>.
- [289] Sigmund O. Design of multiphysics actuators using topology optimization – Part II: Two-material structures. *Comput Methods Appl Mech Eng*. 2001;190: 6605–27. [https://doi.org/10.1016/S0045-7825\(01\)00252-3](https://doi.org/10.1016/S0045-7825(01)00252-3).
- [290] Sigmund O. Design of multiphysics actuators using topology optimization – Part I: One-material structures. *Comput Methods Appl Mech Eng*. 2001;190: 6577–604. [https://doi.org/10.1016/S0045-7825\(01\)00251-1](https://doi.org/10.1016/S0045-7825(01)00251-1).
- [291] Jain N, Saxena R. Effect of self-weight on topological optimization of static loading structures. *Alex Eng J* 2018;27:527–35.
- [292] Novotny AA, Lopes CG, Santos RB. Topological derivative-based topology optimization of structures subject to self-weight loading. *Struct Multidiscip Optim* 2021;63. <https://doi.org/10.1007/s00158-020-02780-4>.
- [293] Holmberg E, Thore CJ, Klarbring A. Worst-case topology optimization of self-weight loaded structures using semi-definite programming. *Struct Multidiscip Optim* 2015;52. <https://doi.org/10.1007/s00158-015-1285-1>.
- [294] Zhang S, Li H, Huang Y. An improved multi-objective topology optimization model based on SIMP method for continuum structures including self-weight. *Struct Multidiscip Optim* 2021;63. <https://doi.org/10.1007/s00158-020-02685-2>.
- [295] Chen BC, Kikuchi N. Topology optimization with design-dependent loads. *Finite Elem Anal Des* 2001;37:57–70.
- [296] Bruyneel M, Duysinx P. Note on topology optimization of structures including self-weight. *Struct Multidiscip Optim* 2005.
- [297] Bruyneel M, Duysinx P. Selection of approximation schemes in Topology Optimization; n.d.
- [298] Zhou M, Sigmund O. On fully stressed design and ρ^* -norm measures in structural optimization. *Struct Multidiscip Optim* 2017;56.
- [299] Giraldo-Londoño O, Paulino GH. A unified approach for topology optimization with local stress constraints considering various failure criteria: Von Mises, Drucker-Prager, Tresca, Mohr-Coulomb, Bresler- Pister and Willam-Warnke. *Proc Roy Soc A: Math, Phys Eng Sci* (2020). <https://doi.org/10.1098/rspa.2019.0861>.

- [300] Holmberg E, Torstenfelt B, Klarbring A. Stress constrained topology optimization. *Struct Multidiscip Optim* 2013. <https://doi.org/10.1007/s00158-012-0880-7>.
- [301] Duysinx P, Sigmund O. New Developments in Handling Optimal Stress Constraints in Optimal Material Distributions. In: 7th Symposium in Multidisciplinary Analysis and Optimization, AIAA/USAF/NASA/ISSMO, 1998: pp. 1501–1509.
- [302] Lee E, James KA, Martins JRRR. Stress-constrained topology optimization with design dependent loads. *Struct Multidiscip Optim* 2012.
- [303] Senhora FV, Giraldo-Londoño O, Menezes IFM, Paulino GH. Topology optimization with local stress constraints: a stress aggregation-free approach. *Struct Multidiscip Optim* 2020. <https://doi.org/10.1007/s00158-020-02573-9>.
- [304] da Silva GA, Beck AT, Sigmund O. Stress-constrained topology optimization considering uniform manufacturing uncertainties. *Comput Methods Appl Mech Eng*. 2019. <https://doi.org/10.1016/j.cma.2018.10.020>.
- [305] Giraldo-Londoño O, Paulino GH. PolyStress: a Matlab implementation for local stress-constrained topology optimization using the augmented Lagrangian method. *Struct Multidiscip Optim* 2021. <https://doi.org/10.1007/s00158-020-02760-8>.
- [306] Cheng G. Non-smoothness in optimal design of solid, elastic plates. *Int J Solids Struct*. 1981;17:795–810.
- [307] Verbart A, Langelaar M, van Keulen F. A unified aggregation and relaxation approach for stress-constrained topology optimization. *Struct Multidiscip Optim* 2017;55:663–79.
- [308] Cheng GD, Guo X. ϵ -relaxed approach in structural topology optimization. *Structural Optimization*. 1997;13. <https://doi.org/10.1007/BF01197454>.
- [309] Bruggi M. On an alternative approach to stress constraints relaxation in topology optimization. *Struct Multidiscip Optim* 2008;36:125–41. <https://doi.org/10.1007/s00158-007-0203-6>.
- [310] Buhl T, Pedersen CBW, Sigmund O. Stiffness design of geometrical nonlinear structures using topology optimization. *Struct Multidiscip Optim* 2000;19.
- [311] Klarbring A, Strömberg N. Topology optimization of hyperelastic bodies including non-zero prescribed displacements. *Struct Multidiscip Optim* 2013;47: 37–48. <https://doi.org/10.1007/s00158-012-0819-z>.
- [312] Wang F, Lazarov BS, Sigmund O, Jensen JS. Interpolation scheme for fictitious domain techniques and topology optimization of finite strain elastic problems. *Comput Methods Appl Mech Eng*. 2014;276:453–72. <https://doi.org/10.1016/j.cma.2014.03.021>.
- [313] Lahuerta RD, Simões ET, Campello EMB, Pimenta PM, Silva ECN. Toward the stabilization of the low density elements in topology optimization with large deformation. *Comput Mech*. 2013;52:779–97.
- [314] Bruns TE, Tortorelli TA. An element removal and reintroduction strategy for the topology optimization of structures and compliant mechanisms. *Int J Numer Methods Eng*. 2003;57:1413–30.
- [315] Behrou R, Lotfi R, Carstensen JV, Ferrari F, Guest JK. Revisiting element removal for density-based structural topology optimization with reintroduction by Heaviside projection. *Comput Methods Appl Mech Eng*. 2020;380:113799. <https://doi.org/10.1016/j.cma.2021.113799>.
- [316] Dalklint A, Wallin M, Tortorelli DA. Eigenfrequency constrained topology optimization of finite strain hyperelastic structures. *Struct Multidiscip Optim* 2020; 61:2577–94. <https://doi.org/10.1007/s00158-020-02557-9>.
- [317] Wu CC, Arora JS. Design sensitivity analysis of non-linear buckling load. *Comput Mech*. 1988;3:129–40.
- [318] Kemmler R, Lipka A, Ramm E. Large deformations and stability in topology optimization. *Struct Multidiscip Optim* 2005;30:459–76.
- [319] Rahmatalla S, Swan CC. Continuum topology optimization of buckling-sensitive structures. *AIAA J* 2003;41:1180–9.
- [320] Russ JB, Waisman H. A novel elastoplastic topology optimization formulation for enhanced failure resistance via local ductile failure constraints and linear buckling analysis. *Comput Methods Appl Mech Eng*. 2021. <https://doi.org/10.1016/j.cma.2020.113478>.
- [321] Reitinger R, Ramm E. Buckling and imperfection sensitivity in the optimization of shell structures. *Thin Walled Struct* 1995;23:159–77.
- [322] Lindgaard E, Dahl J. On compliance and buckling objective functions in topology optimization of snap-through problems. *Struct Multidiscip Optim* 2013;47: 409–21.
- [323] Thomsen CR, Wang F, Sigmund O. Buckling strength topology optimization of 2(D) periodic materials based on linearized bifurcation analysis. *Comput Methods Appl Mech Eng*. 2018;339:115–36.
- [324] 'Bluhm GL', 'Christensen K', 'Poulios K', 'Sigmund O. Experimental verification of a novel hierarchical lattice material with superior buckling strength. *APL Mater*. 2022;10.
- [325] Wang F, Sigmund O. 3D architected isotropic materials with tunable stiffness and buckling strength. *J Mech Phys Solids*. 2021. <https://doi.org/10.1016/j.jmps.2021.104415>.
- [326] Thompson JMT, Hunt CW. Dangers of structural optimization. *Eng Optim* 1974;1:99–110. <https://doi.org/10.1080/03052157408960580>.
- [327] Thompson JMT, Supple WJ. Erosion of optimum designs by compound branching phenomena. *J. Mech. Phys. Solids*. 1973;21:135–44.
- [328] Neves MM, Rodrigues H, Guedes JM. Generalized topology design of structures with a buckling load criterion. *Struct Optim* 1995;10:71–8.
- [329] Neves MM, Sigmund O, Bendsoe MP, Bendsoe MP. Topology optimization of periodic microstructures with a penalization of highly localized buckling modes. *Int J Numer Methods Eng*. 2002;54:809–34. <https://doi.org/10.1002/nme.449>.
- [330] Rodrigues HC, Guedes JM, Bendsoe MP. Necessary conditions for optimal design of structures with a nonsmooth eigenvalue based criterion. *Struct Optim* 1995;9:52–6.
- [331] Folgado J, Rodrigues H. Structural optimization with a non-smooth buckling load criterion. *Control Cybern* 1998;27.
- [332] Bruyneel M, Colson B, Remouchamps A. Discussion on some convergence problems in buckling optimisation. *Struct Multidiscip Optim* 2008;35:181–6.
- [333] Ferrari F, Sigmund O. Revisiting topology optimization with buckling constraints. *Struct Multidiscip Optim* 2019;59:1401–15. <https://doi.org/10.1007/s00158-019-02253-3>.
- [334] Ohsaki M, Fujisawa K, Katoh N, Kanno Y, Fujisawa N, Katoh N, et al. Semi-definite programming for topology optimization of trusses under multiple eigenvalue constraints. *Comput Methods Appl Mech Eng*. 1999;180:203–17. [https://doi.org/10.1016/S0045-7825\(99\)00056-0](https://doi.org/10.1016/S0045-7825(99)00056-0).
- [335] Ohsaki M, Ikeda K. Stability and optimization of structures: {G}eneralized sensitivity analysis. Springer; 2007.
- [336] Seyranian AP, Lund E, Olhoff N. Multiple eigenvalues in structural optimization problems. *Struct Optim* 1994;8:207–27.
- [337] Olhoff N. Multicriterion structural optimization via bound formulation and mathematical programming. *Struct Optim* 1989;1:11–7. <https://doi.org/10.1007/BF01743805>.
- [338] Gao X, Ma H. Topology optimization of continuum structures under buckling constraints. *Comput Struct*. 2015;157:142–52.
- [339] Ferrari F, Sigmund O. Towards solving large-scale topology optimization problems with buckling constraints at the cost of linear analyses. *Comput Methods Appl Mech Eng*. 2020;363:112911. <https://doi.org/10.1016/j.cma.2020.112911>.
- [340] Bian X, Feng Y. Large-scale buckling-constrained topology optimization based on assembly-free finite element analysis. *Adv Mech Eng* 2017;9:1–12.
- [341] Dunning PD, Ovtchinnikov E, Scott J, Kim A. Level-set topology optimization with many linear buckling constraints using an efficient and robust eigensolver. *Int J Numer Methods Eng* 2016.
- [342] Clausen A, Aage N, Sigmund O. Exploiting Additive Manufacturing Infill in Topology Optimization for Improved Buckling Load. *Engineering* 2016;2:250–7. <https://doi.org/10.1016/J.ENG.2016.02.006>.
- [343] Thomsen CR, Wang F, Sigmund O. Buckling strength topology optimization of 2D periodic materials based on linearized bifurcation analysis. *Comput Methods Appl Mech Eng*. 2018;339. <https://doi.org/10.1016/j.cma.2018.04.031>.
- [344] Wang F, Sigmund O. Numerical investigation of stiffness and buckling response of simple and optimized infill structures. *Struct Multidiscip Optim* 2020. <https://doi.org/10.1007/s00158-020-02525-3>.
- [345] Wang F, Sigmund O. 3D architected isotropic materials with tunable stiffness and buckling strength. *J Mech Phys Solids*. 2021;152. <https://doi.org/10.1016/j.jmps.2021.104415>.
- [346] Geymonat G, Müller S, Triantafyllidis N. Homogenization of nonlinearly elastic materials, microscopic bifurcation and macroscopic loss of rank-one convexity. *Arch Ration Mech Anal*. 1993. <https://doi.org/10.1007/BF00380256>.
- [347] Triantafyllidis N, Schnaidt WC. Comparison of microscopic and macroscopic instabilities in a class of two-dimensional periodic composites. *J Mech Phys Solids*. 1993;41:1533–65. [https://doi.org/10.1016/0022-5096\(93\)90039-I](https://doi.org/10.1016/0022-5096(93)90039-I).

- [348] Alexandersen J, Andreasen CS. A review of topology optimisation for fluid-based problems. *Fluids*. 2020. <https://doi.org/10.3390/fluids5010029>.
- [349] Dbouk T. A review about the engineering design of optimal heat transfer systems using topology optimization. *Appl Therm Eng*. 2017. <https://doi.org/10.1016/j.applthermaleng.2016.10.134>.
- [350] Zhou M, Alexandersen J, Sigmund O, Claus CB. Industrial application of topology optimization for combined conductive and convective heat transfer problems. *Struct Multidiscip Optim* 2016. <https://doi.org/10.1007/s00158-016-1433-2>.
- [351] Bejan A. Constructal-theory network of conducting paths for cooling a heat generating volume. *Int J Heat Mass Transf*. 1997;40:799–816. [https://doi.org/10.1016/0017-9310\(96\)00175-5](https://doi.org/10.1016/0017-9310(96)00175-5).
- [352] Gersborg-Hansen A, Bendsoe MP, Sigmund O. Topology optimization of heat conduction problems using the finite volume method. *Struct Multidiscip Optim* 2006. <https://doi.org/10.1007/s00158-005-0584-3>.
- [353] Marck G, Nemer M, Harion JL, Russeil S, Bougeard D. Topology optimization using the SIMP method for multiobjective conductive problems. *Numerical Heat Transfer, Part B: Fundamentals*. 2012;61:439–70. <https://doi.org/10.1080/10407790.2012.687979>.
- [354] Yan S, Wang F, Sigmund O. On the non-optimality of tree structures for heat conduction. *Int J Heat Mass Transf*. 2018;122:660–80. <https://doi.org/10.1016/j.ijheatmasstransfer.2018.01.114>.
- [355] Carstensen JV, Guest JK. Projection-based two-phase minimum and maximum length scale control in topology optimization. *Struct Multidiscip Optim* 2018;58:1845–60. <https://doi.org/10.1007/s00158-018-2066-4>.
- [356] Alexandersen J, Aage N, Andreasen CS, Sigmund O. Topology optimisation for natural convection problems. *Int J Numer Methods Fluids*. 2014;76:699–721. <https://doi.org/10.1002/fld.3954>.
- [357] Yoon GH. Topological design of heat dissipating structure with forced convective heat transfer. *J Mech Sci Technol* 2010;24:1225–33. <https://doi.org/10.1007/s12206-010-0328-1>.
- [358] Ahn SH, Cho S. Level set-based topological shape optimization of heat conduction problems considering design-dependent convection boundary, *Numerical Heat Transfer. Part B: Fundamentals*. 2010. <https://doi.org/10.1080/10407790.2010.522869>.
- [359] van Dijk NP, Yoon GH, van Keulen F, Langelaar M. A level-set based topology optimization using the element connectivity parameterization method. *Struct Multidiscip Optim* 2010. <https://doi.org/10.1007/s00158-010-0485-y>.
- [360] Bruns TE. Topology optimization of convection-dominated, steady-state heat transfer problems. *Int J Heat Mass Transf*. 2007;50:2859–73. <https://doi.org/10.1016/j.ijheatmasstransfer.2007.01.039>.
- [361] Iga A, Nishiwaki S, Izui K, Yoshimura M. Topology optimization for thermal conductors considering design-dependent effects, including heat conduction and convection. *Int J Heat Mass Transf*. 2009;52:2721–32. <https://doi.org/10.1016/j.ijheatmasstransfer.2008.12.013>.
- [362] Joo Y, Lee I, Kim SJ. Efficient three-dimensional topology optimization of heat sinks in natural convection using the shape-dependent convection model. *Int J Heat Mass Transf*. 2018;127:32–40. <https://doi.org/10.1016/j.ijheatmasstransfer.2018.08.009>.
- [363] Dede EM, Joshi SN, Zhou F. Topology Optimization, Additive Layer Manufacturing, and Experimental Testing of an Air-Cooled Heat Sink, *Journal of Mechanical Design*. Trans ASME. 2015. <https://doi.org/10.1115/1.4030989>.
- [364] Yin L, Ananthasuresh GK. A novel topology design scheme for the multi-physics problems of electro-thermally actuated compliant micromechanisms. *Sens Actuators A Phys*. 2002;97–98:599–609. [https://doi.org/10.1016/S0924-4247\(01\)00853-6](https://doi.org/10.1016/S0924-4247(01)00853-6).
- [365] Alexandersen J, Sigmund O, Aage N. Large scale three-dimensional topology optimisation of heat sinks cooled by natural convection. *Int J Heat Mass Transf*. 2016;100:876–91. <https://doi.org/10.1016/j.ijheatmasstransfer.2016.05.013>.
- [366] Marck G, Privat Y. On some shape and topology optimization problems in conductive and convective heat transfers. In: OPT-i 2014 - 1st International Conference on Engineering and Applied Sciences Optimization, Proceedings; 2014.
- [367] Asmussen J, Alexandersen J, Sigmund O, Andreasen CS. A “poor man’s” approach to topology optimization of natural convection problems. *Struct Multidiscip Optim* 2019;59:1105–24. <https://doi.org/10.1007/s00158-019-02215-9>.
- [368] Pollini N, Sigmund O, Andreasen CS, Alexandersen J. A “poor man’s” approach for high-resolution three-dimensional topology design for natural convection problems. *Adv Eng Softw* 2020;140:102736. <https://doi.org/10.1016/j.advengsoft.2019.102736>.
- [369] Lin S, Zhao L, Guest JK, Weihs TP, Liu Z. Topology Optimization of Fixed-Geometry Fluid Diodes, *Journal of Mechanical Design*. Trans ASME. 2015;137. <https://doi.org/10.1115/1.4030297>.
- [370] Dems K, Rousselet B. Sensitivity analysis for transient heat conduction in a solid body ?Part I: External boundary modification. *Struct Optim* 1999;17:36–45. <https://doi.org/10.1007/BF01197711>.
- [371] Dems K, Rousselet B. Sensitivity analysis for transient heat conduction in a solid body ?Part II: Interface modification. *Struct Optim* 1999;17:46–54. <https://doi.org/10.1007/BF01197712>.
- [372] Kang B-S, Park G-J, Arora JS. A review of optimization of structures subjected to transient loads. *Struct Multidiscip Optim* 2006;31:81–95. <https://doi.org/10.1007/s00158-005-0575-4>.
- [373] Wu S, Zhang Y, Liu S. Topology optimization for minimizing the maximum temperature of transient heat conduction structure. *Struct Multidiscip Optim* 2019;60:69–82. <https://doi.org/10.1007/s00158-019-02196-9>.
- [374] Zhuang C, Xiong Z, Ding H. Topology Optimization of the Transient Heat Conduction Problem on a Triangular Mesh. *Numer Heat Transfer, Part B: Fundamentals*. 2013;64:239–62. <https://doi.org/10.1080/10407790.2013.791785>.
- [375] Long K, Wang X, Gu X. Multi-material topology optimization for the transient heat conduction problem using a sequential quadratic programming algorithm. *Eng Optim* 2018;50:2091–107. <https://doi.org/10.1080/0305215X.2017.1417401>.
- [376] Li Q, Steven GP, Xie YM. Thermoelastic topology optimization for problems with varying temperature fields. *J Therm Stresses* 2001. <https://doi.org/10.1080/01495730151078153>.
- [377] Zhuang C, Xiong Z, Ding H. Topology optimization of transient nonlinear heat conduction using an adaptive parameterized level-set method. *Eng Optim* 2021;53:2017–39. <https://doi.org/10.1080/0305215X.2020.1843162>.
- [378] Wu S, Zhang Y, Liu S. Transient thermal dissipation efficiency based method for topology optimization of transient heat conduction structures. *Int J Heat Mass Transf*. 2021. <https://doi.org/10.1016/j.ijheatmasstransfer.2021.121004>.
- [379] Zhuang C, Xiong Z. A Global Heat Compliance Measure Based Topology Optimization for the Transient Heat Conduction Problem. *Numer Heat Transfer, Part B: Fundamentals*. 2014;65:445–71. <https://doi.org/10.1080/10407790.2013.873309>.
- [380] Hyun J, Kim HA. Level-set topology optimization for effective control of transient conductive heat response using eigenvalue. *Int J Heat Mass Transf*. 2021;176:121374. <https://doi.org/10.1016/j.ijheatmasstransfer.2021.121374>.
- [381] Zeng T, Wang H, Yang M, Alexandersen J. Topology optimization of heat sinks for instantaneous chip cooling using a transient pseudo-3D thermofluid model. *Int J Heat Mass Transf*. 2020. <https://doi.org/10.1016/j.ijheatmasstransfer.2020.119681>.
- [382] Yoon GH, Dede EM, Nomura T, Schmalenberg P. Topology optimization of time-transient heat conduction for thermo-optic silicon modulators. *Int J Heat Mass Transf*. 2020;157:119862. <https://doi.org/10.1016/j.ijheatmasstransfer.2020.119862>.
- [383] Rodrigues H, Fernandes P. A material based model for topology optimization of thermoelastic structures. *Int J Numer Methods Eng*. 1995;38:1951–65. <https://doi.org/10.1002/nme.1620381202>.
- [384] Jog C. Distributed-parameter optimization and topology design for non-linear thermoelasticity. *Comput Methods Appl Mech Eng*. 1996;132:117–34. [https://doi.org/10.1016/0045-7825\(95\)00990-6](https://doi.org/10.1016/0045-7825(95)00990-6).
- [385] Sigmund O, Torquato S. Design of materials with extreme thermal expansion using a three-phase topology optimization method. *J Mech Phys Solids*. 1997;45:1037–67.
- [386] Wang B, Yan J, Cheng G. Optimal structure design with low thermal directional expansion and high stiffness. *Eng Optim* 2011;43:581–95. <https://doi.org/10.1080/0305215X.2010.499941>.
- [387] Gao T, Zhang W. Topology optimization involving thermo-elastic stress loads. *Struct Multidiscip Optim* 2010;42:725–38. <https://doi.org/10.1007/s00158-010-0527-5>.

- [388] Matsumori T, Kawamoto A, Kondoh T. Topology optimization for thermal stress reduction in power semiconductor module. *Struct Multidiscip Optim* 2019;60: 2615–20. <https://doi.org/10.1007/s00158-019-02341-4>.
- [389] Tamijani AY. Stress and stiffness-based topology optimization of two-material thermal structures. *Comput Struct*. 2021;256:106641. <https://doi.org/10.1016/j.compstruc.2021.106641>.
- [390] Deaton JD, Grandhi RV. Stress-based design of thermal structures via topology optimization. *Struct Multidiscip Optim* 2016;53:253–70. <https://doi.org/10.1007/s00158-015-1331-z>.
- [391] Wu C, Fang J, Li Q. Multi-material topology optimization for thermal buckling criteria. *Comput Methods Appl Mech Eng*. 2019;346:1136–55. <https://doi.org/10.1016/j.cma.2018.08.015>.
- [392] Kim MS, Kim SR, Han SY, Yi BJ. Topology optimization of a PCB substrate considering mechanical constraints and heat conductivity. *J Mech Sci Technol* 2007. <https://doi.org/10.1007/BF03177462>.
- [393] Takezawa A, Yoon GH, Jeong SH, Kobashi M, Kitamura M. Structural topology optimization with strength and heat conduction constraints. *Comput Methods Appl Mech Eng*. 2014;276:341–61. <https://doi.org/10.1016/j.cma.2014.04.003>.
- [394] Kambampati S, Gray JS, Kim HA. Level set topology optimization of load carrying heat dissipation devices. In: *AIAA Aviation 2019 Forum*; 2019. <https://doi.org/10.2514/6.2019-3558>.
- [395] Leader MK, Kennedy G. Thermoelastic Topology Optimization Using Steady-State and Transient Analysis for Stress and Thermal Performance. In: *AIAA Scitech 2021 Forum, American Institute of Aeronautics and Astronautics, Reston, Virginia*; 2021. <https://doi.org/10.2514/6.2021-1895>.
- [396] Stoll HW. *Design for manufacture: An overview*. *Appl Mech Rev*. 1986;39.
- [397] Zhou M, Fleury R, Shyy YK, Thomas H, Brennan JM. Progress in topology optimization with manufacturing constraints. In: *9th AIAA/ISSMO Symposium on Multidisciplinary Analysis and Optimization*; 2002. <https://doi.org/10.2514/6.2002-5614>.
- [398] Zuo KT, Chen LP, Zhang YQ, Yang J. Manufacturing- and machining-based topology optimization. *Int J Adv Manuf Technol* 2006;27. <https://doi.org/10.1007/s00170-004-2210-8>.
- [399] Langelaar M. Topology optimization for multi-axis machining. *Comput Methods Appl Mech Eng*. 2019;351. <https://doi.org/10.1016/j.cma.2019.03.037>.
- [400] Mirzendehtel AM, Behandish M, Nelaturi S. Topology optimization with accessibility constraint for multi-axis machining. *CAD Computer Aided Design*. 2020; 122. <https://doi.org/10.1016/j.cad.2020.102825>.
- [401] Lee HY, Zhu M, Guest JK. Topology optimization considering multi-axis machining constraints using projection methods. *Comput Methods Appl Mech Eng*. 2022;390. <https://doi.org/10.1016/j.cma.2021.114464>.
- [402] Gersborg AR, Andreasen CS. An explicit parameterization for casting constraints in gradient driven topology optimization. *Struct Multidiscip Optim* 2011;44. <https://doi.org/10.1007/s00158-011-0632-0>.
- [403] Li Q, Chen W, Liu S, Fan H. Topology optimization design of cast parts based on virtual temperature method. *CAD Computer Aided Design*. 2018;94. <https://doi.org/10.1016/j.cad.2017.08.002>.
- [404] Vatanabe SL, Lippi TN, de Lima CR, Paulino GH, Silva EGN. Topology optimization with manufacturing constraints: A unified projection-based approach. *Adv Eng Softw* 2016;100. <https://doi.org/10.1016/j.advengsoft.2016.07.002>.
- [405] Liu J, Ma Y. A survey of manufacturing oriented topology optimization methods. *Adv Eng Softw* 2016;100. <https://doi.org/10.1016/j.advengsoft.2016.07.017>.
- [406] Zegard T, Paulino GH. Bridging topology optimization and additive manufacturing. *Struct Multidiscip Optim* 2016;53. <https://doi.org/10.1007/s00158-015-1274-4>.
- [407] Brackett D, Ashcroft I, Hague R. Topology optimization for additive manufacturing. In: *Proceedings of the Solid Freeform Fabrication Symposium, Austin, TX*; 2011: pp. 348–362.
- [408] Leary M, Merli L, Torti F, Mazur M, Brandt M. *Optimal topology for additive manufacture: A method for enabling additive manufacture of support-free optimal structures*. *Mater Des*. 2014;63:678–90.
- [409] Adam GAO, Zimmer D. On design for additive manufacturing: Evaluating geometrical limitations. *Rapid Prototyp J*. 2015;21. <https://doi.org/10.1108/RPJ-06-2013-0060>.
- [410] Rebaioli L, Fassi I. A review on benchmark artifacts for evaluating the geometrical performance of additive manufacturing processes. *Int J Adv Manuf Technol* 2017;93. <https://doi.org/10.1007/s00170-017-0570-0>.
- [411] Ko H, Witherell P, Lu Y, Kim S, Rosen DW. Machine learning and knowledge graph based design rule construction for additive manufacturing. *Addit Manuf*. 2021;37. <https://doi.org/10.1016/j.addma.2020.101620>.
- [412] Lazarov BS, Wang F, Sigmund O. Length scale and manufacturability in density-based topology optimization. *Arch Appl Mech* 2016;86. <https://doi.org/10.1007/s00419-015-1106-4>.
- [413] Fernández E, Ayas C, Langelaar M, Duysinx P. Topology optimisation for large-scale additive manufacturing: generating designs tailored to the deposition nozzle size. *Virtual Phys Prototyp*. 2021;16:196–220. <https://doi.org/10.1080/17452759.2021.1914893>.
- [414] Allaire G, Jouve F, Michailidis G. Thickness control in structural optimization via a level set method. *Struct Multidiscip Optim* 2016;53. <https://doi.org/10.1007/s00158-016-1453-y>.
- [415] Carstensen JV. Topology optimization with nozzle size restrictions for material extrusion-type additive manufacturing. *Struct Multidiscip Optim* 2020;62. <https://doi.org/10.1007/s00158-020-02620-5>.
- [416] Mertens R, Clijsters S, Kempen K, Kruth J-P. *Optimization of Scan Strategies in Selective Laser Melting of Aluminum Parts With Downfacing Areas*. *J Manuf Sci Eng*. 2014;136:61012.
- [417] Kranz J, Herzog D, Emmelmann C. Design guidelines for laser additive manufacturing of lightweight structures in TiAl6V4. *J Laser Appl*. 2015;27:S14001.
- [418] Jiang J, Stringer J, Xu X, Zhong RY. Investigation of printable threshold overhang angle in extrusion-based additive manufacturing for reducing support waste. *Int J Comput Integr Manuf*. 2018;31. <https://doi.org/10.1080/0951192X.2018.1466398>.
- [419] Yang T, Liu T, Liao W, Wei H, Zhang C, Chen X, et al. Effect of processing parameters on overhanging surface roughness during laser powder bed fusion of AlSi10Mg. *J Manuf Process*. 2021;61. <https://doi.org/10.1016/j.jmapro.2020.11.030>.
- [420] Allaire G, Dapogny C, Estevez R, Faure A, Michailidis G. Structural optimization under overhang constraints imposed by additive manufacturing technologies. *J Comput Phys*. 2017;351. <https://doi.org/10.1016/j.jcp.2017.09.041>.
- [421] Mezzadri F, Qian X. A second-order measure of boundary oscillations for overhang control in topology optimization. *J Comput Phys*. 2020;410. <https://doi.org/10.1016/j.jcp.2020.109365>.
- [422] Zhang K, Cheng G, Xu L. Topology optimization considering overhang constraint in additive manufacturing. *Comput Struct*. 2019;212. <https://doi.org/10.1016/j.compstruc.2018.10.011>.
- [423] Garaigordobil A, Ansola R, Fernandez de Bustos I. On preventing the dripping effect of overhang constraints in topology optimization for additive manufacturing. *Struct Multidiscip Optim* 2021;64. <https://doi.org/10.1007/s00158-021-03077-w>.
- [424] Qian X. Undercut and overhang angle control in topology optimization: a density gradient based integral approach. *Int J Numer Methods Eng*. 2017. <https://doi.org/10.1002/nme.5461>.
- [425] Guo X, Zhou J, Zhang W, Du Z, Liu C, Liu Y. Self-supporting structure design in additive manufacturing through explicit topology optimization. *Comput Methods Appl Mech Eng* 2017.
- [426] Zhou L, Sigmund O, Zhang W. Self-supporting structure design with feature-driven optimization approach for additive manufacturing. *Comput Methods Appl Mech Eng*. 2021;386. <https://doi.org/10.1016/j.cma.2021.114110>.
- [427] Gaynor AT, Guest JK. Topology optimization considering overhang constraints: Eliminating sacrificial support material in additive manufacturing through design. *Struct Multidiscip Optim* 2016;54:1157–72.
- [428] Langelaar M. Topology optimization of 3D self-supporting structures for additive manufacturing. *Addit Manuf*. 2016;12:60–70.
- [429] Hoffarth M, Gerzen N, Pedersen C. ALM Overhang Constraint in Topology Optimization for Industrial Applications. In: *Proceedings of the 12th World Congress on Structural and Multidisciplinary Optimisation, Braunschweig, Germany, 5-9 June, 2017*.

- [430] van de Ven E, Maas R, Ayas C, Langelaar M, van Keulen F. Overhang control based on front propagation in 3D topology optimization for additive manufacturing. *Comput Methods Appl Mech Eng.* 2020;369.
- [431] van de Ven E, Maas R, Ayas C, Langelaar M, van Keulen F. Overhang control in topology optimization: a comparison of continuous front propagation-based and discrete layer-by-layer overhang control. *Struct Multidiscip Optim* 2021;64. <https://doi.org/10.1007/s00158-021-02887-2>.
- [432] Delissen A, Boots E, Laro D, Kleijnen H, van Keulen F, Langelaar M. Realization and assessment of metal additive manufacturing and topology optimization for high-precision motion systems. *Addit Manuf.* 2022;58:103012.
- [433] Pellens J, Lombaert G, Lazarov B, Schevenels M. Combined length scale and overhang angle control in minimum compliance topology optimization for additive manufacturing. *Struct Multidiscip Optim* 2019;59. <https://doi.org/10.1007/s00158-018-2168-z>.
- [434] Thore CJ, Grundström HA, Torstenfelt B, Klarbring A. Penalty regulation of overhang in topology optimization for additive manufacturing. *Struct Multidiscip Optim* 2019;60. <https://doi.org/10.1007/s00158-019-02194-x>.
- [435] Allaire G, Dapogny C, Faure A, Michailidis G. Shape optimization of a layer by layer mechanical constraint for additive manufacturing. *C R Math.* 2017;355:699–717.
- [436] Liu S, Li Q, Chen W, Tong L, Cheng G. An identification method for enclosed voids restriction in manufacturability design for additive manufacturing structures. *Frontiers of Mech Eng* 2015;10:126–37.
- [437] Luo Y, Sigmund O, Li Q, Liu S. Additive manufacturing oriented topology optimization of structures with self-supported enclosed voids. *Comput Methods Appl Mech Eng.* 2020;372. <https://doi.org/10.1016/j.cma.2020.113385>.
- [438] Sabiston G, Kim IY. Void region restriction for additive manufacturing via a diffusion physics approach. *Int J Numer Methods Eng.* 2020;121. <https://doi.org/10.1002/nme.6434>.
- [439] Donoso A, Aranda E, Ruiz D. A new approach based on spectral graph theory to avoiding enclosed holes in topology optimization. *Comput Methods Appl Mech Eng.* 2022;393. <https://doi.org/10.1016/j.cma.2022.114769>.
- [440] Zhou L, Zhang W. Topology optimization method with elimination of enclosed voids. *Struct Multidiscip Optim* 2019;60. <https://doi.org/10.1007/s00158-019-02204-y>.
- [441] Gaynor AT, Johnson TE. Eliminating occluded voids in additive manufacturing design via a projection-based topology optimization scheme. *Addit Manuf.* 2020;33. <https://doi.org/10.1016/j.addma.2020.101149>.
- [442] Xiong Y, Yao S, Zhao ZL, Xie YM. A new approach to eliminating enclosed voids in topology optimization for additive manufacturing. *Addit Manuf.* 2020;32. <https://doi.org/10.1016/j.addma.2019.101006>.
- [443] van de Ven E, Ayas C, Langelaar M, Maas R, van Keulen F. Accessibility of support structures in topology optimization for additive manufacturing. *Int J Numer Methods Eng.* 2021;122. <https://doi.org/10.1002/nme.6611>.
- [444] Wang C. Simultaneous optimization of build orientation and topology for self-supported enclosed voids in additive manufacturing. *Comput Methods Appl Mech Eng.* 2022;388. <https://doi.org/10.1016/j.cma.2021.114227>.
- [445] Langelaar M. Topology optimization for additive manufacturing with controllable support structure costs. In: VII European Congress on Computational Methods in Applied Sciences and Engineering, Crete Island, Greece, 5–10 June 2016, 2016.
- [446] Mezzadri F, Bourriakov V, Qian X. Topology optimization of self-supporting support structures for additive manufacturing. *Addit Manuf.* 2018;21. <https://doi.org/10.1016/j.addma.2018.04.016>.
- [447] Liu Y, Li Z, Wei P, Chen S. Generating support structures for additive manufacturing with continuum topology optimization methods. *Rapid Prototyp J.* 2019;25. <https://doi.org/10.1108/RPJ-10-2017-0213>.
- [448] Mirzendehtel AM, Suresh K. Support structure constrained topology optimization for additive manufacturing. *Comput Aided Des* 2016;81:1–13.
- [449] Zhou M, Liu Y, Wei C. Topology optimization of easy-removal support structures for additive manufacturing. *Struct Multidiscip Optim* 2020;61. <https://doi.org/10.1007/s00158-020-02607-2>.
- [450] Mirzendehtel AM, Behandish M, Nelaturi S. Topology Optimization for Manufacturing with Accessible Support Structures. *CAD Computer Aided Design.* 2022;142. <https://doi.org/10.1016/j.cad.2021.103117>.
- [451] Langelaar M. Integrated component-support topology optimization for additive manufacturing with post-machining. *Rapid Prototyp J.* 2019;25:255–65. <https://doi.org/10.1108/RPJ-12-2017-0246>.
- [452] Liu J, To AC. Topology optimization for hybrid additive-subtractive manufacturing. *Struct Multidiscip Optim* 2017;55. <https://doi.org/10.1007/s00158-016-1565-4>.
- [453] Bhatt PM, Malhan RK, Rajendran P, Gupta SK. Building free-form thin shell parts using supportless extrusion-based additive manufacturing. *Addit Manuf.* 2020;32. <https://doi.org/10.1016/j.addma.2019.101003>.
- [454] Das P, Chandran R, Samant R, Anand S. Optimum Part Build Orientation in Additive Manufacturing for Minimizing Part Errors and Support Structures. *Procedia Manuf* 2015. <https://doi.org/10.1016/j.promfg.2015.09.041>.
- [455] Langelaar M. Combined optimization of part topology, support structure layout and build orientation for additive manufacturing. *Struct Multidiscip Optim* 2018;57. <https://doi.org/10.1007/s00158-017-1877-z>.
- [456] Wang C, Qian X. Simultaneous optimization of build orientation and topology for additive manufacturing. *Addit Manuf.* 2020;34. <https://doi.org/10.1016/j.addma.2020.101246>.
- [457] Olsen J, Kim IY. Design for additive manufacturing: 3D simultaneous topology and build orientation optimization. *Struct Multidiscip Optim* 2020;62. <https://doi.org/10.1007/s00158-020-02590-8>.
- [458] Simonelli M, Tse YY, Tuck C. Effect of the build orientation on the mechanical properties and fracture modes of SLM Ti-6Al-4V. *Mater Sci Eng A* 2014;616. <https://doi.org/10.1016/j.msea.2014.07.086>.
- [459] Yadollahi A, Shamsaei N, Thompson SM, Elwany A, Bian L. Effects of building orientation and heat treatment on fatigue behavior of selective laser melted 17–4 PH stainless steel. *Int J Fatigue.* 2017;94. <https://doi.org/10.1016/j.ijfatigue.2016.03.014>.
- [460] Zhang P, Liu J, To AC. Role of anisotropic properties on topology optimization of additive manufactured load bearing structures. *Scr Mater.* 2017;135. <https://doi.org/10.1016/j.scriptamat.2016.10.021>.
- [461] Bruggi M, Laghi V, Trombetti T. Simultaneous design of the topology and the build orientation of Wire-and-Arc Additively Manufactured structural elements. *Comput Struct.* 2021;242. <https://doi.org/10.1016/j.compstruc.2020.106370>.
- [462] Liu J, To AC. Deposition path planning-integrated structural topology optimization for 3D additive manufacturing subject to self-support constraint. *CAD Computer Aided Design.* 2017;91. <https://doi.org/10.1016/j.cad.2017.05.003>.
- [463] Mishra V, Ayas C, Langelaar M, van Keulen F. Simultaneous topology and deposition direction optimization for Wire and Arc Additive Manufacturing. *Manuf Lett.* 2022;31. <https://doi.org/10.1016/j.mfglet.2021.05.011>.
- [464] Dapogny C, Estevez R, Faure A, Michailidis G. Shape and topology optimization considering anisotropic features induced by additive manufacturing processes. *Comput Methods Appl Mech Eng.* 2019;344:626–65. <https://doi.org/10.1016/j.cma.2018.09.036>.
- [465] Liu J, To AC. Deposition path planning-integrated structural topology optimization for 3D additive manufacturing subject to self-support constraint. *CAD Computer Aided Design.* 2017;91:27–45. <https://doi.org/10.1016/j.cad.2017.05.003>.
- [466] Dávila JL, Neto PI, Noritomi PY, Coelho RT, da Silva JVL. Hybrid manufacturing: a review of the synergy between directed energy deposition and subtractive processes. *Int J Adv Manuf Technol* 2020;110. <https://doi.org/10.1007/s00170-020-06062-7>.
- [467] Bambach M, Sizova I, Sydow B, Hemes S, Meiners F. Hybrid manufacturing of components from Ti-6Al-4V by metal forming and wire-arc additive manufacturing. *J Mater Process Technol.* 2020;282. <https://doi.org/10.1016/j.jmatprotec.2020.116689>.
- [468] Grzesik W. Hybrid additive and subtractive manufacturing processes and systems: A review. *J Mach Eng* 2018;18. <https://doi.org/10.5604/01.3001.0012.7629>.
- [469] Han YS, Xu B, Zhao L, Xie YM. Topology optimization of continuum structures under hybrid additive-subtractive manufacturing constraints. *Struct Multidiscip Optim* 2019;60. <https://doi.org/10.1007/s00158-019-02334-3>.

- [470] Sommer D, Götzendorfer B, Esen C, Hellmann R. Design rules for hybrid additive manufacturing combining selective laser melting and micromilling. *Materials*. 2021;14. <https://doi.org/10.3390/ma14195753>.
- [471] Saadlaoui Y, Milan JL, Rossi JM, Chabrand P. Topology optimization and additive manufacturing: Comparison of conception methods using industrial codes. *J Manuf Syst*. 2017;43. <https://doi.org/10.1016/j.jmsy.2017.03.006>.
- [472] Cooper K, Steele P, Cheng B, Chou K. Contact-free support structures for part overhangs in powder-bed metal additive manufacturing. *Inventions*. 2018;3. <https://doi.org/10.3390/inventions3010002>.
- [473] Sames WJ, List FA, Pannala S, Dehoff RR, Babu SS. The metallurgy and processing science of metal additive manufacturing. *Int Mater Rev* 2016;61:315–60. <https://doi.org/10.1080/09506608.2015.1116649>.
- [474] Mercelis P, Kruth J. Residual stresses in selective laser sintering and selective laser melting. *Rapid Prototyp J*. 2006;12:254–65. <https://doi.org/10.1108/13552540610707013>.
- [475] Craeghs T, Clijsters S, Kruth JP, Bechmann F, Ebert MC. Detection of Process Failures in Layerwise Laser Melting with Optical Process Monitoring. In: *Phys Procedia*, Elsevier B.V., 2012. pp. 753–759. <https://doi.org/10.1016/j.phpro.2012.10.097>.
- [476] Zhou M, Liu Y, Lin Z. Topology optimization of thermal conductive support structures for laser additive manufacturing. *Comput Methods Appl Mech Eng*. 2019;353. <https://doi.org/10.1016/j.cma.2019.03.054>.
- [477] Ranjan R, Ayas C, Langelaar M, van Keulen F. Controlling local overheating in topology optimization for additive manufacturing. *Struct Multidiscip Optim* 2022;65. <https://doi.org/10.1007/s00158-022-03258-1>.
- [478] Ranjan R, Ayas C, Langelaar M, van Keulen F. Fast detection of heat accumulation in powder bed fusion using computationally efficient thermal models. *Materials*. 2020;13:1–25. <https://doi.org/10.3390/ma13204576>.
- [479] Ranjan R, Ayas C, Langelaar M, van Keulen F. Fast Detection of Heat Accumulation in Powder Bed Fusion Using Computationally Efficient Thermal Models. *Materials*. 2020;13:4576. <https://doi.org/10.3390/ma13204576>.
- [480] Ranjan R, Ayas C, Langelaar M, van Keulen F. Overheating control in additive manufacturing using a 3D topology optimization method and experimental validation. *Addit Manuf*. 2023;61. <https://doi.org/10.1016/j.addma.2022.103339>.
- [481] Ranjan R, Ayas C, Langelaar M, van Keulen F. Controlling local overheating in topology optimization for additive manufacturing. *Struct Multidiscip Optim* 2022;65:162. <https://doi.org/10.1007/s00158-022-03258-1>.
- [482] Keller N, Ploshikhin V. New method for fast predictions of residual stress and distortion of AM parts. In: 25th Annual International Solid Freeform Fabrication Symposium & #65533; An Additive Manufacturing Conference, SFF 2014; 2014.
- [483] Denlinger ER, Irwin J, Michaleris P. Thermomechanical modeling of additive manufacturing large parts, *Journal of Manufacturing Science and Engineering*. *Trans ASME*. 2014;136. <https://doi.org/10.1115/1.4028669>.
- [484] Ueda Y, Fukuda K, Nakacho K, Endo S. A New Measuring Method of Residual Stresses with the Aid of Finite Element Method and Reliability of Estimated Values. *J Soc Naval Architects Japan* 1975;1975. https://doi.org/10.2534/jjasnaoe1968.1975.138_499.
- [485] Chen Q, Taylor H, Takezawa A, Liang X, Jimenez X, Wicker R, et al. Island scanning pattern optimization for residual deformation mitigation in laser powder bed fusion via sequential inherent strain method and sensitivity analysis. *Addit Manuf*. 2021;46. <https://doi.org/10.1016/j.addma.2021.102116>.
- [486] Xu S, Huang J, Liu J, Ma Y. An Island Scanning Path-Patten Optimization for Metal Additive Manufacturing Based on Inherent Strain Method. *Comput Aided Des Appl*. 2022;19. <https://doi.org/10.14733/cadaps.2022.812-824>.
- [487] Chen Q, Liu J, Liang X, To AC. A level-set based continuous scanning path optimization method for reducing residual stress and deformation in metal additive manufacturing. *Comput Methods Appl Mech Eng*. 2020;360. <https://doi.org/10.1016/j.cma.2019.112719>.
- [488] Takezawa A, Guo H, Kobayashi R, Chen Q, To AC. Simultaneous optimization of hatching orientations and lattice density distribution for residual warpage reduction in laser powder bed fusion considering layerwise residual stress stacking. *Addit Manuf*. 2022;60. <https://doi.org/10.1016/j.addma.2022.103194>.
- [489] Amir O, Mass Y. Topology optimization for staged construction. *Struct Multidiscip Optim* 2018;57. <https://doi.org/10.1007/s00158-017-1837-7>.
- [490] Allaire G, Dapogny C, Estevez R, Faure A, Michailidis G. Structural optimization under overhang constraints imposed by additive manufacturing technologies. *J Comput Phys*. 2017;351:295–328. <https://doi.org/10.1016/j.jcp.2017.09.041>.
- [491] Amir E, Amir O. Concurrent high-resolution topology optimization of structures and their supports for additive manufacturing. *Struct Multidiscip Optim* 2021; 63:2589–612. <https://doi.org/10.1007/s00158-020-02835-6>.
- [492] Michaleris P. Modeling metal deposition in heat transfer analyses of additive manufacturing processes. *Finite Elem Anal Des* 2014;86:51–60. <https://doi.org/10.1016/j.finel.2014.04.003>.
- [493] Misiun G, van de Ven E, Langelaar M, Geijselaers H, van Keulen F, van den Boogaard T, et al. Topology Optimization for additive manufacturing with distortion constraints. *Comput Methods Appl Mech Eng*. 2021;386:114095. <https://doi.org/10.1016/j.cma.2021.114095>.
- [494] Xu S, Liu J, Ma Y. Residual stress constrained self-support topology optimization for metal additive manufacturing. *Comput Methods Appl Mech Eng*. 2022; 389. <https://doi.org/10.1016/j.cma.2021.114380>.
- [495] Bihl M, Allaire G, Betbeder-Lauque X, Bogosel B, Bordeu F, Querois J. Part and supports optimization in metal powder bed additive manufacturing using simplified process simulation. *Comput Methods Appl Mech Eng*. 2022;395. <https://doi.org/10.1016/j.cma.2022.114975>.
- [496] Munro D, Ayas C, Langelaar M, van Keulen F. On process-step parallel computability and linear superposition of mechanical responses in additive manufacturing process simulation. *Addit Manuf*. 2019;28:738–49. <https://doi.org/10.1016/j.addma.2019.06.023>.
- [497] Wildman RA, Gaynor AT. Topology optimization for reducing additive manufacturing processing distortions; 2017.
- [498] Allaire G, Jakabain L. Taking into account thermal residual stresses in topology optimization of structures built by additive manufacturing. *Math Models Methods Appl Sci* 2018;28. <https://doi.org/10.1142/S0218202518500501>.
- [499] Wang W, Munro D, Wang CCL, van Keulen F, Wu J. Space-time topology optimization for additive manufacturing. *Struct Multidiscip Optim* 2020;61. <https://doi.org/10.1007/s00158-019-02420-6>.
- [500] Wang W, van Keulen F, Wu J. Fabrication Sequence Optimization for Minimizing Distortion in Multi-Axis Additive Manufacturing - Under review; 2022.
- [501] Boissier M, Allaire G, Tournier C. Additive manufacturing scanning paths optimization using shape optimization tools. *Struct Multidiscip Optim* 2020;61: 2437–66. <https://doi.org/10.1007/s00158-020-02614-3>.
- [502] Boissier M, Allaire G, Tournier C. Concurrent shape optimization of the part and scanning path for additive manufacturing; 2021.
- [503] Jihong ZHU, Han Z, Chuang W, Lu Z, Shangqin Y, Zhang W. A review of topology optimization for additive manufacturing: Status and challenges. *Chin J Aeronaut* 2021;34:91–110.
- [504] Boissier M, Allaire G, Tournier C. Time Dependent Scanning Path Optimization for the Powder Bed Fusion Additive Manufacturing Process. *CAD Computer Aided Design*. 2022;142. <https://doi.org/10.1016/j.cad.2021.103122>.
- [505] Vibhas M, Ayas C, Langelaar M, van Keulen F. Controlling cooling rates through topology optimization for required microstructure in additive manufacturing process. In: *ASPE and Euspen Summer Topical Meeting on Advancing Precision in Additive Manufacturing*; 2022. pp. 8–12.
- [506] Turner BN, Strong R, Gold SA. A review of melt extrusion additive manufacturing processes: I. Process design and modeling. *Rapid Prototyp J*. 2014;20: 192–204. <https://doi.org/10.1108/RPJ-01-2013-0012>.
- [507] Gonzalez-Gutierrez J, Cano S, Schuschnigg S, Kukla C, Sapkota J, Holzer C. Additive manufacturing of metallic and ceramic components by the material extrusion of highly-filled polymers: A review and future perspectives. *Materials*. 2018;11. <https://doi.org/10.3390/ma11050840>.
- [508] Kun K. Reconstruction and development of a 3D printer using FDM technology. *Procedia Eng*. 2016;149:203–11. <https://doi.org/10.1016/j.proeng.2016.06.657>.
- [509] Kishore V, Hassen AA. Polymer and composites additive manufacturing: Material extrusion processes. *Elsevier Inc.*; 2021. <https://doi.org/10.1016/B978-0-12-818411-0.00021-5>.
- [510] Bos F, Wolfs R, Ahmed Z, Salet T. Additive manufacturing of concrete in construction: potentials and challenges of 3D concrete printing. *Virtual Phys Prototyp*. 2016;11:209–25. <https://doi.org/10.1080/17452759.2016.1209867>.

- [511] Chen Z, Li Z, Li J, Liu C, Lao C, Fu Y, et al. 3D printing of ceramics: A review. *J Eur Ceram Soc.* 2019;39:661–87. <https://doi.org/10.1016/j.jeurceramsoc.2018.11.013>.
- [512] Karolina Pierchala M, Kadumudi FB, Mehrali M, Zsurzsan TG, Kempen PJ, Serdeczny MP, et al. Soft Electronic Materials with Combinatorial Properties Generated via Mussel-Inspired Chemistry and Halloysite Nanotube Reinforcement. *ACS Nano* 2021;15:9531–49. <https://doi.org/10.1021/acsnano.0c09204>.
- [513] Mohamed OA, Masood SH, Bhowmik JL. Optimization of fused deposition modeling process parameters: a review of current research and future prospects. *Adv Manuf.* 2015;3:42–53. <https://doi.org/10.1007/s40436-014-0097-7>.
- [514] Bikas H, Stavropoulos P, Chryssoulouris G. Additive manufacturing methods and modeling approaches: A critical review. *Int J Adv Manuf Technol* 2016;83:389–405. <https://doi.org/10.1007/s00170-015-7576-2>.
- [515] Hebda M, McLroy C, Whiteside B, Caton-Rose F, Coates P. A method for predicting geometric characteristics of polymer deposition during fused-filament-fabrication. *Addit Manuf.* 2019;27:99–108. <https://doi.org/10.1016/j.addma.2019.02.013>.
- [516] Gleadall A, Ashcroft I, Segal J. VOLCO: A predictive model for 3D printed microarchitecture. *Addit Manuf.* 2018;21:605–18. <https://doi.org/10.1016/j.addma.2018.04.004>.
- [517] Rodrigue JF, Thomas JP, Renaud JE. Characterization of the mesostructure of fused-deposition acrylonitrile-butadiene-styrene materials. *Rapid Prototyp J.* 2000;6:175–85. <https://doi.org/10.1108/13552540010337056>.
- [518] Abbott AC, Tandon GP, Bradford RL, Koerner H, Baur JW. Process-structure-property effects on ABS bond strength in fused filament fabrication. *Addit Manuf.* 2018;19:29–38. <https://doi.org/10.1016/j.addma.2017.11.002>.
- [519] Davis CS, Hillgartner KE, Han SH, Seppala JE. Mechanical strength of welding zones produced by polymer extrusion additive manufacturing. *Addit Manuf.* 2017;16:162–6. <https://doi.org/10.1016/j.addma.2017.06.006>.
- [520] Rodrigue JF, Thomas JP, Renaud JE. Mechanical behavior of acrylonitrile butadiene styrene fused deposition materials modeling. *Rapid Prototyp J.* 2003;9:219–30. <https://doi.org/10.1108/13552540310489604>.
- [521] Go J, Schiffres SN, Stevens AG, Hart AJ. Rate limits of additive manufacturing by fused filament fabrication and guidelines for high-throughput system design. *Addit Manuf.* 2017;16:1–11. <https://doi.org/10.1016/j.addma.2017.03.007>.
- [522] Mackay ME. The importance of rheological behavior in the additive manufacturing technique material extrusion. *J Rheol (N Y N Y).* 2018;62:1549–61. <https://doi.org/10.1122/1.5037687>.
- [523] Peng F, Vogt BD, Cakmak M. Complex flow and temperature history during melt extrusion in material extrusion additive manufacturing. *Addit Manuf.* 2018;22:197–206. <https://doi.org/10.1016/j.addma.2018.05.015>.
- [524] Bakrani Balani S, Chabert F, Nassiet V, Cantarel A. Influence of printing parameters on the stability of deposited beads in fused filament fabrication of poly (lactic) acid. *Addit Manuf.* 2019;25:112–21. <https://doi.org/10.1016/j.addma.2018.10.012>.
- [525] Bellini A, Güçeri S, Bertoldi M. Liquefier dynamics in fused deposition. *J Manuf Sci Eng.* 2004;126:237–46. <https://doi.org/10.1115/1.1688377>.
- [526] Phan DD, Swain ZR, Mackay ME. Rheological and heat transfer effects in fused filament fabrication. *J Rheol (N Y N Y).* 2018;62:1097–107. <https://doi.org/10.1122/1.5022982>.
- [527] Osswald TA, Puentes J, Kattinger J. Fused filament fabrication melting model. *Addit Manuf.* 2018;22:51–9. <https://doi.org/10.1016/j.addma.2018.04.030>.
- [528] Serdeczny MP, Comminal R, Pedersen DB, Spangenberg J. Experimental and analytical study of the polymer melt flow through the hot-end in material extrusion additive manufacturing. *Addit Manuf.* 2020;32:100997. <https://doi.org/10.1016/j.addma.2019.100997>.
- [529] Ramanath HS, Chua CK, Leong KF, Shah KD. Melt flow behaviour of poly-ε-caprolactone in fused deposition modelling. *J Mater Sci Mater Med.* 2008;19:2541–50. <https://doi.org/10.1007/s10856-007-3203-6>.
- [530] Verma AF, Vishnoi P, Sukhotskiy V. Numerical Simulation of Extrusion Additive Manufacturing: Fused Deposition Modeling, *TechConnect Briefs.* (2018) 118–121.
- [531] Phan DD, Horner JS, Swain ZR, Beris AN, Mackay ME. Computational fluid dynamics simulation of the melting process in the fused filament fabrication additive manufacturing technique. *Addit Manuf.* 2020;33:101161. <https://doi.org/10.1016/j.addma.2020.101161>.
- [532] Serdeczny MP, Comminal R, Mollah MT, Pedersen DB, Spangenberg J. Numerical modeling of the polymer flow through the hot-end in filament-based material extrusion additive manufacturing. *Addit Manuf.* 2020;36:101454. <https://doi.org/10.1016/j.addma.2020.101454>.
- [533] Serdeczny MP, Comminal R, Mollah MT, Pedersen DB, Spangenberg J. Viscoelastic simulation and optimisation of the polymer flow through the hot-end during filament-based material extrusion additive manufacturing. *Virtual Phys Prototyp.* 2022;17:205–19. <https://doi.org/10.1080/17452759.2022.2028522>.
- [534] Comminal R, Hattel JH, Spangenberg J. Numerical Simulations of Planar Extrusion and Fused Filament Fabrication of Non-Newtonian Fluids. *Ann Trans Nordic Rheol Soc* 2017.
- [535] Du J, Wei Z, Wang X, Wang J, Chen Z. An improved fused deposition modeling process for forming large-size thin-walled parts. *J Mater Process Technol.* 2016;234:332–41. <https://doi.org/10.1016/j.jmatprotec.2016.04.005>.
- [536] Comminal R, Serdeczny MP, Pedersen DB, Spangenberg J. Numerical modeling of the strand deposition flow in extrusion-based additive manufacturing. *Addit Manuf.* 2018;20:68–76. <https://doi.org/10.1016/j.addma.2017.12.013>.
- [537] Comminal R, Serdeczny MP, Pedersen DB, Spangenberg J. Numerical Modeling of the Material Deposition and Contouring. 2017, 1855–1864.
- [538] Comminal R, Serdeczny MP, Pedersen DB, Spangenberg J. Motion planning and numerical simulation of material deposition at corners in extrusion additive manufacturing. *Addit Manuf.* 2019;29:100753. <https://doi.org/10.1016/j.addma.2019.06.005>.
- [539] Serdeczny MP, Comminal R, Pedersen DB, Spangenberg J. Numerical prediction of the porosity of parts fabricated with fused deposition modeling, *Solid Freeform Fabrication 2018: Proceedings of the 29th Annual International Solid Freeform Fabrication Symposium - An Additive Manufacturing Conference, SFF 2018.* (2020) 1849–1854.
- [540] Serdeczny MP, Comminal R, Pedersen DB, Spangenberg J. Numerical simulations of the mesostructure formation in material extrusion additive manufacturing. *Addit Manuf.* 2019;28:419–29. <https://doi.org/10.1016/j.addma.2019.05.024>.
- [541] Mollah MT, Comminal R, Serdeczny MP, Pedersen DB, Spangenberg J. Stability and deformations of deposited layers in material extrusion additive manufacturing. *Addit Manuf.* 2021;46. <https://doi.org/10.1016/j.addma.2021.102193>.
- [542] Seta B, Mollah MT, Kumar V, Pokkalla DK, Kim S, Hassen AA, et al. Modelling fiber orientation during additive manufacturing-compression molding processes. *Solid Freeform Fabrication.* 2022.
- [543] Mechtcherine V, Bos FP, Perrot A, da Silva WRL, Nerella VN, Fataei S, et al. Extrusion-based additive manufacturing with cement-based materials – Production steps, processes, and their underlying physics: A review. *Cem Concr Res.* 2020;132:106037. <https://doi.org/10.1016/j.cemconres.2020.106037>.
- [544] Roussel N, Spangenberg J, Wallevik J, Wolfs R. Numerical simulations of concrete processing: From standard formative casting to additive manufacturing. *Cem Concr Res.* 2020;135:106075. <https://doi.org/10.1016/j.cemconres.2020.106075>.
- [545] Mollah MT, Comminal R, Serdeczny MP, Pedersen DB, Spangenberg J. Numerical Predictions of Bottom Layer Stability in Material Extrusion Additive Manufacturing. *JOM* 2022;74:1096–101. <https://doi.org/10.1007/s11837-021-05035-9>.
- [546] Reinold J, Meschke G. Particle Finite Element Simulation of Extrusion; 2019, 428–439.
- [547] Reinold J, Meschke G. Particle Finite Element Simulation of Fresh Cement Paste – Inspired by Additive Manufacturing Techniques. *Pamm.* 2019;19:4–5. <https://doi.org/10.1002/pamm.201900198>.
- [548] Comminal R, da Silva WRL, Andersen TJ, Stang H, Spangenberg J. Influence of processing parameters on the layer geometry in 3D concrete printing: experiments and modelling. In: *RILEM International Conference on Concrete and Digital Fabrication*, n.d.: pp. 852–862.
- [549] Comminal R, Leal da Silva WR, Andersen TJ, Stang H, Spangenberg J. Modelling of 3D concrete printing based on computational fluid dynamics. *Cem Concr Res.* 2020;138:106256. <https://doi.org/10.1016/j.cemconres.2020.106256>.
- [550] Spangenberg J, da Silva WRL, Comminal R, Mollah MT, Andersen TJ, Stang H. Numerical simulation of multi-layer 3d concrete printing. *RILEM Tech Lett* 2021;6:119–23. <https://doi.org/10.21809/RILEMTECHLETT.2021.142>.
- [551] Spangenberg J, Leal da Silva WR, Mollah MT, Comminal R, Juul Andersen T, Stang H. *Integrating Reinforcement with 3D Concrete Printing: Experiments and Numerical Modelling.* Springer International Publishing; 2022. https://doi.org/10.1007/978-3-031-06116-5_56.

- [552] Kumar V, Alwekar SP, Kunc V, Cakmak E, Kishore V, Smith T, et al. High-performance molded composites using additively manufactured preforms with controlled fiber and pore morphology. *Addit Manuf.* 2021;37:101733. <https://doi.org/10.1016/j.addma.2020.101733>.
- [553] Hassen AA, Dinwiddie RB, Kim S, Tekinap HL, Kumar V, Lindahl J, et al. Anisotropic thermal behavior of extrusion-based large scale additively manufactured carbon-fiber reinforced thermoplastic structures. *Polym Compos.* 2022;43:3678–90. <https://doi.org/10.1002/pc.26645>.
- [554] Seta B, Sandberg M, Brander M, Pokkalla D, Kumar V, Spangenberg J. Controlling fiber orientation in material extrusion additive manufacturing (under review); 2022.
- [555] Heller BP, Smith DE, Jack DA. Planar deposition flow modeling of fiber filled composites in large area additive manufacturing. *Addit Manuf.* 2019;25:227–38. <https://doi.org/10.1016/j.addma.2018.10.031>.
- [556] Heller BP, Smith DE, Jack DA. Effects of extrudate swell and nozzle geometry on fiber orientation in Fused Filament Fabrication nozzle flow. *Addit Manuf.* 2016;12:252–64. <https://doi.org/10.1016/j.addma.2016.06.005>.
- [557] Wang Z, Smith DE. Rheology effects on predicted fiber orientation and elastic properties in large scale polymer composite additive manufacturing, *Journal of Composites. Science* 2018;2:1–18. <https://doi.org/10.3390/jcs2010010>.
- [558] Seta B, Mollah MT, Kumar V, Pokkalla DK, Kim S, Hassen AA. Spang, Modelling fiber orientation during additive manufacturing-compression molding processes; n.d.
- [559] Ouyang Z, Bertevas E, Wang D, Khoo BC, Férec J, Ausias G, et al. A smoothed particle hydrodynamics study of a non-isothermal and thermally anisotropic fused deposition modeling process for a fiber-filled composite. *Phys Fluids* 2020;32. <https://doi.org/10.1063/5.0004527>.
- [560] Bertevas E, Férec J, Khoo BC, Ausias G, Phan-Thien N. Smoothed particle hydrodynamics (SPH) modeling of fiber orientation in a 3D printing process. *Phys Fluids* 2018;30. <https://doi.org/10.1063/1.5047088>.
- [561] Ouyang Z, Bertevas E, Parc L, Khoo BC, Phan-Thien N, Férec J, et al. A smoothed particle hydrodynamics simulation of fiber-filled composites in a non-isothermal three-dimensional printing process. *Phys Fluids* 2019;31. <https://doi.org/10.1063/1.5130711>.
- [562] Advani SG, Tucker CL. The Use of Tensors to Describe and Predict Fiber Orientation in Short Fiber Composites. *J Rheol (N Y N Y)*. 1987;31:751–84. <https://doi.org/10.1122/1.549945>.
- [563] Jeffery GB. *The Motion of Ellipsoidal Particles Immersed, The Royal. Society* 1922;102:161–79.
- [564] Yang D, Wu K, Wan L, Sheng Y. A particle element approach for modelling the 3d printing process of fibre reinforced polymer composites. *J Manuf Mater Process* 2017;1. <https://doi.org/10.3390/jmmp1010010>.
- [565] Pagac M, Hajnys J, Ma QP, Jancar L, Jansa J, Stefek P, et al. A review of vat photopolymerization technology: Materials, applications, challenges, and future trends of 3d printing. *Polymers (Basel)*. 2021;13:1–20. <https://doi.org/10.3390/polym13040598>.
- [566] Goodner MD, Bowman CN. Development of a comprehensive free radical photopolymerization model incorporating heat and mass transfer effects in thick films. *Chem Eng Sci.* 2002;57:887–900. [https://doi.org/10.1016/S0009-2509\(01\)00287-1](https://doi.org/10.1016/S0009-2509(01)00287-1).
- [567] Moad G, Solomon DH. *The Chemistry of Radical Polymerization*; 2006.
- [568] Decker C, Jenkins AD. Kinetic Approach of $\alpha 2$ Inhibition in Ultraviolet and Laser-Induced Polymerizations. *Macromolecules* 1985;18:1241–4. <https://doi.org/10.1021/ma00148a034>.
- [569] Tang Y. *Stereolithography cure process modelling*. Georgia Institute of Technology; 2005.
- [570] Boddapati A. *Modeling Cure Depth During Photopolymerization of Multifunctional Acrylates*; 2010.
- [571] Jacobs PF. Rapid prototyping & manufacturing— Fundamentals of stereolithography. *J Manuf Syst.* 1993;12:430–3. [https://doi.org/10.1016/0278-6125\(93\)90311-g](https://doi.org/10.1016/0278-6125(93)90311-g).
- [572] Lee JH, Prud'homme RK, Aksay IA. Cure depth in photopolymerization: Experiments and theory. *J Mater Res.* 2001;16:3536–44. <https://doi.org/10.1557/JMR.2001.0485>.
- [573] Jariwala AS, Ding F, Boddapati A, Breedveld V, Grover MA, Henderson CL, et al. Modeling effects of oxygen inhibition in mask-based stereolithography. *Rapid Prototyp J.* 2011;17:168–75. <https://doi.org/10.1108/13552541111124734>.
- [574] Taki K. A simplified 2D numerical simulation of photopolymerization kinetics and oxygen diffusion-reaction for the continuous liquid interface production (CLIP) system. *Polymers (Basel)*. 2020;12. <https://doi.org/10.3390/POLYM12040875>.
- [575] Wang Q, Wang J, Zhang Y, Liu Y, Zheng J, Li Y. Multi-physics simulation and experimental study of the reaction kinetics process of oxygen inhibition zone formation in constrained-surface stereolithography process. *Addit Manuf.* 2021;47:102280. <https://doi.org/10.1016/j.addma.2021.102280>.
- [576] O'Brien AK, Bowman CN. Modeling the effect of oxygen on photopolymerization kinetics. *Macromol Theory Simul.* 2006;15:176–82. <https://doi.org/10.1002/mats.200500056>.
- [577] Wu J, Zhao Z, Hamel CM, Mu X, Kuang X, Guo Z, et al. Evolution of material properties during free radical photopolymerization. *J Mech Phys Solids.* 2018;112: 25–49. <https://doi.org/10.1016/j.jmps.2017.11.018>.
- [578] Westbeek S, Remmers JJC, van Dommelen JAW, Maalderink HH, Geers MGD. Prediction of the deformed geometry of vat photo-polymerized components using a multi-physical modeling framework. *Addit Manuf.* 2021;40:101922. <https://doi.org/10.1016/j.addma.2021.101922>.
- [579] Rehbein T, Lion A, Johlitz M, Constantinescu A. Experimental investigation and modelling of the curing behaviour of photopolymers. *Polym Test.* 2020;83: 106356. <https://doi.org/10.1016/j.polymertesting.2020.106356>.
- [580] Classens K, Hafkamp T, Westbeek S, Remmers JJC, Weiland S. Multiphysical modeling and optimal control of material properties for photopolymerization processes. *Addit Manuf.* 2021;38:101520. <https://doi.org/10.1016/j.addma.2020.101520>.
- [581] Kang HW, Park JH, Cho DW. A pixel based solidification model for projection based stereolithography technology. *Sens Actuators A Phys.* 2012;178:223–9. <https://doi.org/10.1016/j.sna.2012.01.016>.
- [582] Zhang Q, Weng S, Hamel CM, Montgomery SM, Wu J, Kuang X, et al. Design for the reduction of volume shrinkage-induced distortion in digital light processing 3D printing. *Extreme Mech Lett.* 2021;48:101403. <https://doi.org/10.1016/j.eml.2021.101403>.
- [583] Al Rashid A, Ahmed W, Khalid MY, Koç M. Vat photopolymerization of polymers and polymer composites: Processes and applications. *Addit Manuf.* 2021;47: 102279. <https://doi.org/10.1016/j.addma.2021.102279>.
- [584] Zhang F, Zhu L, Li Z, Wang S, Shi J, Tang W, et al. The recent development of vat photopolymerization: A review. *Addit Manuf.* 2021;48. <https://doi.org/10.1016/j.addma.2021.102423>.
- [585] Zhou X, Hou Y, Lin J. A review on the processing accuracy of two-photon polymerization. *ALP Adv.* 2015;5. <https://doi.org/10.1063/1.4916886>.
- [586] Gao Y, Xu L, Zhao Y, You Z, Guan Q. 3D printing preview for stereo-lithography based on photopolymerization kinetic models. *Bioact Mater.* 2020;5:798–807. <https://doi.org/10.1016/j.bioactmat.2020.05.006>.
- [587] Wang S, Ma Y, Deng Z, Zhang K, Dai S. Implementation of an elastoplastic constitutive model for 3D-printed materials fabricated by stereolithography. *Addit Manuf.* 2020;33:101104. <https://doi.org/10.1016/j.addma.2020.101104>.
- [588] Zheng Z, Eglin D, Alini M, Richards GR, Qin L, Lai Y. Visible Light-Induced 3D Bioprinting Technologies and Corresponding Bioink Materials for Tissue Engineering: A Review. *Engineering* 2021;7:966–78. <https://doi.org/10.1016/j.eng.2020.05.021>.
- [589] Tumbleston JR, Shirvanyants D, Ermoshkin N, Janusziewicz R, Johnson AR, Kelly D, et al. Continuous liquid interface production of 3D objects. *Science* 1979; 347(2015):1349–52. <https://doi.org/10.1126/science.aaa2397>.
- [590] Wang Z, Liang H, Dobrynin AV. Computer Simulations of Continuous 3-D Printing. *Macromolecules* 2017;50:7794–800. <https://doi.org/10.1021/acs.macromol.7b01719>.
- [591] Hofstätter T, Spangenberg J, Pedersen DB, Tosello G, Hansen HN. Flow characteristics of a thermoset fiber composite photopolymer resin in a vat polymerization additive manufacturing process. *AIP Conference Proceedings* 2019;2065. <https://doi.org/10.1063/1.5088257>.
- [592] Kelly B, Bhattacharya I, Shusteff M, Panas RM, Taylor HK, Spadaccini CM. Computed Axial Lithography (CAL): Toward Single Step 3D Printing of Arbitrary Geometries; 2017.
- [593] Loterie D, Delrot P, Moser C. High-resolution tomographic volumetric additive manufacturing. *Nat Commun.* 2020;11:1–6. <https://doi.org/10.1038/s41467-020-14630-4>.

- [594] Loterie D, Delrot P, Moser C. Volumetric 3D printing of elastomers by tomographic back-projections. *Research Gate* (2018) 1–11. <https://doi.org/10.13140/RG.2.2.20027.46889>.
- [595] Kelly BE, Bhattacharya I, Heidari H, Shusteff M, Spadaccini CM, Taylor HK. Volumetric additive manufacturing via tomographic reconstruction. *Science* 1979; 363(2019):1075–9. <https://doi.org/10.1126/science.aau7114>.
- [596] Rackson CM, Toombs JT, De Beer MP, Cook CC, Shusteff M, Taylor HK, et al. Latent image volumetric additive manufacturing. *Opt Lett*. 2022;47:1279. <https://doi.org/10.1364/ol.449220>.
- [597] Regehly M, Garmshausen Y, Reuter M, König NF, Israel E, Kelly DP, et al. Xolography for linear volumetric 3D printing. *Nature* 2020;588:620–4. <https://doi.org/10.1038/s41586-020-3029-7>.
- [598] Shusteff M, Browar AEM, Kelly BE, Henriksson J, Weisgraber TH, Panas RM, et al. One-step volumetric additive manufacturing of complex polymer structures. *Sci Adv*. 2017;3. <https://doi.org/10.1126/sciadv.aao5496>.
- [599] Salajeghe R, Meile DH, Kruse CS, Marla D, Spangenberg J. Numerical modeling of part sedimentation during volumetric additive manufacturing; n.d.
- [600] Salajeghe R, Kruse CS, Meile DH, Marla D, Spangenberg J. Investigating the influence of thermal and mechanical properties of resin on the sedimentation rate of the printed geometry in the volumetric additive manufacturing technique. In: *Solid Freeform Fabrication 2021*; n.d.
- [601] Zhang Y, Jarosinski W, Jung YG, Zhang J. Additive manufacturing processes and equipment. In: *Additive Manufacturing: Materials, Processes, Quantifications and Applications*. Elsevier; 2018: pp. 39–51. <https://doi.org/10.1016/B978-0-12-812155-9.00002-5>.
- [602] Krathy A. Production of hard metal alloys; 1937.
- [603] Farmer Jr, Howard N. Process of rebuilding steel structures; 1970.
- [604] Housholder RF. United States Patent; 1981.
- [605] Brown Clyde O, Breinan EM, Kear BH. United States Patent; n.d.
- [606] Meiners W, Wissenbach K, Gasser A. United States Patent; 2001.
- [607] Wang F, Mei J, Wu X. Compositionally graded Ti6Al4V + TiC made by direct laser fabrication using powder and wire. *Mater Des*. 2007;28:2040–6. <https://doi.org/10.1016/j.matdes.2006.06.010>.
- [608] Syed WUH, Pinkerton AJ, Li L. Combining wire and coaxial powder feeding in laser direct metal deposition for rapid prototyping. *Appl Surf Sci*. 2006;252: 4803–8. <https://doi.org/10.1016/j.apsusc.2005.08.118>.
- [609] Zhang H, Xu J, Wang G. Fundamental study on plasma deposition manufacturing. *Surf Coat Technol*. 2003;171:112–8. [https://doi.org/10.1016/S0257-8972\(03\)00250-0](https://doi.org/10.1016/S0257-8972(03)00250-0).
- [610] Kahlen FJ, Kar A. Tensile strengths for laser-fabricated parts and similarity parameters for rapid manufacturing. *J Manuf Sci E T ASME* 2001;123:38–44. <https://doi.org/10.1115/1.1286472>.
- [611] Chen H, Yan W. Acta Materialia Spattering and denudation in laser powder bed fusion process : Multiphase flow modelling. 196 (2020) 154–167. <https://doi.org/10.1016/j.actamat.2020.06.033>.
- [612] Zinoviev A, Zinovieva O, Ploshikhin V, Romanova V, Balokhonov R. Evolution of grain structure during laser additive manufacturing. Simulation by a cellular automata method. *Mater Des*. 2016;106:321–9. <https://doi.org/10.1016/j.matdes.2016.05.125>.
- [613] Rai A, Markl M, Körner C. A coupled Cellular Automaton-Lattice Boltzmann model for grain structure simulation during additive manufacturing. *Comput Mater Sci*. 2016;124:37–48. <https://doi.org/10.1016/j.commatsci.2016.07.005>.
- [614] Sahoo S, Chou K. Phase-field simulation of microstructure evolution of Ti–6Al–4V in electron beam additive manufacturing process. *Addit Manuf*. 2016;9: 14–24. <https://doi.org/10.1016/j.addma.2015.12.005>.
- [615] Kelly SM, Kampe SL. Thermal and microstructure modeling of metal deposition processes with application to Ti–6Al–4V; 2004. <https://vtechworks.lib.vt.edu/handle/10919/29731>.
- [616] Kobryn PA, Semiatin SL. Microstructure and texture evolution during solidification processing of Ti–6Al–4V. *J Mater Process Technol*. 2003;135:330–9. [https://doi.org/10.1016/S0924-0136\(02\)00865-8](https://doi.org/10.1016/S0924-0136(02)00865-8).
- [617] Charles Murgau C, Pederson R, Lindgren LE. A model for Ti–6Al–4V microstructure evolution for arbitrary temperature changes, *Model Simul. Mat Sci Eng*. 2012;20:55006. <https://doi.org/10.1088/0965-0393/20/5/055006>.
- [618] Zinovieva O, Romanova V, Balokhonov R. Predictive Simulation of Microstructural Pattern in AM for Metals in Powder Bed Fusion. In: *Kadkhodapour J, Schmauder S, Sajadi F, editors. Quality Analysis of Additively Manufactured Metals*. Elsevier; 2022.
- [619] DebRoy T, Wei HL, Zuback JS, Mukherjee T, Elmer JW, Milewski JO, et al. Additive manufacturing of metallic components – Process, structure and properties. *Prog Mater Sci*. 2018;92:112–224. <https://doi.org/10.1016/j.pmatsci.2017.10.001>.
- [620] Oliveira JP, Santos TG, Miranda RM. Revisiting fundamental welding concepts to improve additive manufacturing: From theory to practice. *Prog Mater Sci*. 2020;107:100590. <https://doi.org/10.1016/j.pmatsci.2019.100590>.
- [621] Messler Jr RW. Weld Fusion Zone Solidification. In: *Principles of Welding*. Weinheim: WILEY-VCH Verlag GmbH & Co. KGaA; 1999. p. 373–453. <https://doi.org/10.1002/9783527617487.ch13>.
- [622] Gunasegaram DR, Steinbach I. Modelling of microstructure formation in metal additive manufacturing: recent progress, research gaps and perspectives. *Metals (Basel)*. 2021;11:1425. <https://www.mdpi.com/2075-4701/11/9/1425>.
- [623] Körner C, Markl M, Koepf JA. Modeling and simulation of microstructure evolution for additive manufacturing of metals: a critical review. *Metall Mater Trans A* 2020;51:4970–83. <https://doi.org/10.1007/s11661-020-05946-3>.
- [624] Tan JHK, Sing SL, Yeong WY. Microstructure modelling for metallic additive manufacturing: a review. *Virtual Phys Prototyp*. 2020;15:87–105. <https://doi.org/10.1080/17452759.2019.1677345>.
- [625] Stefanescu DM. *Science and Engineering of Casting Solidification*. 3rd ed., Springer Cham; 2015.
- [626] Raabe D. *Computational Materials Science: the Simulation of Materials, Microstructures and Properties*. Wiley-VCH, Weinheim; New York; Chichester; Brisbane; Singapore; Toronto, 1998.
- [627] Kergafner A, Mergheim J, Steinmann P. Modeling of additively manufactured materials using gradient-enhanced crystal plasticity. *Comput Math Appl* 2019; 78:2338–50. <https://doi.org/10.1016/j.camwa.2018.05.016>.
- [628] Romanova V, Zinovieva O, Balokhonov R, Dymnich E, Moskvichev E, Filippov A, et al. Effects of the grain shape and crystallographic texture on the grain-scale mechanical behavior of additively manufactured aluminum alloys. *Addit Manuf*. 2021;48:102415. <https://doi.org/10.1016/j.addma.2021.102415>.
- [629] Vajragupta N, Ahmed S, Boeff M, Ma A, Hartmaier A. Micromechanical modeling approach to derive the yield surface for BCC and FCC steels using statistically informed microstructure models and nonlocal crystal plasticity. *Phys Mesomech* 2017;20:343–52. <https://doi.org/10.1134/S1029959917030109>.
- [630] Romanova V, Balokhonov R, Emelianova E, Zinovieva O, Zinoviev A. Microstructure-based simulations of quasistatic deformation using an explicit dynamic approach, *Facta Universitatis, Series. Mech Eng* 2019;17:243–54. <https://doi.org/10.22190/FUME190403028R>.
- [631] Romanova V, Zinovieva O, Balokhonov R, Zinoviev A, Ploshikhin V, Emelianova E, et al. Modeling of 3D microstructures produced by additive manufacturing. *AIP Conf Proc* 2018;2051:20256. <https://doi.org/10.1063/1.5083499>.
- [632] Wang YM, Voisin T, McKeown JT, Ye J, Calta NP, Li Z, et al. Additively manufactured hierarchical stainless steels with high strength and ductility. *Nat Mater*. 2018;17:63–71. <https://doi.org/10.1038/nmat5021>.
- [633] Wang F, Williams S, Rush M. Morphology investigation on direct current pulsed gas tungsten arc welded additive layer manufactured Ti6Al4V alloy. *Int J Adv Manuf Technol* 2011;57:597–603. <https://doi.org/10.1007/s00170-011-3299-1>.
- [634] Osipovich K, Vorontsov A, Chumaevskii A, Moskvichev E, Zakharevich I, Dobrovolsky A, et al. Features of microstructure and texture formation of large-sized blocks of C11000 copper produced by electron beam wire-feed additive technology. *Materials*. 2022;15:814. <https://www.mdpi.com/1996-1944/15/3/814>.
- [635] Rosenthal I, Stern A, Frage N. Microstructure and mechanical properties of AlSi10Mg parts produced by the laser beam additive manufacturing (AM) technology. *Metallogr, Microstruct, Anal* 2014;3:448–53. <https://doi.org/10.1007/s13632-014-0168-y>.
- [636] Yan Q, Song B, Shi Y. Comparative study of performance comparison of AlSi10Mg alloy prepared by selective laser melting and casting. *J Mater Sci Technol*. 2020;41:199–208. <https://doi.org/10.1016/j.jmst.2019.08.049>.

- [637] Casati R, Lemke J, Vedani M. Microstructure and fracture behavior of 316L austenitic stainless steel produced by selective laser melting. *J Mater Sci Technol*. 2016;32:738–44. <https://doi.org/10.1016/j.jmst.2016.06.016>.
- [638] Garibaldi M, Ashcroft I, Simonelli M, Hague R. Metallurgy of high-silicon steel parts produced using Selective Laser Melting. *Acta Mater*. 2016;110:207–16. <https://doi.org/10.1016/j.actamat.2016.03.037>.
- [639] Raghavan N, Stump BC, Fernandez-Zelaia P, Kirka MM, Simunovic S. Influence of geometry on columnar to equiaxed transition during electron beam powder bed fusion of IN718. *Addit Manuf*. 2021;47:102209. <https://doi.org/10.1016/j.addma.2021.102209>.
- [640] Fernandez-Zelaia P, Kirka MM, Dryepondt SN, Gussev MN. Crystallographic texture control in electron beam additive manufacturing via conductive manipulation. *Mater Des*. 2020;195:109010. <https://doi.org/10.1016/j.matdes.2020.109010>.
- [641] Koepf JA, Gotterbarm MR, Markl M, Körner C. 3D multi-layer grain structure simulation of powder bed fusion additive manufacturing. *Acta Mater*. 2018;152:119–26. <https://doi.org/10.1016/j.actamat.2018.04.030>.
- [642] Andreau O, Koutiri I, Peyre P, Penot J-D, Sainnier N, Pessard E, et al. Texture control of 316L parts by modulation of the melt pool morphology in selective laser melting. *J Mater Process Technol*. 2019;264:21–31. <https://doi.org/10.1016/j.jmatprotec.2018.08.049>.
- [643] Zinovieva O, Romanova V, Balokhonov R. Effects of scanning pattern on the grain structure and elastic properties of additively manufactured 316L austenitic stainless steel. *Mater Sci Eng A* 2022;832:142447. <https://doi.org/10.1016/j.msea.2021.142447>.
- [644] Marattukulam JJ, Karlsson D, Pacheco V, Beran P, Wiklund U, et al. The effect of laser scanning strategies on texture, mechanical properties, and site-specific grain orientation in selective laser melted 316L SS. *Mater Des*. 2020;193:108852. <https://doi.org/10.1016/j.matdes.2020.108852>.
- [645] Gokcekaya O, Ishimoto T, Hibino S, Yasutomi J, Narushima T, Nakano T. Unique crystallographic texture formation in Inconel 718 by laser powder bed fusion and its effect on mechanical anisotropy. *Acta Mater*. 2021;212:116876. <https://doi.org/10.1016/j.actamat.2021.116876>.
- [646] Hibino S, Todo T, Ishimoto T, Gokcekaya O, Koizumi Y, Igashira K, et al. Control of crystallographic texture and mechanical properties of Hastelloy-X via laser powder bed fusion. *Crystals* (Basel). 2021;11. <https://doi.org/10.3390/cryst11091064>.
- [647] Pauza JG, Tayon WA, Rollett AD. Computer simulation of microstructure development in powder-bed additive manufacturing with crystallographic texture. *Model Simul Mat Sci Eng*. 2021;29:55019. <https://doi.org/10.1088/1361-651x/ac03a6>.
- [648] Piglione A, Dovgvy B, Liu C, Gourlay CM, Hooper PA, Pham MS. Printability and microstructure of the CoCrFeMnNi high-entropy alloy fabricated by laser powder bed fusion. *Mater Lett*. 2018;224:22–5. <https://doi.org/10.1016/j.matlet.2018.04.052>.
- [649] Bahshwan M, Gee M, Nunn J, Myant CW, Reddyhoff T. In situ observation of anisotropic tribological contact evolution in 316L steel formed by selective laser melting. *Wear* 2022;490–491:204193. <https://doi.org/10.1016/j.wear.2021.204193>.
- [650] Guldberg S, Ryum N. Microstructure and crystallographic orientation relationship in directionally solidified Mg–Mg17Al12-eutectic. *Mater Sci Eng A* 2000;289:143–50. [https://doi.org/10.1016/S0921-5093\(00\)00945-X](https://doi.org/10.1016/S0921-5093(00)00945-X).
- [651] Rappaz M, Gandin CA. Probabilistic modelling of microstructure formation in solidification processes. *Acta Metall Mater* 1993;41:345–60. [https://doi.org/10.1016/0956-7151\(93\)90065-Z](https://doi.org/10.1016/0956-7151(93)90065-Z).
- [652] Lampman S. *Weld Integrity and Performance*. ASM International; 1997.
- [653] Zinovieva O, Zinoviev A, Romanova V, Balokhonov R. Three-dimensional analysis of grain structure and texture of additively manufactured 316L austenitic stainless steel. *Addit Manuf*. 2020;36:101521. <https://doi.org/10.1016/j.addma.2020.101521>.
- [654] Dinda G, Dasgupta A, Mazumder J. Texture control during laser deposition of nickel-based superalloy. *Scr Mater*. 2012;67:503–6.
- [655] Sofinowski KA, Raman S, Wang X, Gaskey B, Seita M. Layer-wise engineering of grain orientation (LEGO) in laser powder bed fusion of stainless steel 316L. *Addit Manuf*. 2021;38:101809. <https://doi.org/10.1016/j.addma.2020.101809>.
- [656] Baumard A, Ayrault D, Fandeur O, Bordreuil C, Deschaux-Beaume F. Numerical prediction of grain structure formation during laser powder bed fusion of 316 L stainless steel. *Mater Des*. 2021;199:109434. <https://doi.org/10.1016/j.matdes.2020.109434>.
- [657] Koepf JA, Soldner D, Ramsperger M, Mergheim J, Markl M, Körner C. Numerical microstructure prediction by a coupled finite element cellular automaton model for selective electron beam melting. *Comput Mater Sci*. 2019;162:148–55. <https://doi.org/10.1016/j.commatsci.2019.03.004>.
- [658] Rai A, Helmer H, Körner C. Simulation of grain structure evolution during powder bed based additive manufacturing. *Addit Manuf*. 2017;13:124–34. <https://doi.org/10.1016/j.addma.2016.10.007>.
- [659] Antonyssamy AA, Meyer J, Prangnell PB. Effect of build geometry on the β -grain structure and texture in additive manufacture of Ti6Al4V by selective electron beam melting. *Mater Charact*. 2013;84:153–68. <https://doi.org/10.1016/j.matchar.2013.07.012>.
- [660] Pham M-S, Dovgvy B, Hooper PA, Gourlay CM, Piglione A. The role of side-branching in microstructure development in laser powder-bed fusion. *Nat Commun*. 2020;11:749. <https://doi.org/10.1038/s41467-020-14453-3>.
- [661] Birmingham M, StJohn D, Easton M, Yuan L, Dargusch M. Revealing the mechanisms of grain nucleation and formation during additive manufacturing. *JOM* 2020;72:1065–73. <https://doi.org/10.1007/s11837-020-04019-5>.
- [662] Davis AE, Breheny CI, Fellowes J, Nwankpa U, Martina F, Ding J, et al. Mechanical performance and microstructural characterisation of titanium alloy-alloy composites built by wire-arc additive manufacture. *Mater Sci Eng A* 2019;765:138289. <https://doi.org/10.1016/j.msea.2019.138289>.
- [663] Birmingham MJ, McDonald SD, Dargusch MS, StJohn DH. Grain-refinement mechanisms in titanium alloys. *J Mater Res*. 2008;23:97–104. <https://doi.org/10.1557/JMR.2008.0002>.
- [664] Zinovieva O, Zinoviev A, Ploshikhin V. Three-dimensional modeling of the microstructure evolution during metal additive manufacturing. *Comput Mater Sci*. 2018;141:207–20. <https://doi.org/10.1016/j.commatsci.2017.09.018>.
- [665] Song J, Chew Y, Bi G, Yao X, Zhang B, Bai J, et al. Numerical and experimental study of laser aided additive manufacturing for melt-pool profile and grain orientation analysis. *Mater Des*. 2018;137:286–97. <https://doi.org/10.1016/j.matdes.2017.10.033>.
- [666] Panwisawas C, Qiu C, Anderson MJ, Sovani Y, Turner RP, Attallah MM, et al. Mesoscale modelling of selective laser melting: Thermal fluid dynamics and microstructural evolution. *Comput Mater Sci*. 2017;126:479–90. <https://doi.org/10.1016/j.commatsci.2016.10.011>.
- [667] Liu S, Shin YC. Integrated 2D cellular automata-phase field modeling of solidification and microstructure evolution during additive manufacturing of Ti6Al4V. *Comput Mater Sci*. 2020;183:109889. <https://doi.org/10.1016/j.commatsci.2020.109889>.
- [668] Sun W, Shan F, Zong N, Dong H, Jing T. Simulation of solidified β grain for Ti–6Al–4V during wire laser additive manufacturing by three-dimensional cellular automaton method. *Model Simul Mat Sci Eng*. 2021;29:65006. <https://doi.org/10.1088/1361-651x/ac0c23>.
- [669] Chen S, Xu Y, Jiao Y. A hybrid finite-element and cellular-automaton framework for modeling 3D microstructure of Ti–6Al–4V alloy during solid–solid phase transformation in additive manufacturing. *Model Simul Mat Sci Eng*. 2018;26:45011. <https://doi.org/10.1088/1361-651x/aaabcd>.
- [670] Liu S, Shin YC. Prediction of 3D microstructure and phase distributions of Ti6Al4V built by the directed energy deposition process via combined multi-physics models. *Addit Manuf*. 2020;34:101234. <https://doi.org/10.1016/j.addma.2020.101234>.
- [671] Wei HL, Elmer JW, DebRoy T. Three-dimensional modeling of grain structure evolution during welding of an aluminum alloy. *Acta Mater*. 2017;126:413–25. <https://doi.org/10.1016/j.actamat.2016.12.073>.
- [672] Britt C, Montgomery CJ, Brand MJ, Liu Z-K, Carpenter JS, Beese AM. Effect of processing parameters and strut dimensions on the microstructures and hardness of stainless steel 316L lattice-emulating structures made by powder bed fusion. *Addit Manuf*. 2021;40:101943. <https://doi.org/10.1016/j.addma.2021.101943>.
- [673] Schmidtke K, Palm F, Hawkins A, Emmelmann C. Process and mechanical properties: applicability of a scandium modified Al-alloy for laser additive manufacturing. *Phys Procedia*. 2011;12:369–74. <https://doi.org/10.1016/j.phpro.2011.03.047>.
- [674] Croteau JR, Griffiths S, Rossell MD, Leinenbach C, Kenel C, Jansen V, et al. Microstructure and mechanical properties of Al–Mg–Zr alloys processed by selective laser melting. *Acta Mater*. 2018;153:35–44. <https://doi.org/10.1016/j.actamat.2018.04.053>.
- [675] von Neumann J. The general and logical theory of automata, *Cerebral Mechanisms in Behavior; the Hixon Symposium*; 1951, 1–41.
- [676] Ulam S. Random processes and transformations. In: *International Congress of Mathematicians*, Amer. Math. Soc., Cambridge, Mass., 1950: pp. 264–275.
- [677] A.W. (Ed.) Burks, *Essays on cellular automata*, Univ. of Illinois Press, Urbana; 1970.

- [678] Hesselbarth HW, Göbel IR. Simulation of recrystallization by cellular automata. *Acta Metall Mater* 1991;39:2135–43. [https://doi.org/10.1016/0956-7151\(91\)90183-2](https://doi.org/10.1016/0956-7151(91)90183-2).
- [679] Shuping H, Weimin Z, Fuzhan R. Progress in the micro-modeling of the casting solidification process. *J Mater Process Technol.* 2002;123:361–70. [https://doi.org/10.1016/S0924-0136\(02\)00074-2](https://doi.org/10.1016/S0924-0136(02)00074-2).
- [680] Liu B, Xu Q. Advances on microstructure modeling of solidification process of shape casting. *Tsinghua. Sci Technol.* 2004;9:497–505.
- [681] Rappaz M, Gandin CA, Desbiolles JL, Thévoz P. Prediction of grain structures in various solidification processes. *Metall Mater Trans A* 1996;27:695–705. <https://doi.org/10.1007/BF02648956>.
- [682] Wang L, Fang G, Qian L. Modeling of dynamic recrystallization of magnesium alloy using cellular automata considering initial topology of grains. *Mater Sci Eng A* 2018;711:268–83. <https://doi.org/10.1016/j.msea.2017.11.024>.
- [683] Zinovieva O, Zinoviev A, Ploshikhin V, Romanova V, Balokhonov R. A solution to the problem of the mesh anisotropy in cellular automata simulations of grain growth. *Comput Mater Sci.* 2015;108:168–76. <https://doi.org/10.1016/j.commatsci.2015.06.026>.
- [684] Pavlyk V, Dilthey U. Numerical Simulation of Solidification Structures during Fusion Welding. In: Raabe D, Roters F, Barlat F, Chen L-Q, editors. *Continuum Scale Simulation of Engineering Materials*. WILEY-VCH Verlag GmbH & Co. KGaA; 2004. p. 727–43.
- [685] Shi R, Khairallah SA, Roehling TT, Heo TW, McKeown JT, Matthews MJ. Microstructural control in metal laser powder bed fusion additive manufacturing using laser beam shaping strategy. *Acta Mater.* 2020;184:284–305. <https://doi.org/10.1016/j.actamat.2019.11.053>.
- [686] Chen S, Guillemot G, Gandin C-A. Three-dimensional cellular automaton-finite element modeling of solidification grain structures for arc-welding processes. *Acta Mater.* 2016;115:448–67. <https://doi.org/10.1016/j.actamat.2016.05.011>.
- [687] Oldfield W. A quantitative approach to casting solidification: freezing of cast iron. *Trans Am Soc Metals* 1966;59:945–59.
- [688] Thévoz P. Modélisation de la solidification dendritique équiaxe; 1988. <https://doi.org/10.5075/epfl-thesis-765>.
- [689] Thévoz P, Desbiolles JL, Rappaz M. Modeling of equiaxed microstructure formation in casting. *Metall Trans A* 1989;20:311–22. <https://doi.org/10.1007/BF02670257>.
- [690] Rappaz M. Modelling of microstructure formation in solidification processes. *Int Mater Rev* 1989;34:93–124. <https://doi.org/10.1179/imr.1989.34.1.93>.
- [691] Dezfoli ARA, Hwang W-S, Huang W-C, Tsai T-W. Determination and controlling of grain structure of metals after laser incidence: Theoretical approach. *Sci Rep.* 2017;7:41527. <https://doi.org/10.1038/srep41527>.
- [692] Lopez-Botello O, Martinez-Hernandez U, Ramirez J, Pinna C, Mumtaz K. Two-dimensional simulation of grain structure growth within selective laser melted AA-2024. *Mater Des.* 2017;113:369–76. <https://doi.org/10.1016/j.matdes.2016.11.031>.
- [693] Rolchigo MR, LeSar R. Application of alloy solidification theory to cellular automata modeling of near-rapid constrained solidification. *Comput Mater Sci.* 2019;163:148–61. <https://doi.org/10.1016/j.commatsci.2019.03.012>.
- [694] Lian Y, Lin S, Yan W, Liu WK, Wagner GJ. A parallelized three-dimensional cellular automaton model for grain growth during additive manufacturing. *Comput Mech.* 2018;61:543–58. <https://doi.org/10.1007/s00466-017-1535-8>.
- [695] Zhang Y, Zhang J. Modeling of solidification microstructure evolution in laser powder bed fusion fabricated 316L stainless steel using combined computational fluid dynamics and cellular automata. *Addit Manuf.* 2019;28:750–65. <https://doi.org/10.1016/j.addma.2019.06.024>.
- [696] Nastac L. *Modeling and Simulation of Microstructure Evolution in Solidifying Alloys*. New York, New York: Springer; 2004. <https://doi.org/10.1007/b118340>.
- [697] Nastac L. 3D modeling of the solidification structure evolution of superalloys in powder bed fusion additive manufacturing processes. *Metals (Basel)*. 2021;11. <https://doi.org/10.3390/met11121995>.
- [698] Akram J, Chalavadi P, Pal D, Stucker B. Understanding grain evolution in additive manufacturing through modeling. *Addit Manuf.* 2018;21:255–68. <https://doi.org/10.1016/j.addma.2018.03.021>.
- [699] Nie P, Ojo OA, Li Z. Numerical modeling of microstructure evolution during laser additive manufacturing of a nickel-based superalloy. *Acta Mater.* 2014;77:85–95. <https://doi.org/10.1016/j.actamat.2014.05.039>.
- [700] Teferra K, Rowenhorst DJ. Optimizing the cellular automata finite element model for additive manufacturing to simulate large microstructures. *Acta Mater.* 2021;213:116930. <https://doi.org/10.1016/j.actamat.2021.116930>.
- [701] Chalmers B. *Principles of Solidification*. 1st ed. New York: Wiley; 1964.
- [702] Kurz W, Fisher DJ. Dendrite growth at the limit of stability: tip radius and spacing. *Acta Metall* 1981;29:11–20. [https://doi.org/10.1016/0001-6160\(81\)90082-1](https://doi.org/10.1016/0001-6160(81)90082-1).
- [703] Ivantsov GP. The temperature field around a spherical, cylindrical, or pointed crystal growing in a cooling solution. *Dokl. Acad. Nauk USSR.* 1947;58:567–9.
- [704] Kurz W, Giovanola B, Trivedi R. Theory of microstructural development during rapid solidification. *Acta Metall* 1986;34:823–30. [https://doi.org/10.1016/0001-6160\(86\)90056-8](https://doi.org/10.1016/0001-6160(86)90056-8).
- [705] Lipton J, Kurz W, Trivedi R. Rapid dendrite growth in undercooled alloys. *Acta Metall* 1987;35:957–64. [https://doi.org/10.1016/0001-6160\(87\)90174-X](https://doi.org/10.1016/0001-6160(87)90174-X).
- [706] Mohebbi MS, Ploshikhin V. Implementation of nucleation in cellular automaton simulation of microstructural evolution during additive manufacturing of Al alloys. *Addit Manuf.* 2020;36:101726. <https://doi.org/10.1016/j.addma.2020.101726>.
- [707] Yang J, Yu H, Yang H, Li F, Wang Z, Zeng X. Prediction of microstructure in selective laser melted Ti6Al4V alloy by cellular automaton. *J Alloys Compd.* 2018;748:281–90. <https://doi.org/10.1016/j.jallcom.2018.03.116>.
- [708] Gandin CA, Rappaz M. A 3D Cellular Automaton algorithm for the prediction of dendritic grain growth. *Acta Mater.* 1997;45:2187–95. [https://doi.org/10.1016/S1359-6454\(96\)00303-5](https://doi.org/10.1016/S1359-6454(96)00303-5).
- [709] Wang W, Lee PD, McLean M. A model of solidification microstructures in nickel-based superalloys: predicting primary dendrite spacing selection. *Acta Mater.* 2003;51:2971–87. [https://doi.org/10.1016/S1359-6454\(03\)00110-1](https://doi.org/10.1016/S1359-6454(03)00110-1).
- [710] Akamatsu S, Faivre G, Ihle T. Symmetry-broken double fingers and seaweed patterns in thin-film directional solidification of a nonfaceted cubic crystal. *Phys Rev E.* 1995;51:4751–73. <https://doi.org/10.1103/PhysRevE.51.4751>.
- [711] Wang W, Luo S, Zhu M. Dendritic growth of high carbon iron-based alloy under constrained melt flow. *Comput Mater Sci.* 2014;95:136–48. <https://doi.org/10.1016/j.commatsci.2014.07.017>.
- [712] Boettinger WJ, Coriell SR, Greer AL, Karma A, Kurz W, Rappaz M, et al. Solidification microstructures: recent developments, future directions. *Acta Mater.* 2000;48:43–70. [https://doi.org/10.1016/S1359-6454\(99\)00287-6](https://doi.org/10.1016/S1359-6454(99)00287-6).
- [713] Rolchigo MR, Mendoza MY, Samimi P, Brice DA, Martin B, Collins PC, et al. Modeling of Ti-W solidification microstructures under additive manufacturing conditions. *Metall Mater Trans A* 2017;48:3606–22. <https://doi.org/10.1007/s11661-017-4120-z>.
- [714] Rolchigo MR, LeSar R. Modeling of binary alloy solidification under conditions representative of Additive Manufacturing. *Comput Mater Sci.* 2018;150:535–45. <https://doi.org/10.1016/j.commatsci.2018.04.004>.
- [715] Metropolis N, Rosenbluth AW, Rosenbluth MN, Teller AH, Teller E. Equation of state calculations by fast computing machines. *J Chem Phys.* 1953;21:1087–92. <https://doi.org/10.1063/1.1699114>.
- [716] Anderson MP, Srolovitz DJ, Grest GS, Sahni PS. Computer simulation of grain growth—I. Kinetics. *Acta Metallurgica.* 1984;32:783–91. [https://doi.org/10.1016/0001-6160\(84\)90151-2](https://doi.org/10.1016/0001-6160(84)90151-2).
- [717] Gilmer GH. Computer models of crystal growth. *Science* 1979;208(1980):355–63. <https://doi.org/10.1126/science.208.4442.355>.
- [718] Sahni PS, Grest GS, Anderson MP, Srolovitz DJ. Kinetics of the Q-state Potts model in two dimensions. *Phys Rev Lett.* 1983;50:263–6. <https://doi.org/10.1103/PhysRevLett.50.263>.
- [719] Srolovitz DJ, Anderson MP, Sahni PS, Grest GS. Computer simulation of grain growth—II. Grain size distribution, topology, and local dynamics. *Acta Metallurgica.* 1984;32:793–802. [https://doi.org/10.1016/0001-6160\(84\)90152-4](https://doi.org/10.1016/0001-6160(84)90152-4).
- [720] Srolovitz DJ, Grest GS, Anderson MP. Computer simulation of grain growth—V. Abnormal grain growth. *Acta Metallurgica.* 1985;33:2233–47. [https://doi.org/10.1016/0001-6160\(85\)90185-3](https://doi.org/10.1016/0001-6160(85)90185-3).
- [721] Potts RB. Some generalized order-disorder transformations. *Math Proc Cambridge Philos Soc* 1952; 48: 106–109. <https://doi.org/10.1017/S0305004100027419>.

- [722] Patterson BR. Relationship between mean grain face curvature and number of faces in normal grain growth: The meaning of normalized integral mean curvature. *Acta Mater.* 2022;229:117724. <https://doi.org/10.1016/j.actamat.2022.117724>.
- [723] Xu H, Shu X, Zuo J, Yin A, Wang Y. Kinetic Monte Carlo simulation of abnormal grain growth in textured systems with anisotropic grain boundary energy and mobility. *Mater Today Commun.* 2022;30:103133. <https://doi.org/10.1016/j.mtcomm.2022.103133>.
- [724] Tavernier P, Szpunar JA. A Monte-Carlo simulation applied to the modelling of nucleation of texture. *Acta Metall Mater* 1991;39:557–67. [https://doi.org/10.1016/0956-7151\(91\)90124-J](https://doi.org/10.1016/0956-7151(91)90124-J).
- [725] Srolovitz DJ, Grest GS, Anderson MP. Computer simulation of recrystallization—I. Homogeneous nucleation and growth. *Acta Metallurgica.* 1986;34:1833–45. [https://doi.org/10.1016/0001-6160\(86\)90128-8](https://doi.org/10.1016/0001-6160(86)90128-8).
- [726] Rollett AD, Luton MJ, Srolovitz DJ. Microstructural simulation of dynamic recrystallization. *Acta Metall Mater* 1992;40:43–55. [https://doi.org/10.1016/0956-7151\(92\)90198-N](https://doi.org/10.1016/0956-7151(92)90198-N).
- [727] Yu P, Wu C, Shi L. Analysis and characterization of dynamic recrystallization and grain structure evolution in friction stir welding of aluminum plates. *Acta Mater.* 2021;207:116692. <https://doi.org/10.1016/j.actamat.2021.116692>.
- [728] Rodgers TM, Madison JD, Tikare V. Simulation of metal additive manufacturing microstructures using kinetic Monte Carlo. *Comput Mater Sci.* 2017;135:78–89. <https://doi.org/10.1016/j.commatsci.2017.03.053>.
- [729] Ouyang K, Kuang Y. Quantitative simulation study of metal additive manufacturing by kinetic Monte Carlo. *J Appl Math Phys* 2022;10:1587–601. <https://doi.org/10.4236/jamp.2022.105110>.
- [730] Zhang Z, Ge P, Li JY, Ren DX, Wu T. Monte Carlo simulations of solidification and solid-state phase transformation during directed energy deposition additive manufacturing. *Progress Additive Manuf* 2022;7:671–82. <https://doi.org/10.1007/s40964-021-00253-8>.
- [731] Sunny S, Yu H, Mathews R, Malik A, Li W. Improved grain structure prediction in metal additive manufacturing using a Dynamic Kinetic Monte Carlo framework. *Addit Manuf.* 2021;37:101649. <https://doi.org/10.1016/j.addma.2020.101649>.
- [732] Ge P, Zhang Z, Tan ZJ, Hu CP, Zhao GZ, Guo X. An integrated modeling of process-structure-property relationship in laser additive manufacturing of duplex titanium alloy. *Int J Therm Sci* 2019;140:329–43. <https://doi.org/10.1016/j.ijthermalsci.2019.03.013>.
- [733] Wei HL, Knapp GL, Mukherjee T, DebRoy T. Three-dimensional grain growth during multi-layer printing of a nickel-based alloy Inconel 718. *Addit Manuf.* 2019;25:448–59. <https://doi.org/10.1016/j.addma.2018.11.028>.
- [734] Rodgers TM, Moser D, Abdeljawad F, Jackson ODU, Carroll JD, Jared BH, et al. Simulation of powder bed metal additive manufacturing microstructures with coupled finite difference-Monte Carlo method. *Addit Manuf.* 2021;41:101953. <https://doi.org/10.1016/j.addma.2021.101953>.
- [735] Holm EA, Battaile CC. The computer simulation of microstructural evolution. *JOM* 2001;53:20–3. <https://doi.org/10.1007/s11837-001-0063-2>.
- [736] Raabe D. Scaling Monte Carlo kinetics of the Potts model using rate theory. *Acta Mater.* 2000;48:1617–28. [https://doi.org/10.1016/S1359-6454\(99\)00451-6](https://doi.org/10.1016/S1359-6454(99)00451-6).
- [737] Zöllner D. A new point of view to determine the simulation temperature for the Potts model simulation of grain growth. *Comput Mater Sci.* 2014;86:99–107. <https://doi.org/10.1016/j.commatsci.2014.01.044>.
- [738] Turnbull D. Theory of grain boundary migration rates. *JOM* 1951;3:661–5. <https://doi.org/10.1007/BF03397362>.
- [739] Limoge Y, Bocquet JL. Monte Carlo simulation in diffusion studies: Time scale problems. *Acta Metall* 1988;36:1717–22. [https://doi.org/10.1016/0001-6160\(88\)90239-8](https://doi.org/10.1016/0001-6160(88)90239-8).
- [740] Tikare V, Braginsky M, Bouvard D, Vagnon A. Numerical simulation of microstructural evolution during sintering at the mesoscale in a 3D powder compact. *Comput Mater Sci.* 2010;48:317–25. <https://doi.org/10.1016/j.commatsci.2010.01.013>.
- [741] Safran SA, Sahni PS, Grest GS. Kinetics of ordering in two dimensions. I. Model systems. *Phys Rev B.* 1983;28:2693–704. <https://doi.org/10.1103/PhysRevB.28.2693>.
- [742] Mehnert K, Klimanek P. On time scaling in Monte Carlo simulation. In: Borchers P, Bubak M, Maksymowicz A, editors. *The 8th Joint EPS-APS International Conference on Physics Computing: PC'96. Kraków, Poland: Academic Computer Centre CYFRONET; 1996. p. 57.*
- [743] Gao J, Thompson RG. Real time-temperature models for Monte Carlo simulations of normal grain growth. *Acta Mater.* 1996;44:4565–70. [https://doi.org/10.1016/1359-6454\(96\)00079-1](https://doi.org/10.1016/1359-6454(96)00079-1).
- [744] Rollett AD, Manohar P. The Monte Carlo Method. In: Raabe D, Roters F, Barlat F, Chen L-Q, editors. *Continuum Scale Simulation of Engineering Materials. WILEY-VCH Verlag GmbH & Co. KGaA; 2004. p. 77–114.*
- [745] Karma A, Rappel W-J. Phase-field method for computationally efficient modeling of solidification with arbitrary interface kinetics. *Phys Rev E.* 1996;53:R3017–20. <https://doi.org/10.1103/PhysRevE.53.R3017>.
- [746] Fix G. Phase field models for free boundary problems. In: Fasano A, Primicerio M, editors. *Free Boundary Problems: Theory and Applications. Pitman Advanced Publishing Program; 1983. p. 580–9.*
- [747] Collins JB, Levine H. Diffuse interface model of diffusion-limited crystal growth. *Phys Rev B.* 1985;31:6119–22. <https://doi.org/10.1103/PhysRevB.31.6119>.
- [748] Langer JS. Models of pattern formation in first-order phase transitions. In: *Directions in Condensed Matter Physics. World Scientific; 1986. p. 165–86.*
- [749] Chen L-Q. Phase-field models for microstructure evolution. *Annu Rev Mater Res.* 2002;32:113–40. <https://doi.org/10.1146/annurev.matsci.32.112001.132041>.
- [750] Naimark OB, Bayandin YV, Zocher MA. Collective properties of defects, multiscale plasticity, and shock induced phenomena in solids. *Phys Mesomech* 2017;20:10–30. <https://doi.org/10.1134/S1029959917010027>.
- [751] Moelans N, Blanpain B, Wollants P. An introduction to phase-field modeling of microstructure evolution. *Calphad* 2008;32:268–94. <https://doi.org/10.1016/j.calphad.2007.11.003>.
- [752] Yurkiv V, Foroozan T, Ramasubramanian A, Shahbazian-Yassar R, Mashayek F. Phase-field modeling of solid electrolyte interface (SEI) influence on Li dendritic behavior. *Electrochim Acta.* 2018;265:609–19. <https://doi.org/10.1016/j.electacta.2018.01.212>.
- [753] Karayagiz K, Johnson L, Seede R, Attari V, Zhang B, Huang X, et al. Finite interface dissipation phase field modeling of Ni–Nb under additive manufacturing conditions. *Acta Mater.* 2020;185:320–39. <https://doi.org/10.1016/j.actamat.2019.11.057>.
- [754] Sethian JA, Strain J. Crystal growth and dendritic solidification. *J Comput Phys.* 1992;98:231–53. [https://doi.org/10.1016/0021-9991\(92\)90140-T](https://doi.org/10.1016/0021-9991(92)90140-T).
- [755] Roosen AR, Taylor JE. Modeling crystal growth in a diffusion field using fully faceted interfaces. *J Comput Phys.* 1994;114:113–28. <https://doi.org/10.1006/jcph.1994.1153>.
- [756] Almgren R. Variational algorithms and pattern formation in dendritic solidification. *J Comput Phys.* 1993;106:337–54. [https://doi.org/10.1016/S0021-9991\(83\)71112-5](https://doi.org/10.1016/S0021-9991(83)71112-5).
- [757] Juric D, Tryggvason G. A front-tracking method for dendritic solidification. *J. Comput. Phys.* 1996;123:127–48. <https://doi.org/10.1006/jcph.1996.0011>.
- [758] Beckermann C, Diepers HJ, Steinbach I, Karma A, Tong X. Modeling melt convection in phase-field simulations of solidification. *J Comput Phys.* 1999;154:468–96. <https://doi.org/10.1006/jcph.1999.6323>.
- [759] Echebarria B, Folch R, Karma A, Plapp M. Quantitative phase-field model of alloy solidification. *Phys Rev E.* 2004;70:61604. <https://doi.org/10.1103/PhysRevE.70.061604>.
- [760] Chen S, Merriman B, Osher S, Smereka P. A simple level set method for solving Stefan problems. *J Comput Phys.* 1997;135:8–29. <https://doi.org/10.1006/jcph.1997.5721>.
- [761] Boettinger WJ, Warren JA, Beckermann C, Karma A. Phase-field simulation of solidification. *Annu Rev Mater Res.* 2002;32:163–94. <https://doi.org/10.1146/annurev.matsci.32.101901.155803>.
- [762] Wang X, Liu PW, Ji Y, Liu Y, Horstemeyer MH, Chen L. Investigation on microsegregation of IN718 alloy during additive manufacturing via integrated phase-field and finite-element modeling. *J Mater Eng Perform.* 2019;28:657–65. <https://doi.org/10.1007/s11665-018-3620-3>.
- [763] Gong X, Chou K. Phase-field modeling of microstructure evolution in electron beam additive manufacturing. *JOM* 2015;67:1176–82. <https://doi.org/10.1007/s11837-015-1352-5>.
- [764] Lu L-X, Sridhar N, Zhang Y-W. Phase field simulation of powder bed-based additive manufacturing. *Acta Mater.* 2018;144:801–9. <https://doi.org/10.1016/j.actamat.2017.11.033>.

- [765] Yang M, Wang L, Yan W. Phase-field modeling of grain evolutions in additive manufacturing from nucleation, growth, to coarsening. NPJ Comput Mater. 2021; 7:56. <https://doi.org/10.1038/s41524-021-00524-6>.
- [766] Mirzade FK. A coupled diffusion-deformational phase field formulation for precipitate growth during laser-aided additive manufacturing process. J Phys Conf Ser. 2018;1109:12014. <https://doi.org/10.1088/1742-6596/1109/1/012014>.
- [767] Bragard J, Karma A, Lee YH, Plapp M. Linking phase-field and atomistic simulations to model dendritic solidification in highly undercooled melts. Interface Sci 2002;10:121–36. <https://doi.org/10.1023/A:1015815928191>.
- [768] Saunders N, Miodownik AP. CALPHAD (Calculation of Phase Diagrams): A Comprehensive Guide. Pergamon; 1998.
- [769] Francois MM, Sun A, King WE, Henson NJ, Tourret D, Bronkhorst CA, et al. Modeling of additive manufacturing processes for metals: Challenges and opportunities. Curr Opin Solid State Mater Sci. 2017;21:198–206. <https://doi.org/10.1016/j.cossms.2016.12.001>.
- [770] Ahmadein M, Pustal B, Berger R, Subasić R, Bührig-Polaczek A. Grain nucleation parameters for aluminum alloys: experimental determination and model validation. Metall Mater Trans A 2009;40:646–53.
- [771] Gandin C, Rappaz M. A coupled finite element-cellular automaton model for the prediction of dendritic grain structures in solidification processes. Acta Metall Mater 1994;42:2233–46.
- [772] Ping WS, Rong LD, Jie GJ, Yun LC, Qing SY, Zhi FH. Numerical simulation of microstructure evolution of Ti-6Al-4V alloy in vertical centrifugal casting. Mater Sci Eng A 2006;426:240–9. <https://doi.org/10.1016/j.msea.2006.04.014>.
- [773] Boettinger WJ. Microstructural variations in rapidly solidified alloys. Mater Sci Eng 1988;98:123–30. [https://doi.org/10.1016/0025-5416\(88\)90140-1](https://doi.org/10.1016/0025-5416(88)90140-1).
- [774] Michi RA, Plotkowski A, Shyam A, Dehoff RR, Babu SS. Towards high-temperature applications of aluminium alloys enabled by additive manufacturing. Int Mater Rev 2022;67:298–345. <https://doi.org/10.1080/09506608.2021.1951580>.
- [775] Acharya R, Sharon JA, Staroselsky A. Prediction of microstructure in laser powder bed fusion process. Acta Mater. 2017;124:360–71. <https://doi.org/10.1016/j.actamat.2016.11.018>.
- [776] Thanki A, Goossens L, Ompusungu AP, Bayat M, Bey-Temsamani A, van Hooreweder B, et al. Melt pool feature analysis using a high-speed coaxial monitoring system for laser powder bed fusion of Ti-6Al-4 V grade 23. Int J Adv Manuf Technol 2022;120:6497–514. <https://doi.org/10.1007/s00170-022-09168-2>.
- [777] Ly S, Rubenchik AM, Khairallah SA, Guss G, Matthews MJ. Metal vapor micro-jet controls material redistribution in laser powder bed fusion additive manufacturing. Sci Rep. 2017;7:1–12. <https://doi.org/10.1038/s41598-017-04237-z>.
- [778] Bidare P, Bitharas I, Ward RM, Attallah MM, Moore AJ. Laser powder bed fusion in high-pressure atmospheres. Int J Adv Manuf Technol 2018;99:543–55. <https://doi.org/10.1007/s00170-018-2495-7>.
- [779] Matthews MJ, Guss G, Khairallah SA, Rubenchik AM, Depond PJ, King WE. Denudation of metal powder layers in laser powder bed fusion processes. Acta Mater. 2016;114:33–42. <https://doi.org/10.1016/j.actamat.2016.05.017>.
- [780] Masmoudi A, Bolot R, Coddet C. Investigation of the laser-powder-atmosphere interaction zone during the selective laser melting process. J Mater Process Technol. 2015;225:122–32. <https://doi.org/10.1016/j.jmatprotec.2015.05.008>.
- [781] Bidare P, Bitharas I, Ward RM, Attallah MM, Moore AJ. Acta Materialia Fluid and particle dynamics in laser powder bed fusion. Acta Mater. 2018;142:107–20. <https://doi.org/10.1016/j.actamat.2017.09.051>.
- [782] Hosseini Motlagh NS, Parvin P, Jandaghi M, Torkamany MJ. The influence of different volume ratios of He and Ar in shielding gas mixture on the power waste parameters for Nd:YAG and CO₂ laser welding. Opt Laser Technol. 2013;54:191–8. <https://doi.org/10.1016/j.optlastec.2013.04.027>.
- [783] Yan C, Wen-Jing X, Sue W, Da-Wei S, Yixiong W. Numerical and experimental study of the effect of groove on plasma plume during high power laser welding. J Laser Appl. 2013;25.
- [784] Bitharas I, Burton A, Ross AJ, Moore AJ. Visualisation and numerical analysis of laser powder bed fusion under cross-flow. Addit Manuf. 2021;37:101690. <https://doi.org/10.1016/j.addma.2020.101690>.
- [785] Li X, Tan W. Numerical Modeling of Powder Gas Interaction Relative to Laser Powder Bed Fusion Process. 143 (2021) 1–7. <https://doi.org/10.1115/1.4048443>.
- [786] Chen H, Yan W. Spattering and denudation in laser powder bed fusion process: Multiphase flow modelling. Acta Mater. 2020;196:154–67. <https://doi.org/10.1016/j.actamat.2020.06.033>.
- [787] Le T, Lo Y, Chen K, Hung W. Numerical and experimental investigation into powder entrainment and denudation phenomena in laser powder bed fusion process. Powder Technol. 2022;410:117907. <https://doi.org/10.1016/j.powtec.2022.117907>.
- [788] Stokes MA, Khairallah SA, Volkov AN, Rubenchik AM. Fundamental physics effects of background gas species and pressure on vapor plume structure and spatter entrainment in laser melting. Addit Manuf. 2022;55:102819. <https://doi.org/10.1016/j.addma.2022.102819>.
- [789] Lin J. Laser attenuation of the focused powder streams in coaxial laser cladding. J Laser Appl. 2000;12:28–33.
- [790] Pinkerton AJ, Lin L. Modelling powder concentration distribution from a coaxial deposition nozzle for laser-based rapid tooling. J Manuf Sci Eng. 2004;126: 33–41. <https://doi.org/10.1115/1.1643748>.
- [791] Pinkerton AJ. An analytical model of beam attenuation and powder heating during coaxial laser, 2007. <https://doi.org/10.1088/0022-3727/40/23/012>.
- [792] Fu Y, Loreda A, Martin B, Vannes AB. A theoretical model for laser and powder particles interaction during laser cladding. J Mater Process Technol. 2002;128: 106–12. [https://doi.org/10.1016/S0924-0136\(02\)00433-8](https://doi.org/10.1016/S0924-0136(02)00433-8).
- [793] Lin J. Numerical simulation of the focused powder streams in coaxial laser cladding. J Mater Process Technol. 2000;105:17–23. [https://doi.org/10.1016/S0924-0136\(00\)00584-7](https://doi.org/10.1016/S0924-0136(00)00584-7).
- [794] Marzouk OA, David Huckaby E. Simulation of a swirling gas-particle flow using different k-epsilon models and particle-parcel relationships. Eng Lett 2010;18.
- [795] Lew AJ, Buscaglia GC, Carrica PM. A Note on the Numerical Treatment of the k-epsilon Turbulence Model. Int J Comput Fluid Dyn. 2001;14:201–9. <https://doi.org/10.1080/10618560108940724>.
- [796] Deylami HM, Amanifard N, Hosseinezhad SS, Dolati F. Numerical investigation of the wake flow control past a circular cylinder with Electrohydrodynamic actuator. Eur J Mech, B/Fluids. 2017;66:71–80. <https://doi.org/10.1016/j.euromechflu.2017.06.002>.
- [797] Zekovic S, Divedi R, Kovacevic R. Numerical simulation and experimental investigation of gas-powder flow from radially symmetrical nozzles in laser-based direct metal deposition. Int J Mach Tools Manuf. 2007;47:112–23. <https://doi.org/10.1016/j.ijmactools.2006.02.004>.
- [798] Zhang A, Li D, Zhou Z, Zhu G, Lu B. Numerical simulation of powder flow field on coaxial powder nozzle in laser metal direct manufacturing. Int J Adv Manuf Technol 2010;49:853–9. <https://doi.org/10.1007/s00170-010-2657-8>.
- [799] Kovalev OB, Zaitsev AV, Novichenko D, Smurov I. Theoretical and experimental investigation of gas flows, powder transport and heating in coaxial laser direct metal deposition (DMD) process. J Therm Spray Technol 2011;20:465–78. <https://doi.org/10.1007/s11666-010-9539-3>.
- [800] Wen SY, Shin YC, Murthy JY, Sojka PE. Modeling of coaxial powder flow for the laser direct deposition process. Int J Heat Mass Transf. 2009;52:5867–77. <https://doi.org/10.1016/j.ijheatmasstransfer.2009.07.018>.
- [801] Liu H, He XL, Yu G, Bin Wang Z, Li SX, Zheng CY, et al. Numerical simulation of powder transport behavior in laser cladding with coaxial powder feeding. Sci China Phys Mech Astron. 2015;58. <https://doi.org/10.1007/s11433-015-5705-4>.
- [802] Taberner I, Lamikiz A, Ukar E, López De Lacalle LN, Angulo C, Urbikain G. Numerical simulation and experimental validation of powder flux distribution in coaxial laser cladding. J Mater Process Technol. 2010;210:2125–34. <https://doi.org/10.1016/j.jmatprotec.2010.07.036>.
- [803] Taberner I, Lamikiz A, Martínez S, Ukar E, López De Lacalle LN. Modelling of energy attenuation due to powder flow-laser beam interaction during laser cladding process. J Mater Process Technol. 2012;212:516–22. <https://doi.org/10.1016/j.jmatprotec.2011.10.019>.
- [804] Guan X, Zhao YF. Numerical modeling of coaxial powder stream in laser-powder-based Directed Energy Deposition process. Addit Manuf. 2020;34:101226. <https://doi.org/10.1016/j.addma.2020.101226>.
- [805] Vetter P-A, Fontaine J, Engel T, Lagrange L, Marchione T. Characterization of laser-material interaction during laser cladding process, Transactions on. Eng Sci 1993;2:185–94.
- [806] Ibarra-Medina J, Pinkerton AJ. Numerical investigation of powder heating in coaxial laser metal deposition. Surf Eng 2011;27:754–61. <https://doi.org/10.1179/1743294411Y.0000000017>.

- [807] Ibarra-Medina J, Pinkerton AJ. A CFD model of the laser, coaxial powder stream and substrate interaction in laser cladding. *Phys Procedia*. 2010;5:337–46. <https://doi.org/10.1016/j.phpro.2010.08.060>.
- [808] Kar A, Mazumder J. One-dimensional diffusion model for extended solid solution in laser cladding. *J Appl Phys*. 1987;61:2645–55. <https://doi.org/10.1063/1.337895>.
- [809] Carslaw RS, Jaeger JC. *Conduction of Heat in Solids*. 2nd ed. London: Clarendon; 1959.
- [810] Bontha S, Klingbeil NW, Kobryn PA, Fraser HL. Thermal process maps for predicting solidification microstructure in laser fabrication of thin-wall structures. *J Mater Process Technol*. 2006;178:135–42. <https://doi.org/10.1016/j.jmatprotec.2006.03.155>.
- [811] Bontha S, Klingbeil NW, Kobryn PA, Fraser HL. Effects of process variables and size-scale on solidification microstructure in beam-based fabrication of bulky 3D structures. *Mater Sci Eng A* 2009;513–514:311–8. <https://doi.org/10.1016/j.msea.2009.02.019>.
- [812] Eagar TW, Tsai NS. Temperature fields produced by traveling distributed heat sources. *Weld J*. 1983;62:346–55.
- [813] El Cheikh H, Courant B, Hascoët JY, Guillén R. Prediction and analytical description of the single laser track geometry in direct laser fabrication from process parameters and energy balance reasoning. *J Mater Process Technol*. 2012;212:1832–9. <https://doi.org/10.1016/j.jmatprotec.2012.03.016>.
- [814] Lalas C, Tsirbas K, Salonitis K, Chrysosouris G. An analytical model of the laser clad geometry. *Int J Adv Manuf Technol* 2007;32:34–41. <https://doi.org/10.1007/s00170-005-0318-0>.
- [815] Huang Y, Ansari M, Asgari H, Hossein M. Rapid prediction of real-time thermal characteristics, solidification parameters and microstructure in laser directed energy deposition (powder-fed additive manufacturing). *J Mater Process Tech*. 2019;274:116286. <https://doi.org/10.1016/j.jmatprotec.2019.116286>.
- [816] Huang Y, Khamesee MB, Toyserkani E. A new physics-based model for laser directed energy deposition (powder-fed additive manufacturing): From single-track to multi-track and multi-layer. *Opt Laser Technol*. 2019;109:584–99. <https://doi.org/10.1016/j.optlastec.2018.08.015>.
- [817] Patil RB, Yadava V. Finite element analysis of temperature distribution in single metallic powder layer during metal laser sintering. *Int J Mach Tools Manuf*. 2007;47:1069–80. <https://doi.org/10.1016/j.ijmactools.2006.09.025>.
- [818] Yin J, Zhu H, Ke L, Lei W, Dai C, Zuo D. Simulation of temperature distribution in single metallic powder layer for laser micro-sintering. *Comput Mater Sci*. 2012;53:333–9. <https://doi.org/10.1016/j.commatsci.2011.09.012>.
- [819] Shuai C, Feng P, Gao C, Zhou Y, Peng S. Simulation of dynamic temperature field during selective laser sintering of ceramic powder. *Math Comput Model Dyn Syst*. 2013;19:1–11. <https://doi.org/10.1080/13873954.2012.689769>.
- [820] Zhao H, Zhang G, Yin Z, Wu L. A 3D dynamic analysis of thermal behavior during single-pass multi-layer weld-based rapid prototyping. *J Mater Process Technol*. 2011;211:488–95. <https://doi.org/10.1016/j.jmatprotec.2010.11.002>.
- [821] Dai K, Shaw L. Distortion minimization of laser-processed components through control of laser scanning patterns. *Rapid Prototyp J*. 2002;8:270–6. <https://doi.org/10.1108/13552540210451732>.
- [822] Hoadley AFA, Rappaz M. A thermal model of laser cladding by powder injection. *Metall Trans B* 1992;23:631–42. <https://doi.org/10.1007/BF02649723>.
- [823] Kumar S, Roy S. Development of a theoretical process map for laser cladding using two-dimensional conduction heat transfer model. *Comput Mater Sci*. 2008;41:457–66. <https://doi.org/10.1016/j.commatsci.2007.05.002>.
- [824] Ya W, Pathiraj B, Liu S. 2D modelling of clad geometry and resulting thermal cycles during laser cladding. *J Mater Process Technol*. 2016;230:217–32.
- [825] Ciraless LE, Arsoy YM, Özel T. Sensitivity analysis of material and process parameters in finite element modeling of selective laser melting of Inconel 625. *Int J Adv Manuf Technol* 2016;86:2653–66. <https://doi.org/10.1007/s00170-015-8329-y>.
- [826] Dong L, Makradi A, Ahzi S, Remond Y. Three-dimensional transient finite element analysis of the selective laser sintering process. *J Mater Process Technol*. 2009;209:700–6. <https://doi.org/10.1016/j.jmatprotec.2008.02.040>.
- [827] Rombouts M, Froyen L, Gusarov AV, Bentefour EH, Glorieux C. Photopyroelectric measurement of thermal conductivity of metallic powders. *J Appl Phys*. 2005;97. <https://doi.org/10.1063/1.1832740>.
- [828] Shishkovsky IV. Thermoviscoplasticity of powder composition under selective laser sintering. *Seventh Int Conf Laser Laser-Form Technol* 2002;4644:446. <https://doi.org/10.1117/12.464180>.
- [829] Zhang DQ, Cai QZ, Liu JH, Zhang L, Li RD. Select laser melting of W-Ni-Fe powders: Simulation and experimental study. *Int J Adv Manuf Technol* 2010;51:649–58. <https://doi.org/10.1007/s00170-010-2641-3>.
- [830] Shi Q, Gu D, Xia M, Cao S, Rong T. Effects of laser processing parameters on thermal behavior and melting/solidification mechanism during selective laser melting of TiC/Inconel 718 composites. *Opt Laser Technol*. 2016;84:9–22. <https://doi.org/10.1016/j.optlastec.2016.04.009>.
- [831] Sih SS, Barlow JW. The prediction of the thermal conductivity of powders. In: *Proceedings of 6th Annual Solid Freeform Fabrication Symposium*, The University of Texas at Austin; 1994: pp. 321–329.
- [832] Antony K, Arivazhagan N, Senthilkumaran K. Numerical and experimental investigations on laser melting of stainless steel 316L metal powders. *J Manuf Process*. 2014;16:345–55. <https://doi.org/10.1016/j.jmapro.2014.04.001>.
- [833] Bugada G, Cervera M, Lombera G. Numerical prediction of temperature and density distributions in selective laser sintering processes. *Rapid Prototyp J*. 1999;5:21–6. <https://doi.org/10.1108/13552549910251846>.
- [834] Yadroitsev I, Gusarov A, Yadroitsava I, Smurov I. Single track formation in selective laser melting of metal powders. *J Mater Process Technol*. 2010;210:1624–31. <https://doi.org/10.1016/j.jmatprotec.2010.05.010>.
- [835] Zhang Y, Faghri A. Melting and resolidification of a subcooled mixed powder bed with moving gaussian heat source. *J Heat Transfer*. 1998;120:883–91. <https://doi.org/10.1115/1.2825907>.
- [836] Li Y, Gu D. Parametric analysis of thermal behavior during selective laser melting additive manufacturing of aluminum alloy powder. *Mater Des*. 2014;63:856–67. <https://doi.org/10.1016/j.matdes.2014.07.006>.
- [837] Li Y, Gu D. Thermal behavior during selective laser melting of commercially pure titanium powder: Numerical simulation and experimental study. *Addit Manuf*. 2014;1:99–109. <https://doi.org/10.1016/j.addma.2014.09.001>.
- [838] Li Y, Zhou K, Tor SB, Chua CK, Leong KF. Heat transfer and phase transition in the selective laser melting process. *Int J Heat Mass Transf*. 2017;108:2408–16. <https://doi.org/10.1016/j.ijheatmasstransfer.2017.01.093>.
- [839] Loh LE, Chua CK, Yeong WY, Song J, Mapar M, Sing SL, et al. Numerical investigation and an effective modelling on the Selective Laser Melting (SLM) process with aluminium alloy 6061. *Int J Heat Mass Transf*. 2015;80:288–300. <https://doi.org/10.1016/j.ijheatmasstransfer.2014.09.014>.
- [840] Yang D, Wang G, Zhang G. Thermal analysis for single-pass multi-layer GMAW based additive manufacturing using infrared thermography. *J Mater Process Technol*. 2017;244:215–24. <https://doi.org/10.1016/j.jmatprotec.2017.01.024>.
- [841] Wu B, Ding D, Pan Z, Cuiuri D, Li H, Han J, et al. Effects of heat accumulation on the arc characteristics and metal transfer behavior in Wire Arc Additive Manufacturing of Ti6Al4V. *J Mater Process Technol*. 2017;250:304–12. <https://doi.org/10.1016/j.jmatprotec.2017.07.037>.
- [842] Zhao Y, Koizumi Y, Aoyagi K, Yamanaka K, Chiba A. Manipulating local heat accumulation towards controlled quality and microstructure of a Co-Cr-Mo alloy in powder bed fusion with electron beam. *Mater Lett*. 2019;254:269–72. <https://doi.org/10.1016/j.matlet.2019.07.078>.
- [843] Roberts IA, Wang CJ, Esterlein R, Stanford M, Mynors DJ. A three-dimensional finite element analysis of the temperature field during laser melting of metal powders in additive layer manufacturing. *Int J Mach Tools Manuf*. 2009;49:916–23. <https://doi.org/10.1016/j.ijmactools.2009.07.004>.
- [844] Liu Y, Zhang J, Pang Z. Numerical and experimental investigation into the subsequent thermal cycling during selective laser melting of multi-layer 316L stainless steel. *Opt Laser Technol*. 2018;98:23–32. <https://doi.org/10.1016/j.optlastec.2017.07.034>.
- [845] Imran MK, Masood SH, Brandt M, Bhattacharya S, Mazumder J. Direct metal deposition (DMD) of H13 tool steel on copper alloy substrate: Evaluation of mechanical properties. *Mater Sci Eng A* 2011;528:3342–9. <https://doi.org/10.1016/j.msea.2010.12.099>.
- [846] Keist JS, Palmer TA. Role of geometry on properties of additively manufactured Ti-6Al-4V structures fabricated using laser based directed energy deposition. *Mater Des*. 2016;106:482–94. <https://doi.org/10.1016/j.matdes.2016.05.045>.
- [847] Ma M, Wang Z, Zeng X. Effect of energy input on microstructural evolution of direct laser fabricated IN718 alloy. *Mater Charact*. 2015;106:420–7. <https://doi.org/10.1016/j.matchar.2015.06.027>.

- [848] Malukhin K, Ehmann K. Material characterization of NiTi based memory alloys fabricated by the laser direct metal deposition process. *J Manuf Sci E T ASME* 2006;128:691–6. <https://doi.org/10.1115/1.2193553>.
- [849] Riza SH, Masood SH, Wen C, Ruan D, Xu S. Dynamic behaviour of high strength steel parts developed through laser assisted direct metal deposition. *Mater Des*. 2014;64:650–9. <https://doi.org/10.1016/j.mates.2014.08.026>.
- [850] Mower TM, Long MJ. Mechanical behavior of additive manufactured, powder-bed laser-fused materials. *Mater Sci Eng A* 2016;651:198–213. <https://doi.org/10.1016/j.msea.2015.10.068>.
- [851] Kamath C. Data mining and statistical inference in selective laser melting. *Int J Adv Manuf Technol* 2016;86:1659–77. <https://doi.org/10.1007/s00170-015-8289-2>.
- [852] Ma M, Wang Z, Zeng X. A comparison on metallurgical behaviors of 316L stainless steel by selective laser melting and laser cladding deposition. *Mater Sci Eng A* 2017;685:265–73. <https://doi.org/10.1016/j.msea.2016.12.112>.
- [853] Manvatkar VD, Gokhale AA, Jagan Reddy G, Venkataramana A, De A. Estimation of melt pool dimensions, thermal cycle, and hardness distribution in the laser-engineered net shaping process of austenitic stainless steel. *Metall Mater Trans A Phys Metall Mater Sci*. 2011;42:4080–7. <https://doi.org/10.1007/s11661-011-0787-8>.
- [854] Costa L, Vilar R, Reti T, Deus AM. Rapid tooling by laser powder deposition: Process simulation using finite element analysis. *Acta Mater*. 2005;53:3987–99. <https://doi.org/10.1016/j.actamat.2005.05.003>.
- [855] Neto D, Vilar R. Physical-computational model to describe the interaction between a laser beam and a powder jet in laser surface processing. *J Laser Appl*. 2000;14:46–51.
- [856] Suárez A, Tobar MJ, Yáñez A, Pérez I, Sampedro J, Amigó V, et al. Modeling of phase transformations of Ti6Al4V during laser metal deposition. *Phys Procedia*. 2011;12:666–73. <https://doi.org/10.1016/j.phpro.2011.03.083>.
- [857] Lakhkar RS, Shin YC, Krane MJM. Predictive modeling of multi-track laser hardening of AISI 4140 steel. *Mater Sci Eng A* 2008;480:209–17. <https://doi.org/10.1016/j.msea.2007.07.054>.
- [858] Raghavan N, Dehoff R, Pannala S, Simunovic S, Kirka M, Turner J, et al. Numerical modeling of heat-transfer and the influence of process parameters on tailoring the grain morphology of IN718 in electron beam additive manufacturing *. *Acta Mater*. 2016;112:303–14. <https://doi.org/10.1016/j.actamat.2016.03.063>.
- [859] Yin J, Peng G, Chen C, Yang J, Zhu H, Ke L, et al. Thermal behavior and grain growth orientation during selective laser melting of Ti-6Al-4V alloy. *J Mater Process Technol*. 2018;260:57–65. <https://doi.org/10.1016/j.jmatprotec.2018.04.035>.
- [860] Zhang J, Liou F, Seufzer W, Taminger K. A coupled finite element cellular automaton model to predict thermal history and grain morphology of Ti-6Al-4V during direct metal deposition (DMD). *Addit Manuf*. 2016;11:32–9. <https://doi.org/10.1016/j.addma.2016.04.004>.
- [861] Tolochko NK, Khlopkov YV, Mozharov SE, Ignatiev MB, Laoui T, Titov VI. Absorptance of powder materials suitable for laser sintering. *Rapid Prototyp J*. 2000;6.
- [862] Gusarov AV, Kruth JP. Modelling of radiation transfer in metallic powders at laser treatment. *Int J Heat Mass Transf*. 2005;48:3423–34. <https://doi.org/10.1016/j.ijheatmasstransfer.2005.01.044>.
- [863] Foroozmehr A, Badrossamay M, Foroozmehr E, Golabi S. Finite Element Simulation of Selective Laser Melting process considering Optical Penetration Depth of laser in powder bed. *Mater Des*. 2016;89:255–63. <https://doi.org/10.1016/j.matdes.2015.10.002>.
- [864] Tran HC, Lo YL. Heat transfer simulations of selective laser melting process based on volumetric heat source with powder size consideration. *J Mater Process Technol*. 2018;255:411–25. <https://doi.org/10.1016/j.jmatprotec.2017.12.024>.
- [865] Tran HC, Lo YL, Huang MH. Analysis of Scattering and Absorption Characteristics of Metal Powder Layer for Selective Laser Sintering. *IEEE/ASME Trans Mechatron* 2017;22:1807–17. <https://doi.org/10.1109/TMECH.2017.2705090>.
- [866] Ye R, Smugersky JE, Zheng B, Zhou Y, Lavernia EJ. Numerical modeling of the thermal behavior during the LENS® process. *Mater Sci Eng A* 2006;428:47–53. <https://doi.org/10.1016/j.msea.2006.04.079>.
- [867] Neela V, De A. Three-dimensional heat transfer analysis of LENS™ process using finite element method. *Int J Adv Manuf Technol* 2009;45:935–43. <https://doi.org/10.1007/s00170-009-2024-9>.
- [868] Wang L, Felicelli S. Analysis of thermal phenomena in LENS™ deposition. *Mater Sci Eng A* 2006;435–436:625–31. <https://doi.org/10.1016/j.msea.2006.07.087>.
- [869] Luo F, Yao J, Hua, Hu X, Chai G, Zhong. Effect of Laser Power on the Cladding Temperature Field and the Heat Affected Zone. *J Iron Steel Res Int* 2011;18:73–8. [https://doi.org/10.1016/S1006-706X\(11\)60014-9](https://doi.org/10.1016/S1006-706X(11)60014-9).
- [870] Hao M, Sun Y. A FEM model for simulating temperature field in coaxial laser cladding of Ti6Al4V alloy using an inverse modeling approach. *Int J Heat Mass Transf*. 2013;64:352–60. <https://doi.org/10.1016/j.ijheatmasstransfer.2013.04.050>.
- [871] Gao W, Zhao S, Wang Y, Zhang Z, Liu F, Lin X. Numerical simulation of thermal field and Fe-based coating doped Ti. *Int J Heat Mass Transf*. 2016;92:83–90. <https://doi.org/10.1016/j.ijheatmasstransfer.2015.08.082>.
- [872] Bailey NS, Katinas C, Shin YC. Laser direct deposition of AISI H13 tool steel powder with numerical modeling of solid phase transformation, hardness, and residual stresses. *J Mater Process Tech*. 2017;247:223–33. <https://doi.org/10.1016/j.jmatprotec.2017.04.020>.
- [873] Denlinger ER, Michaleris P. Effect of stress relaxation on distortion in additive manufacturing process modeling. *Addit Manuf*. 2016;12:51–9. <https://doi.org/10.1016/j.addma.2016.06.011>.
- [874] Alberto Santi. Thermomechanical modelling of metal additive manufacturing with focus on residual stresses and deformations, Master, Technical University of Denmark – DTU; 2022.
- [875] Tutum CC, Hattel JH. Optimisation of process parameters in friction stir welding based on residual stress analysis: A feasibility study. *Sci Technol Weld Join* 2010;15:369–77. <https://doi.org/10.1179/136217110X12707333260455>.
- [876] Labudovic M, Hu D, Kovacevic R. A three dimensional model for direct laser metal powder deposition and rapid prototyping. *J Mater Sci*. 2003;38:35–49. <https://doi.org/10.1023/A:1021153513925>.
- [877] Kamara AM, Marimuthu S, Li L. A numerical investigation into residual stress characteristics in laser deposited multiple layer waspaloy parts. *J Manuf Sci E T ASME* 2011;133:1–9. <https://doi.org/10.1115/1.4003833>.
- [878] Farahmand P, Kovacevic R. Optics & Laser Technology An experimental – numerical investigation of heat distribution and stress field in single- and multi-track laser cladding by a high-power direct diode laser. *Opt Laser Technol*. 2014;63:154–68. <https://doi.org/10.1016/j.optlastec.2014.04.016>.
- [879] Yang Q, Zhang P, Cheng L, Min Z, Chyu M, To AC. Finite element modeling and validation of thermomechanical behavior of Ti-6Al-4V in directed energy deposition additive manufacturing. *Addit Manuf*. 2016;12:169–77. <https://doi.org/10.1016/j.addma.2016.06.012>.
- [880] Ghosh S, Choi J. Modeling and Experimental verification of transient/residual stresses and microstructure formation of multi-layer laser aided DMD process. *J Heat Transfer*. 2006;128:662–79. <https://doi.org/10.1115/1.2194037>.
- [881] Wang L, Felicelli SD, Pratt P. Residual stresses in LENS-deposited AISI 410 stainless steel plates. *Mater Sci Eng A* 2008;496:234–41. <https://doi.org/10.1016/j.msea.2008.05.044>.
- [882] Heigel JC, Michaleris P, Reutzel EW. Thermo-mechanical model development and validation of directed energy deposition additive manufacturing of Ti – 6Al – 4V. *Addit Manuf*. 2015;5:9–19. <https://doi.org/10.1016/j.addma.2014.10.003>.
- [883] Li C, Denlinger ER, Gouge MF, Irwin JE, Michaleris P. Numerical verification of an Octree mesh coarsening strategy for simulating additive manufacturing processes. *Addit Manuf*. 2019;30. <https://doi.org/10.1016/j.addma.2019.100903>.
- [884] Li Y, Zhou K, Tan P, Tor SB, Chua CK, Leong KF. Modeling temperature and residual stress fields in selective laser melting. *Int J Mech Sci*. 2018;136:24–35. <https://doi.org/10.1016/j.ijmecsci.2017.12.001>.
- [885] Hodge NE, Ferencz RM, Solberg JM. Implementation of a thermomechanical model for the simulation of selective laser melting. *Comput Mech*. 2014;54:33–51. <https://doi.org/10.1007/s00466-014-1024-2>.

- [886] Wu J, Wang L, An X. Numerical analysis of residual stress evolution of AlSi10Mg manufactured by selective laser melting. *Optik (Stuttg)*. 2017;137:65–78. <https://doi.org/10.1016/j.jlileo.2017.02.060>.
- [887] Hussein A, Hao L, Yan C, Everson R. Finite element simulation of the temperature and stress fields in single layers built without-support in selective laser melting. *Mater Des*. 2013;52:638–47. <https://doi.org/10.1016/j.matdes.2013.05.070>.
- [888] Cheng B, Shrestha S, Chou K. Stress and deformation evaluations of scanning strategy effect in selective laser melting. *Addit Manuf*. 2016;12:240–51. <https://doi.org/10.1016/j.addma.2016.05.007>.
- [889] Parry L, Ashcroft IA, Wildman RD. Understanding the effect of laser scan strategy on residual stress in selective laser melting through thermo-mechanical simulation. *Addit Manuf*. 2016;12:1–15. <https://doi.org/10.1016/j.addma.2016.05.014>.
- [890] Chen C, Yin J, Zhu H, Xiao Z, Zhang L, Zeng X. Effect of overlap rate and pattern on residual stress in selective laser melting. *Int J Mach Tools Manuf*. 2019;145:103433. <https://doi.org/10.1016/j.ijmactools.2019.103433>.
- [891] Tan P, Shen F, Li B, Zhou K. A thermo-metallurgical-mechanical model for selective laser melting of Ti6Al4V. *Mater Des*. 2019;168:107642. <https://doi.org/10.1016/j.matdes.2019.107642>.
- [892] Ladani L, Romano J, Brindley W, Burlatsky S. Effective liquid conductivity for improved simulation of thermal transport in laser beam melting powder bed technology. *Addit Manuf*. 2017;14:13–23. <https://doi.org/10.1016/j.addma.2016.12.004>.
- [893] Ancellotti S, Fontanari V, Molinari A, Iacob E, Bellutti P, Luchin V, et al. Numerical/experimental strategies to infer enhanced liquid thermal conductivity and roughness in laser powder-bed fusion processes. *Addit Manuf*. 2019;27:552–64. <https://doi.org/10.1016/j.addma.2019.04.007>.
- [894] Safdar S, Pinkerton AJ, Li L, Sheikh MA, Withers PJ. An anisotropic enhanced thermal conductivity approach for modelling laser melt pools for Ni-base super alloys. *Appl Math Model*. 2013;37:1187–95. <https://doi.org/10.1016/j.apm.2012.03.028>.
- [895] Kamara AM, Wang W, Marimuthu S, Li L. Modelling of the melt pool geometry in the laser deposition of nickel alloys using the anisotropic enhanced thermal conductivity approach. 225 (2010) 87–99. <https://doi.org/10.1177/09544054JEM2129>.
- [896] De A, DebRoy T. A smart model to estimate effective thermal conductivity and viscosity in the weld pool. *J Appl Phys*. 2004;95:5230–40. <https://doi.org/10.1063/1.1695593>.
- [897] Chen Q, Guillemot G, Gandin CA, Bellet M. Numerical modelling of the impact of energy distribution and Marangoni surface tension on track shape in selective laser melting of ceramic material. *Addit Manuf*. 2018;21:713–23. <https://doi.org/10.1016/j.addma.2018.03.003>.
- [898] Mills KC, Keene BJ. Factors affecting variable weld penetration. *Int Mater Rev* 1990;35:185–216.
- [899] He X, Fuerschbach PW, DebRoy T. Heat transfer and fluid flow during laser spot welding of 304 stainless steel. *J Phys D Appl Phys*. 2003;36:1388–98. <https://doi.org/10.1088/0022-3727/36/12/306>.
- [900] Mills KC, Keene BJ, Brooks RF, Shirlali A. Marangoni effects in welding. 1998; 911–925.
- [901] Mills KC, Keene BJ, Brooks RF, Olusanya A. The surface tensions of 304 and 316 type stainless steels and their effect on weld penetration; 1984.
- [902] Sahoo P, Debroy T, McNallan MJ. Surface tension of binary metal-surface active solute systems under conditions relevant to welding metallurgy. *Metall Trans B* 1988;19:483–91. <https://doi.org/10.1007/BF02657748>.
- [903] Ozawa S, Takahashi S, Watanabe N, Fukuyama H. Influence of oxygen adsorption on surface tension of molten nickel measured under reducing gas atmosphere. *Int J Thermophys*. 2014;35:1705–11. <https://doi.org/10.1007/s10765-014-1674-5>.
- [904] Hibiya T, Ozawa S. Effect of oxygen partial pressure on the marangoni flow of molten metals. *Cryst Res Technol* 2013;48:208–13. <https://doi.org/10.1002/crat.201200514>.
- [905] Šeta B, Dubert D, Massons J, Gavalda J, Mounir Bou-Ali M, Ruiz X. Effect of Marangoni induced instabilities on a melting bridge under microgravity conditions. *Int. J Heat Mass Transf*. 2021;179. <https://doi.org/10.1016/j.ijheatmasstransfer.2021.121665>.
- [906] Bayat M, Nadipalli VK, Mohanty S, Hattel JH. Resolving the effects of local convective heat transfer via adjustment of thermo-physical properties in pure heat conduction simulation of Laser Powder Bed Fusion (L-PBF). In: *MCWASP XV: Modelling of Casting, Welding and Advanced Solidification Processes*; 2020.
- [907] Egly I, Ricci E, Novakovic R, Ozawa S. Surface tension of liquid metals and alloys — Recent developments. *Adv Colloid Interface Sci*. 2010;159:198–212. <https://doi.org/10.1016/j.cis.2010.06.009>.
- [908] Voller VR, Prakash C. A fixed grid numerical modelling methodology for convection-diffusion mushy region phase-change problems. *Int J Heat Mass Transf*. 1987;30:1709–19. [https://doi.org/10.1016/0017-9310\(87\)90317-6](https://doi.org/10.1016/0017-9310(87)90317-6).
- [909] Šeta B, Dubert D, Prats M, Gavalda J, Massons J, Bou-Ali MM, Ruiz X, Shevtsova V. Transitions between nonlinear regimes in melting and liquid bridges in microgravity. *Int J Heat Mass Transf*. 2022;193. <https://doi.org/10.1016/j.ijheatmasstransfer.2022.122984>.
- [910] Bayat M, Mohanty S, Hattel JH. Thermo-fluid-metallurgical modelling of laser-based powder bed fusion process. In: *COMSOL Multiphysics Conference, Lausanne Switzerland*; 2018.
- [911] Fan Z, Liou F. Numerical modeling of the additive manufacturing (AM) processes of titanium alloy. Titanium alloys-towards achieving enhanced properties for diversified applications, 3-28, 2012.
- [912] Yuan P, Gu D, Dai D. Particulate migration behavior and its mechanism during selective laser melting of TiC reinforced Al matrix nanocomposites. *Mater Des*. 2015;82:46–55. <https://doi.org/10.1016/j.matdes.2015.05.041>.
- [913] Dai D, Gu D. Thermal behavior and densification mechanism during selective laser melting of copper matrix composites: Simulation and experiments. *Mater Des*. 2014;55:482–91. <https://doi.org/10.1016/j.matdes.2013.10.006>.
- [914] Mukherjee T, Wei HL, De A, DebRoy T. Heat and fluid flow in additive manufacturing—Part I: Modeling of powder bed fusion. *Comput Mater Sci*. 2018;150:304–13. <https://doi.org/10.1016/j.commatsci.2018.04.022>.
- [915] Mukherjee T, Wei HL, De A, DebRoy T. Heat and fluid flow in additive manufacturing – Part II: Powder bed fusion of stainless steel, and titanium, nickel and aluminum base alloys. *Comput Mater Sci*. 2018;150:369–80. <https://doi.org/10.1016/j.commatsci.2018.04.027>.
- [916] Mukherjee T, DebRoy T. Mitigation of lack of fusion defects in powder bed fusion additive manufacturing. *J Manuf Process*. 2018;36:442–9. <https://doi.org/10.1016/j.jmapro.2018.10.028>.
- [917] Le TN, Lo YL. Effects of sulfur concentration and Marangoni convection on melt-pool formation in transition mode of selective laser melting process. *Mater Des*. 2019;179:107866. <https://doi.org/10.1016/j.matdes.2019.107866>.
- [918] Bayat M, Mohanty S, Hattel JH. A systematic investigation of the effects of process parameters on heat and fluid flow and metallurgical conditions during laser-based powder bed fusion of Ti6Al4V alloy. *Int J Heat Mass Transf*. 2019;139:213–30. <https://doi.org/10.1016/j.ijheatmasstransfer.2019.05.017>.
- [919] Zhang D, Zhang P, Liu Z, Feng Z, Wang C, Guo Y. Thermo-fluid field of molten pool and its effects during selective laser melting (SLM) of Inconel 718 alloy. *Addit Manuf*. 2018;21:567–78. <https://doi.org/10.1016/j.addma.2018.03.031>.
- [920] Aboulkhair NT, Everitt NM, Ashcroft I, Tuck C. Reducing porosity in AlSi10Mg parts processed by selective laser melting. *Addit Manuf*. 2014;1:77–86. <https://doi.org/10.1016/j.addma.2014.08.001>.
- [921] Manvatkar V, De A, DebRoy T. Heat transfer and material flow during laser assisted multi-layer additive manufacturing. *J Appl Phys*. 2014;116. <https://doi.org/10.1063/1.4896751>.
- [922] Wei HL, Mazumder J, DebRoy T. Evolution of solidification texture during additive manufacturing. *Sci Rep*. 2015;5:1–7. <https://doi.org/10.1038/srep16446>.
- [923] Manvatkar V, De A, DebRoy T. Spatial variation of melt pool geometry, peak temperature and solidification parameters during laser assisted additive manufacturing process. *Mater Sci Technol (United Kingdom)*. 2015;31:924–30. <https://doi.org/10.1179/1743284714Y.0000000701>.
- [924] Singh AK, Mundada Y, Bajaj P, Wilms MB, Patil JP, Mishra SK, et al. Investigation of temperature distribution and solidification morphology in multilayered directed energy deposition of Al-0.5Sc-0.5Si alloy. *Int. J Heat Mass Transf*. 2022;186. <https://doi.org/10.1016/j.ijheatmasstransfer.2021.122492>.
- [925] Jiang Y, Cheng Y, Zhang X, Yang J, Yang X, Cheng Z. Simulation and experimental investigations on the effect of Marangoni convection on thermal field during laser cladding process. *Optik (Stuttg)*. 2020;203:164044. <https://doi.org/10.1016/j.jlileo.2019.164044>.
- [926] Knapp GL, Mukherjee T, Zuback JS, Wei HL, Palmer TA, De A, et al. Building blocks for a digital twin of additive manufacturing. *Acta Mater*. 2017;135:390–9. <https://doi.org/10.1016/j.actamat.2017.06.039>.

- [927] Cao Y, Zhu S, Liang X, Wang W. Overlapping model of beads and curve fitting of bead section for rapid manufacturing by robotic MAG welding process. *Robot Comput Integr Manuf.* 2011;27:641–5. <https://doi.org/10.1016/j.rcim.2010.11.002>.
- [928] Mukherjee T, DebRoy T, Lienert TJ, Maloy SA, Hosemann P. Spatial and temporal variation of hardness of a printed steel part. *Acta Mater.* 2021;209:116775. <https://doi.org/10.1016/j.actamat.2021.116775>.
- [929] Zhang Q, Xie J, Gao Z, London T, Griffiths D, Oancea V. A metallurgical phase transformation framework applied to SLM additive manufacturing processes. *Mater Des.* 2019;166. <https://doi.org/10.1016/j.matdes.2019.107618>.
- [930] Mishra S, Kumar A, DebRoy T, Elmer JW. Genetic algorithm based optimization of Johnson Mehl Avrami equation parameters for ferrite to austenite transformation in steel welds. *ASM Proc Int Conf: Trends Weld Res* 2005;2005:1001–6.
- [931] Ocelík V, Furár I, De Hosson JTM. Microstructure and properties of laser clad coatings studied by orientation imaging microscopy. *Acta Mater.* 2010;58:6763–72. <https://doi.org/10.1016/j.actamat.2010.09.002>.
- [932] Gan Z, Yu G, He X, Li S. Numerical simulation of thermal behavior and multicomponent mass transfer in direct laser deposition of Co-base alloy on steel. *Int J Heat Mass Transf.* 2017;104:28–38. <https://doi.org/10.1016/j.ijheatmasstransfer.2016.08.049>.
- [933] Li C, Yu Z, Gao J, Zhao J, Han X. Numerical simulation and experimental study of cladding Fe60 on an ASTM 1045 substrate by laser cladding. *Surf Coat Technol.* 2019;357:965–77. <https://doi.org/10.1016/j.surfcoat.2018.10.099>.
- [934] Gan Z, Yu G, He X, Li S. Surface-active element transport and its effect on liquid metal flow in laser-assisted additive manufacturing. *Int Commun Heat Mass Transf.* 2017;86:206–14. <https://doi.org/10.1016/j.icheatmasstransfer.2017.06.007>.
- [935] Wu J, Ren S, Zhang Y, Cao Y, Zhang D, Yin C. Influence of spatial laser beam profiles on thermal-fluid transport during laser-based directed energy deposition. *Virtual Phys Prototyp.* 2021;16:444–59. <https://doi.org/10.1080/17452759.2021.1960734>.
- [936] Wolff SJ, Gan Z, Lin S, Bennett JL, Yan W, Hyatt G, et al. Experimentally validated predictions of thermal history and microhardness in laser-deposited Inconel 718 on carbon steel. *Addit Manuf.* 2019;27:540–51. <https://doi.org/10.1016/j.addma.2019.03.019>.
- [937] Kumar A, Roy S. Effect of three-dimensional melt pool convection on process characteristics during laser cladding. *Comput Mater Sci.* 2009;46:495–506. <https://doi.org/10.1016/j.commatsci.2009.04.002>.
- [938] Gan Z, Liu H, Li S, He X, Yu G. Modeling of thermal behavior and mass transport in multi-layer laser additive manufacturing of Ni-based alloy on cast iron. *Int J Heat Mass Transf.* 2017;111:709–22. <https://doi.org/10.1016/j.ijheatmasstransfer.2017.04.055>.
- [939] Zhao Z, Zhu Q, Yan J. A thermal multi-phase flow model for directed energy deposition processes via a moving signed distance function. *Comput Methods Appl Mech Eng.* 2021;373:113518. <https://doi.org/10.1016/j.cma.2020.113518>.
- [940] Ou W, Knapp GL, Mukherjee T, Wei Y, DebRoy T. An improved heat transfer and fluid flow model of wire-arc additive manufacturing. *Int J Heat Mass Transf.* 2021;167. <https://doi.org/10.1016/j.ijheatmasstransfer.2020.120835>.
- [941] Sethian JA. *Level set methods and fast marching methods: evolving interfaces in computational geometry, fluid mechanics, computer vision, and materials science.* Cambridge University Press; 1999.
- [942] Hirt CW, Nichols BD. Volume of Fluid (VOF) Method for the Dynamics of Free Boundaries. *J Comput Phys.* 1981;39:201–25.
- [943] Huang Y, Liang G, Su J. 3-D transient numerical simulation on the process of laser cladding by powder feeding. *Int J Miner Metall Mater* 2004;1:13–7.
- [944] Qi H, Mazumder J, Ki H. Numerical simulation of heat transfer and fluid flow in coaxial laser cladding process for direct metal deposition. *J Appl Phys.* 2006;100. <https://doi.org/10.1063/1.2209807>.
- [945] He X, Mazumder J. Transport phenomena during direct metal deposition. *J Appl Phys.* 2007;101. <https://doi.org/10.1063/1.2710780>.
- [946] He X, Yu G, Mazumder J. Temperature and composition profile during double-track laser cladding of H13 tool steel. *J Phys D Appl Phys.* 2010;43. <https://doi.org/10.1088/0022-3727/43/1/015502>.
- [947] Wen S, Shin YC. Modeling of transport phenomena in direct laser deposition of metal matrix composite. *Int J Heat Mass Transf.* 2011;54:5319–26. <https://doi.org/10.1016/j.ijheatmasstransfer.2011.08.011>.
- [948] Queva A, Guillemot G, Moriconi C, Metton C, Bellet M. Numerical study of the impact of vaporisation on melt pool dynamics in Laser Powder Bed Fusion - Application to IN718 and Ti-6Al-4V. *Addit Manuf.* 2020;35:101249. <https://doi.org/10.1016/j.addma.2020.101249>.
- [949] Kouraytem N, Li X, Cunningham R, Zhao C, Parab N, Sun T, et al. Effect of Laser-Matter Interaction on Molten Pool Flow and Keyhole Dynamics. *Phys Rev Appl.* 2019;11:064054. <https://doi.org/10.1103/PhysRevApplied.11.064054>.
- [950] Tan W, Bailey NS, Shin YC. Investigation of keyhole plume and molten pool based on a three-dimensional dynamic model with sharp interface formulation. *J Phys D Appl Phys.* 2013;46. <https://doi.org/10.1088/0022-3727/46/5/055501>.
- [951] Tan W, Shin YC. Analysis of multi-phase interaction and its effects on keyhole dynamics with a multi-physics numerical model. *J Phys D Appl Phys.* 2014;47. <https://doi.org/10.1088/0022-3727/47/34/345501>.
- [952] Tan W, Shin YC. Multi-scale modeling of solidification and microstructure development in laser keyhole welding process for austenitic stainless steel. *Comput Mater Sci.* 2015;98:446–58. <https://doi.org/10.1016/j.commatsci.2014.10.063>.
- [953] Desmaison O, Bellet M, Guillemot G. A level set approach for the simulation of the multipass hybrid laser/GMA welding process. *Comput Mater Sci.* 2014;91:240–50. <https://doi.org/10.1016/j.commatsci.2014.04.036>.
- [954] Brackbill JU, Kothe DB, Zemach C. A continuum method for modeling surface tension. *J Comput Phys.* 1992;100:335–54. [https://doi.org/10.1016/0021-9991\(92\)90240-Y](https://doi.org/10.1016/0021-9991(92)90240-Y).
- [955] Sun Y, Beckermann C. Diffuse interface modeling of two-phase flows based on averaging: Mass and momentum equations. *Phys D* 2004;198:281–308. <https://doi.org/10.1016/j.physd.2004.09.003>.
- [956] Wei HL, Liu FQ, Liao WH, Liu TT. Prediction of spatiotemporal variations of deposit profiles and inter-track voids during laser directed energy deposition. *Addit Manuf.* 2020;34:101219. <https://doi.org/10.1016/j.addma.2020.101219>.
- [957] Xie J, Kar A, Rothenflue JA, Latham WP. Temperature-dependent absorptivity and cutting capability of CO₂, Nd:YAG and chemical oxygen–iodine lasers. *J Laser Appl.* 1997;9:77–85. <https://doi.org/10.2351/1.4745447>.
- [958] Pottlacher G, Hosaeus H, Kaschnitz E, Seifert A. Thermophysical properties of solid and liquid Inconel 718 alloy. *Scand J Metall* 2002;31:161–8.
- [959] Yu G, Gu D, Dai D, Xia M, Ma C, Shi Q. On the role of processing parameters in thermal behavior, surface morphology and accuracy during laser 3D printing of aluminum alloy. *J Phys D Appl Phys.* 2016;49. <https://doi.org/10.1088/0022-3727/49/13/135501>.
- [960] Xia M, Gu D, Yu G, Dai D, Chen H, Shi Q. Influence of hatch spacing on heat and mass transfer, thermodynamics and laser processability during additive manufacturing of Inconel 718 alloy. *Int J Mach Tools Manuf.* 2016;109:147–57. <https://doi.org/10.1016/j.ijmactools.2016.07.010>.
- [961] Xia M, Gu D, Yu G, Dai D, Chen H, Shi Q. Porosity evolution and its thermodynamic mechanism of randomly packed powder-bed during selective laser melting of Inconel 718 alloy. *Int J Mach Tools Manuf.* 2017;116:96–106. <https://doi.org/10.1016/j.ijmactools.2017.01.005>.
- [962] Yuan W, Chen H, Cheng T, Wei Q. Effects of laser scanning speeds on different states of the molten pool during selective laser melting: Simulation and experiment. *Mater Des.* 2020;189:108542. <https://doi.org/10.1016/j.matdes.2020.108542>.
- [963] Tan JL, Tang C, Wong CH. A Computational Study on Porosity Evolution in Parts Produced by Selective Laser Melting. *Metal Mater Trans A Phys Metall Mater Sci.* 2018;49:3663–73. <https://doi.org/10.1007/s11661-018-4697-x>.
- [964] Tan JL, Tang C, Wong CH. Study and modeling of melt pool evolution in selective laser melting process of SS316L. *MRS Commun.* 2018;8:1178–83. <https://doi.org/10.1557/mrc.2018.180>.
- [965] Tan JL, Tang C, Wong CH. Thermal fluid modelling of selective laser melting. In: *Proceedings of the International Conference on Progress in Additive Manufacturing.* 2018-May (2018) 557–562. <https://doi.org/10.25341/D43S3S>.
- [966] Salarian M, Asgari H, Vlasea M. Pore space characteristics and corresponding effect on tensile properties of Inconel 625 fabricated via laser powder bed fusion. *Mater Sci Eng A* 2020;769:138525. <https://doi.org/10.1016/j.msea.2019.138525>.
- [967] Bayat M, Mohanty S, Hattel JH. Multiphysics modelling of lack-of-fusion voids formation and evolution in IN718 made by multi-track/multi-layer L-PBF. *Int J Heat Mass Transf.* 2019;139:95–114. <https://doi.org/10.1016/j.ijheatmasstransfer.2019.05.003>.

- [968] Lin R, Wang H ping, Lu F, Solomon J, Carlson BE. Numerical study of keyhole dynamics and keyhole-induced porosity formation in remote laser welding of Al alloys. *Int J Heat Mass Transf.* 2017;108:244–56. <https://doi.org/10.1016/j.ijheatmasstransfer.2016.12.019>.
- [969] Panwisawas C, Perumal B, Ward RM, Turner N, Turner RP, Brooks JW, et al. Keyhole formation and thermal fluid flow-induced porosity during laser fusion welding in titanium alloys: Experimental and modelling. *Acta Mater.* 2017;126:251–63. <https://doi.org/10.1016/j.actamat.2016.12.062>.
- [970] Panwisawas C, Sovani Y, Turner RP, Brooks JW, Basoalto HC, Choquet I. Modelling of thermal fluid dynamics for fusion welding. *J Mater Process Technol.* 2018;252:176–82. <https://doi.org/10.1016/j.jmatprot.2017.09.019>.
- [971] Bayat M, Thanki A, Mohanty S, Witvrouw A, Yang S, Thorborg J, et al. Keyhole-induced porosities in Laser-based Powder Bed Fusion (L-PBF) of Ti6Al4V: High-fidelity modelling and experimental validation. *Addit Manuf.* 2019;30. <https://doi.org/10.1016/j.addma.2019.100835>.
- [972] Le KQ, Tang C, Wong CH. On the study of keyhole-mode melting in selective laser melting process. *Int J Therm Sci* 2019;145. <https://doi.org/10.1016/j.ijthermalsci.2019.105992>.
- [973] Tang C, Tan JL, Wong CH. A numerical investigation on the physical mechanisms of single track defects in selective laser melting. *Int J Heat Mass Transf.* 2018; 126:957–68. <https://doi.org/10.1016/j.ijheatmasstransfer.2018.06.073>.
- [974] Yan W, Ge W, Qian Y, Lin S, Zhou B, Liu WK, et al. Multi-physics modeling of single/multiple-track defect mechanisms in electron beam selective melting. *Acta Mater.* 2017;134:324–33. <https://doi.org/10.1016/j.actamat.2017.05.061>.
- [975] Zheng M, Wei L, Chen J, Zhang Q, Zhong C, Lin X, et al. A novel method for the molten pool and porosity formation modelling in selective laser melting. *Int J Heat Mass Transf.* 2019;140:1091–105. <https://doi.org/10.1016/j.ijheatmasstransfer.2019.06.038>.
- [976] Tang C, Le KQ, Wong CH. Physics of humping formation in laser powder bed fusion. *Int J Heat Mass Transf.* 2020;149. <https://doi.org/10.1016/j.ijheatmasstransfer.2019.119172>.
- [977] Charles A, Bayat M, Elkaseer A, Thijs L, Hattel JH, Scholz S. Elucidation of dross formation in laser powder bed fusion at down-facing surfaces: Phenomenon-oriented multiphysics simulation and experimental validation. *Addit Manuf.* 2022;50. <https://doi.org/10.1016/j.addma.2021.102551>.
- [978] Yan W, Qian Y, Ge W, Lin S, Liu WK, Lin F, et al. Meso-scale modeling of multiple-layer fabrication process in Selective Electron Beam Melting: Inter-layer/track voids formation. *Mater Des.* 2018;141:210–9. <https://doi.org/10.1016/j.matdes.2017.12.031>.
- [979] Le KQ, Wong CH, Chua KHG, Tang C, Du H. Discontinuity of overhanging melt track in selective laser melting process. *Int J Heat Mass Transf.* 2020;162. <https://doi.org/10.1016/j.ijheatmasstransfer.2020.120284>.
- [980] Bayat M, Nadimpalli VK, Pedersen DB, Hattel JH. A fundamental investigation of thermo-capillarity in laser powder bed fusion of metals and alloys. *Int J Heat Mass Transf.* 2021;166. <https://doi.org/10.1016/j.ijheatmasstransfer.2020.120766>.
- [981] Tseng CC, Li CJ. Numerical investigation of interfacial dynamics for the melt pool of Ti-6Al-4V powders under a selective laser. *Int J Heat Mass Transf.* 2019; 134:906–19. <https://doi.org/10.1016/j.ijheatmasstransfer.2019.01.030>.
- [982] Wu YC, San CH, Chang CH, Lin HJ, Marwan R, Baba S, et al. Numerical modeling of melt-pool behavior in selective laser melting with random powder distribution and experimental validation. *J Mater Process Technol.* 2018;254:72–8. <https://doi.org/10.1016/j.jmatprot.2017.11.032>.
- [983] Lee YS, Zhang W. Modeling of heat transfer, fluid flow and solidification microstructure of nickel-base superalloy fabricated by laser powder bed fusion. *Addit Manuf.* 2016;12:178–88. <https://doi.org/10.1016/j.addma.2016.05.003>.
- [984] Cao L. Mesoscopic-scale simulation of pore evolution during laser powder bed fusion process. *Comput Mater Sci.* 2020;179:109686. <https://doi.org/10.1016/j.commatsci.2020.109686>.
- [985] Cao L. Workpiece-scale numerical simulations of SLM molten pool dynamic behavior of 316L stainless steel. *Comput Math Appl* 2020. <https://doi.org/10.1016/j.camwa.2020.04.020>.
- [986] Pei W, Zhengying W, Zhen C, Junfeng L, Shuzhe Z, Jun D. Numerical simulation and parametric analysis of selective laser melting process of AlSi10Mg powder. *Appl Phys A Mater Sci Process.* 2017;123:1–15. <https://doi.org/10.1007/s00339-017-1143-7>.
- [987] Wang Z, Yan W, Liu WK, Liu M. Powder-scale multi-physics modeling of multi-layer multi-track selective laser melting with sharp interface capturing method. *Comput Mech.* 2019;63:649–61. <https://doi.org/10.1007/s00466-018-1614-5>.
- [988] Gu H, Li L. International Journal of Heat and Mass Transfer Computational fluid dynamic simulation of gravity and pressure effects in laser metal deposition for potential additive manufacturing in space. *Int J Heat Mass Transf.* 2019;140:51–65. <https://doi.org/10.1016/j.ijheatmasstransfer.2019.05.081>.
- [989] Körner C, Bauereiß A, Attar E. Fundamental consolidation mechanisms during selective beam melting of powders. *Model Simul Mat Sci Eng.* 2013;21. <https://doi.org/10.1088/0965-0393/21/8/085011>.
- [990] Körner C, Attar E, Heintl P. Mesoscopic simulation of selective beam melting processes. *J Mater Process Technol.* 2011;211:978–87. <https://doi.org/10.1016/j.jmatprot.2010.12.016>.
- [991] Markl M, Ammer R, Rüdte U, Körner C. Numerical investigations on hatching process strategies for powder-bed-based additive manufacturing using an electron beam. *Int J Adv Manuf Technol* 2015;78:239–47. <https://doi.org/10.1007/s00170-014-6594-9>.
- [992] Zheng M, Wei L, Chen J, Zhang Q, Li J, Sui S, et al. Surface morphology evolution during pulsed selective laser melting: Numerical and experimental investigations. *Appl Surf Sci.* 2019;496:143649. <https://doi.org/10.1016/j.apsusc.2019.143649>.
- [993] König VE, Scherr R, Markl M, Körner C. Multi-material model for the simulation of powder bed fusion additive manufacturing. *Comput Mater Sci.* 2021;194. <https://doi.org/10.1016/j.commatsci.2021.110415>.
- [994] Sun Z, Chueh YH, Li L. Multiphase mesoscopic simulation of multiple and functionally gradient materials laser powder bed fusion additive manufacturing processes. *Addit Manuf.* 2020;35:101448. <https://doi.org/10.1016/j.addma.2020.101448>.
- [995] Gu H, Wei C, Li L, Ryan M, Setchi R, Han Q, et al. Numerical and experimental study of molten pool behaviour and defect formation in multi-material and functionally graded materials laser powder bed fusion. *Adv Powder Technol* 2021;32:4303–21. <https://doi.org/10.1016/j.apt.2021.09.036>.
- [996] Yao L, Huang S, Ramamurty U, Xiao Z. On the formation of “Fish-scale” morphology with curved grain interfacial microstructures during selective laser melting of dissimilar alloys. *Acta Mater.* 2021;220:117331. <https://doi.org/10.1016/j.actamat.2021.117331>.
- [997] ALE3D for Industry (ALE3D4I); n.d.
- [998] McCallen C. ALE3D: arbitrary lagrange eulerian three-and two dimensional modeling and simulation capability. In: Lawrence Livermore National Laboratory (LLNL); 2012.
- [999] Khairallah SA, Anderson A. Mesoscopic simulation model of selective laser melting of stainless steel powder. *J Mater Process Technol.* 2014;214:2627–36. <https://doi.org/10.1016/j.jmatprot.2014.06.001>.
- [1000] Khairallah SA, Anderson AT, Rubenchik A, King WE. Laser powder-bed fusion additive manufacturing: Physics of complex melt flow and formation mechanisms of pores, spatter, and denudation zones. *Acta Mater.* 2016;108:36–45. <https://doi.org/10.1016/j.actamat.2016.02.014>.
- [1001] Roehling JD, Khairallah SA, Shen Y, Bayramian A, Boley CD, Rubenchik AM, et al. Physics of large-area pulsed laser powder bed fusion. *Addit Manuf.* 2021; 46:102186. <https://doi.org/10.1016/j.addma.2021.102186>.
- [1002] Meier C, Fuchs SL, Hart AJ, Wall WA. A novel smoothed particle hydrodynamics formulation for thermo-capillary phase change problems with focus on metal additive manufacturing melt pool modeling. *Comput Methods Appl Mech Eng.* 2021;381:113812. <https://doi.org/10.1016/j.cma.2021.113812>.
- [1003] Liu S, Liu J, Chen J, Liu X. Influence of surface tension on the molten pool morphology in laser melting. *Int J Therm Sci* 2019;146:106075. <https://doi.org/10.1016/j.ijthermalsci.2019.106075>.
- [1004] Magana A, Yoshioka J, Eshraghi M, Allu P. Multiphysics Modeling of Thermal Behavior, Melt Pool Geometry, and Surface Topology During Laser Additive Manufacturing. *Mater Des.* 2022;219:110831. <https://doi.org/10.1016/j.matdes.2022.110831>.
- [1005] Zhang YM, Lim CWJ, Tang C, Li B. Numerical investigation on heat transfer of melt pool and clad generation in directed energy deposition of stainless steel. *Int J Therm Sci* 2021;165. <https://doi.org/10.1016/j.ijthermalsci.2021.106954>.
- [1006] Sun Z, Guo W, Li L. Numerical modelling of heat transfer, mass transport and microstructure formation in a high deposition rate laser directed energy deposition process. *Addit Manuf.* 2020;33.
- [1007] Song B, Yu T, Jiang X, Xi W, Lin X, Ma Z, et al. Development of the molten pool and solidification characterization in single bead multilayer direct energy deposition. *Addit Manuf.* 2022;49:102479. <https://doi.org/10.1016/j.addma.2021.102479>.

- [1008] Song B, Yu T, Jiang X, Xi W. Numerical model of transient convection pattern and forming mechanism of molten pool in laser cladding. *Numer Heat Transf A Appl.* 2019;75:855–73. <https://doi.org/10.1080/10407782.2019.1608777>.
- [1009] Meng X, Qin G, Zou Z. Investigation of humping defect in high speed gas tungsten arc welding by numerical modelling. *Mater Des.* 2016;94:69–78. <https://doi.org/10.1016/j.mates.2016.01.019>.
- [1010] Bayat M, Nadimpalli VK, Biondani FG, Jafarzadeh S, Thorborg J, Tiedje NS, et al. On the role of the powder stream on the heat and fluid flow conditions during Directed Energy Deposition of maraging steel—Multiphysics modeling and experimental validation. *Addit Manuf.* 2021;43. <https://doi.org/10.1016/j.addma.2021.102021>.
- [1011] Wu CS, Dorn L. Computer simulation of fluid dynamics and heat transfer in full-penetrated TIG weld pools with surface depression; 1994.
- [1012] Wu CS, Tsao KC. Modelling the three-dimensional fluid flow and heat transfer in a moving weld pool; 1990.
- [1013] Bai X, Colegrove P, Ding J, Zhou X, Diao C, Bridgeman P, et al. Numerical analysis of heat transfer and fluid flow in multilayer deposition of PAW-based wire and arc additive manufacturing. *Int J Heat Mass Transf.* 2018;124:504–16. <https://doi.org/10.1016/j.ijheatmasstransfer.2018.03.085>.
- [1014] Ke WC, Oliveira JP, Cong BQ, Ao SS, Qi ZW, Peng B, et al. Multi-layer deposition mechanism in ultra high-frequency pulsed wire arc additive manufacturing (WAAM) of NiTi shape memory alloys. *Addit Manuf.* 2022;50. <https://doi.org/10.1016/j.addma.2021.102513>.
- [1015] Ogino Y, Asai S, Hirata Y. Numerical simulation of WAAM process by a GMAW weld pool model. *Welding in the World.* 2018;62:393–401. <https://doi.org/10.1007/s40194-018-0556-z>.
- [1016] Ji F, Qin X, Hu Z, Xiong X, Ni M, Wu M. Influence of ultrasonic vibration on molten pool behavior and deposition layer forming morphology for wire and arc additive manufacturing. *Int Congr Heat Mass Transfer* 2022;130:105789. <https://doi.org/10.1016/j.icheatmasstransfer.2021.105789>.
- [1017] Li X, Zhao C, Sun T, Tan W. Revealing transient powder-gas interaction in laser powder bed fusion process through multi-physics modeling and high-speed synchrotron x-ray imaging. *Addit Manuf.* 2020;35:101362. <https://doi.org/10.1016/j.addma.2020.101362>.
- [1018] Jakumeit J, Zheng G, Laqua R, Clark SJ, Zielinski J, Schleifenbaum JH, et al. Modelling the complex evaporated gas flow and its impact on particle spattering during laser powder bed fusion. *Addit Manuf.* 2021;47:102332. <https://doi.org/10.1016/j.addma.2021.102332>.
- [1019] Wen S, Shin YC. Modeling of transport phenomena during the coaxial laser direct deposition process. *J Appl Phys.* 2010;108. <https://doi.org/10.1063/1.3474655>.
- [1020] Wen S, Shin YC. Modeling of the off-axis high power diode laser cladding process. *J Heat Transfer.* 2011;133. <https://doi.org/10.1115/1.4002447>.
- [1021] Ibarra-medina JR, Michael Vogel, Pinkerton AJ. A CFD model of laser cladding : From deposition head to melt pool dynamics. *Int Congr Appl Lasers Electro-Optics* 2011;1:378–86. <https://doi.org/10.2351/1.5062261>.
- [1022] Kovalev OB, Bedenko DV, Zaitsev AV. Development and application of laser cladding modeling technique : From coaxial powder feeding to surface deposition and bead formation. *Appl Math Model.* 2018;57:339–59. <https://doi.org/10.1016/j.apm.2017.09.043>.
- [1023] Bedenko DV, Kovalev OB, Smurov I, Zaitsev AV. International Journal of Heat and Mass Transfer Numerical simulation of transport phenomena, formation the bead and thermal behavior in application to industrial DMD technology. *Int J Heat Mass Transf.* 2016;95:902–12. <https://doi.org/10.1016/j.ijheatmasstransfer.2015.12.046>.
- [1024] Bayat M, Nadipalli VK, Biondani FG, Jafarzadeh S, Thorborg J, Tiedje Niels.S, et al. On the role of the powder stream on the heat and fluid flow conditions during Directed Energy Deposition of maraging steel - Multiphysics modelling and experimental validation. *Addit Manuf.* (2021) 102021. <https://doi.org/10.1016/j.addma.2021.102021>.
- [1025] Yang Z, Wang S, Zhu L, Ning J, Xin B, Dun Y, et al. Manipulating molten pool dynamics during metal 3D printing by ultrasound. *Appl Phys Rev.* 2022;9:021416. <https://doi.org/10.1063/5.0082461>.
- [1026] Wang S, Zhu L, Dun Y, Yang Z, Fuh JYH, Yan W. Multi-physics modeling of direct energy deposition process of thin-walled structures: defect analysis. *Comput Mech.* 2021;67:1229–42. <https://doi.org/10.1007/s00466-021-01992-9>.
- [1027] Wang S, Zhu L, Ying J, Fuh H, Zhang H, Yan W. Multi-physics modeling and Gaussian process regression analysis of cladding track geometry for direct energy deposition. *Opt Lasers Eng.* 2020;127:105950. <https://doi.org/10.1016/j.optlaseng.2019.105950>.
- [1028] Choi J, Han L, Hua Y. Modeling and Experiments of Laser Cladding With Droplet Injection. *J Hea* 2005;127:978–86. <https://doi.org/10.1115/1.2005273>.
- [1029] Aggarwal A, Chouhan A, Patel S, Yadav DK, Kumar A, Vinod AR, et al. Role of impinging powder particles on melt pool hydrodynamics, thermal behaviour and microstructure in laser-assisted DED process: A particle-scale DEM – CFD – CA approach. *Int J Heat Mass Transf.* 2020;158:119989. <https://doi.org/10.1016/j.ijheatmasstransfer.2020.119989>.
- [1030] Horstemeyer MF. Integrated computational materials engineering (ICME) for metals: Concepts and case studies; 2017. <https://doi.org/10.1002/9781119018377>.
- [1031] Wang Y, Arabnejad S, Tanzer M, Pasini D. Hip implant design with three-dimensional porous architecture of optimized graded density, *Journal of Mechanical Design.* *Trans ASME* 2018;140. <https://doi.org/10.1115/1.4041208>.
- [1032] Bensoussan A, Lions J-L, Papanicolaou G. *Asymptotic Analysis for Periodic Structures*; 2011. <https://doi.org/10.1090/chel/374>.
- [1033] Andreasen E, Andreasen CS. How to determine composite material properties using numerical homogenization. *Comput Mater Sci.* 2014;83. <https://doi.org/10.1016/j.commatsci.2013.09.006>.
- [1034] Wulfinghoff S, Cavaliere F, Reese S. Model order reduction of nonlinear homogenization problems using a Hashin-Shtrikman type finite element method. *Comput Methods Appl Mech Eng.* 2018;330. <https://doi.org/10.1016/j.cma.2017.10.019>.
- [1035] Schmidt I. Numerical homogenisation of an elasto-plastic model-material with large elastic strains: Macroscopic yield surfaces and the Eulerian normality rule. *Comput Mech.* 2011;48. <https://doi.org/10.1007/s00466-011-0601-x>.
- [1036] Okada J, Washio T, Hisada T. Study of efficient homogenization algorithms for nonlinear problems. *Comput Mech.* 2010;46. <https://doi.org/10.1007/s00466-009-0432-1>.
- [1037] Matous K, Maniatty AM. Multiscale modeling of elasto-viscoplastic polycrystals subjected to finite deformations. *Interaction Multiscale Mech* 2009;2. <https://doi.org/10.12989/imm.2009.2.4.375>.
- [1038] Ameen MM, Peerlings RHJ, Geers MGD. A quantitative assessment of the scale separation limits of classical and higher-order asymptotic homogenization. *Eur J Mech A/Solids.* 2018;71. <https://doi.org/10.1016/j.euromechsol.2018.02.011>.
- [1039] Yvonnet J, Auffray N, Monchiet V. Computational second-order homogenization of materials with effective anisotropic strain-gradient behavior. *Int J Solids Struct.* 2020;191–192. <https://doi.org/10.1016/j.ijsolstr.2020.01.006>.
- [1040] Rokoš O, Ameen MM, Peerlings RHJ, Geers MGD. Micromorphic computational homogenization for mechanical metamaterials with patterning fluctuation fields. *J Mech Phys Solids.* 2019;123. <https://doi.org/10.1016/j.jmps.2018.08.019>.
- [1041] Lesičar T, Tonković Z, Sorčić J. A second-order two-scale homogenization procedure using C1 macrolevel discretization. *Comput Mech.* 2014;54. <https://doi.org/10.1007/s00466-014-0995-3>.
- [1042] Poh LH. Scale transition of a higher order plasticity model - A consistent homogenization theory from meso to macro. *J Mech Phys Solids.* 2013;61. <https://doi.org/10.1016/j.jmps.2013.09.004>.
- [1043] Geers MGD, Kouznetsova VG, Brekelmans WAM. Multi-scale computational homogenization: Trends and challenges. *J Comput Appl Math* 2010. <https://doi.org/10.1016/j.cam.2009.08.077>.
- [1044] Feyel F. Multiscale FE2 elastoviscoplastic analysis of composite structures. *Comput Mater Sci.* 1999;16. [https://doi.org/10.1016/s0927-0256\(99\)00077-4](https://doi.org/10.1016/s0927-0256(99)00077-4).
- [1045] Efendiev Y, Galvis J, Wu XH. Multiscale finite element methods for high-contrast problems using local spectral basis functions. *J Comput Phys.* 2011;230. <https://doi.org/10.1016/j.jcp.2010.09.026>.
- [1046] Geers MGD, Kouznetsova VG, Matouš K, Yvonnet J. Homogenization Methods and Multiscale Modeling: Nonlinear Problems. In: *Encyclopedia of Computational Mechanics Second Edition*; 2017. <https://doi.org/10.1002/9781119176817.ecm2107>.
- [1047] Adam L, Lietaer O, Mathieu S, Doghri I. Numerical simulation of additive manufacturing of polymers and polymer-based composites. In: *Structure and Properties of Additive Manufactured Polymer Components*, 2020. <https://doi.org/10.1016/B978-0-12-819535-2.00005-3>.

- [1048] Somlo K, Poulos K, Funch CV, Niordson CF. Anisotropic tensile behaviour of additively manufactured Ti-6Al-4V simulated with crystal plasticity. *Mech Mater* 2021;162. <https://doi.org/10.1016/j.mechmat.2021.104034>.
- [1049] Kanit T, Forest S, Galliet I, Mounoury V, Jeulin D. Determination of the size of the representative volume element for random composites: Statistical and numerical approach. *Int J Solids Struct*. 2003;40. [https://doi.org/10.1016/S0020-7683\(03\)00143-4](https://doi.org/10.1016/S0020-7683(03)00143-4).
- [1050] Bargmann S, Klusemann B, Markmann J, Schnabel JE, Schneider K, Soyarslan C, et al. Generation of 3D representative volume elements for heterogeneous materials: A review. *Prog Mater Sci*. 2018;96. <https://doi.org/10.1016/j.pmatsci.2018.02.003>.
- [1051] Peirce D, Asaro RJ, Needleman A. Material rate dependence and localized deformation in crystalline solids. *Acta Metall* 1983;31. [https://doi.org/10.1016/0001-6160\(83\)90014-7](https://doi.org/10.1016/0001-6160(83)90014-7).
- [1052] Roters F, Diehl M, Shanthraj P, Eisenlohr P, Reuber C, Wong SL, et al. DAMASK – The Düsseldorf Advanced Material Simulation Kit for modeling multi-physics crystal plasticity, thermal, and damage phenomena from the single crystal up to the component scale. *Comput Mater Sci*. 2019;158. <https://doi.org/10.1016/j.commatsci.2018.04.030>.
- [1053] Quey R, Dawson PR, Barbe F. Large-scale 3D random polycrystals for the finite element method: Generation, meshing and remeshing. *Comput Methods Appl Mech Eng*. 2011;200. <https://doi.org/10.1016/j.cma.2011.01.002>.
- [1054] Groeber MA, Jackson MA. DREAM.3D: A Digital Representation Environment for the Analysis of Microstructure in 3D. *Integr Mater Manuf Innov*. 2014;3. <https://doi.org/10.1186/2193-9772-3-5>.
- [1055] Motaman SAH, Roters F, Haase C. Anisotropic polycrystal plasticity due to microstructural heterogeneity: A multi-scale experimental and numerical study on additively manufactured metallic materials. *Acta Mater*. 2020;185. <https://doi.org/10.1016/j.actamat.2019.12.003>.
- [1056] Charmi A, Falkenberg R, Ávila L, Mohr G, Sommer K, Ulbricht A, et al. Mechanical anisotropy of additively manufactured stainless steel 316L: An experimental and numerical study. *Mater Sci Eng A* 2021;799. <https://doi.org/10.1016/j.msea.2020.140154>.
- [1057] Riyad IA, Feather WG, Vasilev E, Lebensohn RA, McWilliams BA, Pilchak AL, et al. Modeling the role of local crystallographic correlations in microstructures of Ti-6Al-4V using a correlated structure visco-plastic self-consistent polycrystal plasticity formulation. *Acta Mater*. 2021;203. <https://doi.org/10.1016/j.actamat.2020.116502>.
- [1058] Hill R. A theory of the yielding and plastic flow of anisotropic metals. *Proc R Soc Lond A Math Phys Sci*. 1948;193. <https://doi.org/10.1098/rspa.1948.0045>.
- [1059] Barlat F, Aretz H, Yoon JW, Karabin ME, Brem JC, Dick RE. Linear transformation-based anisotropic yield functions. *Int J Plast*. 2005;21. <https://doi.org/10.1016/j.ijplas.2004.06.004>.
- [1060] Karafillis AP, Boyce MC. A general anisotropic yield criterion using bounds and a transformation weighting tensor. *J Mech Phys Solids*. 1993;41. [https://doi.org/10.1016/0022-5096\(93\)90073-O](https://doi.org/10.1016/0022-5096(93)90073-O).
- [1061] Zhang H, Diehl M, Roters F, Raabe D. A virtual laboratory using high resolution crystal plasticity simulations to determine the initial yield surface for sheet metal forming operations. *Int J Plast*. 2016;80. <https://doi.org/10.1016/j.ijplas.2016.01.002>.
- [1062] Kraska M, Doig M, Tikhomirov D, Raabe D, Roters F. Virtual material testing for stamping simulations based on polycrystal plasticity. *Comput Mater Sci*. 2009;46. <https://doi.org/10.1016/j.commatsci.2009.03.025>.
- [1063] Frodal BH, Dæhli LEB, Børvik T, Hopperstad OS. Modelling and simulation of ductile failure in textured aluminium alloys subjected to compression-tension loading. *Int J Plast*. 2019;118. <https://doi.org/10.1016/j.ijplas.2019.01.008>.
- [1064] Wilson-Heid AE, Qin S, Beese AM. Anisotropic multiaxial plasticity model for laser powder bed fusion additively manufactured Ti-6Al-4V. *Mater Sci Eng A* 2018;738. <https://doi.org/10.1016/j.msea.2018.09.077>.
- [1065] Somlo K, Frodal BH, Funch CV, Poulos K, Winther G, Hopperstad OS, Børvik T, Niordson CF. Anisotropic yield surfaces of additively manufactured metals simulated with crystal plasticity. *Eur J Mech, A/Solids*. 2022;94. <https://doi.org/10.1016/j.euromechsol.2022.104506>.
- [1066] Hosford WF. A generalized isotropic yield criterion. *Journal of Applied Mechanics*. Transactions ASME. 1972;39. <https://doi.org/10.1115/1.3422732>.
- [1067] Seifi M, Dahar M, Aman R, Harrysson O, Beuth J, Lewandowski JJ. Evaluation of Orientation Dependence of Fracture Toughness and Fatigue Crack Propagation Behavior of As-Deposited ARCAM EBM Ti-6Al-4V. *JOM* 2015;67. <https://doi.org/10.1007/s11837-015-1298-7>.
- [1068] Agius D, Kourousis KI, Wallbrink C, Song T. Cyclic plasticity and microstructure of as-built SLM Ti-6Al-4V: The effect of build orientation. *Mater Sci Eng A* 2017;701. <https://doi.org/10.1016/j.msea.2017.06.069>.
- [1069] ter Haar GM, Becker TH. Selective laser melting produced Ti-6Al-4V: Post-process heat treatments to achieve superior tensile properties. *Materials*. 2018;11. <https://doi.org/10.3390/ma11010146>.
- [1070] Surreddi KB, Oikonomou C, Karlsson P, Olsson M, Pejryd L. In-situ micro-tensile testing of additive manufactured maraging steels in the SEM: Influence of build orientation, thickness and roughness on the resulting mechanical properties. *Proceedings Euro PM 2017: International Powder Metallurgy Congress and Exhibition*. 2017.
- [1071] Halama R, Kourousis K, Pagáč M, Paška Z. Cyclic plasticity of additively manufactured metals. In: *Cyclic Plasticity of Metals: Modeling Fundamentals and Applications*, 2021. <https://doi.org/10.1016/B978-0-12-819293-1.00022-X>.
- [1072] Chen W, Voisin T, Zhang Y, Florian JB, Spadaccini CM, McDowell DL, et al. Microscale residual stresses in additively manufactured stainless steel. *Nat Commun*. 2019;10. <https://doi.org/10.1038/s41467-019-12265-8>.
- [1073] Hu D, Grilli N, Wang L, Yang M, Yan W. Microscale residual stresses in additively manufactured stainless steel: Computational simulation. *J Mech Phys Solids*. 2022;161. <https://doi.org/10.1016/j.jmps.2022.104822>.
- [1074] Mercelis P, Kruth JP. Residual stresses in selective laser sintering and selective laser melting. *Rapid Prototyp J*. 2006;12. <https://doi.org/10.1108/13552540610707013>.
- [1075] Ali H, Ghadbeigi H, Mumtaz K. Effect of scanning strategies on residual stress and mechanical properties of Selective Laser Melted Ti6Al4V. *Mater Sci Eng A* 2018;712. <https://doi.org/10.1016/j.msea.2017.11.103>.
- [1076] Gibson LJ, Ashby MF. *Cellular solids: Structure and properties*, second edition; 2014. <https://doi.org/10.1017/CBO9781139878326>.
- [1077] Schaedler TA, Carter WB. *Architected Cellular Materials*. *Annu Rev Mater Res*. 2016;46:187–210. <https://doi.org/10.1146/annurev-matsci-070115-031624>.
- [1078] Bonatti C, Mohr D. Mechanical performance of additively-manufactured anisotropic and isotropic smooth shell-lattice materials: Simulations & experiments. *J Mech Phys Solids*. 2019;122. <https://doi.org/10.1016/j.jmps.2018.08.022>.
- [1079] Fleck NA, Deshpande VS, Ashby MF. Micro-architected materials: Past, present and future. In: *Proceedings of the Royal Society A: Mathematical, Physical and Engineering Sciences*; 2010. <https://doi.org/10.1098/rspa.2010.0215>.
- [1080] Chen LY, Liang SX, Liu Y, Zhang LC. Additive manufacturing of metallic lattice structures: Unconstrained design, accurate fabrication, fascinated performances, and challenges. *Mater Sci Eng R Rep* 2021;146. <https://doi.org/10.1016/j.mser.2021.100648>.
- [1081] Rys J, Steenhuisen S, Schumacher C, Cronauer C, Daraio C. Locally addressable material properties in 3D micro-architectures. *Extreme Mech Lett*. 2019;28. <https://doi.org/10.1016/j.eml.2019.02.001>.
- [1082] Wang Y, Sigmund O. Quasiperiodic mechanical metamaterials with extreme isotropic stiffness. *Extreme Mech Lett*. 2020;34. <https://doi.org/10.1016/j.eml.2019.100596>.
- [1083] Phani AS, Woodhouse J, Fleck NA. Wave propagation in two-dimensional periodic lattices. *J Acoust Soc Am*. 2006;119. <https://doi.org/10.1121/1.2179748>.
- [1084] Andreassen E, Jensen JS. Topology optimization of periodic microstructures for enhanced dynamic properties of viscoelastic composite materials. *Struct Multidiscip Optim* 2014;49. <https://doi.org/10.1007/s00158-013-1018-2>.
- [1085] Schultz J, Griese D, Ju J, Shankar P, Summers JD, Thompson L. Design of honeycomb mesostructures for crushing energy absorption, *Journal of Mechanical Design*. Trans ASME. 2012;134. <https://doi.org/10.1115/1.4006739>.
- [1086] Robbins J, Owen SJ, Clark BW, Voth TE. An efficient and scalable approach for generating topologically optimized cellular structures for additive manufacturing. *Addit Manuf*. 2016;12. <https://doi.org/10.1016/j.addma.2016.06.013>.
- [1087] Niknam H, Akbarzadeh AH, Rodrigue D, Theriault D. Architected multi-directional functionally graded cellular plates. *Mater Des*. 2018;148. <https://doi.org/10.1016/j.matdes.2018.02.058>.

- [1088] Bendsøe MP, Kikuchi N. Generating optimal topologies in structural design using a homogenization method. *Comput Methods Appl Mech Eng.* 1988;71. [https://doi.org/10.1016/0045-7825\(88\)90086-2](https://doi.org/10.1016/0045-7825(88)90086-2).
- [1089] Tancogne-Dejean T, Mohr D. Elastically-isotropic truss lattice materials of reduced plastic anisotropy. *Int J Solids Struct.* 2018;138. <https://doi.org/10.1016/j.ijsolstr.2017.12.025>.
- [1090] Ma Q, Zhang L, Ding J, Qu S, Fu J, Zhou M, et al. Elastically-isotropic open-cell minimal surface shell lattices with superior stiffness via variable thickness design. *Addit Manuf.* 2021;47. <https://doi.org/10.1016/j.addma.2021.102293>.
- [1091] Doyoyo M, Hu JW. Multi-axial failure of metallic strut-lattice materials composed of short and slender struts. *Int J Solids Struct.* 2006;43. <https://doi.org/10.1016/j.ijsolstr.2005.12.001>.
- [1092] Smith J, Liu WK, Cao J. A general anisotropic yield criterion for pressure-dependent materials. *Int J Plast.* 2015;75. <https://doi.org/10.1016/j.ijsplas.2015.08.009>.
- [1093] Deshpande VS, Fleck NA, Ashby MF. Effective properties of the octet-truss lattice material. *J Mech Phys Solids.* 2001;49. [https://doi.org/10.1016/S0022-5096\(01\)00010-2](https://doi.org/10.1016/S0022-5096(01)00010-2).
- [1094] Eynbeygui M, Arghavani J, Akbarzadeh AH, Naghdabadi R. Anisotropic elastic-plastic behavior of architected pyramidal lattice materials. *Acta Mater.* 2020; 183. <https://doi.org/10.1016/j.actamat.2019.10.038>.
- [1095] da Silva GA, Aage N, Beck AT, Sigmund O. Local versus global stress constraint strategies in topology optimization: A comparative study. *Int J Numer Methods Eng.* 2021;122. <https://doi.org/10.1002/nme.6781>.
- [1096] Wu J, Aage N, Westermann R, Sigmund O. Infill Optimization for Additive Manufacturing-Approaching Bone-Like Porous Structures. *IEEE Trans Vis Comput Graph.* 2018;24. <https://doi.org/10.1109/TVCG.2017.2655523>.
- [1097] Lazarov BS. Topology optimization using multiscale finite element method for high-contrast media. In: *Lecture Notes in Computer Science (Including Subseries Lecture Notes in Artificial Intelligence and Lecture Notes in Bioinformatics)*; 2014. https://doi.org/10.1007/978-3-662-43880-0_38.
- [1098] Alexandersen J, Lazarov BS. Topology optimisation of manufacturable microstructural details without length scale separation using a spectral coarse basis preconditioner. *Comput Methods Appl Mech Eng.* 2015;290. <https://doi.org/10.1016/j.cma.2015.02.028>.
- [1099] Gorguluarslan RM, Park SI, Rosen DW, Choi SK. A Multilevel Upscaling Method for Material Characterization of Additively Manufactured Part under Uncertainties. *Journal of Mechanical Design.* *Trans ASME.* 2015;137. <https://doi.org/10.1115/1.4031012>.
- [1100] Bayat M, de Baere D, Mohanty S, Hattel J. Multi-scale multiphysics simulation of metal L-PBF AM process and subsequent mechanical analysis. In: *The 12th International Seminar "Numerical Analysis of Weldability, Graz, Austria, 2018*.
- [1101] Zeng K, Pal D, Gong HJ, Patil N, Stucker B. Comparison of 3DSIM thermal modelling of selective laser melting using new dynamic meshing method to ANSYS. *Mater Sci Technol (United Kingdom).* 2015;31:945–56. <https://doi.org/10.1179/1743284714Y.0000000703>.
- [1102] Denlinger ER, Gouge M, Irwin J, Michaleris P. Thermomechanical model development and in situ experimental validation of the Laser Powder-Bed Fusion process. *Addit Manuf.* 2017;16:73–80. <https://doi.org/10.1016/j.addma.2017.05.001>.
- [1103] Olleak A, Xi Z. A scan-wise adaptive remeshing framework for thermal simulation of the selective laser melting process. *Int J Adv Manuf Technol* 2020;107: 573–84. <https://doi.org/10.1007/s00170-020-04995-7>.
- [1104] Moran TP, Warner DH, Phan N. Scan-by-scan part-scale thermal modelling for defect prediction in metal additive manufacturing. *Addit Manuf.* 2021;37: 101667. <https://doi.org/10.1016/j.addma.2020.101667>.
- [1105] Moran TP, Li P, Warner DH, Phan N. Utility of superposition-based finite element approach for part-scale thermal simulation in additive manufacturing. *Addit Manuf.* 2018;21:215–9. <https://doi.org/10.1016/j.addma.2018.02.015>.
- [1106] Yang Y, Knol MF, van Keulen F, Ayas C. A semi-analytical thermal modelling approach for selective laser melting. *Addit Manuf.* 2018;21:284–97. <https://doi.org/10.1016/j.addma.2018.03.002>.
- [1107] Yang Y, van Keulen F, Ayas C. A computationally efficient thermal model for selective laser melting. *Addit Manuf.* 2020;31:100955. <https://doi.org/10.1016/j.addma.2019.100955>.
- [1108] Yang Y, Zhou X, Li Q, Ayas C. A computationally efficient thermo-mechanical model for wire arc additive manufacturing. *Addit Manuf.* 2021;46. <https://doi.org/10.1016/j.addma.2021.102090>.
- [1109] Zhang W, Tong M, Harrison NM. Resolution, energy and time dependency on layer scaling in finite element modelling of laser beam powder bed fusion additive manufacturing. *Addit Manuf.* 2019;28:610–20. <https://doi.org/10.1016/j.addma.2019.05.002>.
- [1110] Zaeh MF, Branner G. Investigations on residual stresses and deformations in selective laser melting. *Prod Eng* 2010;4:35–45. <https://doi.org/10.1007/s11740-009-0192-y>.
- [1111] Prabhakar P, Sames WJ, Dehoff R, Babu SS. Computational modeling of residual stress formation during the electron beam melting process for Inconel 718. *Addit Manuf.* 2015;7:83–91. <https://doi.org/10.1016/j.addma.2015.03.003>.
- [1112] Chiumenti M, Neiva E, Salsi E, Cervera M, Badia S, Moya J, et al. Numerical modelling and experimental validation in Selective Laser Melting. *Addit Manuf.* 2017;18:171–85. <https://doi.org/10.1016/j.addma.2017.09.002>.
- [1113] Zhang Y, Gandin CA, Bellet M. Finite Element Modeling of Powder Bed Fusion at Part Scale by a Super-Layer Deposition Method Based on Level Set and Mesh Adaptation. *Journal of Manufacturing Science and Engineering.* *Trans ASME.* 2022;144. <https://doi.org/10.1115/1.4052386>.
- [1114] Bayat M, Klingaa A, de Baere D, Thorborg J, Tiedje NS, Hattel JH. Part-scale thermo-mechanical modelling of distortions in L-PBF – Analysis of the sequential flash heating method with experimental validation. *Addit Manuf.* under revi (2020).
- [1115] Neiva E, Chiumenti M, Cervera M, Salsi E, Piscopo G, Badia S, et al. Numerical modelling of heat transfer and experimental validation in Powder-Bed Fusion with the Virtual Domain Approximation. (2018) 1–26. <http://arxiv.org/abs/1811.12372>.
- [1116] Bayat M, Klingaa CG, Mohanty S, de Baere D, Thorborg J, Tiedje NS, et al. Part-scale thermo-mechanical modelling of distortions in Laser Powder Bed Fusion – Analysis of the sequential flash heating method with experimental validation. *Addit Manuf.* 2020;36. <https://doi.org/10.1016/j.addma.2020.101508>.
- [1117] Chen Q, Liang X, Hayduke D, Liu J, Cheng L, Oskin J, et al. An inherent strain based multiscale modeling framework for simulating part-scale residual deformation for direct metal laser sintering. *Addit Manuf.* 2019;28:406–18. <https://doi.org/10.1016/j.addma.2019.05.021>.
- [1118] Ueda Y, Fukuda K, Tanigawa M. New Measuring Method of Three Dimensional Residual Stresses Based on Theory of Inherent Strain, *Welding Mechanics, Strength & Design.* (1979).
- [1119] Ueda Y, Fukuda K, Nakacho K, Endo S. A new measuring method of residual stresses with the aid of finite element method and reliability of estimated values. *J Soc Naval Architects Japan* 1975;138:499–507.
- [1120] Liang X, Cheng L, Chen Q, Yang Q, To AC. A modified method for estimating inherent strains from detailed process simulation for fast residual distortion prediction of single-walled structures fabricated by directed energy deposition. *Addit Manuf.* 2018;23:471–86. <https://doi.org/10.1016/j.addma.2018.08.029>.
- [1121] Li C, Guo Y, Fang X, Fang F. A scalable predictive model and validation for residual stress and distortion in selective laser melting. *CIRP Ann* 2018;67:249–52. <https://doi.org/10.1016/j.cirp.2018.04.105>.
- [1122] Li C, Liu JF, Guo YB. Prediction of Residual Stress and Part Distortion in Selective Laser Melting. *Procedia CIRP.* 2016;45:171–4. <https://doi.org/10.1016/j.procir.2016.02.058>.
- [1123] Li C, Liu JF, Fang XY, Guo YB. Efficient predictive model of part distortion and residual stress in selective laser melting. *Addit Manuf.* 2017;17:157–68. <https://doi.org/10.1016/j.addma.2017.08.014>.
- [1124] Gouge M, Denlinger E, Irwin J, Li C, Michaleris P. Experimental Validation of Thermo-mechanical Part-Scale Modeling for Laser Powder Bed Fusion Processes. *Addit Manuf.* 2019;29:100771. <https://doi.org/10.1016/j.addma.2019.06.022>.
- [1125] Liang X, Chen Q, Cheng L, Hayduke D, To AC. Modified inherent strain method for efficient prediction of residual deformation in direct metal laser sintered components. *Comput Mech.* 2019;64:1719–33. <https://doi.org/10.1007/s00466-019-01748-6>.
- [1126] Dong W, Liang X, Chen Q, Hinnebusch S, Zhou Z, To AC. A new procedure for implementing the modified inherent strain method with improved accuracy in predicting both residual stress and deformation for laser powder bed fusion. *Addit Manuf.* 2021;47. <https://doi.org/10.1016/j.addma.2021.102345>.

- [1127] Dong W, Jimenez XA, To AC. Temperature-dependent modified inherent strain method for predicting residual stress and distortion of Ti6Al4V walls manufactured by wire-arc directed energy deposition. *Addit Manuf.* 2023;62. <https://doi.org/10.1016/j.addma.2022.103386>.
- [1128] Wang J, Zhang J, Liang L, Huang A, Yang G, Pang S. A line-based flash heating method for numerical modeling and prediction of directed energy deposition manufacturing process. *J Manuf Process.* 2022;73:822–38. <https://doi.org/10.1016/j.jmapro.2021.11.041>.
- [1129] Durodola JF. Machine learning for design, phase transformation and mechanical properties of alloys. *Prog Mater Sci.* 2022;123. <https://doi.org/10.1016/j.pmatsci.2021.100797>.
- [1130] Raza A, Deen KM, Jaafreh R, Hamad K, Haider A, Haider W. Incorporation of machine learning in additive manufacturing: a review. *Int J Adv Manuf Technol* 2022. <https://doi.org/10.1007/s00170-022-09916-4>.
- [1131] Fu Y, Downey ARJ, Yuan L, Zhang T, Pratt A, Balogun Y. Machine learning algorithms for defect detection in metal laser-based additive manufacturing: A review. *J Manuf Process.* 2022;75:693–710. <https://doi.org/10.1016/j.jmapro.2021.12.061>.
- [1132] Wang P, Yang Y, Moghaddam NS. Process modeling in laser powder bed fusion towards defect detection and quality control via machine learning: The state-of-the-art and research challenges. *J Manuf Process.* 2022;73:961–84. <https://doi.org/10.1016/j.jmapro.2021.11.037>.
- [1133] Qin J, Hu F, Liu Y, Witherell P, Wang CCL, Rosen DW, et al. Research and application of machine learning for additive manufacturing. *Addit Manuf.* 2022;52. <https://doi.org/10.1016/j.addma.2022.102691>.
- [1134] Sharma R, Guo YB. Chapter 8 computational modeling and physics-informed machine learning of metal additive manufacturing: state-of-the-art and future perspective; 2021. www.begellhouse.com.
- [1135] Elambasseril J, Brandt M. Artificial intelligence: way forward to empower metal additive manufacturing product development – an overview. *Mater Today Proc.* 2022;58:461–5. <https://doi.org/10.1016/j.matpr.2022.02.485>.
- [1136] Guo S, Agarwal M, Cooper C, Tian Q, Gao RX, Guo WG, et al. Machine learning for metal additive manufacturing: Towards a physics-informed data-driven paradigm. *J Manuf Syst.* 2022;62:145–63. <https://doi.org/10.1016/j.jmsy.2021.11.003>.
- [1137] Nasiri S, Khosravani MR. Machine learning in predicting mechanical behavior of additively manufactured parts. *J Mater Res Technol* 2021;14:1137–53. <https://doi.org/10.1016/j.jmrt.2021.07.004>.
- [1138] Johnson NS, Vulimiri PS, To AC, Zhang X, Brice CA, Kappes BB, et al. Invited review: Machine learning for materials developments in metals additive manufacturing. *Addit Manuf.* 2020;36. <https://doi.org/10.1016/j.addma.2020.101641>.
- [1139] Jin Z, Zhang Z, Demir K, Gu GX. Machine Learning for Advanced Additive Manufacturing. *Matter.* 2020;3:1541–56. <https://doi.org/10.1016/j.matt.2020.08.023>.
- [1140] Qi X, Chen G, Li Y, Cheng X, Li C. Applying Neural-Network-Based Machine Learning to Additive Manufacturing: Current Applications, Challenges, and Future Perspectives. *Engineering* 2019;5:721–9. <https://doi.org/10.1016/j.eng.2019.04.012>.
- [1141] Zhang Y, Yan W. Applications of machine learning in metal powder-bed fusion in-process monitoring and control: status and challenges. *J Intell Manuf.* 2022. <https://doi.org/10.1007/s10845-022-01972-7>.
- [1142] Yan W, Lu Y, Jones K, Yang Z, Fox J, Witherell P, et al. Data-driven characterization of thermal models for powder-bed-fusion additive manufacturing. *Addit Manuf.* 2020;36. <https://doi.org/10.1016/j.addma.2020.101503>.
- [1143] Ness KL, Paul A, Sun L, Zhang Z. Towards a generic physics-based machine learning model for geometry invariant thermal history prediction in additive manufacturing. *J Mater Process Technol.* 2022;302. <https://doi.org/10.1016/j.jmatprotec.2021.117472>.
- [1144] Liao S, Xue T, Jeong J, Webster S, Ehmann K, Cao J. Hybrid full-field thermal characterization of additive manufacturing processes using physics-informed neural networks with data; 2022. <http://arxiv.org/abs/2206.07756>.
- [1145] Kozjek D, Carter FM, Porter C, Mogonye JE, Ehmann K, Cao J. Data-driven prediction of next-layer melt pool temperatures in laser powder bed fusion based on co-axial high-resolution Planck thermometry measurements. *J Manuf Process.* 2022;79:81–90. <https://doi.org/10.1016/j.jmapro.2022.04.033>.
- [1146] Akbari P, Ogoko F, Kao NY, Meidani K, Yeh CY, Lee W, et al. MeltPoolNet: Melt pool characteristic prediction in Metal Additive Manufacturing using machine learning. *Addit Manuf.* 2022;55. <https://doi.org/10.1016/j.addma.2022.102817>.
- [1147] Estalaki SM, Lough CS, Landers RG, Kinzel EC, Luo T. Predicting Defects in Laser Powder Bed Fusion using in-situ Thermal Imaging Data and Machine Learning; n.d.
- [1148] Gawade V, Singh V, “Grace” Guo W. Leveraging simulated and empirical data-driven insight to supervised-learning for porosity prediction in laser metal deposition. *J Manuf Syst.* 2022;62:875–85. <https://doi.org/10.1016/j.jmsy.2021.07.013>.
- [1149] Smoqi Z, Gaikwad A, Bevans B, Kobir MH, Craig J, Abul-Haj A, et al. Monitoring and prediction of porosity in laser powder bed fusion using physics-informed melt pool signatures and machine learning. *J Mater Process Technol.* 2022;304. <https://doi.org/10.1016/j.jmatprotec.2022.117550>.
- [1150] Du Y, Mukherjee T, DebRoy T. Physics-informed machine learning and mechanistic modeling of additive manufacturing to reduce defects. *Appl Mater Today.* 2021;24. <https://doi.org/10.1016/j.apmt.2021.101123>.
- [1151] Zhang T, Zhou X, Zhang P, Duan Y, Cheng X, Wang X, et al. Hardness Prediction of Laser Powder Bed Fusion Product Based on Melt Pool Radiation Intensity. *Materials.* 2022;15. <https://doi.org/10.3390/ma15134674>.
- [1152] Pandiyani V, Masinelli G, Claire N, Le-Quang T, Hamidi-Nasab M, de Formanoir C, et al. Deep learning-based monitoring of laser powder bed fusion process on variable time-scales using heterogeneous sensing and operando X-ray radiography guidance. *Addit Manuf.* 2022;58. <https://doi.org/10.1016/j.addma.2022.103007>.
- [1153] Huang X, Xie T, Wang Z, Chen L, Zhou Q, Hu Z. A Transfer Learning-Based Multi-Fidelity Point-Cloud Neural Network Approach for Melt Pool Modeling in Additive Manufacturing. *ASCE-ASME Journal of Risk and Uncertainty in Engineering Systems. Part B: Mech Eng.* 2022;8. <https://doi.org/10.1115/1.4051749>.
- [1154] Lapointe S, Guss G, Reese Z, Strantzis M, Matthews MJ, Druzgalski CL. Photodiode-based machine learning for optimization of laser powder bed fusion parameters in complex geometries. *Addit Manuf.* 2022;53. <https://doi.org/10.1016/j.addma.2022.102687>.
- [1155] Hemmasian A, Ogoko F, Akbari P, Malen J, Beuth J, Farimani AB. Surrogate Modeling of Melt Pool Thermal Field using Deep Learning; 2022. <http://arxiv.org/abs/2207.12259>.
- [1156] Hosseini E, Ghanbari PG, Müller O, Molinaro R, Mishra S. Physics Informed Neural Networks for Thermal Analysis of Laser Powder Bed Fusion Process; n.d. <https://ssrn.com/abstract=4189609>.
- [1157] Ren K, Chew Y, Zhang YF, Fuh JYH, Bi GJ. Thermal field prediction for laser scanning paths in laser aided additive manufacturing by physics-based machine learning. *Comput Methods Appl Mech Eng.* 2020;362. <https://doi.org/10.1016/j.cma.2019.112734>.
- [1158] Ansari MA, Crampton A, Garrard R, Cai B, Attallah M. A Convolutional Neural Network (CNN) classification to identify the presence of pores in powder bed fusion images. *Int J Adv Manuf Technol* 2022;120:5133–50. <https://doi.org/10.1007/s00170-022-08995-7>.
- [1159] Li S, Mo B, Wang K, Xiao G, Zhang P. Nonlinear prediction modeling of surface quality during laser powder bed fusion of mixed powder of diamond and Ni-Cr alloy based on residual analysis. *Opt Laser Technol.* 2022;151. <https://doi.org/10.1016/j.optlastec.2022.107980>.
- [1160] Phadke N, Raj R, Srivastava AK, Dwivedi S, Dixit AR. Modeling and parametric optimization of laser powder bed fusion 3D printing technique using artificial neural network for enhancing dimensional accuracy. *Mater Today Proc.* 2022. <https://doi.org/10.1016/j.matpr.2022.02.523>.
- [1161] Hu E, Seetoh IP, Lai CQ. Machine learning assisted investigation of defect influence on the mechanical properties of additively manufactured architected materials. *Int J Mech Sci.* 2022;221. <https://doi.org/10.1016/j.ijmecsci.2022.107190>.
- [1162] Dong G, Wong JC, Lestandi L, Mikula J, Vastola G, Jhon MH, et al. A part-scale, feature-based surrogate model for residual stresses in the laser powder bed fusion process. *J Mater Process Technol.* 2022;304. <https://doi.org/10.1016/j.jmatprotec.2022.117541>.
- [1163] Fang L, Cheng L, Glerum JA, Bennett J, Cao J, Wagner GJ. Data-driven analysis of process, structure, and properties of additively manufactured Inconel 718 thin walls. *NPJ Comput Mater.* 2022;8. <https://doi.org/10.1038/s41524-022-00808-5>.
- [1164] Yang Z, Yang M, Sisson R, Li Y, Liang J. A machine-learning model to predict tensile properties of Ti6Al4V parts prepared by laser powder bed fusion with hot isostatic pressing. *Mater Today Commun.* 2022;33:104205. <https://doi.org/10.1016/j.mtcomm.2022.104205>.

- [1165] Zhang Y, Zhao YF. Hybrid sparse convolutional neural networks for predicting manufacturability of visual defects of laser powder bed fusion processes. *J Manuf Syst.* 2022;62:835–45. <https://doi.org/10.1016/j.jmsy.2021.07.002>.
- [1166] Zhang Y, Yang S, Dong G, Zhao F, Assessment FZPM, Zhao YF. Predictive Manufacturability Assessment System for Laser Powder Bed Fusion Based on a Hybrid Machine Learning Model Predictive Manufacturability Assessment System for Laser Powder Bed Fusion Based on a 1 Hybrid Machine Learning Model 2, (n.d.). <https://hal.archives-ouvertes.fr/hal-03628383>.
- [1167] Francois MM, Sun A, King WE, Henson NJ, Tourret D, Bronkhorst CA, et al. Modeling of additive manufacturing processes for metals: Challenges and opportunities. *Curr Opin Solid State Mater Sci.* 2017;21. <https://doi.org/10.1016/j.cossms.2016.12.001>.
- [1168] Yan W, Lian Y, Yu C, Kafka OL, Liu Z, Liu WK, et al. An integrated process–structure–property modeling framework for additive manufacturing. *Comput Methods Appl Mech Eng.* 2018;339. <https://doi.org/10.1016/j.cma.2018.05.004>.
- [1169] Hashemi SM, Parvizi S, Baghbanijavid H, Tan ATL, Nematollahi M, Ramazani A, et al. Computational modelling of process–structure–property–performance relationships in metal additive manufacturing: a review. *Int Mater Rev* 2022;67. <https://doi.org/10.1080/09506608.2020.1868889>.